ROLLING CONTACT FATIGUE IN HEAVILY LOADED GEAR TRANSMISSION CONTACTS

by

Shaya A. Alshahrany

Thesis submitted in candidature for the degree of
Doctor of Philosophy at Cardiff University

Institute of Mechanics and Advance Materials
Cardiff School of Engineering
Cardiff University

November 2015

Declaration

The work has not previously been accepted in substance for any degree and is not being concurrently submitted in candidature for any degree.

Signed ……...…… (Shaya Awoda Alshahrany)

Date ……

Statement 1

This thesis is the result of my own investigations, except where otherwise stated. Other sources are acknowledged by the provision of explicit references.

Signed ……...…… (Shaya Awoda Alshahrany)

Date ……

Statement 2

I hereby give consent for my thesis, if accepted, to be available for photocopying and for inter-library loan, and for the title and summary to be made available to outside organisations.

Signed ……...…… (Shaya Awoda Alshahrany)

Date ……

Abstract

This thesis examines the influence of asperities such as found on the teeth of gears and discs, and failure mechanisms associated with rough surface Elastohydrodynamic Lubrication (EHL). The principal outcomes of the research provide a good insight into fatigue life, residual stress effects, damage prediction and surface contact failures. In particular, the study is intended to provide understanding into the residual stress distribution resulting from plastic deformation of surface asperities in the running in process. The residual stress is then added to the asperity elastic stress distribution and examined in detail to see the effects on fatigue damage and fatigue life. So, a theoretical model has been developed to assist design against the residual stress effect and surface contact fatigue, such as micropitting.

The technique used in the study starts with developing an elastic plastic model of the rough surface by using the Abaqus Finite Element analysis software package. This is a nonlinear problem and ranges of applied loads have been applied to the as-manufactured surfaces causing the asperity features to experience varying degrees of plastic deformation. The pre and post running roughness profiles are studied in order to assess the level of plastic deformation actually occurring at significant surface asperity features by aligning the pre and post running profiles. This results in a new technique that has helped to identify the level of plastic deformation occurring in the practice, and also to make a comparison with FEA contact analysis for the same asperity features to identify the appropriate residual stress field.

The residual stress field associated with the plastic deformation was extracted and evaluated. The extracted residual stress field was transferred to a form that facilitated

inclusion in stress evaluation code to obtain the stress history for the material subject to loading in an EHL contact.

The research carried out considers surface fatigue analysis with and without a residual stress field, so as to establish the influence of asperity plastic deformation on the fatigue properties of the surface. All the work is based on numerical simulation of surface fatigue failure in EHL situations and carried out numerically. The procedure can be applied quickly and gives the opportunity to apply several models and investigate the influence of all the model parameters on material deformation and fatigue life.

Acknowledgment

First of all, I would like to praise and thank Allah Glory to Him, the Exalted for helping me to complete this thesis.

Most especially I would like to thank my supervisor Prof. H.P Evans, who has provided a constant source of supports, encouragements and advice throughout my research and also for dealing with me as a colleague more than a student.

I would also like to thank my joint supervisors Prof. R.W., Snidle and Dr. Alastair Clarke for their continuous support and encouragements, and Dr. K.J. Sharif for his help in coding some of the software that has been developed for this work.

The work presented in this thesis would not have been possible without the financial support of the Saudi Cultural Bureau in London and RSAF in Riyadh.

My deepest gratitude goes to my parents, and I am also thankful for the endless support of my brothers.

Thanks are also due to my friends A. Alhemali, S. Alshehri, A. Alkrani and to all of my colleagues in the Tribology research group, in particular: Dr. H. Jamali for almost daily discussions about our projects and Dr A. Al Saffar for our useful discussions about Abaqus software.

Finally, but by no means least, I would like to thank my close family, my wife, my daughter and my sons who contributed in one way or another to make my time at Cardiff a memorable one.

Table of contents

Chapter 3
Simulation with Abaqus

Chapter 4
Abaqus analysis and profile repositioning

Chapter 7
Fatigue comparison with and without Residual Stress

Chapter 8
Conclusion and future work

Nomenclature

Symbol	Description	Units
a	Hertz dimension in *x* direction	m
b	Shear fatigue strength exponent	_
c	Shear fatigue ductility exponent	_
D	accumulated damage fraction	_
E	elastic modulus	Pa
E'	Effective elastic modulus	Pa
E_1 , E_2	Elastic modulus, surface 1 and 2	Pa
$F.B$	Fatemi and Socie Parameter, $F.B= \frac{\Delta\gamma_{max}}{2}\left(1+k\frac{\sigma_n^{max}}{\sigma_y}\right)$	_
G	shear modulus	Pa
HP	Hardness, $HP=3\sigma_y$	Pa
H	Hardening parameter $0.5 < H < 1.0.$	
k	Material constant with the range, $0.6 < k < 1.0.$	_
N_f	fatigue lifetime (cycle to fatigue failure)	_
p	Pressure	Pa
R_1,R_2	Radius of curvature, surface 1 and 2	m
v	Poisson ratio	_
σ_n	Normal stress	Pa
σ_n^{max}	The maximum normal tensile stress.	Pa
σ'_f	The fatigue strength coefficient.	_
σ_e	The fatigue limit or endurance limit.	Pa
$\Delta\sigma$	The stress range	Pa
σ_m	The mean stress	Pa
σ_a	The alternating stress (which is called stress amplitude)	Pa
σ_{xx} , σ_{zz} , τ_{xz}	material stress components	Pa
σ_y, σ_O	yield strength for the cyclic stress-strain curve	Pa
$\bar{\sigma}_a$	The effective stress amplitude.	Pa
σ_{ia} (i = 1, 2, 3)	The amplitudes of principal stresses.	Pa
σ_u	Ultimate tensile strength.	Pa
$\tilde{\sigma}_{f_b}$	The corrected true fracture strength.	_
τ'_f	Shear fatigue strength coefficient	Pa
τ_a	Shear stress amplitude	Pa
ε_a	Strain amplitude, $\varepsilon_a = \frac{\lvert\varepsilon_{max}-\varepsilon_{min}\rvert}{2}$	_

$\frac{\Delta\varepsilon_e}{2}$	Elastic strain amplitude.	–
$\frac{\Delta\varepsilon_p}{2}$	The true plastic strain amplitude.	–
γ	A material constant. $\gamma = -0.0002\,\sigma_u + 0.8818$.	–
γ_f'	shear fatigue ductility coefficient	–
γ_a	Amplitude of shear strain, $\gamma_a = \frac{\lvert\gamma_{max} - \gamma_{min}\rvert}{2}$	–
x	X Co-ordinate in the entrainment direction	m
y	y Co-ordinate transverse to the entrainment direction	m
w	Load	N
N.B. Other symbols are defined in the text when their use is local to the section concerned.		

Chapter 1

Introduction and background

1.1 Introduction

The study of fatigue near the top surface layer of the gear tooth contact, taking the deformation in the geometry and other factors that affect fatigue behaviour into account is of considerable interest in adding to the knowledge relating to the life of gear contacts. Gears tend to operate in the mixed lubrication regime where the tooth load is carried by a combination of fluid film pressure and boundary lubrication. The research in this study related to this situation provides beneficial observations about effects of residual stresses, fatigue prediction and the damage caused to the material. The phenomenon of the failure mechanism of the gear surface in contact is referred to as 'micropitting'. This kind of pitting failure takes place at the scale of surface roughness and can range from a mild form of wear to rapid crack growth ultimately leading to complete tooth failure. The failure mechanism is linked with rough surface Elastohydrodynamic Lubrication (EHL). This chapter introduces the scope of Tribology as well as the specialised area of EHL. This is followed by discussion of the thesis layout and the overall approach taken to contact fatigue modelling is introduced.

1.2 Tribology

1.2.1 History of Tribology

In 1966, Tribology was introduced as a conceptual term and given a definition, but the principles associated with it have been used since the first emergence of human kind (Dowson, 1998). Dowson provided a fascinating overview about the evolution and

early use of the technology associated with the features of Tribology. Looking as far back as 200,000 years ago, the first existence of human being in the Palaeolithic period was a practical use of the ideas and concepts covered by Tribology. Early man discovered that heat was produced when two pieces of wood were rubbed together; the resultant heat generated was due to friction and is probably the first proof of the application and awareness of an aspect of Tribology. A number of tribological ideas followed through the expansion of humanity and the emergence of the first civilisations. Nearly 7000 years ago, in the Neolithic period, bearings were the first tribological systems where stone, wood, antlers and bones were utilised in plain rotary drills and door hinges. In 3250 BC, the invention of the potter's wheel marked the usage of lubricants and an appreciation of the purpose of lubrication. Furthermore, remedies to cure 'wear' problems were also developed. Cart wheels have been found dating to around 2750 BC, with the outside of the wooden wheel encased within a metal band with copper nails firmly fixed into it. These concepts and components that make up a part of Tribology were recognised quite early in man's existence. Throughout the years of history, the investigation of these tribological phenomena has been focussed on smaller and smaller scales. Progress in this endeavour has taken place alongside developments in the tools of surface science. Appropriate tribological design has had a significant impact on component contact service life and efficiency (Dowson, 1998).

1.2.2 Definition of Tribology

Tribology was introduced as a separate scientific term in the UK Department of Education and Science report of 1966. Tribology is derived from the Greek word

'tribos' the literal meaning of which is 'rubbing'(Williams, 1994). The Department of Education and Science report defined Tribology in the following words: "The science and technology of interacting surfaces in relative motion and the practices related thereto". Tribology is the study of the interaction between bodies that come in to contact with one another. In a view expressed by Bhushan and Gupta, tribology can be further categorized into three broad areas: friction, wear and lubrication. A brief description of these three areas is given by Bhushan as follows (Gupta, 1991):

1.2.2.1 Friction

The resistance that takes place between two bodies at a contact interface related to a tangential relative displacement is the definition of Friction. There are three main causes of friction:

I. Adhesion.

II. Ploughing.

III. Asperity deformation.

These three components can be summed up to estimate the total friction to a reasonable accuracy. **Adhesion** refers to the galling trend of some materials. Connections are formed at sharpened contacts. These connections are fractured by relative motion. Therefore, adhesive friction is a function of interfacial shear strength. The phenomenon of **ploughing** may happen due to two reasons: when one body is considerably harder than the other, or when hard particles like oxides are present. Due to the property of plasticity, the softer material starts to deform under the effect of the traverse of the hard particle or asperity which 'ploughs' across the softer surface leaving a furrow in its wake. This friction component is basically a function of the tough asperity geometry; however as wear develops, the geometry is changed by the

accumulation of material on the plough. This can explain to an extent why friction coefficients can vary as wear progresses (Rabinowicz, 1966). Lastly **asperity deformation,** forms an important part of the overall friction in metallic contacts (Gupta, 1991). As surface contacts slide across each other the distortions in asperities will take place so that compatibility is maintained. The three categories of the friction components depend on the plasticity property which is a complex subject and plays a key role due to its permanent and dissipating nature. It is therefore to be expected that the friction coefficient is a function of the original material conditions (material combination, heat treatment, surface roughness, and a number of environmental variables and their values such as sliding velocity, sliding distance, normal load and temperature, etc.). From the stated arguments it is clear that friction is a difficult phenomenon and a model for forecasting the friction encountered under an extensive range of different environments has not yet presented.

1.2.2.2 Wear

The deformation mechanisms linked with friction as elaborated above result in damage being caused to material close to the contact interface. Ultimately, this leads to particle detachment, which on the whole is regarded as wear. Therefore, wear can be defined as the removal or dislocation of material from surfaces in contact as a consequence of mechanical, electrical, or chemical actions, the causes of which contribute to the total friction and are also characteristic of wear mechanisms since the material close to the contact interface is removed. Bhushan & Gupta express the view that wear can be specified as belonging to six main categories including causes of friction (adhesion), and others such as abrasion fatigue, erosion, corrosion and electrical arcing (Gupta, 1991).

1.2.2.3 Lubrication

A lubricant is a material introduced into a tribological contact for the purpose of reducing friction and wear. It can be solid, liquid or gaseous. In general, it is comprised of base oil and additives with its properties dependent upon several parameters such as chemical, environmental, thermodynamic, rheological, and additive response properties (Pettersson, 2007). When choosing a lubricant, it is important to consider the properties of performance, environment and longevity. Long life properties will impact on the surface life, while environmental properties (toxicity, bioaccumulation and renewability, etc.) of a lubricant will have a very long sustainable influence even after the product has been taken out of service (Torbacke and Kassfeldt, 2014).A number of functions are performed by lubricants such as reduction of friction, heat transfer, wear control, transporting away debris and contaminants from the contact, preventing corrosion, and the reduction of noise and vibrations.

1.3 Failure models of EHL contact

According to Johnson (1989), the composite nature of rolling contact makes the main modes of failure difficult to divide between individual failures modes. In general, failures occur in components that rely on EHL to function, the reasons being design and external factors along with others that are relevant to the breakdown in the EHL mechanism. Consequently, the main modes of failure in rolling contact surfaces comprise of plastic deformation, wear, contact fatigue, corrugation and scuffing. Contact fatigue is the surface damage process that leads to crack formation at the contact surface or immediately below the surface. Other rolling contact fatigue failures are discussed in detail in the following sections.

1.3.1 Pitting

When microscopic surface scratches and cavities are formed as a result of rolling and sliding contact fatigue, the phenomenon is called pitting. If full EHL film circumstances are achieved and friction at the surface is comparatively small, pitting may build up under the surface; this is principally in the region of the highest subsurface stress because of the Hertzian contact pressure. Pitting is a type of fatigue effect and does not generally come about early in the component's life. Pits usually occur at asperities or at the points on the surface which are subjected to high stresses which have a tendency to encourage cracks which propagate, thus getting rid of the high points in an erosive manner. Prevention of pitting can be achieved by decreasing the operating loads or by increasing the hardness of the surface. Another point of consideration is that pitting can also occur in the area of impurities or inclusions that are weaker in comparison to the surrounding material. Micro-pits have become something of concern because unlike normal pits which are about 0.3mm or more in diameter and related to the Hertzian contact dimensions. Also, Micro-pits are at the scale of the asperities and their diameters fall into the measurement order of microns (Snidle et al., 2004). An example of pitting in gear contacts is shown in figure 1.1 where the spur Gear operating surfaces are badly pitted over the whole of the tooth surface in the left hand example. The right hand case shows in large scale of surface pitting which often caused by wear not exceeding 0.3 to 0.5mm in depth.

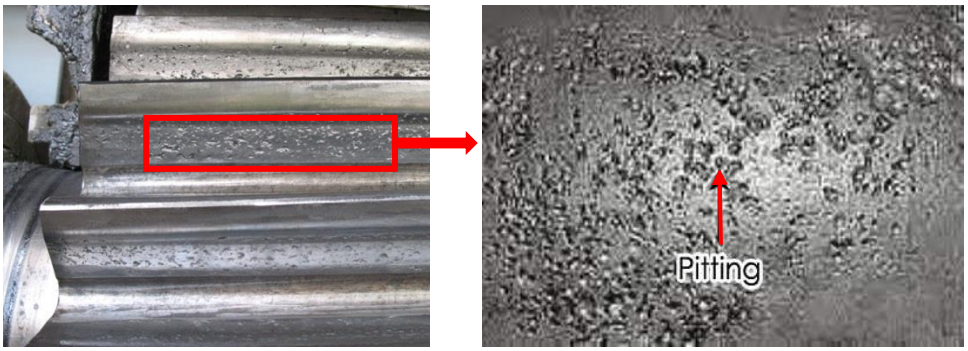

Figure 1.1- Gear surface pitting failure (Novexa.com, 2015).

1.3.2 Micro pitting

Micropitting is a type of fatigue failure mechanism whereby cracks propagate at a low angle to the surface and the depth of the pits is only a few micrometres. It is said that micro-pitting occurs due to creation of thin films that are themselves a consequence of the application of high loads and temperatures. The micro-pitting is not perceptible to the naked eye, but it can usually be seen in the form of a grey stain or frosting appearance on the surface. Micro-pitting is a fatigue-effect that occurs in a similar fashion to that of pitting, whereby cracks are formed at the edges of the asperities which propagate to eventually form micropits. Micro-pitting can easily vanish when surfaces are polished. Micro pits are shown in Figure 1.2a, and Figure 1.2b which shows cracks with branching. The entrance angle of the crack is 20-30° in the direction of rolling which is near to what Alfredsson et al. found during their study on the function of a single surface asperity in rolling contact fatigue (Alfredsson et al., 2008).

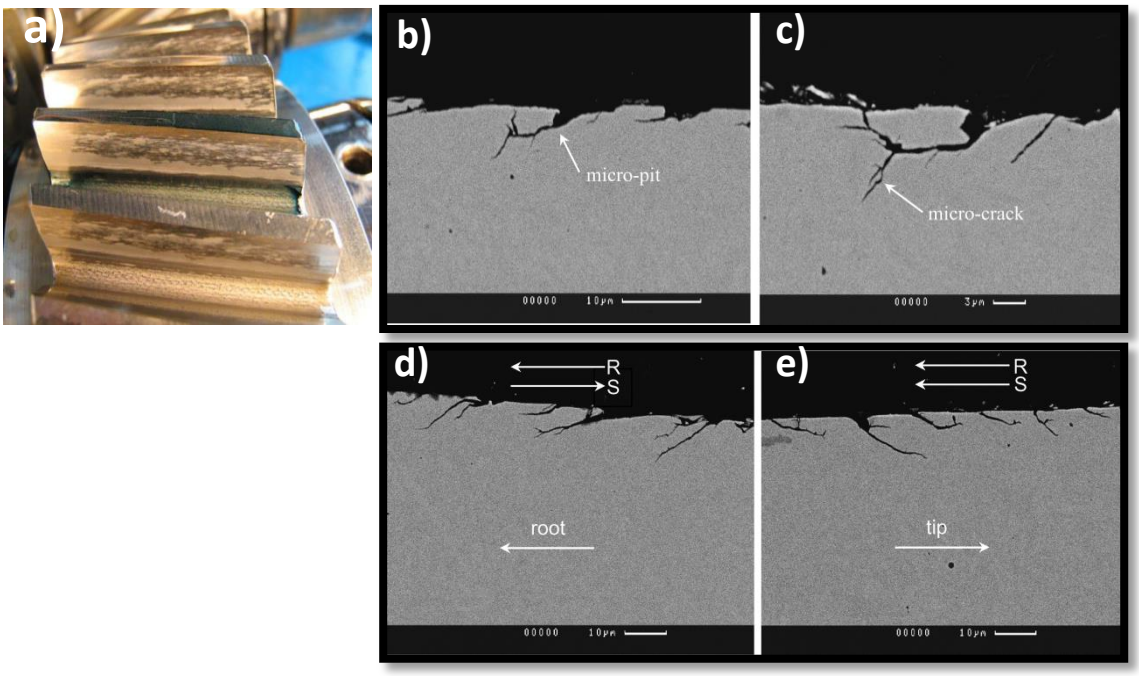

Figure 1.2 - Micropitting failure; a) Helical test gear tooth Micropitting that predominantly in the dedendum region, b-c) Crack growth Sections through micropits, d-e)Sections through micropits showing the characteristic direction of cracks in the dedendum (left) and addendum (right) of the same tooth on the driven gear. Arrows above the surface indicate the rolling contact direction and of the sliding traction with (R), and (S) respectively acting on the tooth (Evans et al., 2012).

1.3.3 Scuffing

Scuffing is a potential failure marked by roughing bands in the involute profile direction that can cause severe adhesive wear as shown in Figure 1.3. In general, the failure approach of scuffing is based on the occurrence of micro-welding and a crucial contact temperature between asperities occurring at which the lubricant film fails. Scuffing usually occurs earlier in the component's life. Concerning gears, scuffing is generally seen at the tip and root of the gear teeth where high sliding is experienced. Scuffing takes place only in systems where the velocity of the two surfaces produces a comparative sliding velocity. When there is no relative sliding in the system, components are prone to fail mainly because of pitting. When scuffing is starts to

occur, the surfaces transform rapidly producing more heat, which can directly cause further scuffing; hence a catastrophic failure becomes probable as a result.

Figure 1.3 - Scuffing due to metal parts rubbing each other at gear teeth.(Novexa.com, 2015)

1.3.4 Running in

The mild wear condition is a good representation of running-in of the surface. In many applications, a running-in of the surfaces can be regarded as normal to mild wear. Flodin pointed out another notable point that mild wear is likely to perform as a catalytic agent for fatigue wear (Flodin and Andersson, 2000). Lately, the mild surface wear of gear flanks has achieved more importance which is because of rapid progress in modelling capabilities and improvements in engineered surface technologies which may include chemical polishing, thin film coating and shot peening. The running-in of the surfaces might be referred to as mild wear or a normal wear condition having a positive effect on the gear performance and service life. On the negative side, this mild wear of material can also trigger surface fatigue, as argued by Flodin (Flodin and Andersson, 2000). Pre-running of the surfaces that has been extensively explored by tribologists is another technique that might be used to reduce the occurrence of scuffing so as to enhance the overall performance. This is commonly referred to as 'running in'. When components are running against one another, a reduced friction

takes place between the components. 'Running in' has the ability to improve the surface topography. Ostvik and Christensen showed that components subjected to running-in can carry a greater load under similar operating conditions in comparison to the components prior to running in (Östvik and Christensen, 1968). In general, 'running in' is carried out at lower loads and, at times, at lower speeds. These loads and speeds are gradually adjusted to the operation settings in phases. The 'running-in' process facilitates the removal of asperity peaks, metallurgical processes like strain hardening, and the formation of oxide layers which can assist in surface protection. Lately, 'running in' has been accompanied by various types of oil which the parts are intended to run with. This enables more uniform surfaces to be developed that offer better resistance to most type of failure such as scuffing (Paliwal, 1987).

1.3.5 Spalling

A macro-scale type Hertzian contact fatigue is 'spalling' which results in the creation of macroscopic hollows in the contact region. Spalling is the same as subsurface pitting, but the spalled areas are greater. It is a general assumption that spalling occurs due to overload situations when destructive pitting takes place in the dedendum part of gear teeth and does not stop, as in the case with normal pitting. The ends of pits can disintegrate and then large asymmetrical shapes are formed that can connect with one another. This sort of surface impairment is called spalling and takes place chiefly due to high contact stresses. However, it can also be prevented through an increase in surface hardness in addition to a reduction of the operating load (Halme and Andersson, 2010).

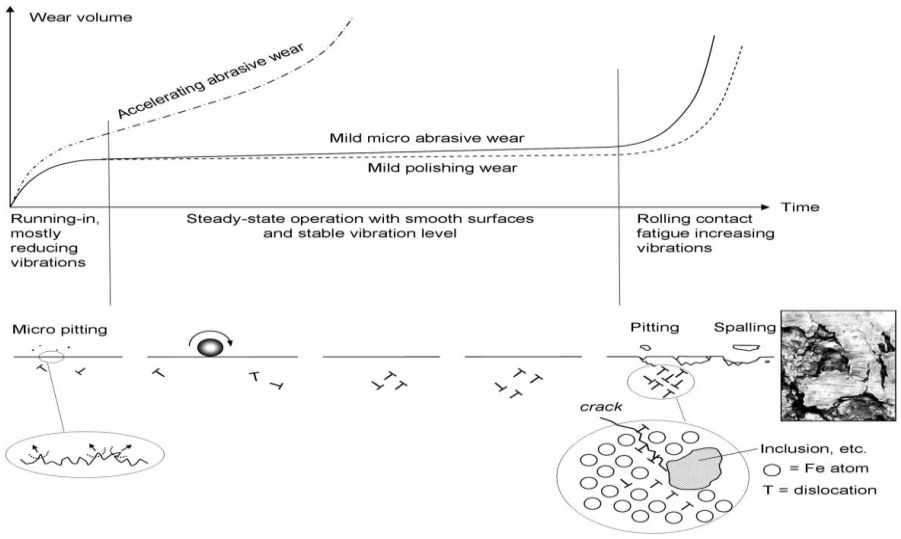

Figure 1.4 - The two figures incorporated show wear volume accumulation from running-in towards rolling contact fatigue failure (spall formation) at the rolling bearing raceway surface and subsurface (rolling contact fatigue failure in roller bearing photograph inserted) (Halme and Andersson, 2010).

1.4 Software uses in research

The research reported in this thesis deals numerically with the study of the profile alignment, importing profiles into Abaqus/CAE to investigate the effect of running on asperity shapes which are modified by plastic deflection. Fatigue calculations are carried out based on surface loading derived from micro or mixed EHL analyses, and these fatigue calculations are also carried out taking the residual stress from asperity plastic deformations into account. All the work is carried out numerically using Macros within the Excel spreadsheet, the FORTRAN programing language and MTLAB in the result analysis. These allow the procedure to be applied quickly and give the researcher the opportunity to apply several fatigue models and investigate the influence of all the model parameters on material deformation and fatigue life. At the beginning of this research, the author had access to available fatigue programme software and Abaqus Scripting Interface commands and a developed Excel Macro used to generate rough surface profiles for export to the Abaqus system. These software

tools had been developed by Qiao for the cumulative fatigue damage calculations(Snidle et al., 2008), and by Bryant for the Abaqus rough surface creation using a Python script (Bryant, 2013).

In this research new subroutines were encoded and introduced to the fatigue damage program to include a number of other Fatigue models which are named in section 1.5 and were suitable to be formulated using the accumulated damage approach. Each fatigue model subroutine can identify and sort points of interest in fatigue analysis, isolate the pressure and shear stress experience for areas centred on these points (asperities), isolate the cycles for the damage calculated for these points , rank the cycles by damage and has the flexibility to calculate the fatigue damage with or without including the residual stress. The software that determines stress analysis history based on the EHL simulation surface loading has been developed in by the Cardiff tribology research group in association with the software for transient EHL analysis of rolling sliding contacts of rough surfaces (Snidle et al., 2008) (Sharif et al., 2012). This stress history is obtained for a near surface block of material containing the asperities under consideration.

1.5 Research methodology

The overall contact fatigue modelling methodology consists of four major components that were successfully integrated in this research. These components are contact simulation with Abaqus, profile alignment to establish the residual stress for the rough surface material, and the fatigue calculation with and without residual stress. Each phase of this analysis has its own steps, including research and literature review. The outcome of all this work matches what has been observed in experiments and

literature reviews. In particular, micropitting, plastic deformation, material damage, and the effect of residual stress are all captured well by the numerical model. The individual steps, mentioned above, are now outlined.

- The research conducted line contact EHL analyses of centre line conditions in disk experiments carried out by Cardiff tribology research group (Weeks, 2015), and corresponding rough surface contact models were created.

- The research conducted with ABAQUS contact analysis was the following:

  - Create rough surface contact models using profilometer data to specify the roughness profile.
  - Develop rough surface contact models benchmarking and checking results by comparison with literature review and Cardiff tribology research group (Bryant, 2013).
  - Introduce elastic perfectly plastic and then elastic plastic behaviour.
  - The variation of the asperities with the associated damage in the research was examined by viewing curves and contours using the ABAQUS drawing tools (Abaqus CAE).
  - Research was conducted with ABAQUS into contact analysis and residual stress distributions were extracted at different loads.

- Residual stress at asperities due to different loads was investigated, and the residual asperity shapes drawn and aligned with the profiles obtained from experiments.

- The level of residual deflection observed in experimental tests was used to determine the appropriate level of residual stress to be added to the asperities.

- The residual stress in the region of interest evaluated on the irregular Abaqus FEA mesh has been interpolated onto a uniform mesh so as to be prepared for the fatigue analysis.

- The research used EHL simulation software to determine the surface loading on the material considered so as to calculate and extract the stress history of a near surface block of area containing the asperities under consideration.

- The residual stress was added to the stress history for EHL model results of test disks data and then used in the fatigue analysis so that the results obtained with and without the residual stress could be compared.

- The residual stress added to the asperities at specific levels was analysed and examined in detail to see its effect on fatigue damage.

- Numerically, the fatigue program was amended and new subroutines were developed to identify high damage points on or near the surface, and sort the points by damage value. This enabled the most highly damaged locations to be examined in detail.

- For the significant points the effective loading cycles were isolated with the corresponding contribution to the accumulated damage and ranked to see which cycles cause most of the damage.

- The research was applied using the available fatigue model (Fatemi and Socie) and compared the Fatigue Parameter obtained by using the critical plane model for two model parameter cases.
- The fatigue program was extended with new subroutines to include a number of other Fatigue models identified in the chapter 6 (Fundamental of fatigue) (listed below) which could be used with the accumulative damage approach, and then fatigue damage and predicted fatigue lives have been calculated.

  - Smith, Watson and Topper approach (SWT (cp)).
  - Chu approach.
  - Goodman approach.
  - Marrow approach.
  - SWT approach.
  - Fatemi and Socie approach.
  - Von Mises approach.
  - Walker approach.
  - Smith, Watson and Topper approach Modified (SWTM).

1.6 Research Objective and aims

The general objective of this research is to study fatigue in mixed EHL line contact based on numerical simulation methods. This leads to a failure of contact surface called micropitting, which is a pitting failure that occurs at the scale of the surface roughness. It can be a mild from a wear but it can lead to a rapid crack growth and complete tooth failure. The principal aims of the research are to provide insight into residual stress effects on fatigue life and surface contact fatigue failure such as micropitting.

1.7 Thesis Organisation

Figure 1.5 illustrates the key elements of the work in this thesis, which presents the fundamental aspects of calculating fatigue life and damage prediction with and without residual stresses. The following listed chapters present the numerical work, theory, methodology and results. Finally, conclusions are drawn and guidance related to future work is given.

Chapter 1 is an overview of the knowledge of the tribology system. This is based on a literature review and books, and also on modules held in Cardiff's School of Engineering.

A literature review relating to rough surfaces and their contact is presented in Chapter 2, which focuses upon areas particularly relevant to this work. This includes tribological problems, damage prediction due to fatigue, residual stress, surface effects, proposed models and the methods used to solve them such as Finite elements.

Chapter 3 is dedicated to investigating the capabilities of a commercial Finite Element analysis package, Abaqus, to model advanced contact problems. Of importance to this thesis is the ability of the package to model the behaviour of the significant asperities on the surface when the local load exceeds the elastic limit. A further challenge is to capture the varying degree of the plastic deformation experienced by the asperities. And then the process of developing different Line contact models involves superimposed profile of roughness.

Chapter 4 presents a detailed analysis of the results and compares experimental observations of plastic deformation in a number of manufactured surface profiles with the profile of the manufactured surface that has been subjected to FEA. Furthermore, the residual deflection was used to determine the appropriate level of residual stress

to which the deformed asperities would be subjected. So, the data for the residual stress from the FEA model is extracted and used later in an overall fatigue analysis in order to investigate the effect of the residual stress on the fatigue life.

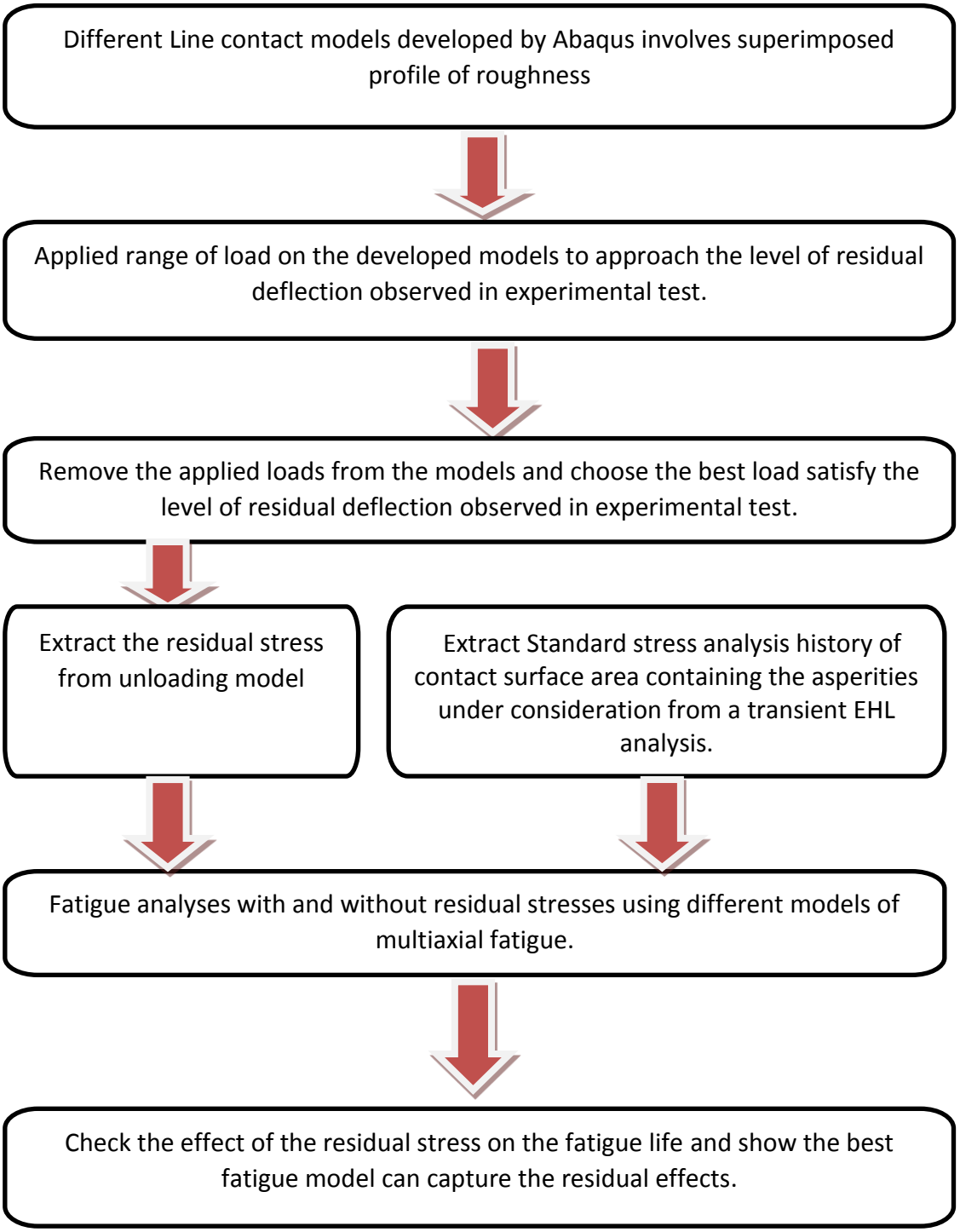

Figure 1.5 - Basic elements of the thesis layout that predict fatigue damage and residual effects under EHL condition.

Chapter 5 starts with a review of mechanical contacts behaviour of the effect of the loads on small contact area. Then it presents a detailed analysis of individual asperity contacts and results of the comparison of residual stress occurring at the surface following contact loading. Also, it shows the process of interpolating the FEA residual stress components that was subsequently used in in the fatigue calculations. Finally, the residual stress components for sample of asperities are investigated, looking for relationships between the asperity damage findings found in the literature and the residual stresses found at the asperities

Chapter 6 introduces some theories of fatigue and investigate the capability of some well-known multiaxial models in fatigue life prediction. These models are evaluated numerically in the area near rough surface contact of the simulated body and also incorporate methods for accumulation of fatigue damage.

Chapter 7 describes the implementation and comparisons between the models of multiaxial fatigue criteria introduced in chapter 6. These models evaluate the fatigue analyses with and without residual stress, where the residual stress distributions are extracted from the FEA of the simulated contact of the body. These implementations and comparisons between the models allow the effects of residual stress on the fatigue life calculations to be evaluated and investigated.

Chapter 8 summarises the conclusions that can be drawn based on the research carried out and also suggests ways in which future work can be carried out to build on the methods developed.

1.8 Contributions

This research was developed using some existing software tools that were available within the research group. These were tailored to the project requirements as necessary and enhanced where new features were required. The contribution made by the author is summarised in Table 1.1.

Table 1.1 . Summary of research's contributions.

	Contribution description
1.	Developing a new technique for determine the Residual stress and aligning the pre and post running roughness profiles, taking the distortion introduced by the profile filtering process into account.
2.	Development of an elastic plastic model of the rough surface by using the Abaqus Finite Element analysis software package that is considered an effective simulated model for the running-in effects in rough surfaces.
3.	Evaluating the strong link between the residual stress effects and: • The material metallurgical features that are subject to plastic deformation. • Mechanical contact surface failure such as micropitting.
4.	The comparative study of different multiaxial fatigue models for mixed EHL contact conditions.
5.	Developing a new version of a fatigue damage program to include : • New fatigue model incorporated. • Inducing residual stress to the EHL stress history. • Subroutines that provide a detailed breakdown of the load cycles identified at specified positions. • A subroutine to Isolate the effective cycles for the damage and show how much damage is produced by each effective cycle.

Chapter 2

Literature review

2.1 Introduction

One of the issues of concern to tribology research concerns study of the "mixed lubrication" regime where the load is supported by two mechanisms, pressure generated in the (elasto) hydrodynamic lubricant film, and direct interaction of surface roughness features present on the contacting surfaces. As it involves direct interaction of asperities this aspect needs to be understood more fully as it is known to generate very high local contact pressures and is likely to be associated with failure of the lubricated contact by a variety of means. The drive to increase efficiency of lubricated contacts has led to use of lower viscosity lubricants so that the frictional losses due to viscosity at the contacts are reduced. Consequently, thinner lubricant films occur in the Elastohydrodynamic contacts. As a result the amount of mixed lubrication in machine element contacts has become more prevalent in spite of its disadvantages. Therefore, it has become fundamental to understand the nature of such contacts and their effects on the environments of the surface, and the life of machine elements such as bearings and gears. The literature review presented in this chapter relates to the environments of the surfaces, fatigue life, residual stresses and tribological problems of mixed lubrication, and focusses upon areas relevant to the asperity contacts under elastic-plastic conditions and corresponding finite element (FE) simulations.

2.2 Elastohydrodynamic lubrication

Elastohydrodynamic lubrication, EHL, is the one of the main branches of the Tribology field. It is the lubrication mechanism that protects contacts between non-conforming

surfaces that are subjected to significant loads. Contact between surfaces is classified into two categories: conforming contacts and non-conforming contacts. Journal bearings are examples of conforming contact elements that fit exactly or closely together before any deformation occurs. A non-conforming contact occurs if contact of the surfaces under zero load happens at a single point or along a straight line. The surfaces have different shapes and under load elastic deflection will occur so that the point or line contact expands to a small area which will carry the load by developing high compressive contact stresses at the interface. The contact area formed is a very small area compared to the size of the contacting elements which leads to highly concentrated stresses and significant elastic deformation of the contact surfaces. The lubrication of such contacts is influenced by the elastic deflection of the surfaces together with the hydrodynamic behaviour of the lubricant, hence elastohydrodynamic. The most common contacts falling into the EHL regime are highly loaded EHL contacts such as those between gear teeth and rolling element bearing components. Accordingly, surface roughness plays a vital role in the occurrence of surface failures such as micropitting (Dowson, 1998). Most failures of surface contact with an EHL lubricant film take place in a mixed EHL regime in which the asperities on the two surfaces come into contact as will be explained in the next section. In order to develop knowledge of the stress history experienced by the contacting material that may lead to surface fatigue, it is essential for the given load to calculate the pressure generated between the contact surfaces. Generally in heavily loaded machine elements the applied loads create pressure distributions of GPa order. Since the material passes through the contact in less than a second the pressure can be very difficult to measure experimentally as, at best, it will rise from zero to the maximum

value and fall back to zero during this time. At the same time the lubricant film thickness can be exceptionally thin, of μm order, and is also very difficult to measure experimentally. Research into EHL problems comprises a combination of experiments in terms of surface profile and film thickness measurements, and numerical simulations of the contacts taking as many of the relevant factors as possible into account. Validation of numerical methods by relating them to accurate experiments then allows the numerical techniques to be applied to examples where experimental measurements within the contact area are extremely difficult.

2.2.1 Effects of Surface roughness EHL

The formation of a lubricant film that completely separates the two contact surfaces is the major difference between dry and lubricated friction. However finely a machine element is manufactured the contacting surfaces exhibit roughness features which influence the contact when the lubricant films are sufficiently small. Krantz et al. (2001) showed strong evidence that superfinishing the gear flank surfaces by reducing the roughness average by about a factor of 5 improves the surface fatigue lives of gears significantly. They found the lives of gears with superfinished teeth were about four times greater compared with the lives of gears with ground teeth but with otherwise similar quality. Another paper by Evans and Snidle (1996) suggested a physical mechanism of scuffing failure based on the surface roughness when complete loss of film lubricant between the asperities in a real contact at the boundaries of the contact area. They showed that failure of this kind can occur due to leakage from the valley features in the transverse direction at the edges of a real elliptical contact. Analysis of idealized valley geometries leads to criteria for significant loss of pressure

between asperity contacts. The failure mechanism (scuffing) proposed is that of sideways leakage of the lubricant in the gaps that are present between the surfaces due to the surface roughness valley features.

Björling et al. (2011) conducted a friction test rig for evaluating and presenting contact friction behaviour in EHL tribological systems with respect to surface roughness, temperature, and oil parameters under various running conditions. The results showed that different types of friction may occur in an EHL contact and can be strongly influenced by changing surface roughness as well as base oil viscosity, base oil type, extreme pressure EP additive content, and operating temperature. This paper concluded that if smoother surfaces are used the transition from full film to mixed lubrication conditions will occur at a lower entrainment speed.

Sharif et al. (2012) use numerical models to investigate the effect of lambda ratio, **ʌ,** which is the ratio of the smooth surface film thickness to the composite surface roughness average. This ratio is normally less than unity when the nominal lubricant film thickness is small compared to the roughness present on the surfaces. These conditions occur in most types of gear tooth contacts and in many other heavily loaded machine elements when they are operating in mixed lubrication. This paper showed lubrication formation conditions that occur at the roughness asperity level (micro-elastohydrodynamic lubrication), and in extreme cases 'mixed' lubrication behaviour in which momentary solid contacts between the surface asperities take place. The paper presents the results of the modelling and shows the effect of lambda ratio in lubricated gear tooth contacts, demonstrating the transition from full-film to micro-

elastohydrodynamic and to mixed lubrication, and the consequences in terms of predicted fatigue damage.

He et al. (2015) modelled 3D plastic-elastohydrodynamic lubrication (PEHL) simulations for contacts taking into account possible plastic deformation and the effects of surface roughness. The analyses considered numerical cases in order to reveal the PEHL characteristics in different types of line contact. It found that 3D roughness and geometric modifications can greatly influence the lubrication characteristics.

Chiefly depending on the thickness of the lubricant film, a system is prone to respond in different ways and according to Olver (2002) three regimes can be defined due to the influence of surface roughness as the following:

2.2.1.1 Micro-EHL

In this regime, the surfaces are completely separated by a continuous full film lubricant; no metal contact takes place while the friction is only caused by shear forces in the viscous lubricant (Bernard J. Hamrock, 2004). Although there is uninterrupted full-film lubrication, the pressure and film thickness are formed and subjected to significant local fluctuations owing to the surface roughness. Consequently, the friction coefficient depends mainly on the film separating them because the surfaces are basically apart.

2.2.1.2 Mixed lubrication

In contrast to the first regime, this type has a discontinuous fluid film. So a fraction of the load is carried by pressure in the hydrodynamic film and some of the load is supported by the contact pressure between the asperities which represent the parts of the surfaces that make direct contact without the help of a hydrodynamic film. The

friction coefficient in this regime is generally affected by the properties of the fluid along with the mechanical properties of the contacts (Halme and Andersson, 2010). Considering the prospective of the asperities, coming into contact with each other, some surface asperities deform plastically and some only elastically.

2.2.1.3 Boundary lubrication

The boundary lubrication regime refers to cases where any lubricant present is limited to the valleys and takes a negligible proportion of the total load. The load is mainly carried by the surface in contact (asperities) so, full contact (solid-solid contact) is achieved in the equivalent Hertzian contact area. Under this regime, the friction coefficient is high, where the mechanical properties and nature of the junctions are the defining criteria for the friction coefficient. The collisions between the asperities of the two surfaces in contact produce friction, heat and wear. The reduction of friction and wear depends on the lubricant chemistry, while the fluid film has no effect (Korres, 2013).

Figure 2.1 is schematic illustration of the progression of a contact from boundary to full film lubrication conditions as the amount of lubricant separating the surfaces is increased. The progression can be due to a number of factors and is easily achieved by increasing the entrainment velocity of the contact, for example.

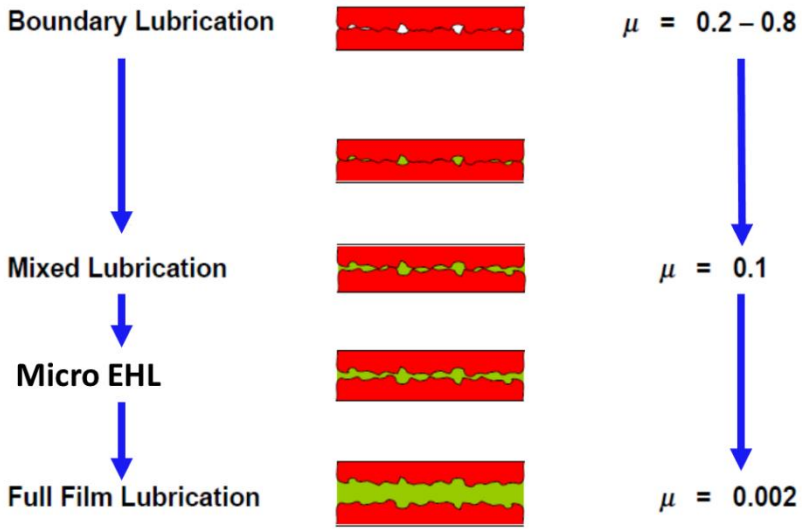

Figure 2.1 – Schematic illustration of the effect of lubrication in bearings showing all types of lubrication regime: Boundary, Mixed, Micro EHL and Full Film Lubrication in sequence together with representative friction coefficients, μ. The rough surfaces in contact are shown in red and the lubricant in green.

2.3 Cyclic contact (shakedown)

Most practical applications of rolling contact have to withstand many repeated passes of the loads which mean their materials are loaded repeatedly such as on roller bearings or a railway track. Shakedown is a process which takes place through repeated loading, which generally makes the pure elastic condition become the steady cyclic load state whereby initial plastic deformation introduces residual stresses. If the material goes through many passes or cycles, the plastic deformation will take place when the first pass exceeds the elastic limit. Consequently, some of the residual stresses will remain in the effected material when the load is removed. In the second cycle, the material experience a load corresponding to the system of residual stress that is left behind from the first cycle and the applied load for the second cycle. In general, the protective residual stress can make yield less likely in the second cycle than was its value in the first cycle, so it is possible that after a number of cycles the

residual stresses build up to such values that the applied loads in the subsequent passes can be carried entirely elastically. To examine the occurrence of the shakedown we can refer to Melan's theorem of stress analysis (Johnson, 1985) which states that If any time independent distribution of residual stress is available which, together with the elastic stresses due to the load, constitutes a system of stress which is everywhere within the elastic limits of the material, then the system will shakedown. However the system wills not shakedown if there is no such distribution of residual stress can be found.

For the assumed elastic-perfectly plastic material, the maximum unloading stress must be less than $2\sigma_y$, where σ_y is the yield of material strength (Fatemi A. et al., 2000). A key factor to be noted in residual stresses is the sign of its direction after unloading. The protective or the desirable residual surface stress is that if the surface region yields in tension during loading, so the residual surface stress will be in compression after the load is removed. On the other hand, the point that we consider in this research and the threat coming from its effect is that the residual surface stress will be in tension after unloading as a result of the compressive yield of the surface upon loading, which is undesirable. Near the surface of the objects in contact, or close to material discontinuities (voids and fillings), the stresses are much higher than the supposed Hertzian stresses and it is here that cracks are most likely to nucleate .The residual stress in a tensile state will accelerate and encourage the cracks to propagate. According to the shakedown theory as shown in Figure 2.2 (Kapoor and Williams, 1994), when a material is loaded repeatedly, the material will gather damage if the stress cycle exceeds a limit termed as the 'shakedown limit' . These authors present the concept in terms of wheel rail-head contacts in railway applications.

If the load is below the elastic limit, as illustrated in fig 2.2(a), then there is no plastic flow and failure will occur due to high cycle fatigue. If the elastic limit is surpassed but the load is below the elastic shakedown limit, then there will be initial plastic flow during the early cycles. This will cause residual stresses to build up and the rail head material will work harden. The rail head shape may also transform sufficiently to reduce the contact stresses in subsequent load cycles. The result of this shakedown process is that after the initial cycles the load is carried elastically so that the failure mode will again be high cycle fatigue.

If the load cycle is higher than the elastic shakedown limit, then each cycle will give an incremental plastic flow, which will lead to low cycle fatigue if the cycles are below the plastic shakedown limit. If this limit is exceeded then failure will occur due to plastic ratcheting. One point related to shakedown that is worth considering through the study of asperity and surface changes is that surface micro-roughness and material microstructure can lead to very high stresses near the contact surface (within around 0.05mm of the surface) and therefore shakedown theory is not accurately valid in this section.

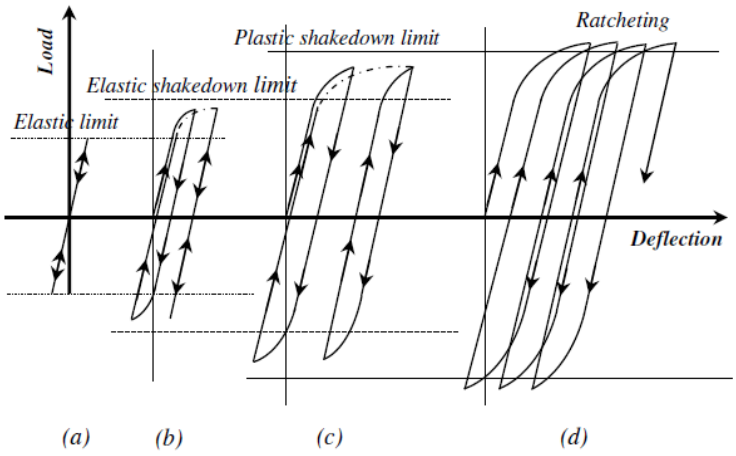

Figure 2.2 – Illustration of the effects of Cyclic loading with a non-zero mean load on the material; (a)Perfectly elastic, (b)Elastic Shakedown, (c)Plastic shakedown, (d)Ratcheting (Kapoor and Williams, 1994).

2.4 Finite element analysis techniques

Green (1955) was the first to model the asperity friction by making two important deductions. The first is that in steady state sliding the two objects must move parallel to each other. The second is that the asperities studied cannot be wedge shaped with rigid-perfectly plastic behaviour as assumed by a number of researchers (Challen and Oxley, 1979, Edwards and Halling, 1968, Torrance et al., 1997).

Researchers then started to use finite element (FE) analysis of elastic–plastic cylindrical and spherical asperities to address the shortcoming in the previous studying and to predict friction coefficients of asperities. Various scientists then applied the FE method to different models; some involving cylindrical asperities, others spherical ones, whilst some involved both. Tangena AG. and PJM. (1985) were the first to apply the finite-element method to model the sliding interaction of two cylindrical elastic–plastic asperities moving in parallel. They studied both the frictionless and frictional cases. Faulkner A. (2000), were subsequently the first to develop a 3D elastic – plastic asperity interaction model using the finite-element method. This model involved two elastic–plastic strain hardening spherical asperities and it was investigated in frictional, frictionless condition, and with a small interfacial friction coefficient (f=0.1) at three different overlap positions. In a former model by Tangent and Wijnhoven (the sliding interaction of two cylindrical elastic–plastic asperities moving in parallel), all asperities had the properties of aluminium and they found that as the asperity overlap was increased, the predicted friction coefficient also increased.

The model developed by Mulvihill et al. (2011) shown in figure 2.3 involved both cylindrical and spherical shaped asperities but, it differed from previous models by

examining asperities with greater degrees of overlap and increasing interface adhesion shear strength, whilst also loading the contacts to the point of material failure. This model was used to predict friction coefficients for a stochastic rough surface. The results of this study suggest that including tangential interface adhesion and plasticity increased friction and the authors were able to obtain good agreement with experimental values.

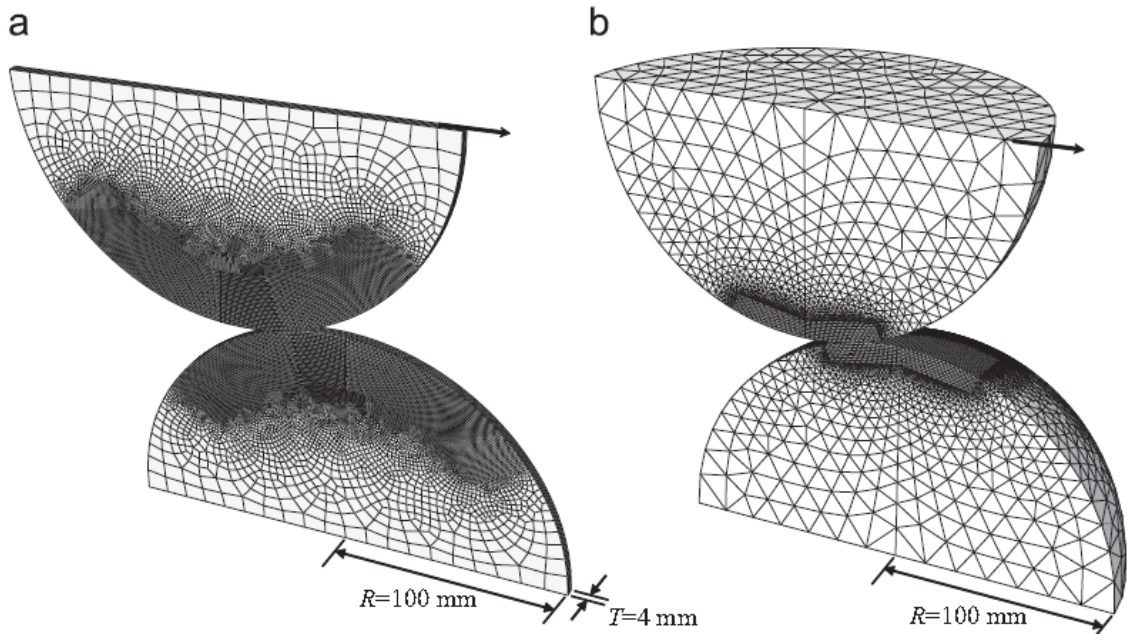

Figure 2.3 - Finite element mesh for; a) cylindrical asperity interaction, b) spherical asperity interaction.(Mulvihill et al., 2011)

Sahoo et al. (2010) performed a study of an elastic-plastic contact analysis of a deformable sphere with a rigid flat using the ANSYS commercial finite element software package as shown in Figure 2.4. The effect of strain hardening on the contact behaviour of a non-adhesive frictionless elastic-plastic contact was investigated. The resistance to the deformation in the material is increased and the material is able to carry a higher amount of load with a smaller contact area when strain hardening is increased.

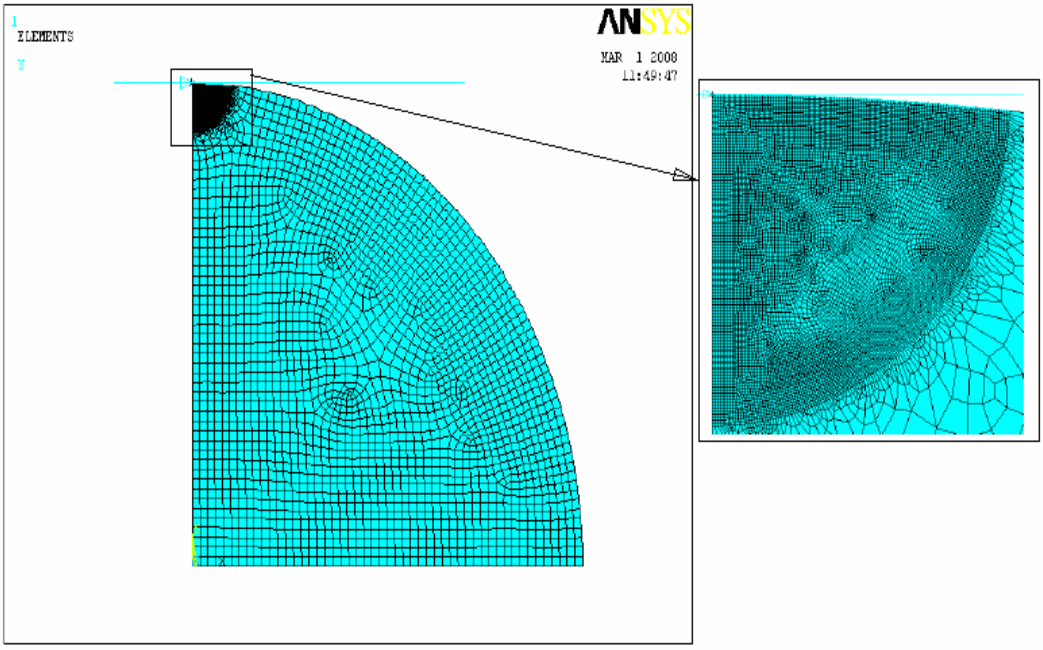

Figure 2.4 - An elastic-plastic contact a sphere model with a rigid flat using the ANSYS commercial finite element. (Sahoo et al., 2010)

Also, the strain hardening effect is based on different values of tangent modulus (E_t) as shown in Table 2.1 is expressed by Sahoo in terms of a parameter known as the Hardening parameter and defined as:

$$H = \frac{E_t}{E - E_t} \qquad 2.1$$

Note that the hardness parameter, *H*, should not be confused with the material hardness, *HP*.

Table 2.1 - presents different values of *H* and E_t used by Sahoo (2010) to study strain Hardening.

H	E_t in % E	E_t (GPa)
0	0.0	0.0
0.1	9.0	6.3
0.2	16.7	11.7
0.3	23.0	16.1
0.4	28.6	20.0
0.5	33.0	23.1

Most of the practical materials fall in the range $0 \le H \le 0.5$. When the value of the tangent modulus equals zero (E_t=0) that indicates elastic perfectly plastic material behaviour which is an idealized material behaviour. Kogut and Etsion (2002) were the first to establish an accurate model of the elastic-plastic contact of a hemisphere against a rigid flat using a finite element method. Under frictionless contact conditions, the model evaluates the plastic zone in elastic-plastic contact between a sphere and rigid flat. Their model study covered a wide range of material properties, a tangent modulus up to 0.1E and a range of sphere sizes. The results of this model study found that the tangent modulus for the most practical materials is smaller than 0.05E. Hence, the model is general enough to accommodate material behaviour of elastic plastic and also encourage this research to use material behaviour other than elastic-perfectly plastic. Also applying a wide range of values of tangent modulus on his model presented the effect of strain hardening in single asperity contact. Jackson and Green (2005) used a similar analysis to the KE Model with various variations in a material property such as hardness. Shankar and Mayuram (2008) followed and extended on the work of the previous two models by assessing the contact of a rigid flat with an axisymmetric hemispherical asperity. They established 2D axisymmetric models of single asperity contact with a fine mesh near the contact and coarser mesh further away using ANSYS for a various variations in a material property. They also agreed with Jackson and Green's criticism of the KE model; that it has constant behaviour for all materials. A another study by Chatterjee and Sahoo (2012) using ANSYS showed that, if conditions of full stick contact are fully considered then, the contact parameters are affected greatly by different values of tangent modulus (strain hardening) on an elastic-plastic contact of a deformable sphere with a rigid flat.

A simulation approach performed by Hegadekatte et al. (2005) implemented using the ABAQUS commercial FE package was used to predict wear and solve the deformable contact problem. This was performed for both 2D and 3D simulations. Through the simulation steps, the geometry was re-meshed following each wear step in order to ensure the mesh remained uniform during subsequent processing, which lead to more accurate computation of the interacting surfaces' behaviour.

2.5 Surface effects

Micropitting is much smaller than pitting and tends to be limited to the surface of a material and can be of the order of up to 10 μ, whereas pitting tends to be of the order of the contact dimension (Olver, 2005). A number of studies have been performed to determine the factors that contribute to micropitting and its propagation into more significant damage. The study by Oila and Bull (2005) demonstrated that the load applied to the surface was the most influential factor in causing micropitting initiation, the other factors considered such as temperature, material surface finish, lubricant and slide/roll ratio had less influence on initiation. However, the slide/roll ratio and speed were the factors that caused and had the greatest effect on the propagation of micropitting failure.

An earlier study by Swahn et al. (1976) showed that martensitic decay can gain heat that's generated due to plastic deformation and which results in a phase transformation of material. He suggested a strong link between this phenomena and the encouragement of micropitting at the regions of stress concentrations and special sites for crack initiation and propagation. Whereas, a later study by Ahlroos et al. (2009) investigated the influence of frictional performance, material properties,

surface treatment, surface roughness and lubricant types on micropitting. It proved that surface roughness contributed the most to micropitting and confirmed the micropits did not occur on any of the polished surfaces (Ra ≈ 0.04 μm) tested. In a similar study by Moorthy and Shaw (2013) showed that rough surfaces displayed local valley features that can lead to stress concentrations in this area, resulting in micropitting. Polishing the surfaces was found to reduce the occurrence of micropitting and superfinishing surfaces is a means of reducing its occurrence. Further studies have also shown other causes of micropitting such as a paper by D'Errico (2011), studied the effect of material treatments on micropitting. Three different combinations of steel were used: hardened and tempered, carburised, and nitrided. The study showed that the more ductile the material, the more hardened and tempered was the steel, the more likely was micropitting and even pitting to occur. This study also showed that alloying of the material with nitrogen can reduce micropitting. Experiments on scuffing were carried out by several researchers to gain more understanding of the effect of the material's properties on frictional behaviour and scuffing resistance. An experiment by Snidle et al. (2008) demonstrated that coating disks with carbon-based hard coating reduced the effects of friction and scuffing resistance but did not improve their durability as far as scuffing is concerned. An example of scuffing failure is shown in figure 2.5(a) which shows the scuffed material on the left and the unscufffed material that retains the grinding lay on the right. Also shown in figures 2.5(b) is an example of scuffing in gear contacts due to excessive load, possibly as a result of misalignment or tooth crowning at regions of contact (Evans and Snidle, 2009).

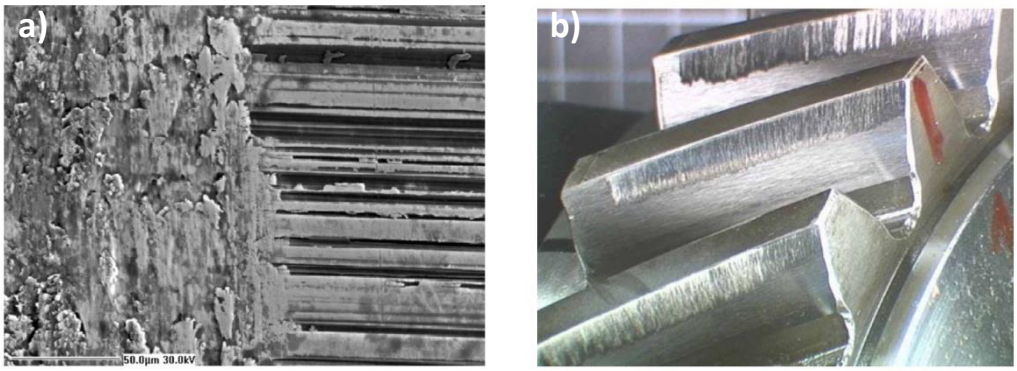

Figure 2.5 - Image of surface after scuffing; a) fast disk surface that has scuffing in the left side and unscuffed in the right, b) scuffing at the tips of helical gear teeth(Evans and Snidle, 2009).

McKelvey and Fatemi (2012) conducted a study comparing smooth-polished surface fatigue behaviour to fatigue behaviour of a hot forged surface finish. From Figure 2.6 below, it can be seen that the polished surface was better at maintaining its strength compared to the forged surface.

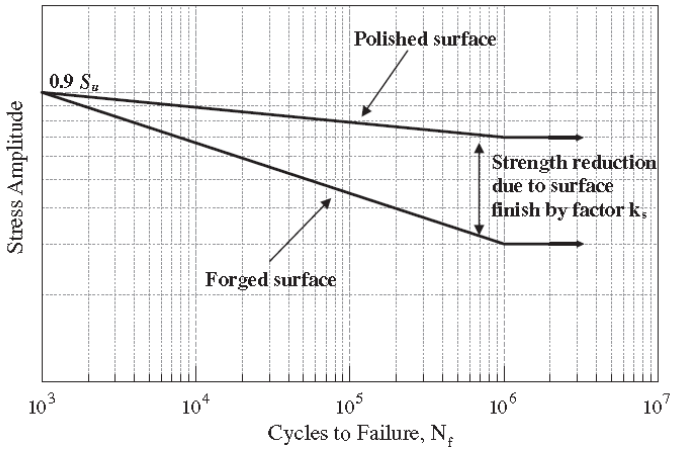

Figure 2.6 - log-log S-N curves for machined and polished surface (upper) and as forged surface (lower).(McKelvey and Fatemi, 2012)

Numerical experiments carried out by Evans et al. (2011) and Sharif et al. (2012) were used to demonstrate the effects of elastohydrodynamic lubrication (EHL). The 2011 study demonstrated a fatigue and damage accumulation analysis and how micropitting was the product of fatigue generated at the asperity contact level. All results were

based on the micro-EHL modelling of the gear tooth contacts as shown in figure 2.7. The gear tooth contacts used for these analyses were taken from micropitting tests of gears where the final manufacture of the hardened steel teeth was carried out with different grinding processes. The 2012 paper outlined a numerical model for the effect of EHL in situations of mixed lubrication and that of micro-EHL. This was so as to understand the effect of localised pressures and how they lead to fatigue at the asperity level which, in turn may result in micropitting.

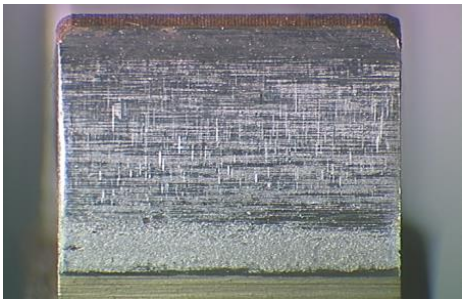

Figure 2.7 - Micropitting generated at the contact level of region of a spur gear tooth (Design Unit, Newcastle University).

Hannes and Alfredsson (2011) showed how the surface roughness that has asperities strongly encourages the initiation of a rolling contact fatigue (RCF) crack. They then went on to show how the spalling crack path as shown in figure 2.8 could be predicted by the asperity point load mechanism. This paper is based on an earlier study by Alfredsson et al. (2008) that presents a model of the contact loading effect of asperities and argues that this is the underlying mechanism of RCF initiated at the surface. To demonstrate this, FEM was used to assess the teeth flanks of driving gear wheels. As a result of the existence of the asperity, the model used had to be a 3D model. The main point to be noted is the magnitude of the local stress on a contact surface that results from the presence of roughness asperities.

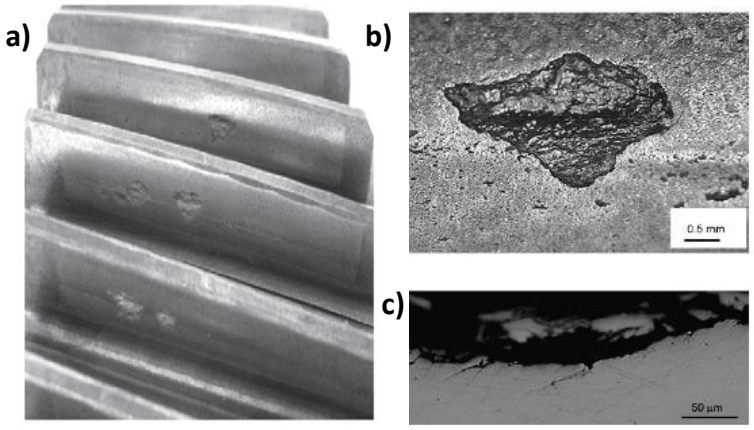

Figure 2.8- Fatigue damage on a helical gear; a) Overview of top helical surface failure, b) Magnification of spall failure, c) Cross section of spall failure .(Alfredsson et al., 2008)

2.6 Rolling contact fatigue

Rolling contact fatigue (RCF) is a common mechanism for failure of the surfaces in an EHL system and is seen as the limiting factor controlling the operational life of rolling element bearings, as an example. RCF is *"the name given to crack growth and material damage generated as a result of high loads transmitted between two surfaces rolling relative to each other*" (Kapoor et al., 2006). Rolling contact occurs in a variety of engineering backgrounds including, gears, cams, and rail wheel contacts in railways, amongst others. Understanding the way RCF develops and being able to predict the life span of equipment or machinery can go a long way towards aiding industries in developing better safety measures. This issue is of special importance to the rail industry in particular where it has caused a number of issues overtime. The accident at Hatfield in October 2000 caused by a break in the rail was found to be the result of the growth of a RCF crack. This propelled studies on RCF to the forefront (Kapoor et al., 2006).

In order to predict fatigue life of RCF crack initiation caused by low-cycle fatigue and ratcheting failure, Ringsberg (2001) used a number of methodologies including multiaxial fatigue crack initiation models together with elastic–plastic FEA used with

the critical plane concept and compared them with the results of numerical analyses and experiments. Alfredsson and Olsson (2001) studied standing contact fatigue (SCF) crack initiation using multiaxial fatigue criteria by applying a stationary pulsating contact load to a case-hardened test specimen as shown in figure 2.9. Various criteria were applied such as the Findley and the Haigh principal stress criterions. This study demonstrated that any individual criterion on its own could not characterise all conditions of the experimental results. Of these criteria the Findley criterion captured the experimental behaviour best overall.

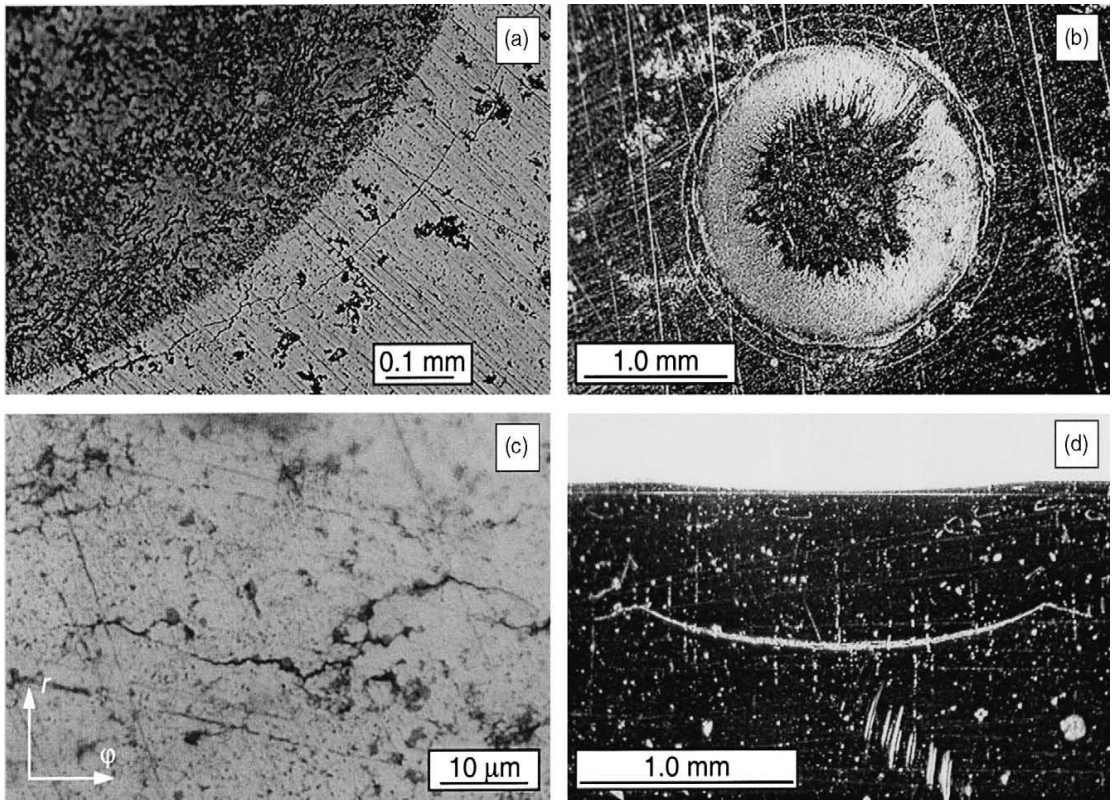

Figure 2.9 - SCF crack results; a) first top ring/cone crack view, b) second top ring/cone crack view, c) initial ring/cone crack formation, d) cut view of lateral crack (Alfredsson and Olsson, 2001).

Choi and Liu (2006) modelled the RCF life of hard finished machined surfaces and the effect of residual stresses and micro-hardness on it. The effect of residual stress was found to be more significant compared to micro-hardness. Also RCF is determined by

various factors including wear and lubrication mechanisms, contact mechanics, friction, material properties, fluid dynamics and lubricant rheology. RCF together with rolling contact wear and plastic deformation can lead to changes in the rolling surfaces. Resultant wear particles can make their way into the lubricant which can aggravate the resultant micropitting. Halme and Andersson (2010) showed the connections between bearing diagnostics and tribological mechanisms as an example of RCF as shown in Figure 1.5 (chapter 1).

As mentioned above, the material itself can affect RCF. A study by Widmark and Melander (1999) looked at how a number of factors, including surface hardening (by carburizing steel alloy composition), shot peening and increased surface hardening were found to influence the contact fatigue resistance. Many other factors also play a role and have been tested in various studies including, lubricant viscosities and additives (Fernandez Rico et al., 2003) (Krantz and Kahraman, 2004) as well as inclusions and operating conditions (D. Nelias et al., 1999) etc. The large number of factors involved makes it difficult to assess RCF crack initiation and propagation. So far, many mathematical models have been developed for RCF prediction. These can be divided into engineering models and research models as outlined by Tallian (1992). The Tallian model attempted to include many of the factors influencing life, such as contact geometry, material fatigue parameters, and defect severity, for example. Also Tallian (1992) and Kudish and Burris (2000) reviewed tens of engineering models.

2.7 Residual stresses influences

Modelling of rough surface contacts enables the determination of residual stresses as a result of surface geometry changes due to asperity contact and deformation. These

residual stresses are potentially a significant influence on the fatigue life of gear tooth surfaces, contributing to such failure mechanisms as micropitting.

Abudaia et al. (2005) demonstrated the result of an investigation of the loaded and residual stresses of a spherical indentation. Under loading conditions the hoop stress found at the edge of the contact area was compressive and became tensile once the load was removed. Experimental analysis of fatigue caused by cyclic indentations confirms this model for both ring cracks resulting from low peak loads and radial cracks from higher peak loads. Both types of cracks were commonplace and found to be more severe in depth and length as a result of increased loads. Shot peening of specimens was carried out in this experimental study prior to FE analysis to see the resultant residual stress. An example of the residual stress induced is shown in Figure 2.10

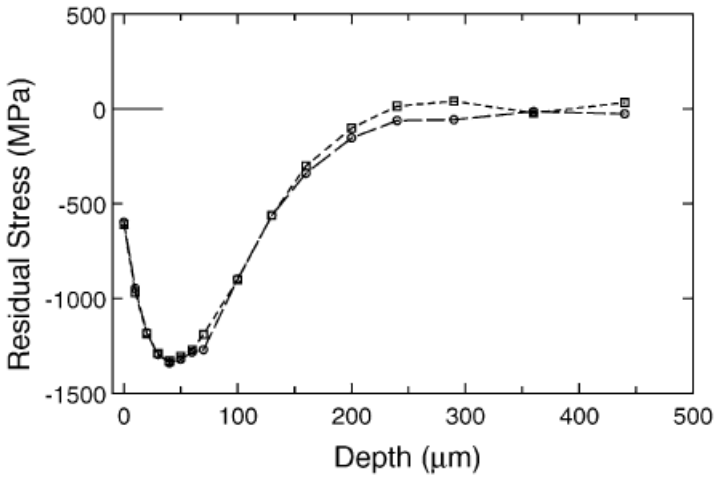

Figure 2.10 - Residual stress due to shot peening (Abudaia et al., 2005).

An FE model using ANSYS was used to examine the effects of residual stress on an elastic material (steel) at varying yield strengths by using a deformable sphere with a rigid flat using a specified interference. Results showed Hertzian behaviour was followed at the smaller interferences and that plastic behaviour occurred at larger

ones. This study was in good agreement with and confirmed the empirical formulations of Kogut and Etsion (2002).

A study on residual effects by Jackson et al. (2005) demonstrated the resulting residual stresses and strains that occur after unloading of an elastoplastic hemispherical contact. It showed the high residual von Mises stresses occurring close to the edge of the contact area after complete unloading. A plot of residual stress development with increasing plastic deformation can be seen in the contours presented in figure 2.11 of the stress tensor components. Also, this paper showed the formation of the residual stress distribution with increasing plastic deformation and analyses the deformation of the surface model (surface of hemisphere) that is dependent on the properties of the material (Young's modulus, Poisson's ratio, and yield strength) and dependent on the interferences.

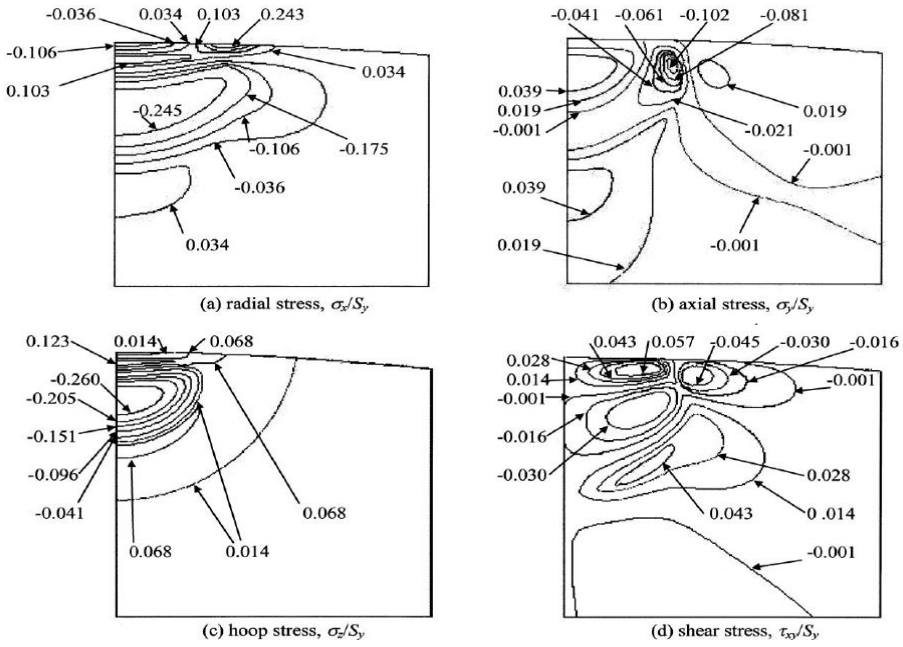

Figure 2.11 - Complete residual stress tensor for hemispherical contact unloaded due to shot peening (Jackson et al., 2005).

The analysis of the effect of residual stress on material fatigue was presented in several studies. One such study was published by Pazdanowski (2014) which studied

railroad rails and their contact with simulated service loads in terms of the influence of residual stresses on material fatigue. The study involves residual stress that was based on the plastic shakedown theory and implements the Dang Van fatigue criterion which has been used by a number of researchers. Due to the results of simulated contact loads in this study that the stress values were found to increase greatly (compression by 23.5% and tension by up to 30.1%), and it insist to be included in fatigue calculations. A second study by Ismail et al. (2013) looked at the steady-state phase of repeated rolling contacts using FEA. His study demonstrated that the residual stress of the first two cycles is significant to the change in its distribution and there is no significant change for the residual stress in the subsequent cycles as can be seen in figure 2.12

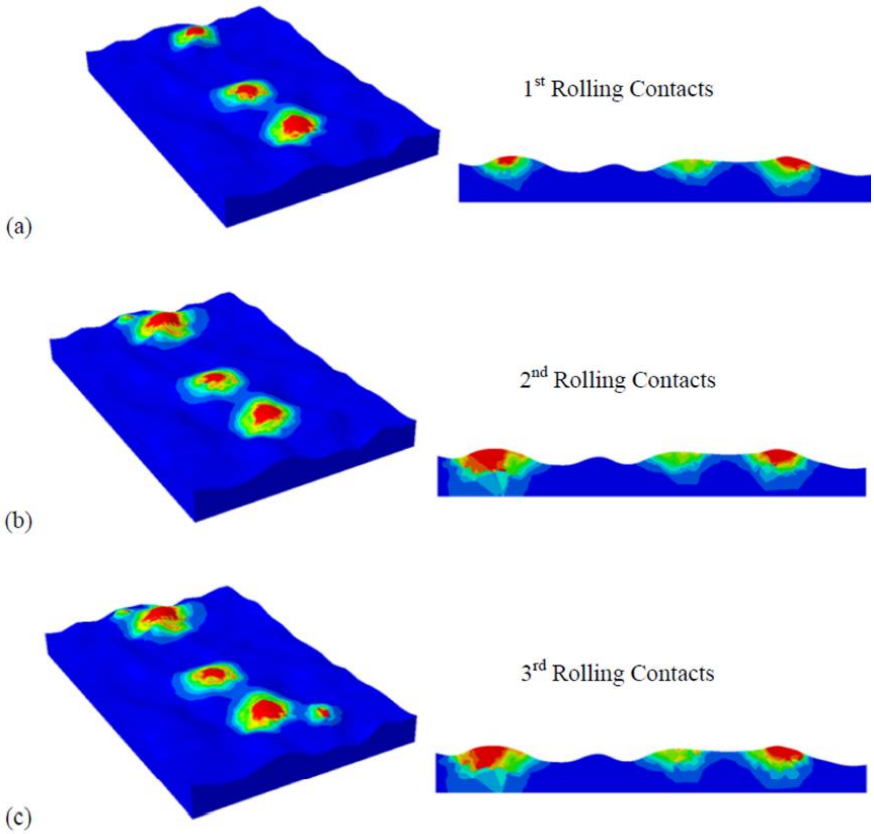

Figure 2.12 - The Von Mises residual stress for; a) first rolling contact, b) second stage rolling contact, c) third stage rolling contact (Ismail, 2013).

Ismail's results showed that the number of deforming asperities and the material experiencing high von Mises residual stress, both at the surface and subsurface, were all affected by the increasing contact load. This distribution gets wider with increasing normal force. A small region of plastic strain (which is captured at the third cycle) is found for the rough surface, thereby indicating that deformation was mostly elastic. This study is in agreement with a similar study by Ismail et al. (2011) and Ismail et al. (2010). However, neither of these two studies Ismail et al. (2013) and Pazdanowski (2014) contain any detailed discussion of fatigue damage with and without residual stress.

An elastoplastic finite element model was developed by Wyman Z. Zhuang a (2001) to demonstrate the benefits of the compressive residual stresses. It considered the various treatments used to induce the residual stresses such as mechanical surface treatment, shot peening, hole expansion, laser shock peening, and low-plasticity burnishing. All of these factors can be highly beneficial to fatigue resistance, and cyclic relaxation of compressive residual stress can reduce the benefit as well. This paper also proposed a calculation for the estimation of residual stress relaxation using an elastic-plastic FE model.

Two studies carried out by Fabre et al. (2011) and in (2013) used a generic roughness profile built with geometrical parameters to simulate the contact between two rough surfaces as shown in the figure 2.13.

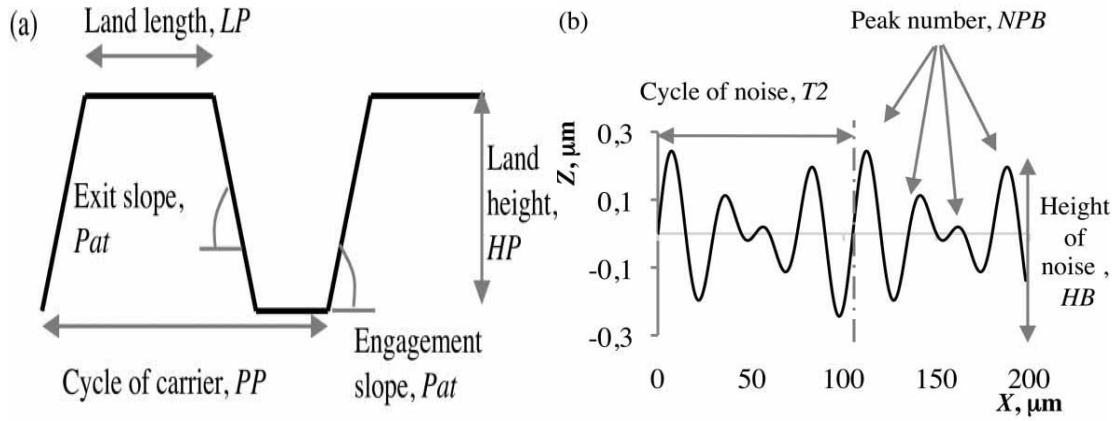

Figure 2.13 - The parameters of the two main parts of the model; a) The four parameters of the carrier profile, b) the three parameters of the higher frequency noise profile (Fabre et al., 2011).

The first paper studied the effect of seven of these model parameters in influencing fatigue lifetime, and the prediction of pitting and micropitting. They identified four parameters that influence pitting at the position of the maximum Hertzian shear stress, and also confirmed the influence of two and three of the parameters on micropitting and fatigue lifetime respectively. Although this approach covered most of the geometrical parameters that can determine fatigue lifetime and predict pitting and micropitting, it did not take the residual stress into account. This was included in the Fabre et al. (2013) paper which investigated the influence of the model parameters together with the influence of induced compressive residual stresses on fatigue lifetime for steel teeth. Micropitting and conventional pitting were found to occur at different values of each parameter. In terms of the compressive residual stress influence, this was shown to reduce the number of points experiencing yield and the number experiencing fatigue failure. However, it did not take the tensile residual stress

into account or contain any detailed discussion of fatigue damage with and without residual stress.

Jamari and Schipper published various papers between 2006 and 2008 (Jamari and Schipper, 2006a, Jamari and Schipper, 2006b, Jamari and Schipper, 2007a, Jamari and Schipper, 2007b, Jamari et al., 2007, Jamari and Schipper, 2008) describing different experiments aimed at confirming their prediction models and assessing different contact surfaces including elastic, elastic-plastic and fully plastic surfaces. This was carried out by analysing contact factors such as contact area, load and pressure. When analysing contact on rough surfaces they considered three deformation responses; asperity plastic deformation, bulk plastic deformation and plastic deformation of both asperity and bulk. Jamari and Schipper's predictions found good agreement with their experimental work. Also they confirmed at the same normal load condition that the contact behaviour becomes elastic soon after the first loading has been applied.

Chapter 3

Simulation with Abaqus

3.1 Introduction

Deformation occurs when two rough surfaces are engaged in contact in the region of the contact spots, creating stresses that oppose the applied load. The type of surface deformation is either elastic or elastic-plastic. The surface interactions cause pressure and shear stress to be developed at the interface, and the resulting subsurface stresses produce a deformation at the region of the interface. These non-linear contact situations can be solved by the Finite Element method (FEM) and this is the method used in the research. The problem considered is a plane strain contact of a surface whose roughness is extruded perpendicular to the plane considered. The FEM is utilised to model these problems by dividing (meshing) the rough surface's area into small and manageable finite elements. This approach is used extensively to solve mechanical engineering problems and has been established to be an effective way to improve understanding of tribological contact performance. This chapter explains the technique used to develop and improve elastic-plastic contact modelling using the Abaqus /CAE 6.12 package.

Two main Abaqus models were created and are considered in detail. Firstly; basic elastic plastic contact models were created to evaluate the modelling approach and to test the suitability of different features of models. Secondly, the study was then extended to a plane strain line contact of an elastic-plastic model obtained in the simulation of the contact between a rigid body and a roller on which a roughness

profile is superimposed to validate the approach. A sequence of various simulation models and modifications were executed and compared accordingly.

3.2 Experimental work of real rough surface contacts

3.2.1 Twin rig disk geometry and material properties

In 1994 Patching designed and constructed a twin disk machine to examine Elastohydrodynamic lubrication and scuffing in aerospace mechanism contacts. In 2006, the twin-disk testing mechanism was developed by Alanou to examine micropitting using the same basic design principles (Alanou, 2006). The geometry of the disks involves a diameter of 76.2 mm, and has a crown radius of 304.8 mm. The fundamental shape of the contact area is elliptical when the disk has been loaded elastically. The major axis of the Hertzian elliptical contact, *a*, is in the axial direction of the disk, while the minor axis, *b*, is in the circumferential direction. The geometry of the disks is shown in Figure 3.1.

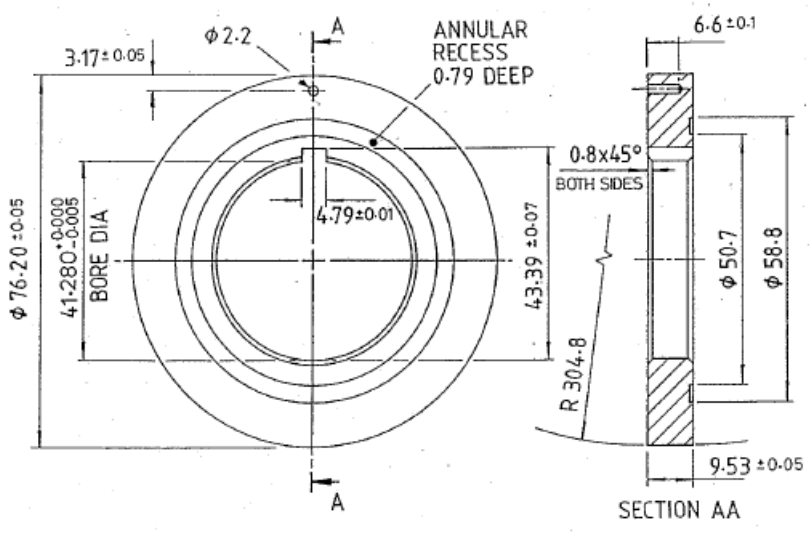

Figure 3.1 - The geometry of the disks rig in Cardiff university lab.

The disks are made of a carburising Nickel-Chromium alloy steel, as per Rolls-Royce gear steel specification RR6010. This material was supplied by the company for previous research projects. Appendix AA_1, Table A.1 shows the composition of RR6010 steel and the disks were heat treated to typical aerospace gear's specification according to the schedule shown in Table A.2. The disks were finish ground after heat treatment to provide a roughness whose lay was essentially axial and traverse to the rolling /sliding direction. The analysis conducted in this research took place alongside experimental tests of the running in process conducted by Weeks (2015). Profile measurements were made by Weeks at the end of manufacture, and then at various stages of loading in his experimental program. These as-manufactured profiles were used for this study and the post-running profiles were available for comparison with the results obtained from the Abaqus contact analysis.

3.2.2 Loading of Rough surface and Extracting Profiles

In order to have a simulation model that is similar to the real case and to compare with experimental results by means of the FEM analysis, the surface roughness profiles before and after applying load were acquired using a Talysurf form profilometer. The profiles were taken in the circumferential direction perpendicular to the roughness lay and parallel to the disk face. A Gaussian filter with a cut off of 0.25 mm was used to remove the circular form and the waviness from the surface profile and the surface roughness profile was retained for analysis. This standard cut off value is of the same order as the Hertzian contact dimension for the disk contacts and is selected accordingly as surface features with longer wavelengths are flattened elastically by the Hertzian contact, i.e. they represent a perturbation to the radius of curvature.

Measurement of the roughness profile was carried out in two main steps. Firstly, eight millimetre long profiles were taken at particular marked locations on the disk circumference before loading. Secondly, post loading profiles were taken at the same specific circumferential locations of the disk. This process was repeated after further running stages and used by Weeks to observe the changes occurring at roughness asperity features. Three Surface roughness profiles (unrun, run/stage1 and run/stage2) are presented in Figure 3.2. These profiles are taken in nominally the same positions and are located relative to each other in the trace direction by use of deep valley features as markers. The effectiveness of the realignment can be seen in Figure 3.2 where it is apparent that the relocation is correct. Comparison of the profiles show clear changes in shape of the prominent asperity features, and also show some deep valley features that have a shift in the profile height direction such as those located between $x = 2.05\ mm$ and $x = 2.10\ mm, x = 2.10\ mm$ and $x = 2.15\ mm$, $x = 2.50\ mm$ and $x = 2.55\ mm$. The question of profile height direction realignment will be elaborated in chapter four.

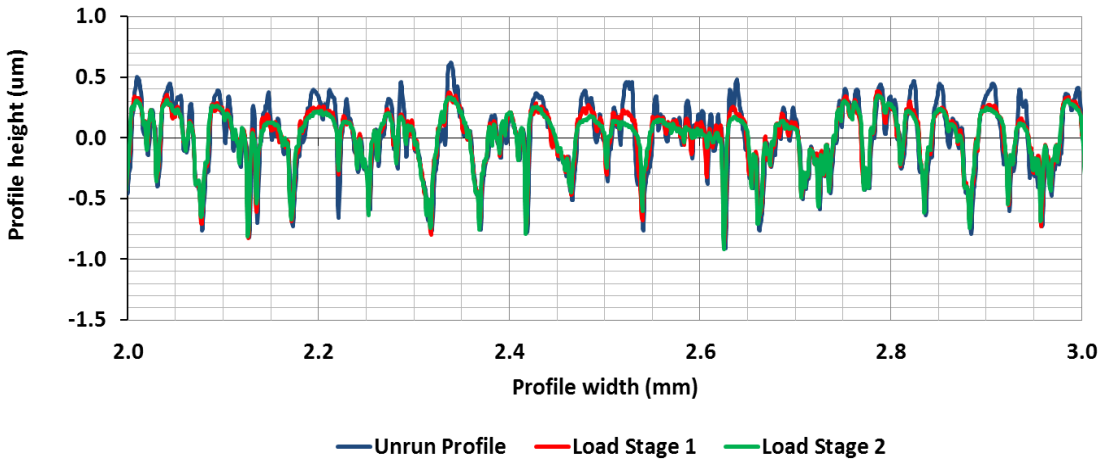

Figure 3.2 - Part of Surface roughness profiles (run, unrun and second run) relocated to align with each other based on deep valley features.

3.3 FEM Modelling using ABAQUS CAE/6.12v

3.3.1 Introduction

The finite element method was first developed by Turner, Clough, Martin and Top In 1956 (Turner, 1956). It is a powerful technique used to investigate and analyse mechanical design problems. The stress distributions obtained can be used to predict and study the fatigue life of mechanical components. The mechanical behaviour of a material under multiaxial elastic-plastic strain is an example of a complex situation that can be modelled with the Abaqus FEA program. Abaqus models use the open source scripting language Python for scripting as well as customization. Each entire finite-element investigation consists of three distinct stages or steps (ABAQUS CAE/6.12v) as shown in Figure 3.3:

- *Pre-processing*: This stage consists of devising an input file. This consists of building a finite element model of the components to be analysed and specifying the loads and boundary conditions.
- Processing: This step consists of running the finite element analysis for the problem specified in the input file. The solution is saved in files that can subsequently be used to illustrate the results graphically and to tabulate any particular values of parameters obtained in the results, for example residual deflection and residual stress in the current research.
- *Post-processing*: This stage is a visual rendering stage also recognised as a report, image, and animation generator from the output file of the model results.

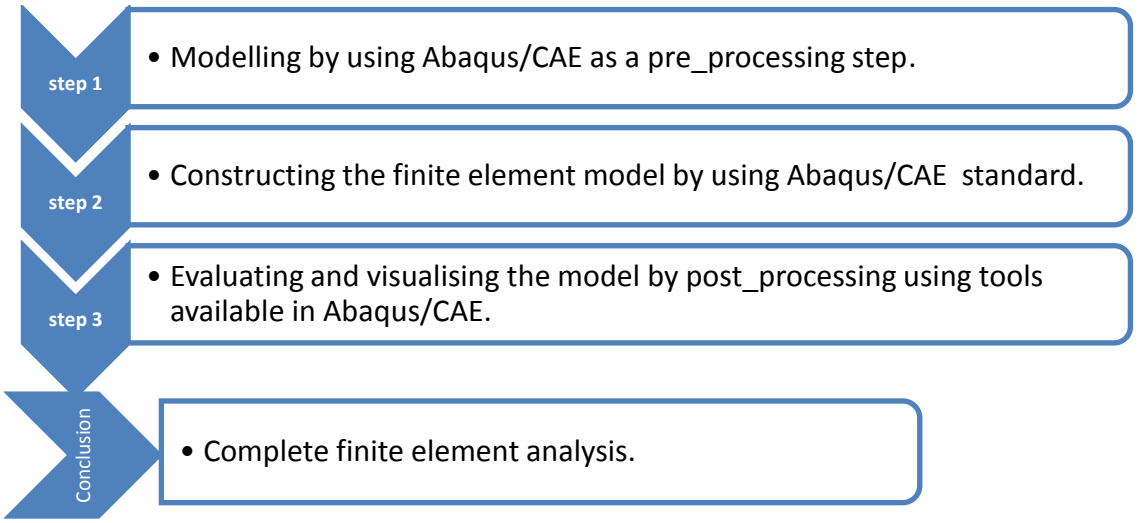

Figure 3.3 - Main component of complete finite-element analysis.

3.3.2 Numerical analysis using Abaqus/CAE 6.12

In the FEM continuous functions are approximated by a discrete model. The body to be studied is divided into several smaller parts, known as finite elements. These elements are connected at nodes on their boundaries. The basic plain-strain formulation relates the deflection components at the nodes of the finite element to the forces applied to those nodes in what is referred to as an element stiffness matrix. The deflection of the element is described by an element shape function which is a polynomial that has the same number of unknowns as the total degrees of freedom (deflection components) at the nodes of the element. The element stiffness matrices are assembled to form a problem stiffness matrix for the whole model. This is a square matrix of size *n* by *n* where *n* is the total number of degrees of freedom. In this assembly process the internal interaction forces at the nodes cancel in accordance with Newton's third law and the only forces in action are the external forces applied to the model at the nodes. Restraints are applied to some nodes to represent the restraints applied to the component in the real situation, and the resulting linear matrix equation has *n*

unknowns, the deflection components at the unrestrained nodes, and the force components at the restrained nodes. In contact problems non-linearity is introduced as the load at the contact surface is not known and has to be determined in an iterative process.

Accuracy generally decreases when the number of nodes decreases, and vice versa. The forces applied on the element geometry are symbolized by load vectors that act on the nodes. The deflections take place at the elements nodal positions is the solution to the equation system and stress values are obtained by evaluation of strain from the differentials of the element shape functions. The complete Abaqus environment provides a simple, consistent interface for constructing, submitting, and monitoring an analysis, as well as evaluating its outcomes. It is divided into modules, where every module defines a logical aspect of the modelling process; for instance, defining geometry, defining material properties, generating a mesh, applying loads and specifying boundary conditions. Moving from module to module, the model is constructed with Abaqus/CAE finally generating an input file that is submitted to the Abaqus/Standard analysis product. The user can also monitor the progress of the job through Abaqus/CAE which has the information from the analysis product. Abaqus/Viewer provides graphical display of Abaqus finite element models as well as analysis outcomes. An Abaqus/CAE model contains the following kinds of objects:

- Parts.
- Materials and sections.
- Assembly.
- Steps.
- Sets and surfaces.
- Different type of loads, boundary conditions.
- Interactions between the parts of models and their properties.
- Different types of meshes.

The package also has further tools and those utilised in this research are detailed when their use is discussed.

3.3.3 Structure of mesh and type of elements

From an engineering perspective, mesh selection is one of the most significant and critical aspects of simulation construction. Increasing the number of elements by reducing their size can produce more accurate results, and results obtained with a low mesh density can be inaccurate. Abaqus /CAE (V6.12) has different mesh control techniques. Considerable care is taken to optimize the mesh size so as to get reliable outcomes. During the analysis of simulation data, element distortion is one of the possibilities that can occur in the contact zone. A coarse mesh with distorted elements gives poor results as will be explained in chapter 5. The Abaqus analysis was carried out with models having different mesh sizes: A finely-meshed region was used around the contact area and progressively larger elements were used outside the contact zone. Each analysis in this research was performed with three main mesh sizes in order to make comparisons and to determine the most effective size as discussed in the next sections. The first (referred to as the fine mesh) had quadrilateral elements whose linear dimensions were 0.5 μm. The second (referred to as the medium mesh) had quadrilateral elements of side 1.0 μm in the region around the contact. The final one was a coarse mesh in which the finest elements had 2.0 μm dimensions and a few cases were also analysed with this mesh. The maximum element size on the periphery of the models was not changed (250 μm). Element type CPE4 (4 node, quadrilateral, plane strain, 2D element) was chosen for all models in this research. Linear

quadrilateral elements were used in preference to quadratic ones as this is strongly advised by Abaqus in relation to contact modelling.

Figure 3.4 shows the mesh for a typical model. The contact zone, with the finest mesh spacing is seen at the top central part. This mesh allows the surface roughness profile under consideration to be incorporated in the model. This central contact zone is part of a much larger model whose boundaries are sufficiently far away from the contact area to ensure that semi-infinite body behaviour occurs (or is well approximated). The additional parts of the model are created independently with coarser mesh sizes which are then tied to the main body using constraints. These techniques allow coarsely resolved area to be interfaced with finely resolved ones without requiring a continuous transition in element size as shown in Figure 3.4. The fine mesh is subjected to a degree of constraint at the interface as the deflection pattern there is limited to that accommodated by the shape functions of the coarser mesh. Care was taken to ensure that the interfaces were far from the contact zone and that the additional restriction on deflection was not an influence in the results obtained. The resulting advantage of being able to ensure that the boundaries of the model were sufficiently far from the contact zone to simulate a semi-infinite body was considerable.

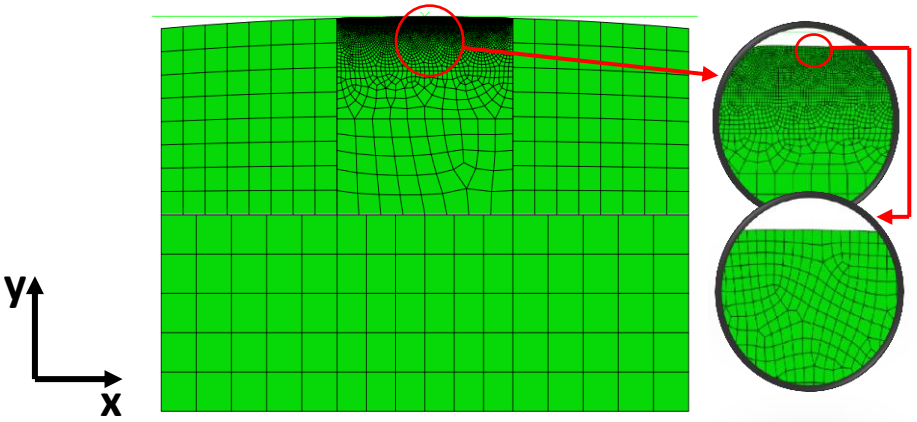

Figure 3.4 - Example of the mesh structure used with details showing the most finely meshed area at the contact surface. Note that the x,y axes have origin at the contact point.

3.3.4 Element distortion

The loading method adopted was to load the rough surface against a flat rigid surface tangential to the underlying smooth roller profile at its highest point. This load case is equivalent to loading the elastic/plastic body against its own mirror image produced by reflection in this rigid flat. Throughout the rough surface contact analysis, satisfactory results were obtained by utilising the 1.0 μm size mesh for all the loads used to determine residual asperity deflections. At the load cases corresponding to complete contact of segments of the rough surface it was observed that significant element distortion occurred when a mesh spacing of 0.5μm was used and so standard 1.0 μm mesh spacing was adopted. The material is stretched considerably in the x-axis direction (perpendicular to the load) through Abaqus analysis as it moves away from the contact area due to interaction with the rigid material body. The surface roughness elements that are beneath the highly deforming asperity material have decreased area as they moves outwards, away from the axis of an asperity. The elements undergo considerable distortions that lead to unacceptable results. To overcome this difficulty a form of adaptive meshing using the ALE function was adopted as elaborated in the next section.

3.3.5 Adaptive mesh functions ALE in Abaqus /CAE 6.12

The adaptive meshing technique, ALE, is a tool that can maintain a high-quality mesh during Abaqus analysis by allowing the mesh to move independently of the material although large loss or deformation of material occurs. It does not alter the topology (connectivity and elements) of the mesh i.e., elements are not destroyed or created. The Abaqus documentation frequently refers to “ALE adaptive meshing” simply as

"adaptive meshing" (Abaqus manual /CAE (6.12). It can be applied through a changeable Abaqus drop-down menu on the tool bar, or can be achieved by using the ALE buttons directly alongside the modelling viewport at the model tree. ALE re-meshes areas where element distortion is becoming excessive to preserve the accuracy of the model as plastic deformation develops. Figure 3.5 illustrates how models incorporating this adaptive meshing avoid the distortion that would otherwise develop in the surface mesh of valley features of a roughness profile. This example is taken from Abaqus manual / CAE (6.12) and considers the contact between a plane surface and a rigid sinusoidal die.

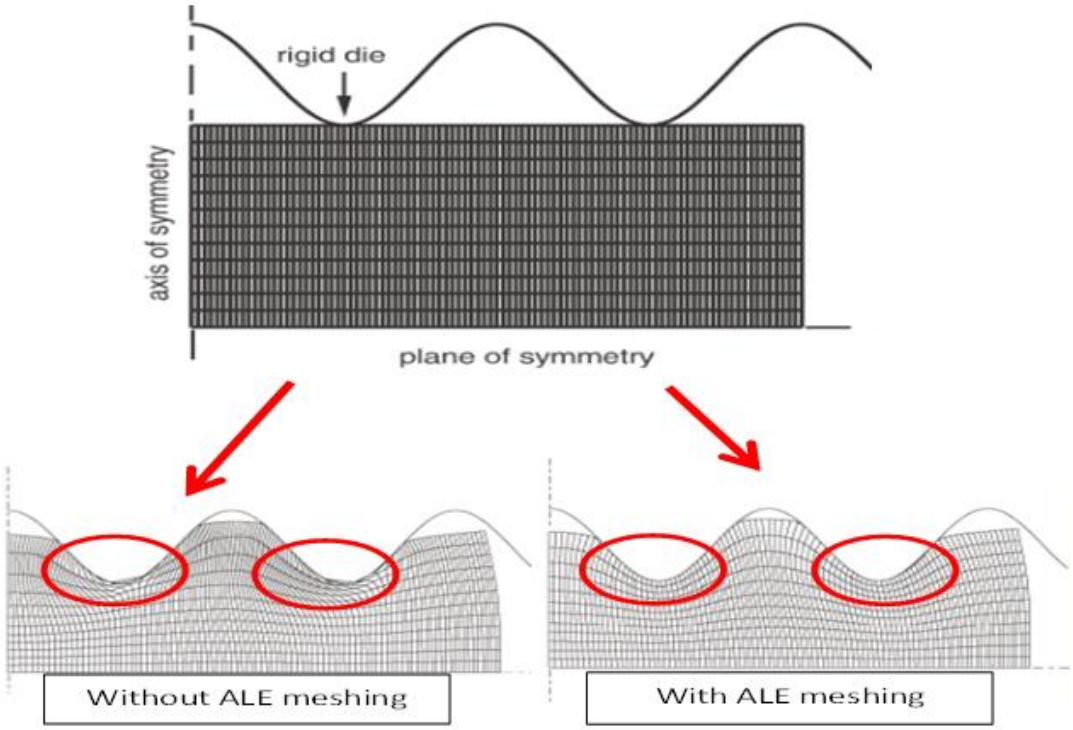

Figure 3.5 - Comparison of contact model result obtained with and without use of ALE meshing showing its effect in controlling the degree of element distortion that occurs (Abaqus /CAE 6.12).

3.3.6 Penetration

Contact analysis in Abaqus is based upon the interactions and constraint characteristics applied to *master* and *slave* surfaces. Every contact analysis requires the definition of two contacting surfaces, one of which is designated the *master* and the other designated the *slave* surface. In addition, it is recommended that the master surface be assigned to the larger body, the stiffer surface (comprising structural considerations, not just material) or the surface that consists of the coarser mesh. Also, as shown in Figure 3.6, the contact interaction between the surfaces can be specified using one of two mechanisms; *node-to-surface* contact and *surface-to-surface* contact. A node-to-surface contact is where an individual node on the slave surface interacts by means of a point of projection on a nearby facet of the master surface. The contact direction is determined by the master surface; however, the shape and normal to the slave surface are not taken into account in the contact formulation. Slave surface nodes are restricted as far as penetration into the master surface is concerned, while master nodes are not explicitly restricted from penetrating the slave surface. This can be mitigated to some extent by ensuring that the slave surface mesh density is sufficiently fine, preventing a large magnitude of penetration.

More accurate contact stresses can be achieved without matching meshes through utilising the surface-to-surface contact option. This option minimises the likelihood of large localized penetrations and the result sensitivity to slave and master roles. All these benefits are gained by using the surface-to-surface contact option because it takes into account the features of both the slave and master surfaces in the contact formulation. Both methods were used during the development stages of the analysis with the surface-to-surface method chosen for the final research results.

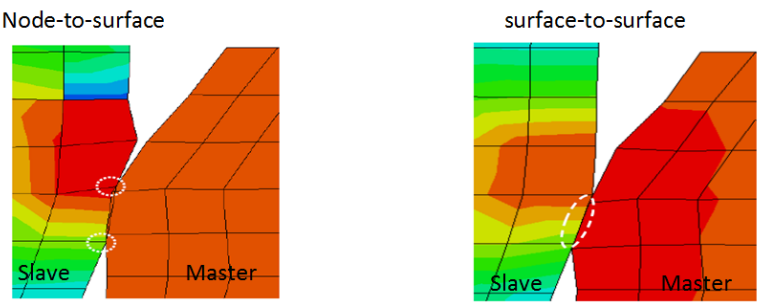

Figure 3.6 - Node-to-surface and surface-to-surface contact interactions (3DS Simulia note, 2014).

3.4 Development of Finite Element Models

The main purpose of this part of work is to carry out a simulation of surface roughness in Abaqus manuals/CAE6.12 by creating a model analogous to the real surface roughness disk experiment conducted in a test rig and calculating the mechanical behaviour under loading. The simulation models are aimed at being able to represent the behaviour of the real contact of the real rough surfaces and to evaluate the likely residual stress effects occurring. They were constructed following several trails of models and versions as presented in the following sections which can be classified into two main divisions, those using basic modelling techniques, and those using advanced modelling techniques. Within each of these divisions further modification were trialled to arrive at the final model used for the analysis.

3.4.1 Basic Model Development

This section illustrates the development of basic contact modelling utilising Abaqus. The trial model simulations were created and subsequently run using an elastic perfectly plastic contact model as a check on modelling techniques and functions to be used. The work then developed utilising elastic-plastic surface contact models incorporating strain hardening for the study. All models built incorporated a contact

surface with a radius R=38.1 mm. The rough surface profile information used in the study consisted of a profile taken from the unrun test disk and a further profile taken at the same location after running as illustrated previously in Figure 3.2. The un-run profile was used to define the surface roughness of the modelled disk, and the post running profile was used for comparison with the FEA model result obtained after loading to elastic-plastic asperity conditions as will be explained in detail in chapter 5. For the first model trial, a plane strain model of line contact between two rollers with identical rough surfaces was carried out as shown in Figure 3.7a. It was used to apply the basic tools and functions of Abaqus for performing basic contact modelling. For the second model that became the basis for the advanced model discussed in the next section, a plane strain model of line contact between a rigid plane and deformable elastic-plastic part of radius 38.1 mm was used as shown in Figure 3.7b. This was found to be an effective means of applying asperity loading as all prominent asperities made contact with the rigid counterface.

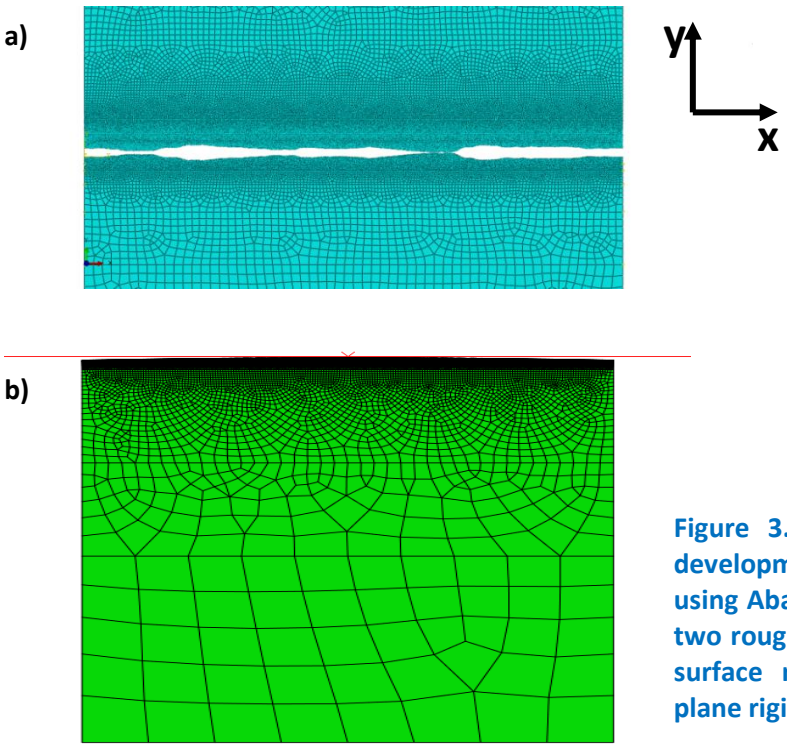

Figure 3.7 - Screen shot of the development of contact modelling using Abaqus; a) Contact model of two rough surface rollers, b) rough surface roller in contact with a plane rigid body.

3.4.1.1 Model configuration

To construct the rough surface part, the portion of interest from the as-manufactured surface profile was selected and placed in an Excel spreadsheet. This would be used to form the crown of the roller part in due course. The profiles available from the experimental evaluation of running-in carried out by Weeks were examined and two were selected for contact analysis based on the roughness asperities that they contained and the measured changes that were observed in comparing the as manufactured profiles with profiles taken after running. At the experimental load the Hertzian contact in the profile direction was about 0.7 mm long (Hertzian contact dimension 0.335 mm). The rough profiles used for the analysis were 1.2 mm and 1.3 mm long so that each was considerably longer than the corresponding contact dimension. These were each extended to a total length of 2mm. The curve was resolved at the profilometer roughness spacing of 0.5 μm, 1.0 μm and 2.0 μm to cover the mesh size study as will be discussed and illustrated in chapter 4. The spreadsheet was then used to add the profile to a smooth surface having the disk radius of 38.1mm as shown in Figure 3.8 and discussed in detail at section 4.3.1. This linear piecewise curve was then used to form one boundary of the four sided surface that would form the contact body using a Python script to create the 2D deformable part. This approach was taken as the contact would not extend to the part of the component that was smooth and further partitions would be added to contacting part so as to increase its size and distance to the boundaries sufficiently for it to behave in the same way as a semi-infinite body. At this stage in the development, the main part was partitioned into five segments as shown in Figure 3.9a to take advantage of the partitioning function. The mesh in each partition was seeded so as to allow more coarsely resolved

mesh areas to be interfaced with finely resolved ones with continuous transition in element size as shown Figure 3.9b. Biased mesh seeds CPE4 were used with varying size. The size of the elements was increased gradually with distance from the contact surface. Given the relatively large size of the contact and the associated model, a large number of elements are required to solve the problem with a sufficient degree of accuracy.

The two selected parts of roughness profile (1.2 mm, 1.3 mm) that were utilised in the research and imported in this way was smaller than the dimension of the deformable part of the model.

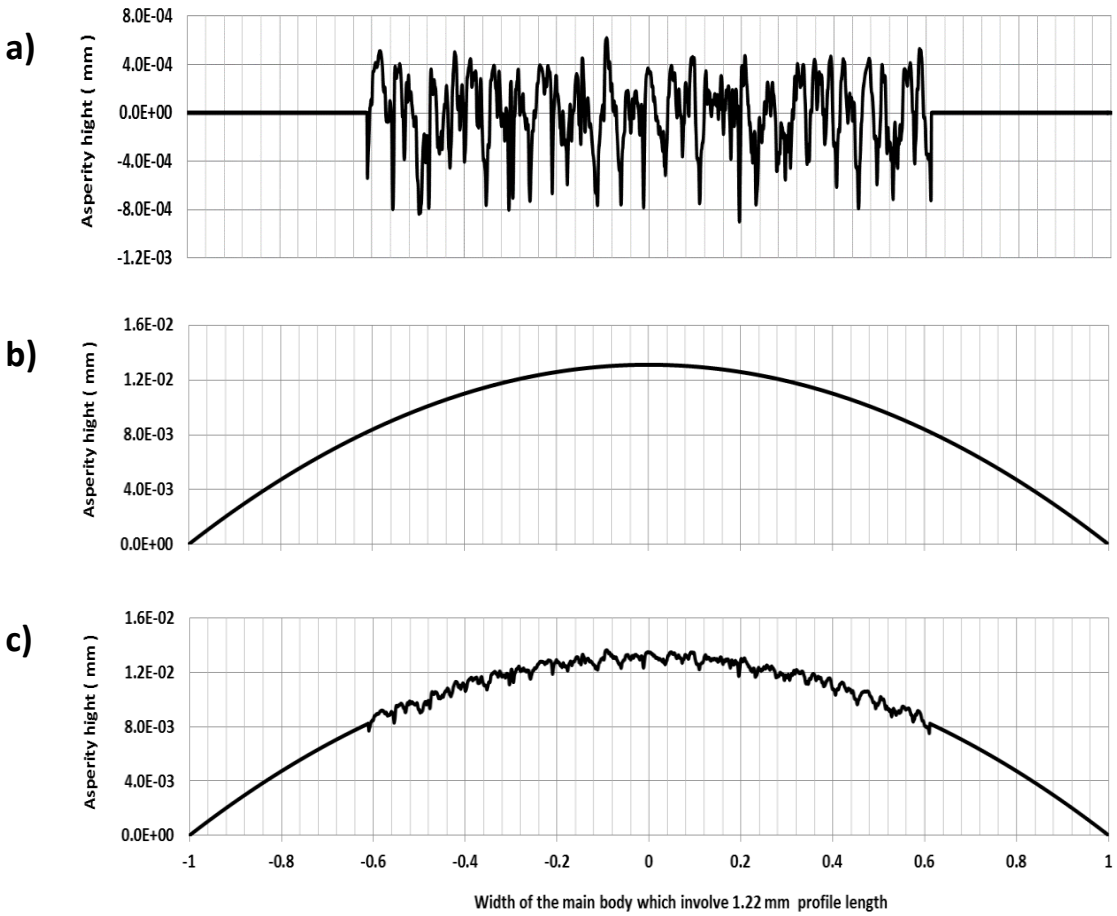

Figure 3.8 - Formation of rough surface roller; a) Filtered test disk roughness profile, b) Smooth roller contour, c) Smooth roller profile superimposed with filtered test disk roughness profile.

The number of elements at the surface is particularly important as this defines the accuracy at each asperity contact and the stresses in the surrounding material. However, the stresses inside the bulk material remote from the immediate subsurface material do not require the same level of resolution so that the mesh can be coarsened progressively in order to reduce computation time. The remote parts were created in order to support the main body that has the real roughness as if it was part of a semi-infinity body. It was found that by utilising partition lines in the surface body sections, a smaller number of elements could be used in the model and smooth transitioning of element sizes in moving progressively further from the surface could take place. Achieving this with biased mesh seeds for the whole body proved to be problematical because of the order of the change in mesh size required. The smooth transitioning of element mesh sizes with progression away from the contact surface was achieved by partition sections at depths of 0.01 mm, 0.03 mm, 0.05 mm, 0.5mm and 1.0 mm below the surface as shown in figure 3.9a. The mesh in the smallest section at the surface is hidden for the reason that, at the scale presented in the figure, the elements are too small to be seen as illustrated previously in Figure 3.4.

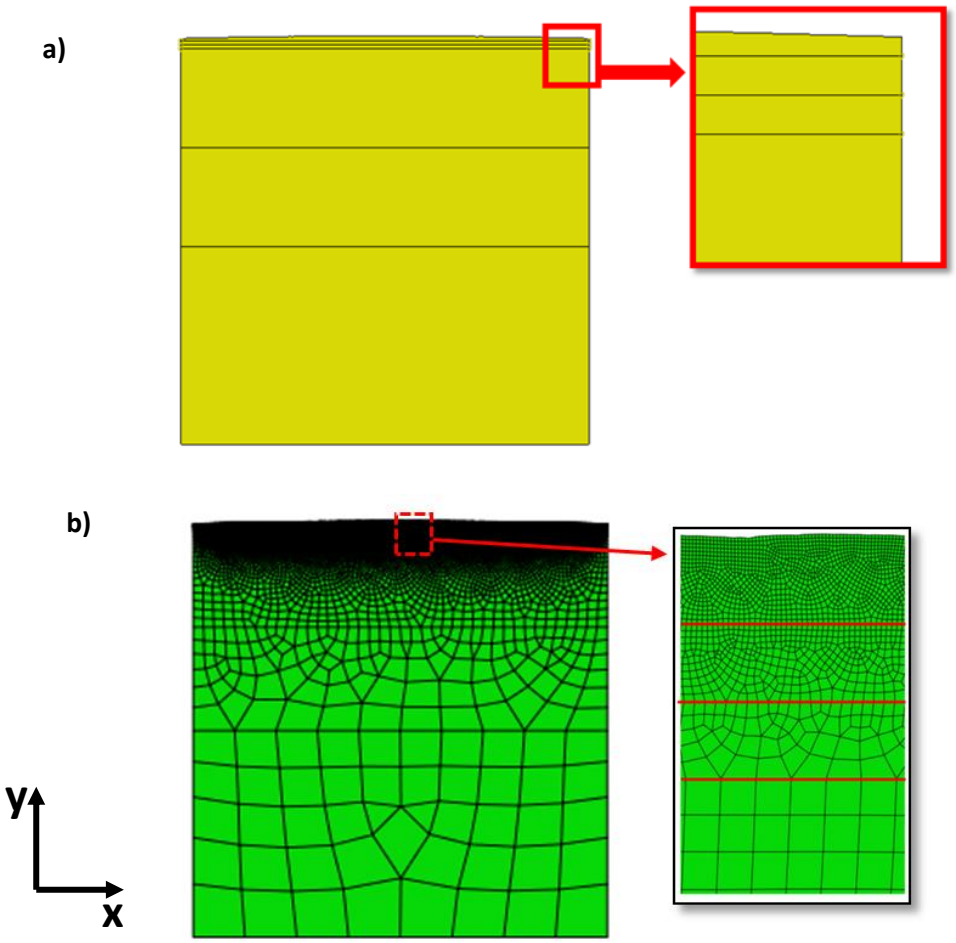

Figure 3.9 – Main body involving; a) The main partitioned sections, b) coarsely resolved mesh areas interfaced with finely resolved ones with continuous transition in element size based on the partitioned line.

3.4.1.2 Model properties

All the models developed were given the same values of elastic modulus and Poisson's ratio, and also required specification of the material's plastic behaviour. Abaqus analysis requires strain and the true stress to be used rather than the nominal stress and strain to specify the elastic-perfectly plastic or elastic-plastic behaviour. Abaqus assumes elastic-perfectly plastic behaviour as shown in figure 3.10(c) when the value of plastic strain is zero as shown in the snapshot figure 3.10(a). More elastic constants are required to characterize the material such as the Elastic modulus and Poisson's ratio and can be defined by adding further entries to the table shown in figure 3.10(b).

More general plastic material models can be defined by adding further entries to the Table shown in figure 3.10(a).

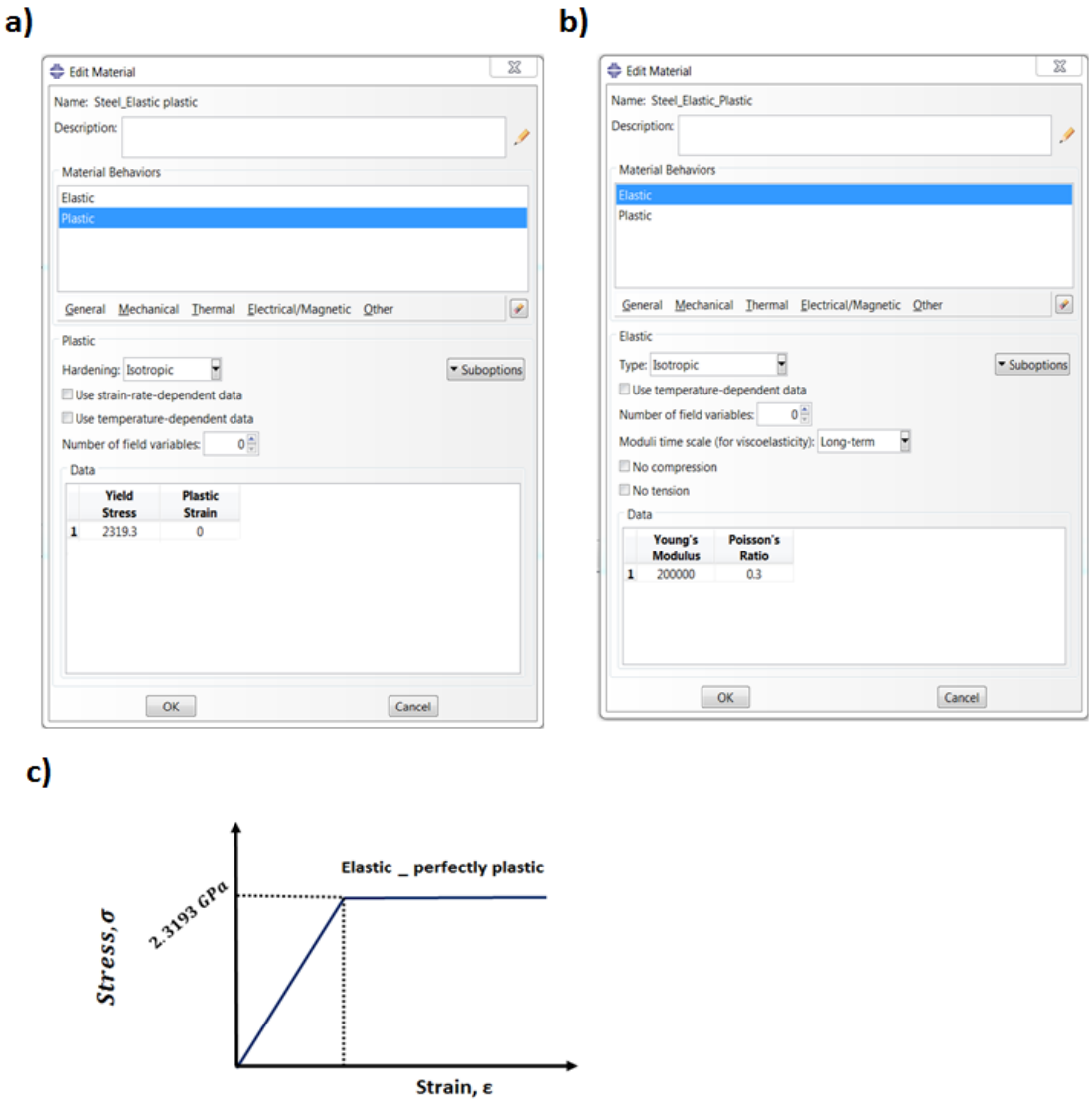

Figure 3.10 –The initial material properties used for model; a) Snapshot Abaqus/CAE 6.12 "Edit Materials" menu for elastic-perfectly plastic, b) Snapshot Abaqus/CAE 6.12 "Edit Materials" menu for two elastic constant to characterize the material, c) elastic-perfectly plastic stress strain curve.

For the initial analyses the material properties were defined to be elastic-perfectly plastic, however difficulties were encountered in getting the model to complete successfully. This is related to the lack of stiffness associated with perfectly plastic behaviour which leads to convergence difficulties in obtaining solutions to the contact problem. So, the plastic behaviour was modified from the elastic-perfectly plastic case

first utilised to comprise linear strain hardening behaviour $E_T/E = 0.05$. As shown in Figure 3.11(a). Including strain hardening in the material model leads to more controlled penetration behaviour in the contact model so that numerical convergence problems that occur with elastic-perfectly plastic behaviour can be avoided. This is also a beneficial choice in being representative of the real material behaviour because in practice, no materials exhibit elastic-perfectly plastic properties. Generally the tangent modulus E_T is varied based on hardening parameter (H) which is explained in detail in Chapter 2 and defined as $H = E_T/(E - E_T)$. The value of (H) is taken in the range $0 \le H \le 0.5$ as most of the practical materials fall in this range. In order to calculate the stress-strain relationship for the plastic behaviour subsequent to initial material yield the stress strain slope then becomes E_T and in the current work generally $E_T/E = 0.05$. The plastic behaviour is described by specifying a true stress of 10 GPa with corresponding plastic strain of 0.332 as shown in figure 3.11 (which is schematic). This is the method required by the Abaqus system and the high true stress value of 10 GPa is specified in order to ensure the required plastic behaviour is observed throughout the material without any perfectly plastic behaviour. For the loading conditions of the simulation analysis this true stress level is not exceeded. The calculation of initial strain input is done by the following equation.

$$\sigma = E\varepsilon \qquad 3.1$$

Abaqus analysis requires strain and the true stress to be used rather than the nominal stress and strain to specify the elastic-plastic behaviour as shown in figure 3.10(c). So, the true stress and strain can be calculated using equation 3.2 and 3.3, respectively,

and the true strain then can be converted into the true plastic strain using equation 3.4.

$$\sigma_{true} = \sigma_{norm}(1+\varepsilon_{norm}) \quad 3.2$$

$$\varepsilon_{true} = \ln(1+\varepsilon_{norm}) \quad 3.3$$

$$\varepsilon_{true}^{pl} = \varepsilon_{true} - \frac{\sigma_{true}}{E} \quad 3.4$$

As shown in Figure 3.11(a-b) the Strain hardening behaviour is specified in almost the same way as the previous yield strength value is defined for elastic-perfectly plastic behaviour by using the Property module, and is specified in the Edit Materials menu. The value of plastic strain of 0.33174 that takes place at a specific stress 10 GPa is inserted in the right and left columns, respectively. (A series of true strain and plastic strain value pairs can be entered in this way to define a curved strain hardening behaviour. The elastic behaviour is given by the Elastic modulus specified and the elastic limit has a true stress value of 2.319 GPa which corresponds to the enigineering stress yield point of 2.29 GPa.

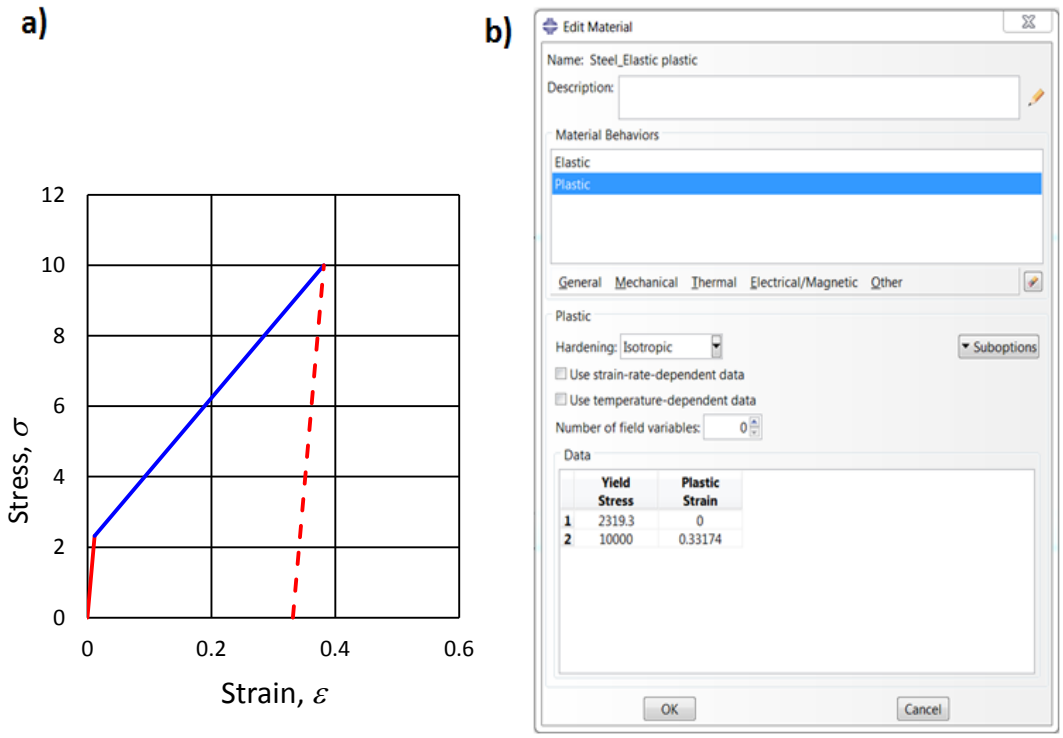

Figure 3.11 – The material properties used for model; a) linear strain hardening, b) Snapshot for Abaqus/CAE 6.12 "Edit Materials" menu for linear strain hardening ($E_T/E = 0.05$).

3.4.1.3 Cyclic boundary models

Alongside the development of a model of the surface roughness contact occurring between disks a model of the rough surface contact in the context of a flat surface was also developed. The purpose was to investigate whether a full disk model was necessary to obtain an understanding of the way in which asperities would deform plastically, or could a repeated roughness profile on a flat surface contact be used for the same purpose utilising cyclic boundary conditions to confine the analysis to a relatively short representative length of the surface. The basis of this model is illustrated schematically in Figure 3.12 where the representative profile is profile length AB. This profile is reflected at B to add reversed profile BA'. The component modelled is then the 'rectangle' BA'C'C. Applying suitable boundary conditions to

edges BC and A'C' enable the component to behave as part of an infinite plane surface with repeated profile AA' in both directions. The necessary boundary conditions are that side boundaries BC and A'C' are restrained from deflecting perpendicular to the boundary and are allowed to deflect parallel to the boundary. Lines of geometrical symmetry BC and A'C' thus remain in the same positions under load as would be the case for the infinite plane body.

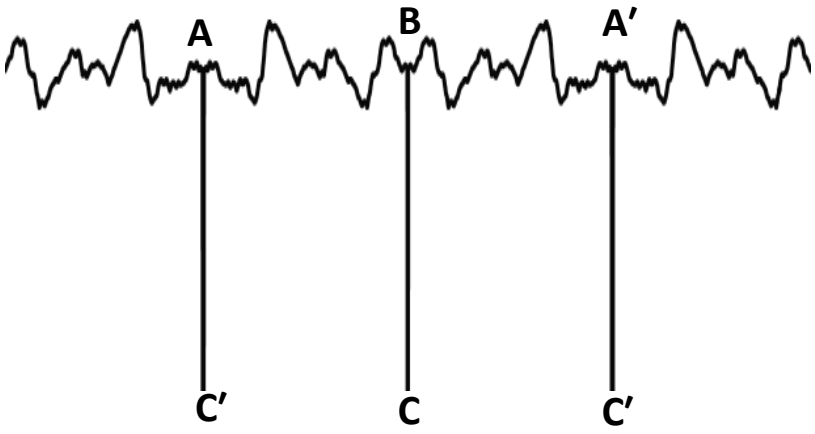

Figure 3.12 - Model boundary condition represent by infinitely reflected edges.

The FEA model developed is illustrated in Figure 3.13 which shows the shape of the model (BA'C'C) and the boundary conditions applied to the sides as illustrated by the red triangles. A distributed load was applied to the bottom edge of the model (the smooth surface) and the part was loaded against the rigid plane surface shown above the rough surface. This requires contact initiation with a small vertical displacement in a separate step called the contact step. This was achieved by applying a specified displacement, or interference, to the contacting body such that the highest asperity made contact with the plane counterface. In the next step, this displacement was removed while simultaneously applying the distributed load illustrated by the purple arrows on surface CC'. The distributed load applied was set to a range of loads from 500 to 4000 MPa in steps of 500 MPa. Each of these load applications is a separate

step of the Abaqus analysis and as the load is increased multiple asperity contacts occur resulting in material plasticity. In the final step, the distributed load was removed to obtain residual deformation and stress fields to be ready for comparison and investigation.

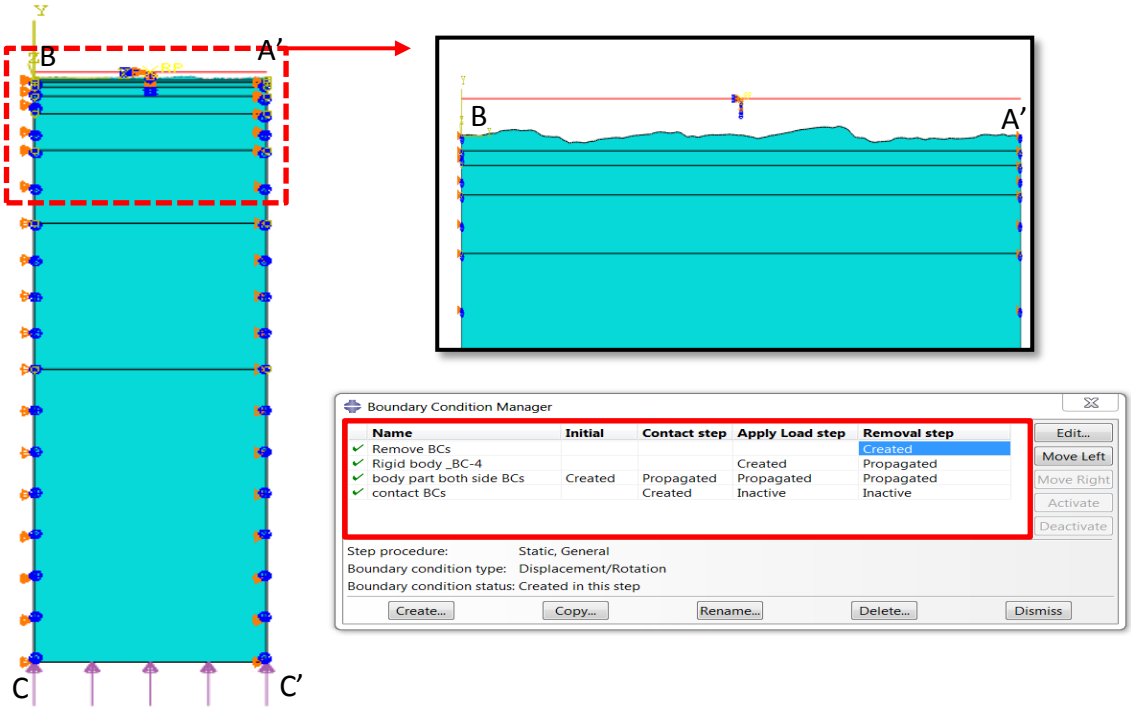

Figure 3.13 - The FEA models developed shows the shape of the model (BA'C'C) and the boundary conditions applied to the sides (red triangles).

3.4.1.4 Model Steps

The basic concept to solve the problem in Abaqus is the separation of the problem history into steps. Thus, a step is any convenient phase of the history such as a creep hold, a dynamic transient, etc. The study procedure can be changed as the analysis moves from one step to other step in any meaningful manner, hence it has great flexibility in performing analyses and in providing an investigation option for the user. Since the state of the model (stresses, strains, deformation, etc.) is updated, the effects and result of prior history are always taken into account in calculating the

response to each new step as it is imposed. This research of contact models is based on four steps, the initial step, the contact step, the load application step, and the load removal step. Boundary conditions are applied in the initial analysis step as required by Abaqus software. This step is reserved for applying boundary conditions only and no external loads can be applied during this step. In all steps, the upper smooth surface roller or the rigid counterface part were restrained in all directions. In the next analysis step (the contact step) contact was initiated by applying a small displacement to the lower edge of the deformable rough surface roller to achieve an interference of zero between the highest asperity and the upper body (the smooth surface roller or rigid part) at zero load. The load is applied in the next step by means of a "load step" as presented in the screen snapshot of steps shown in Figure 3.14, in which a range of loads will be applied. Lastly, the removal load step applied by means of a reversed displacement that is sufficient to separate the bodies so that there is no contact load. This allows the plastic deformation as well as the residual stresses to be obtained.

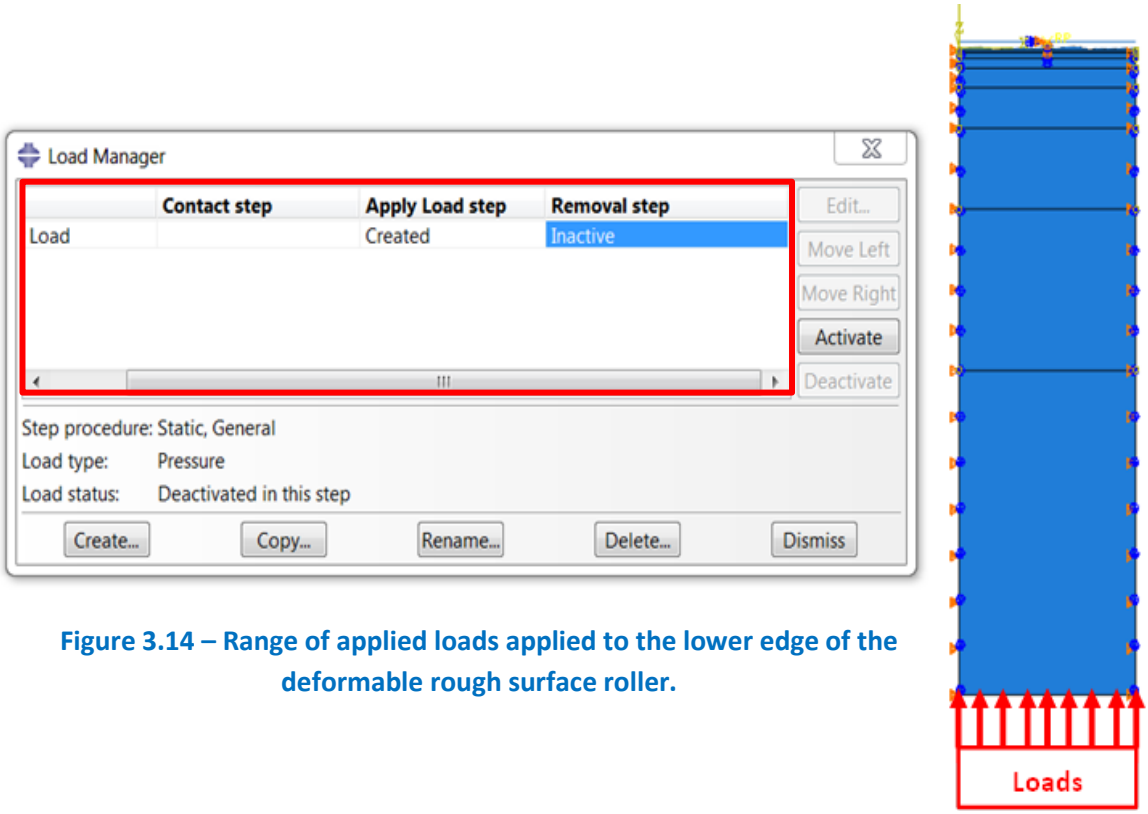

Figure 3.14 – Range of applied loads applied to the lower edge of the deformable rough surface roller.

3.4.2 Advanced Elastic Plastic line contact model

A modelling framework representing the contact behaviour of a real rough surface to simulate the disk test specimen as closely as possible is the main focus of this study. This ideal model will involve several aspects that must be considered such as theoretical issues, practical interest and important items including material models, element types, FE mesh, convergence and boundary conditions. These issues lead to a model that must be detailed enough to be able to capture the important phenomena, but it should not be more complex than necessary to achieve the sought engineering outcomes since this would only increase the computer time needed.

The results obtained with the basic elastic-plastic contact models, described previously, were found to exhibit undesirable aspects in the plastic behaviour predicted such as:

- As load was increased the zone of plastic deformation in the model tended to extend to the transverse boundaries. This was felt to be unrealistic and a consequence of the proximity of the transverse boundary.
- The constraint applied by the transverse boundary conditions load the material so as to prevent transverse motion at these boundaries which adds to the compressive loading of the material.

These features of the basic model affect the value of the residual stress calculated and clearly indicate the need for a reconsideration of the plastic behaviour to ensure that the model corresponded more closely to semi-infinite body conditions.

Instructions in further advanced contact modelling techniques was obtained from the software manufacturer by attending an advanced usage course and this

provided further guidance as to how these difficulties could be avoided in simulating the real situation.

3.4.2.1 Advanced model's geometry and element types

Investigation of the results obtained with the basic model indicated that the transverse boundaries were too close to the roller part to obtain realistic results. Figure 3.15 illustrates the sequence of steps carried out to obtain and extract the residual profile shape and residual stress field that will be discussed in detail in section 4.3.5 for both the basic and the advanced model. The issue to be discussed here is comparison between the two models is in terms of the plastic deformation. The contacts are loaded by applying a specified distributed load to the lower surface of the model in a plane strain analysis, resulting in material plasticity for multiple asperity contacts. Profiles (c) show the loaded contact and for the basic model (upper figure) contact occurs up to the transverse boundary of the model at this load. In reality the material will not be restrained in accordance with the boundary conditions applied for this case as the surrounding disk material will be able to accommodate some transverse deflection and will remain elastic as can be seen for profile (c) of the advanced model (lower figure).

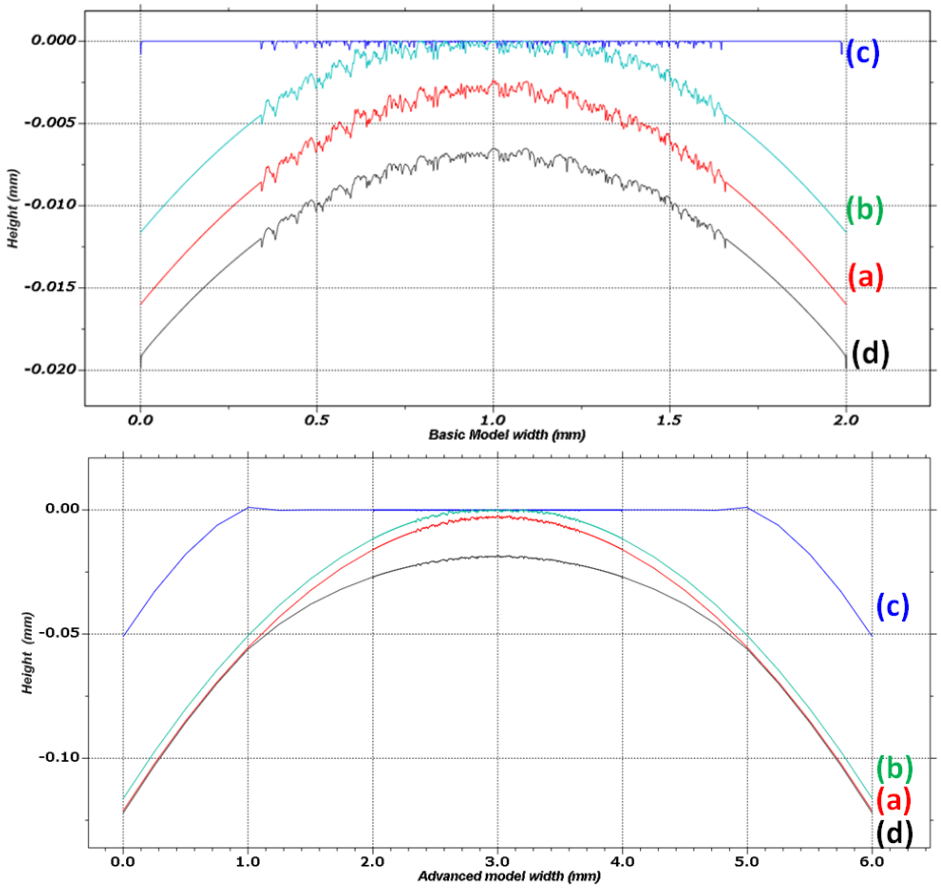

Figure 3.15 – Rough surface boundary at different steps in the loading sequence: upper figure shows the basic model, lower figure shows the advanced model. Profile (a) is the initial unloaded profile, (b) is initial contact, (c) loaded profile, (d) profile after loading.

Consequently, the advanced model had an increased size achieved by incorporating further parts as shown in Figure 3.16. Each of the parts at the top of the model was 2.0 mm wide giving an overall width of 6.0 mm. This approach was taken so that the contact would be wide enough to restrain the transverse expansion of the central part elastically. A further part was also added beneath these parts to increase the distance from the contact surface to the load application boundary sufficiently for it to behave as a semi-infinite body. Each of these parts was connected to the others at their common boundaries using surface ties highlighted in red.

The tie option ensures that the parts deflect so that their interfaces deflect in the same way. As they allow the parts to have different mesh structures, the mesh does not need to be continuous across the boundaries. This allows the additional parts to be meshed coarsely and their function is to provide a suitable elastic buffer between the part loaded by contact, and the displacement boundary conditions applied to the outer surfaces.

Once the surface ties had been applied, the parts were then assembled as the final rough roller model. The total width of the assembled parts is 6.0 mm and the depth is 4.00 mm. The material of the model was discretised with the plane strain elements (element type CPE4).

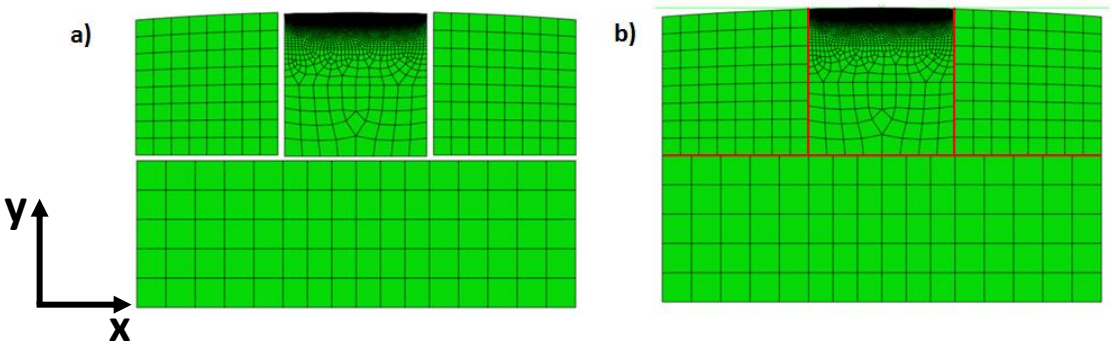

Figure 3.16 - Advanced model parts, a) before assembly, b) After assembly. The sense of the coordinate axis set x,y is indicated and its origin is at the crown of the roller radius.

3.4.2.2 Defining material properties for the advanced model

To construct a model in Abaqus, it is essential to calculate the properties as input data. The advanced model was given elastic-plastic material properties, with yield strength, σ_y of 2.293 GPa as for previous models. Beyond the yield point linear strain hardening was specified with a value of $\frac{E_T}{E} = 0.05$ as discussed in section 3.4.1.2. This property was applied to all elements of the model using the Property module, and specified in

the Edit Materials menu using the mechanical properties' icon to define the elastic plastic behaviour. Following that, the material section editor was utilised to assign the materials property to the four parts of the advanced model. The material name specified for each part is displayed as part of the section assignment manager definition.

3.4.2.3 Advanced model ties (connecting parts)

The boundaries of the main part of the advanced model (that includes the surface roughness profile) were attached to the added parts using a modelling technique known as *surface ties*. Tied contact was used for connecting the parts with each other as shown in the Figure 3.17. According to Abaqus (6.12v), surface ties require the selection of a master and slave surface. Choice of the master surface is along the same lines as discussed in section 3.3.6 for contact surfaces, and in this case the overriding consideration is the difference in resolution of the parts so that the coarse surface is selected as the master surface. Applying a surface tie allows two surfaces to be tied together during the simulation process and constraining each of the nodes of the assigned slave surface to have the same variable values as the equivalent node on the assigned master surface. In this approach of ties, each of the nodes on the fine mesh has the same displacement as the point on the coarse mesh to which it is the closest. This allows for the modelling of normal as well as shear stresses along the entire tied surfaces.

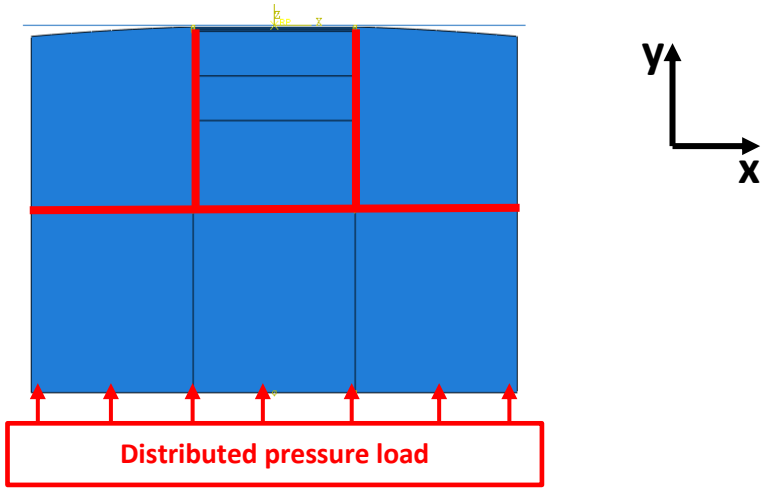

Figure 3.17 - Tied contact was used for connecting the parts with each other.

3.4.2.4 Model Boundary conditions and applied load

The most obvious changes taking place for the advanced model is the increased body dimension in both directions and the boundary condition location changes. The boundary conditions were chosen to enable the pressure load simulation without rotations or bending as the following and shown at Figure 3.18 and Table 3.1:

- The rigid part is set as clamped in all directions at the middle of the body as shown in Figure 3.18_ (1). The pale horizontal line at the top of the figure is the rigid surface as illustrated by the Abaqus software. The symbols illustrated at point (1) are the constraint symbols.
- The transverse boundaries of the model are restrained perpendicular to the side of model and are free to move in the direction of load application as shown in Figure 3.18_ (3 and 4).
- The bottom boundary is restrained in the direction parallel to the base of model and is unrestrained to move in the direction of the pressure load as shown in Figure 3.18_ (2).

In this way the model is free to move in the direction of the distributed force applied to the bottom of the model and is restrained from overall expansion or contraction in the transverse direction. The model was loaded using the surface interaction load scenario, where the parts were arranged to be on the verge of touching and then a small vertical displacement was applied to initiate contact. This small displacement was then replaced by a distributed load which was applied at bottom surface of the model as shown in Figure 3.18 with red arrows. Finally the distributed load was removed and the components separated to identify the residual deflected shape and the residual stress results.

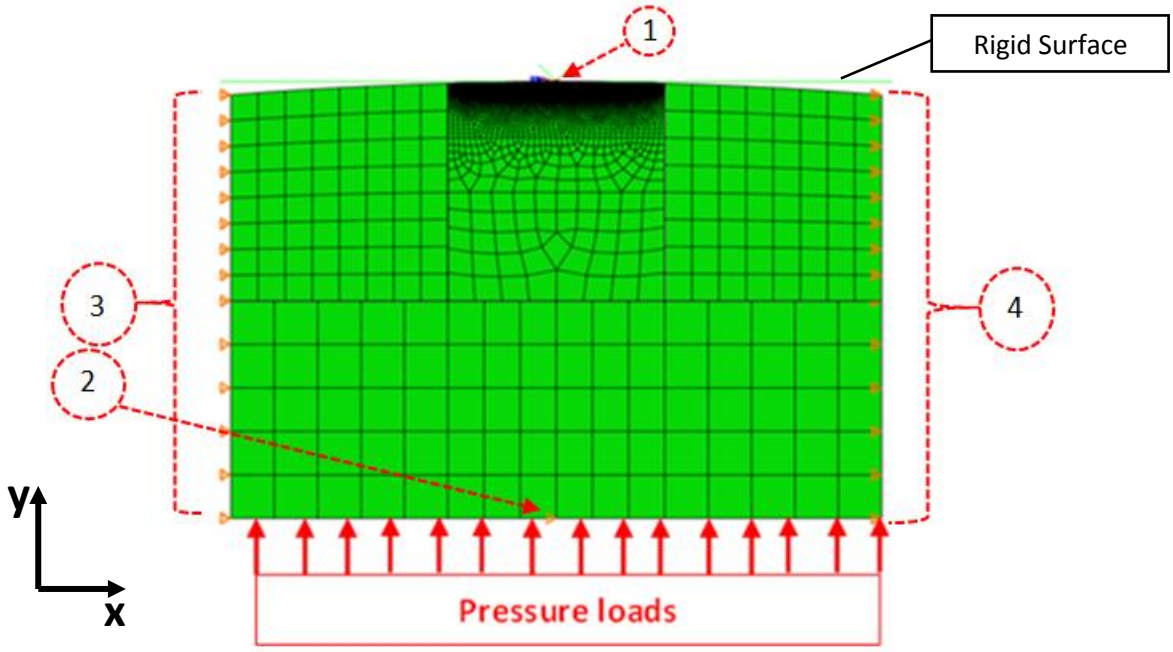

Figure 3.18- Boundary conditions and the load applied on the advanced model.

Table 3.1- Advanced contact model summary.

Part	• Line segment (rigid part)
	• 2D Rough roller consist of separated four sections:
	  ○ 2D smooth roller $R = 38.1\ mm$ (2x2mm) left side section.
	  ○ 2D rough roller $R = 38.1\ mm$ (2x2mm) middle section involves rough profile.
	  ○ 2D smooth roller $R = 38.1\ mm$ (2x2mm) right side section.
	  ○ 2D Rectangular (6x2mm) bottom section.

Material Property	All the part section has isotropic property as: E=200E3 MPa,$\nu = 0.3$,$\sigma_y = 2293\ MPa$, $^{E_T}/_{E} = 0.05$
Assembly	• The entire part sections are tie. • The rigid part position with the main block body assembled in certain contact distance. • The model boundary aligned with edge of the outer section. • Rigid boundary clamped in the middle rigid part.

steps	• Four steps in consequence:
	  ○ Initial step which required by Abaqus.
	  ○ Contact step to make touch between rigid and rough top surface roller.
	  ○ Apply load step.
	  ○ Remove load step to avoid external load effect the result.

Interaction (as advised by the Abaqus Contact Analysis course director)	• Pressure hard contact, with augmented Lagrange constraint enforcement. • Friction less. • Surface to surface. • Finite sliding.
Contact control	Absolute penetration tolerance =10E-3
Load applied	Range of loads, start from 500 MPa to 4000 MPa with step 500 MPa.
Mesh elements	• CPE4 Element type. • Fine mesh around the rough surface 1.0 um. • Course mesh remote from the rough surface.
Boundary conditions	• Rigid body - Encastre (Ux = Uy = Uz = URx = URy = URz=0). • Elastic body - Transverse sides (Ux=Uz=URx=URz=0). • Elastic body – Lower surface (Ux=Uz=URx=URz=0).
partitioned sections	Main block body has partitioned around the rough surface and part ion on distance (10, 30, 50 , 500, 1000 um) from the surface for change mesh purpose.

3.5 Model Verifications

To be able to verify the quality of the contact model, various processes and techniques will be explained in the next chapter that were used to assure that the simulation contact model matches the geometry of the real disk being modelled. Figure 3.19 shows a 0.15 mm roughness profile in blue which was extracted from the simulation contact model after having superimposed it on the model's curved surface and the real rough surface of the disk shown in red after applying a shift between them to clarify the similarity.

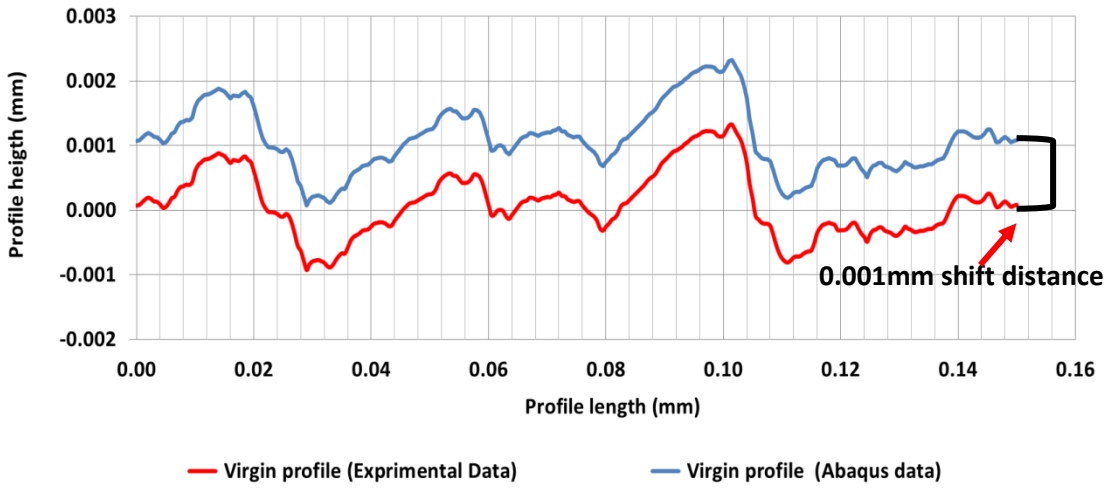

Figure 3.19 - The profile for the simulation model and rough surface disk after applying shift between them.

3.6 Conclusion

This chapter has presented a short description of Abaqus as a means to implement a FE contact analysis model and its techniques which were utilised to build up contact models. Then the contact models constructed and their development to determine the best model geometry were described in terms of the software features. Initially, the significant sample length of surface roughness obtained in the lab was superimposed

onto a smooth surfaced roller and then imported into Abaqus using a Python code. Following that, different 2D axisymmetric a plane strain line contact models were developed. These numerical models were constructed and then verified by comparing results of the simulations with experimental results to ensure that a modelling framework representing the behaviour of the real contact was achieved and verified.

Chapter 4

Abaqus analysis and profile repositioning

4.1 Introduction

Rough surface profile information was obtained from both run and un-run surface disks as shown in chapter 3. The level of residual deflection observed due to running in after the experimental test was obtained by comparing the profiles taken before and after the test. This residual deflection was then used to determine the appropriate level of residual stress to which the deformed asperities would be subjected. The determination of the appropriate level of residual stress to be added to the material beneath the rough surface profile asperities consisted of several phases. This chapter illustrates all the phases which have been used, starting from extracting the surface roughness profile from the real surface of the experimental disk as the first phase and determining the level of residual stress to be added to the rough surface material beneath the asperities as the final phase.

4.2 Repositioning the experimental profile

4.2.1 Surface nature

The texture of the surface is the recurring or random divergence from the nominal surface that forms its three dimensional topography. Generally, the surface texture involves three features after manufacturing: (1) roughness (nano and micro-roughness); (2) waviness (macro roughness); (3) lay and flaws. The fluctuations in the surface produce the 'nano' and micro-roughness where the short and long wavelengths are characterised by hills or peaks called asperities (local maxima) and

valleys (local minima) of shifting amplitude and spacing. These are large in comparison to molecular dimensions. Waviness is the second property associated with surface irregularity. It is called macro roughness. It may arise due to factors such as machine chatter or vibration, work piece bending or heat treatment. Lay is defined as the direction of the principal surface pattern, which is usually determined by the production method. If the production method produces a surface with isotropic roughness, e.g. sand blasting, there is no lay, but in manufacture of hardened gears by grinding there will be a lay which may vary according to the grinding process used. A flaw is unplanned, unforeseen, and unwanted intervention in the texture. These characteristics of roughness are illustrated by (Bhushan, 2002) as shown in Figure 4.1 which shows the case of a flat surface. For any other component shape the roughness is superimposed on the form, which is the ideal shape of the surface being produced.

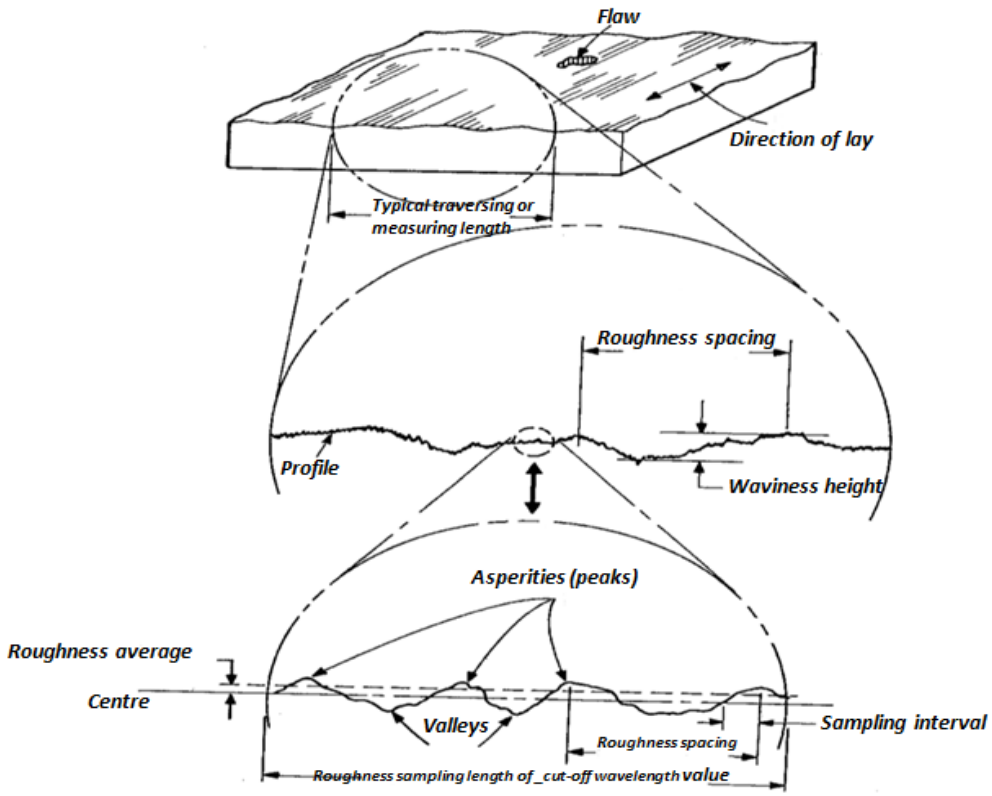

Figure 4.1 - The surface texture involves three features after manufacturing (1) lay and flaws (2) waviness (macro roughness) (3) Roughness (Nano and micro-roughness)(Bhushan, 2002).

4.2.2 The surface measurement technique

A distinction is made between methods of evaluating the nano-scale to the atomic scale, and the micro scale features of surface roughness. Nano to atomic scale roughness is measured using atomic force microscopes of different types and is not a consideration in the research reported in this thesis. For micro scale features, the measurement technique can be divided into two broad categories as far as the different instruments available are concerned, as follows: (1) contact type instruments in which a component of the measurement equipment actually contacts the surface to be considered, and (2) non-contact instruments in which there is no physical contract with the surface being measured. A contact type instrument may damage surfaces when using a sharp stylus tip, particularly on a soft surface, and more details about various other techniques can be found in (Bhushan, 2002) and other references (Williams, 1994). In the research reported in this thesis a portable Form Talysurf (Taylor Hobson) was used to evaluate the 2D surface roughness. The equipment is illustrated in figure 4.2 and incorporates a stylus device with a stylus tip of 2 µm which conforms to national standards.

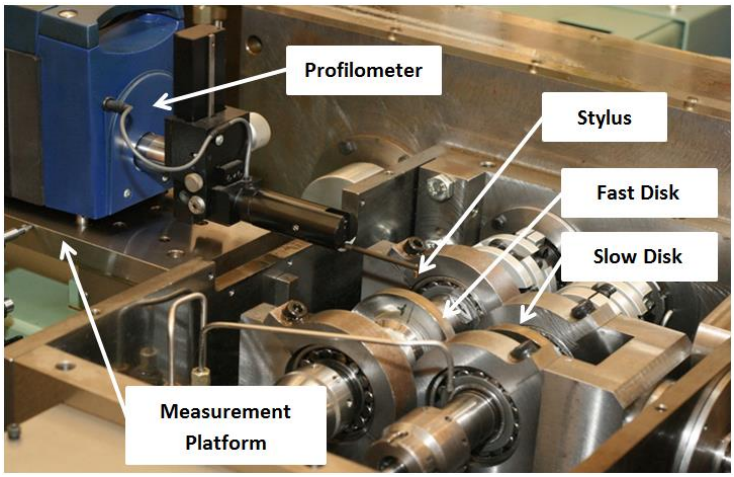

Figure 4.2 - Form Talysurf mounted on measuring platform in the position used to acquire a circumferential profile from the fast test disk (Photo courtesy of Weeks, 2015).

The profilometer is mounted on a measurement platform which is illustrated in figure 4.3. The platform is mounted on the test rig and enables the profilometer to be accurately located in two positions with its measurement axis perpendicular to the disk shafts. The measurement platform has a three point mounting system that can position the profilometer in one of two positions. The first is the backward position as illustrated in figure 4.2 that allows profiles to be taken from the stationary fast disk, the other is the forward position which locates the profilometer in the correct position to acquire a profile from the stationary slow disk. The measurement platform is supported by a traverse that allows the instrument to be moved parallel to the disk axes and the dial gauge shown in the photograph of Figure 4.3 is used to measure the distance moved by the traverse. These features are used to ensure that the profiles acquired from the disks are taken at known axial positions.

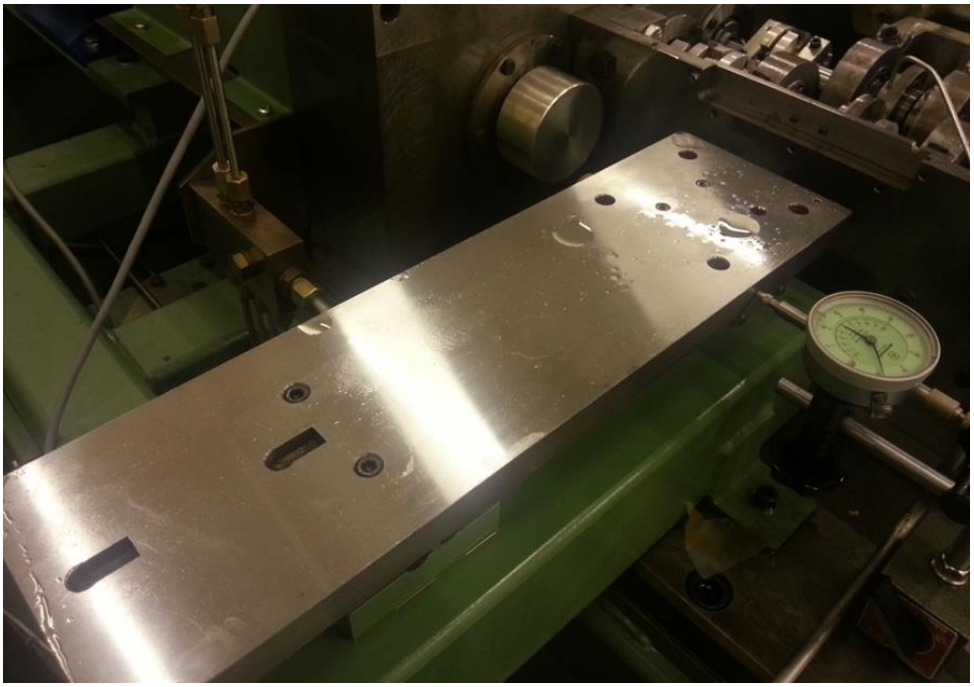

Figure 4.3 - Measuring platform permanently mounted to the test rig structure as a rigid locating support for the profilometer when profiles are measured (Photo courtesy of Weeks 2015).

Real engineering surfaces manufactured using machine tool or equivalent processes generally exhibit variation in the height of the surface relative to the mean surface plane. A range of statistical roughness parameters are used to describe and quantify the surface roughness. These parameters include height parameters that relate the variation in height, and spatial parameters that relate how height varies in the surface plane. Some of these parameters are described in Table 4.1 where z stands for the height of surface measured above the mean level and L refers to the length of measurement. More detail regarding rough surfaces and descriptors are available in the references Williams (1994).

Table 4.1- Main parameters for surface roughness finish.

Average roughness taken over 2-20 samples , R_a	$R_a = \frac{1}{L}\int_0^L \lvert z\rvert \, dx$
RMS roughness, R_q	$R_q = \sqrt{\frac{1}{L}\int_0^L z^2 dx}$
Peak-to-valley height, R_t	Separation of lowest valleys and highest peaks.
Average peak-to-valley height ,R_z	Average of single R_t value over five adjoining sampling lengths.
Maximum peak-to-valley, R_{max}	Largest peak-to-valley height in five adjoining sampling lengths.

4.2.3 Profile Filtering (Cut off)

The cutoff filter length is an international standard definition for the filter length that is used to produce the waviness and roughness data and to specify the range of spatial wavelengths or the spatial frequencies in the waviness and roughness data. It works such as a high pass filter in electronics that pass frequencies higher than its cutoff and block lower frequencies as shown in the Figure 4.4. However, the user must define the cutoff filter and the intended spatial frequencies for surface analysis in either the waviness or roughness data. For the initial modelling attempt in the research, the

profiles were taken from the same disk using the Talysurf before and after applying the load. The profiles were digitally filtered using a standard Gaussian filter to remove wavelengths in excess of the cut off length of 0.25mm. This cut off length was chosen from those available as it is close to the Hertzian contact dimension, *a,* for the experimental contacts considered.

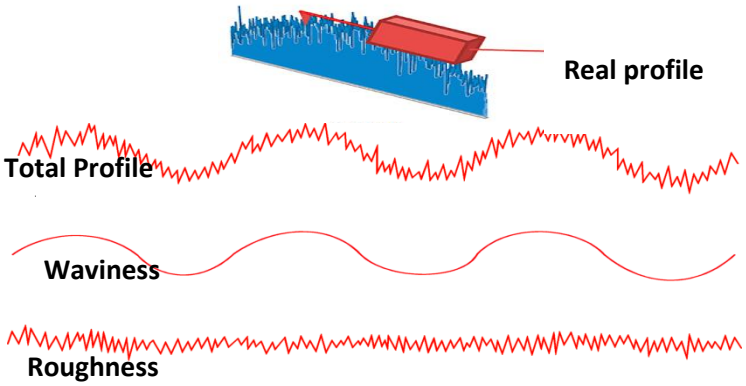

Figure 4.4 - Filtering process.

4.2.4 Extracting disk profiles

In order to develop a simulation model similar to the real case by means of the finite element analysis and to compare experimental results efficiently, it was necessary to read the surface roughness profiles before and after applying load. This was carried out by a colleague carrying out an experimental study of running in and is reported in detail in Weeks (2015), assisted by the current author for some of the experiments. Two circumferential profiles along the mid plane circumference of the experimental disk (transverse to the disk axis) were taken for both the run and un-run (as manufactured) disk surfaces using a standard stylus profilometer at nominally the same position. The disks were mounted in the machine on their shafts and rotated by hand to their nominal measuring position. The profile measurements were then taken in situ by the profilometer. The profilometer support incorporates a traverse in the

direction of the shaft axis which allowed circumferential profiles of the disks to be taken at different axial positions. The axial position was established by using the Talysurf and the traverse to find the chamfer at the face edge of the disk, and then using the traverse to move the instrument to the required position, determined accurately with the use of a dial gauge. The un-run profile for both disks were taken in this way before running the rig, and the profilometer was removed for safe storage. The disk machine was then started and run with no contact with circulating oil until the steady operating temperature was established. A nominal Hertzian contact pressure of 1.7 GPa (4150 N) was then applied for a short period and removed .The machine was then stopped and allowed to cool down to room temperature. The oil adhering to the running surface was removed by wiping and subsequent solvent cleaning. The profilometer was then re-mounted on the test rig and further profiles were obtained at the same specific circumferential locations of the disk .This process was then repeated for a second run of the machine to obtain a further profile after load stage 2. Once these steps had been implemented, three surface roughness profiles (un-run, run /stage1 and second run /stage 2) associated with the applied load were ready for use as shown in chapter 3 figure 3.2. These three profiles were clearly distinguishable by the shape of the asperity peaks. Profiles of the run surface exhibited wider, flatter peaks due to plastic deformation, resulting in a more negative skew in the surface height distribution in comparison with the un-run surface profile. The process causing change in shape of the asperities is illustrated for a single smooth body before and after loading in Figure 4.5 as discussed by Jamari and Schipper (2007) and more details are discussed in chapter 5.

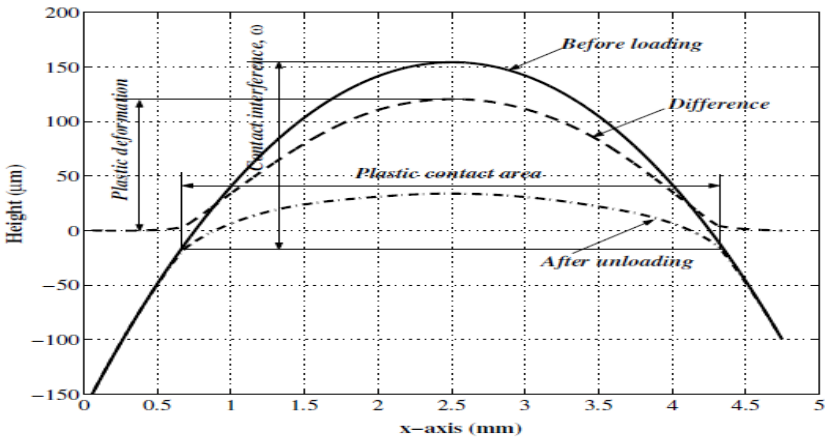

Figure 4.5 - An asperity Surface profile before/ after loading (Jamari and Schipper, 2007).

4.3 Creating and analysing the Abaqus model

For the initial modelling attempt, the profile taken from the un-run disk was superimposed onto a smooth roller to create a part in the Abaqus system in order to simulate the contact of the disks. The disk radius of 38.1 mm was used to specify the part's radius of the curvature and the task of introducing the roughness profile was carried out using the steps described in the following sections.

4.3.1 Creation of model curved surface profile

Tasks using different mesh size referred to in section 3.3.3 led to the need for the roughness to be provided at a 1 μm spacing. To maintain generality in this process, a Matlab shape preserving routine was used so that the spacing could be specified to have any convenient value. Secondly, an Excel spreadsheet was used to superimpose the profile on an arc with a radius R=38.1 mm, chosen to match the size of the experimental disk. The flat surface profile in figure 4.6(a) and the arc profile figure 4.6 (b) were centred and aligned before adding them together as shown in Figure 4.6 (c). This profile was then used as input data for the macro used to create the Abaqus part described in the next section.

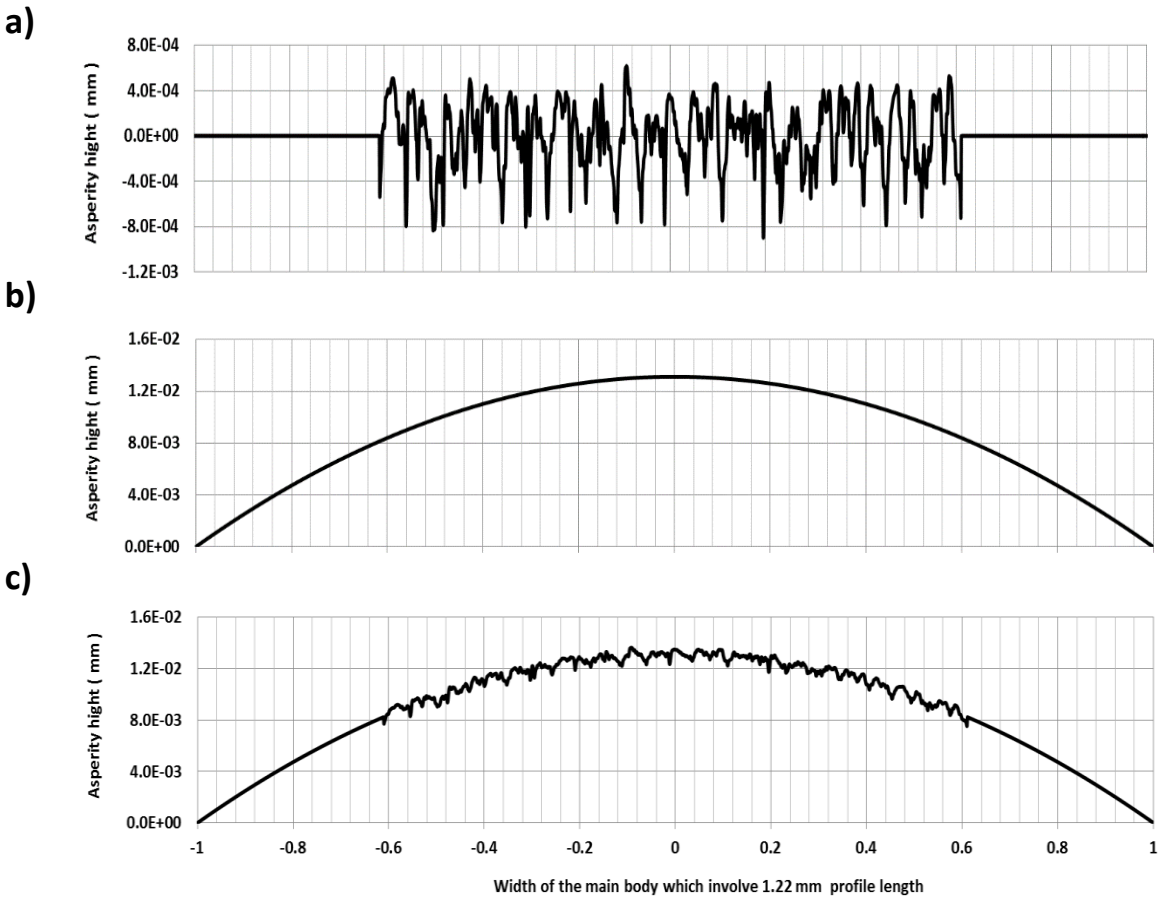

Figure 4.6 - Creation of rough surface roller; a) Filtered test disk roughness profile, b) Smooth circular profile, c) Filtered experimental disk roughness profile superimposed on the smooth roller profile.

4.3.2 Importing profiles into Abaqus/CAE

The rough surface profiles developed and superimposed in the previous section had to be available within Abaqus in order to make the contact model simulation the same as the real rough surfaces in contact. This was achieved using the Abaqus Scripting Interface commands and developing a macro. This approach had been developed by Bryant (2013) within the research group and was adapted for use in the current project. The scripting interface commands were assembled into a macro within the Excel spreadsheet that would create a Python script that could then be used to generate a model with the required profile coordinates in Abaqus. Figure 4.7 illustrates

how Abaqus Scripting Interface commands interact with the Abaqus/CAE kernel schematically.

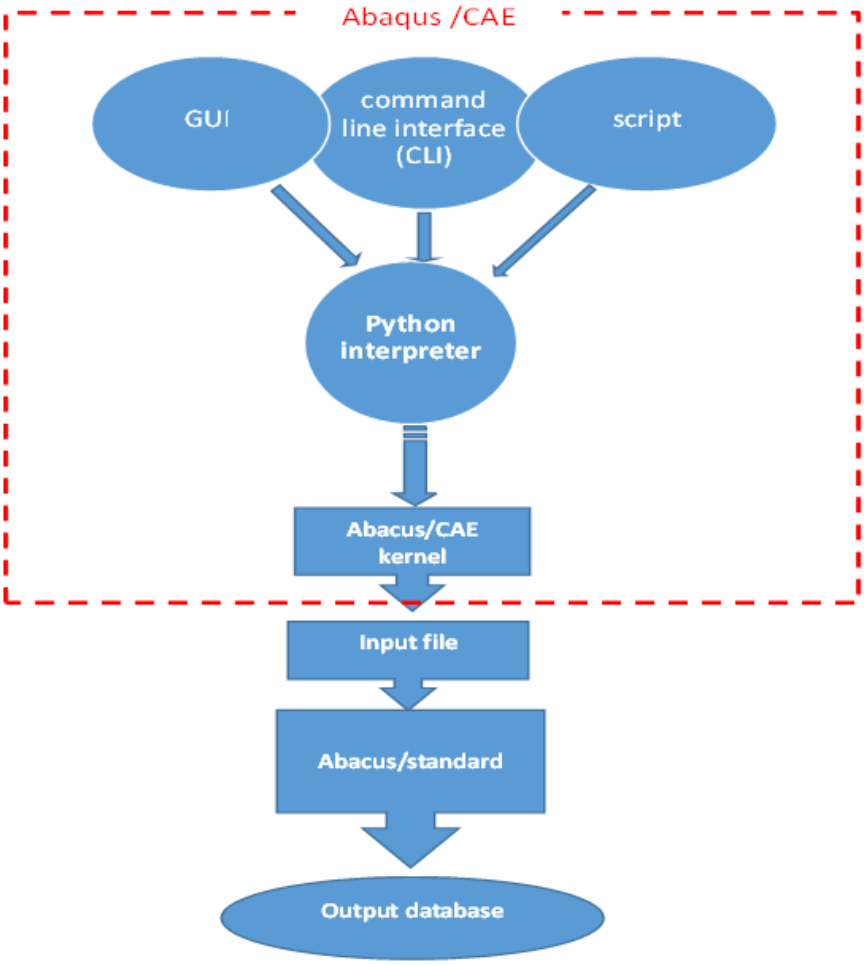

Figure 4.7- Abaqus Scripting Interface commands and Abaqus/CAE (Abaqus v6.12 manual).

In general if a sequence of commands needs to be executed to create a series of models it may be more appropriate to save the set of statements in a file called a script. So a script is a means to contain a sequence of Python statements in a macro. Macros are saved in a file called AbaqusMacroName.py. Abaqus/CAE searches three directories for AbaqusMacroName.py, in the following order:

- The site directory of the Abaqus installation.

- Home directory.
- The current working directory.

The macro used to create a roller with a measured roughness profile had been created to standardise and simplify the process.

4.3.3 Creating python Scripts

The Excel file part creation tool consists of three worksheets. The first worksheet contains the roughness data in the form of an (x, y) table of data points e.g. the profile of Figure 4.6(c). The second worksheet is used to specify dimensions for the model and the spacing of the sheet profile. It also contains a cell that, when selected, implements a series of Excel macros that write the necessary sequence of python script commands to define the boundary of the required part to the third worksheet. Sheet three is then the output file to be used to create the part in Abaqus. It is stored in the current working directory in a suitable file name e.g. profile_name.py.

4.3.4 Creating the part in Abaqus from the Python Script

There are different methods of running a script within an Abaqus/CAE session which involve typing certain commands from the start-up screen or from the File menu (Abaqus v6.12 Manual) .The latter method is the one which has been used in this study. Abaqus/CAE can be opened, and a new model created once the Python script file has been generated by the Macros in the Excel workbook. From the Abaqus taskbar “File” is chosen at the top of the window, and the “Run script” option is selected. A 2D deformable part based on the roughness profile specification and part

dimensions details specified by the user is then developed by running the script. If required, in the same way as with any other Abaqus/CAE model, the user can modify the part and proceed with creating a finite element model. Three parts number 1, 2 and 3 were made by Python script independently, each corresponding to a different feature of the profile to give greater width if necessary in horizontal direction and also a single rectangle part number 4 created to give greater depth if necessary in the vertical direction as well as shown disassembled in Figure 4.8.

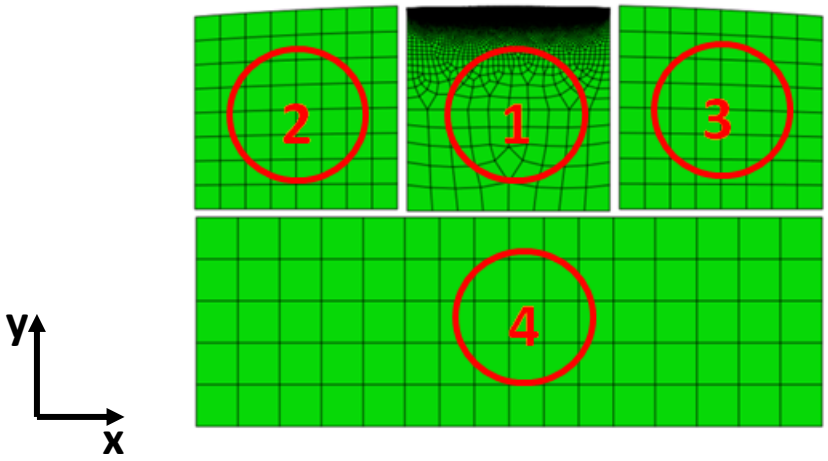

Figure 4.8 – Model parts before assembly.

At the end of running the rough surface script and creating a finite element model, the rough surface is centred and aligned in the middle of the model. At the section assembly step in Abaqus, the section with the surface roughness profile was positioned in the middle of the assembly model to make sure the first contact takes place at the highest point on the roughness profile as shown in Figure 4.9. The red circle shows the position of the surface roughness before and after the section assembly Abaqus step. It would then be ready for applying loads and Abaqus analysis.

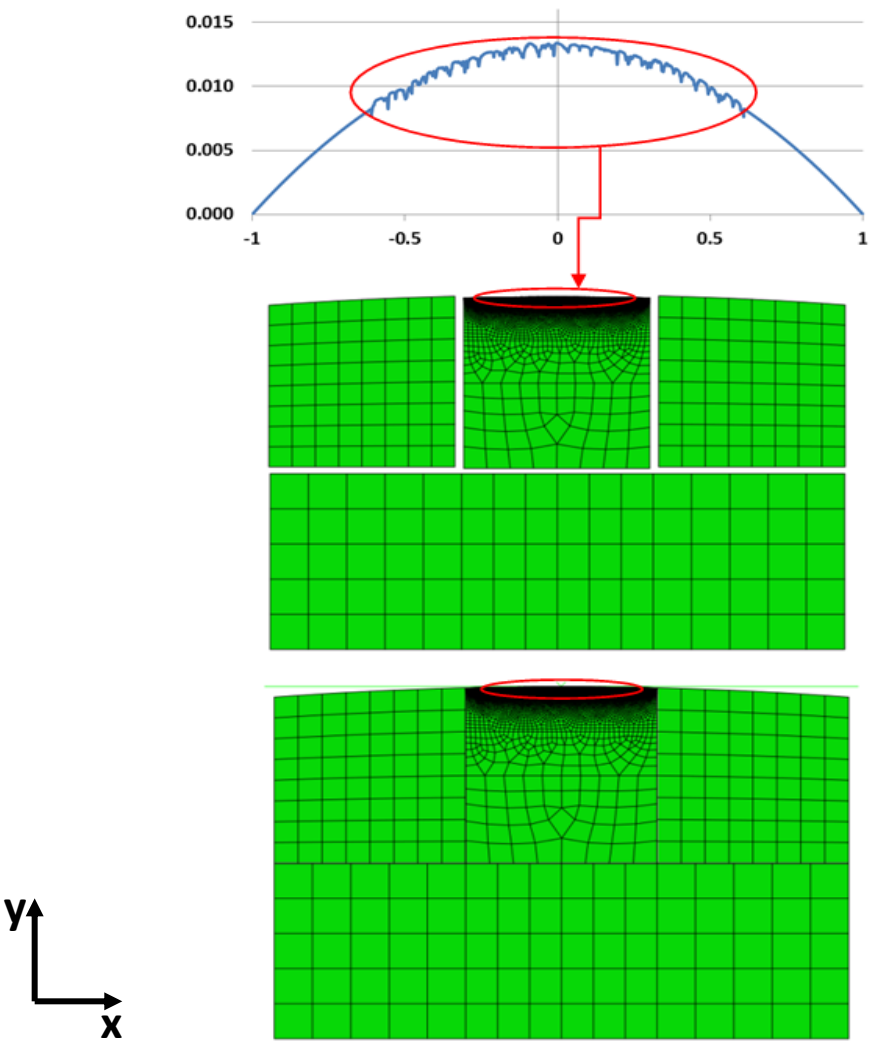

Figure 4.9 - The red circle shows the position of the surface roughness before and after the assembly Abaqus step (the dimensions of the upper figure are mm).

4.3.5 Abaqus analysis

The analyses consist of loading the part against a rigid horizontal counterface with height equal 0.0 mm in figure 4.10 which shows the rough surface profile at four steps in the contact analysis. This essentially loads the part against a reflection of itself in the rigid counterface so that asperities are aligned with their reflected counterparts. The contact was loaded by applying a specified distributed load to the lower surface of the model in a plane strain analysis. After the model had been loaded the load was

removed to give the residual shape of the surface after plastic deformation had occurred. The model also then allowed the residual stress field corresponding to the residual deflection to be illustrated. The residual profile shape and residual stress field were then exported in tabular form to allow further analysis to be carried out based on the results.

Figure 4.10 illustrates the sequence of steps carried out to obtain and extract the residual profile shape and residual stress field. Figure 4.10(a) shows the top surface profile for all steps related to the main body for basic model (number one in figure 4.8) and Figure 4.10(b) shows the top surface profile for all steps related to the main body for advanced model (number one, two and three in figure 4.8). For both figures, profile (a) represents the model before the analysis at the initiating step at which the time equals zero. Profile (b) has initiated contact with a vertical displacement in a separate step called the contact step. It was performed by applying a specified displacement, or interference, to the contacting body so that the highest asperity feature made contact with the rigid counterface. This is the starting position for the component in the iterative contact analysis. In the subsequent step, this displacement was removed while simultaneously the contact is loaded by applying a specified distributed load to the lower surface of the model in a plane strain analysis as shown in Figure 3.17, resulting in material plasticity for multiple asperity contacts to give the profile (c). After the model had been loaded the load was removed and a specified negative displacement applied to give the residual shape of the rough surface as shown in profile (d) after plastic deformation of the asperities has occurred. It also then had the corresponding residual stress available for inspection. The residual profile shape and residual stress field were then extracted for further analysis.

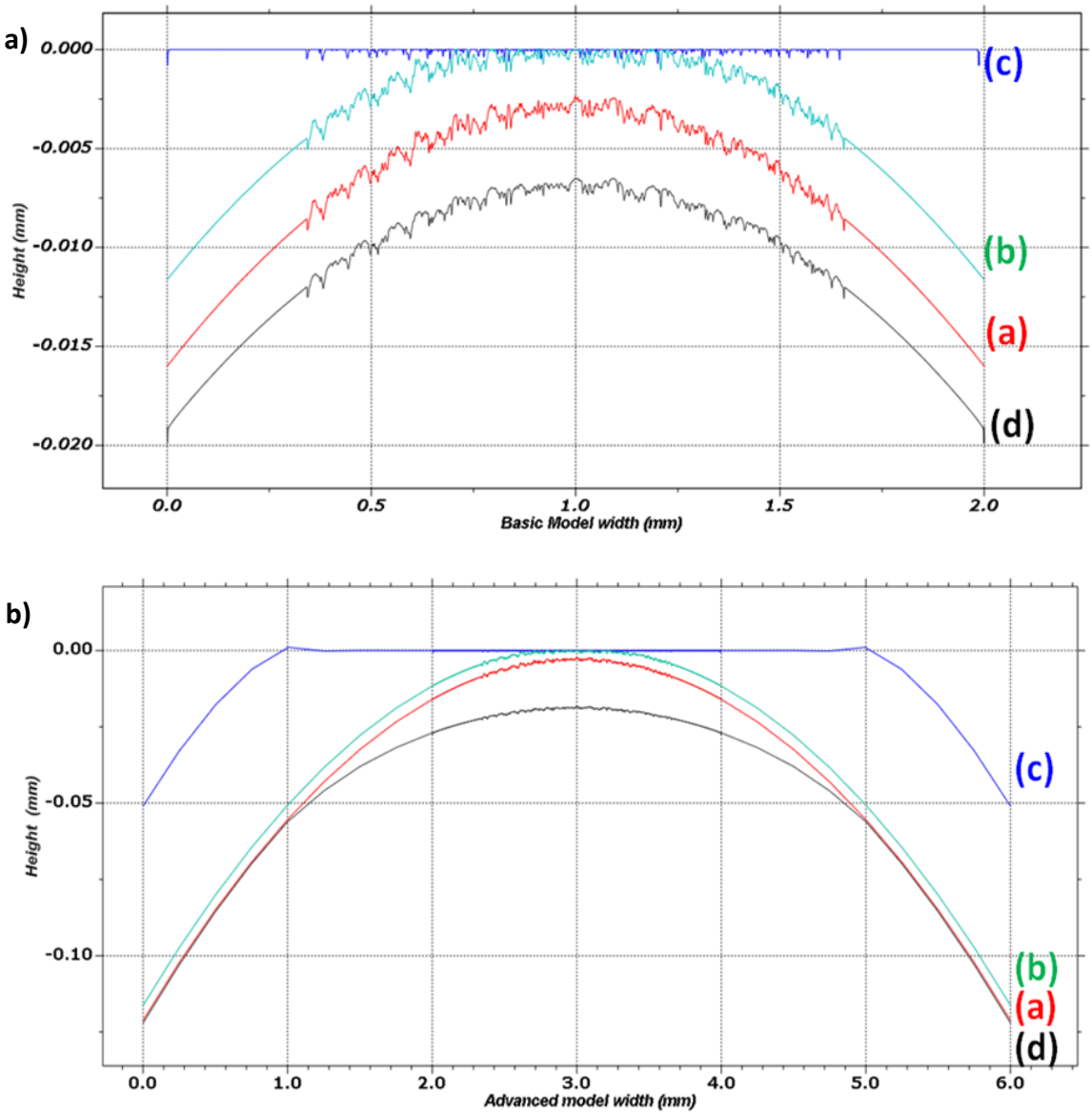

Figure 4.10 - The feature of the profile related to the Abaqus steps for main body at; a) profile position at first time step=0.0, b) profile position at final contact step, c) profile position at final step of complete load, d) profile position of final step of complete removed load. Upper figure shows basic model and lower figure the advanced model.

4.3.6 Interpolate the discrete roughness profile points for comparison

To relate the plastic deformation of asperity features observed in the experimental work to that occurring in the FEA models it is necessary to be able to compare them in detail at the roughness level. This requires the FEA surface profile after loading e.g. figure 4.10(d) to be exported from Abaqus. This can be achieved through Abaqus standard by creating an edge list path for the line path around the contact rough

surface which contains the 38.1mm radius. An Abaqus main menu tool is then used to tabulate the coordinates of the residual profile and the residual stress components at any specific step in the analysis for all the finite element nodes in the edge list path. These data are in the form of separate tables that include the node number with each entry. A FORTRAN programme was written to read these files and to associate the different data items by node number prior to sorting by position, as required for further analysis. This resulted in a table of stress components and node position for each node in the edge list path.

The form was removed from the post loading profile by starting with the profile in the form of Figure 4.10(d) and removing the best fit parabola to obtain the flat residual profile shape in the form of Figure 4.6(a). When the form is removed from the post loading profile, the profiles have the same main features for the same position; however, they are not known at the same discrete points. The reason for that is that they are two groups of data, the first group which was extracted from the experimental disk through Talysurf and the second group which was extracted from the surface of the Abaqus simulation model which has a certain mesh size as specified in section 3.3.3. So, to prepare them for alignment, it is necessary to obtain them at the same discrete data points. The MATLAB Curve fitting tool is used to interpolate the discrete roughness data points from the Abaqus model using Shape-preserving interpolation. This allows the interpolated discrete roughness data points and interpolated experimental data points to be compared at corresponding positions. Based on comparing the pre and post running experimental profiles in this way, the deepest valleys in the pre and post running profile were used as reference positions

for comparison. A FORTRAN programme was developed and used to pick up the sequence of deepest valleys for all the profiles used.

4.4 Comparison of experimental and Abaqus residual profiles

To identify the asperity plastic deformation from the experiment, it's necessary to compare profiles obtained before and after running as illustrated in figures 4.11(a) and (b), respectively. This requires relocation of the profiles in the trace direction so that the asperity features are aligned with each other as shown in figure 4.11 (c). This adjustment is achieved using identifiable local valley features that separate the significant surface asperity features and it can be seen that this process has achieved an effective axial relocation. The profiles shown in figure 4.11 contain the same deep valley features but the asperity shapes have clearly been modified by the running process. Prominent asperities have a significant reduction in height and the radius of curvature of these asperities is modified so that the curvature is reduced. However, close inspection of figure 4.11(c) shows that vertical alignment of the profiles is not achieved as far as the deep valley features are concerned as there are many instances where the deepest valley point appears to have 'deflected' upwards relative to the original profile. Examples of this can be seen located at x values of 0.53 mm, 0.64 mm, 0.71 mm, 0.79 mm, 1.08 mm, 1.11 mm, 1.46 mm, 1.49 mm and 1.61 mm. This is not thought to be a correct interpretation of the profile comparison. Each roughness profile is a trace of the material height relative to the mean line produced by the Gaussian filter, and as the waviness removed in generating the roughness profile will be different for the two cases this can have the effect of raising the deep valley features relative to the mean line.

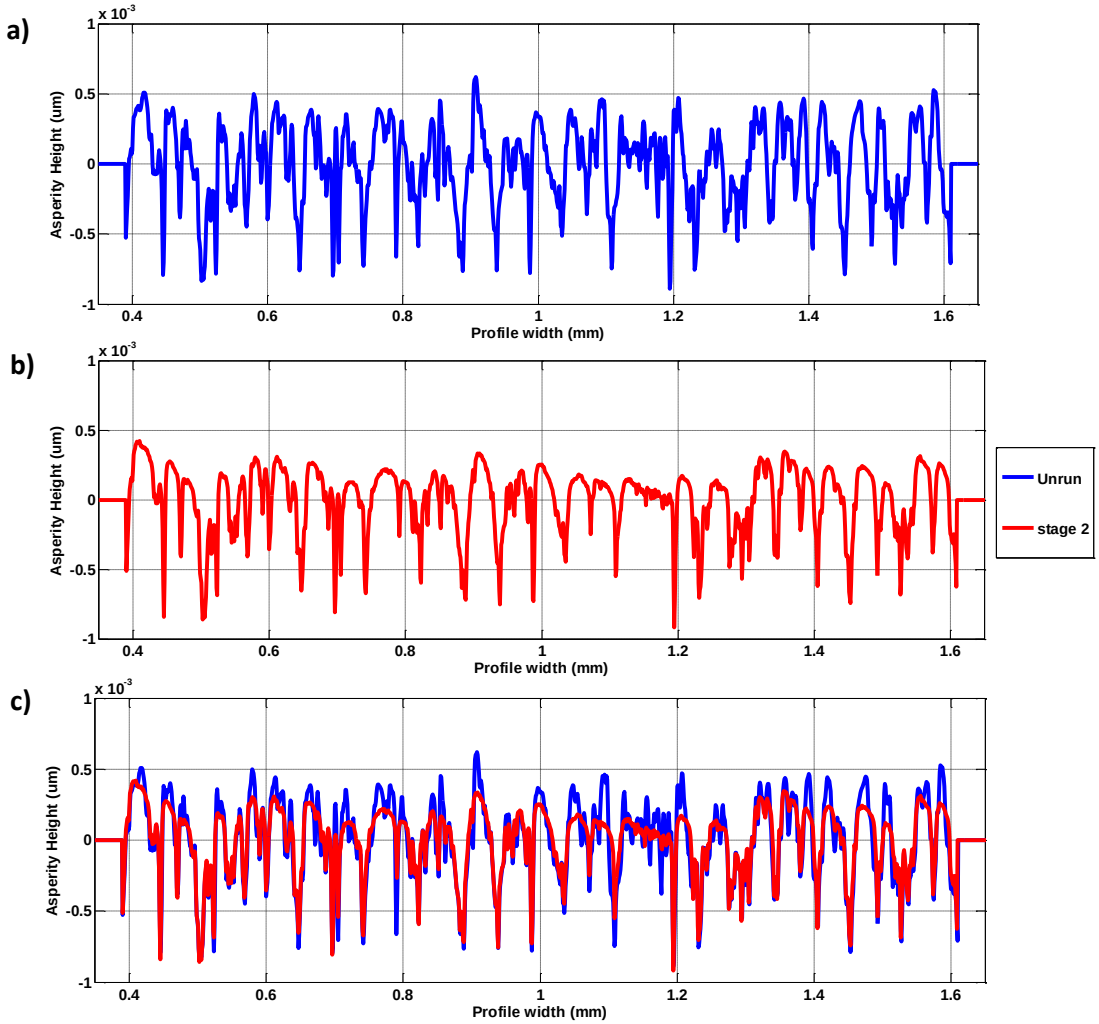

Figure 4.11- 1.2 mm profile after removed the curvature arc shape for; a) as manufactured profile, b) after running, c) pre and post running profile with adjustment using identifiable local valley features that separate the significant surface asperity features.

Adjustment in the height direction requires development of a new technique for aligning the pre and post-running profile, taking into account the distortion introduced by the profile filtering process. The next three sequence steps of this technique to achieve an effective comparison between the pre and post running profiles by different loads extracted from the real surface and from the Abaqus simulation model are illustrated in the next sections.

4.4.1 Developing connection lines between the deepest valleys

The profiles shown in previous figure 4.11 are very different. They are aligned with each other by means of the identifiable deep valley feature but the asperity shapes can be seen to have been modified with prominent features having significant reductions in height. Having identified the deep valley positions in both profiles, connection line curves were determined produced using the Matlab shape preserving interpolation routine and superimposed on the profiles as shown in figure 4.12 (a) and (b). These connection curves are similar but different in shape in places. This difference becomes apparent in figure 4.12(c) which reproduces figures 4.12(a) and (b) but with valley connection curves included. Figure 4.12(d) shows the two connection curves and the difference between them which represents the local vertical distortion introduced by the filtering process on the assumption that the deep valley points should re-align and that they are the most reasonable reference points to adopt in making height comparisons between profiles. This approach requires some judgement and selectivity as a valley feature may not sampled in exactly the same positions and also may acquire some debris particles which will also introduce a vertical deviation in the measured height. Examples of this can be seen located at x values of 0.79 mm, 1.12 mm, 1.16 mm and 1.18 mm.

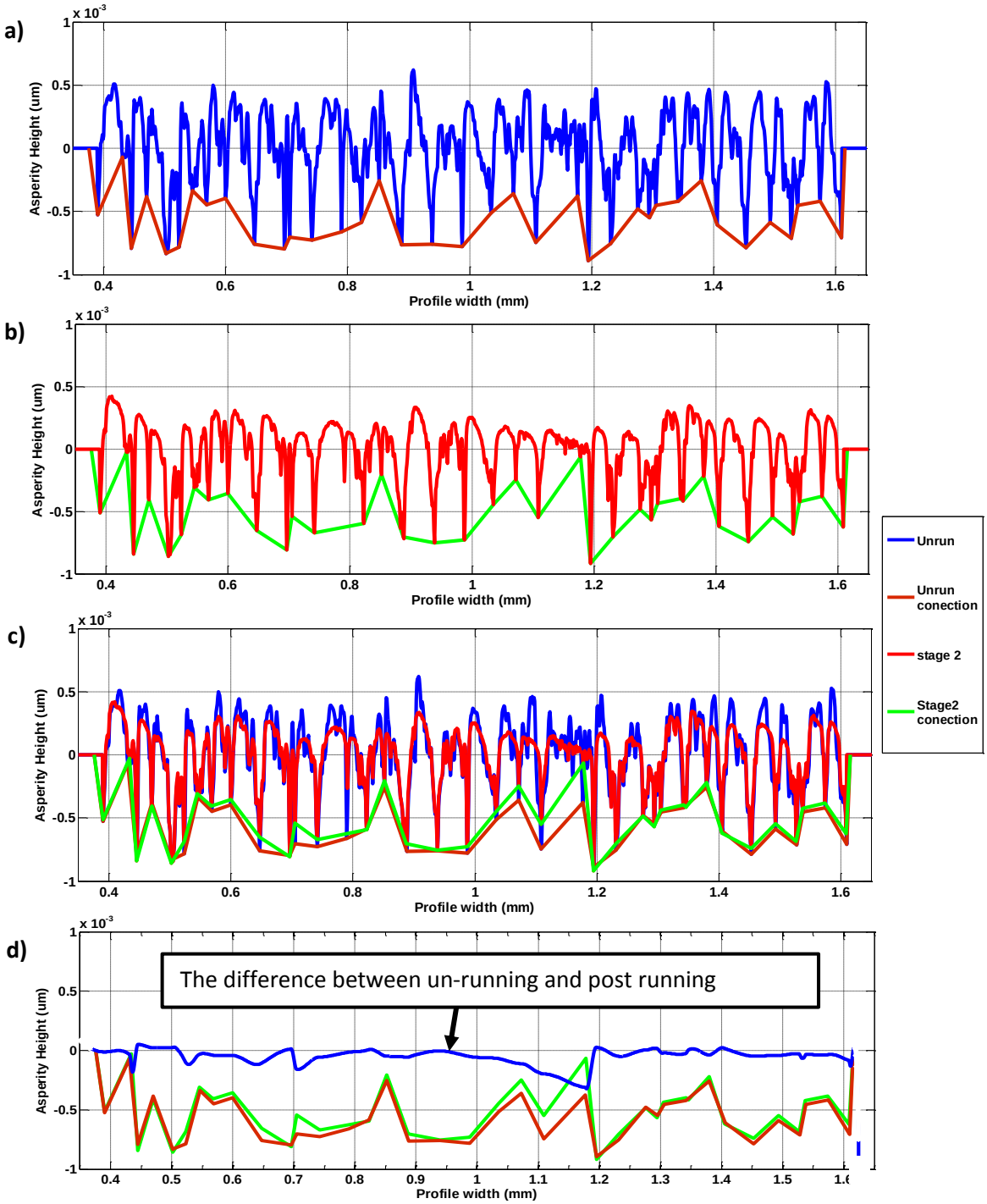

Figure 4.12- Profiles and their deep valley connection line curves; a) as manufactured profile, b) post-running profile, c) superimposed profiles, and d) connection curves and the difference between them.

4.4.2 Localized height realignment of asperities

The deepest valley connection curves were calculated for all the profiles considered, i.e. both the experimental profiles and those obtained following elastic/plastic loading

of the un-run profile as described in sections 4.3. This was carried out with the same discrete data points with a 1.0 μm step by the MATLAB interpolation routine programme and then the difference between the deepest valley connection curves of the pre-running profile and each individual profile's connection curve. This is shown in figure 4.13 for the un-run and second stage run profiles without any local height adjustments. Figure 4.13(a) shows the comparison over the central 1.2 mm of the profile used in the Abaqus analysis, and figures 4.13(b) (c) and (d) show shorter sub-lengths of the profile so that the detail of the comparison is more apparent.

This difference between the connection curves was then added to the stage 2 run profile before superimposition so that both profiles are plotted with the un-run profile's deep valley points as reference positions as shown in Figure 4.14. It can be clearly noticed that there is consistency of the deep valleys between the pre and post running profiles. They match each other in most locations except in some places as explained in the previous section. This technique shows the maximum deflection related to the prominent asperities which indicate the loads that are carried by them in loaded contact. However, some of the asperities do not show any deflection, which are located at the shoulder of the prominent asperities. The main finding of the global shape of the difference in profiles is clear and allows the plastic deformation behaviour at the contact surface to be evaluated easily. The presence of a small scatter in the profile difference might be due to the noise of the measurement. Also it can be seen that the surface roughness is the principal factor in controlling the plastic deformation behaviour of contacting surfaces and it can be expected to correspond to the load applied to the individual asperities.

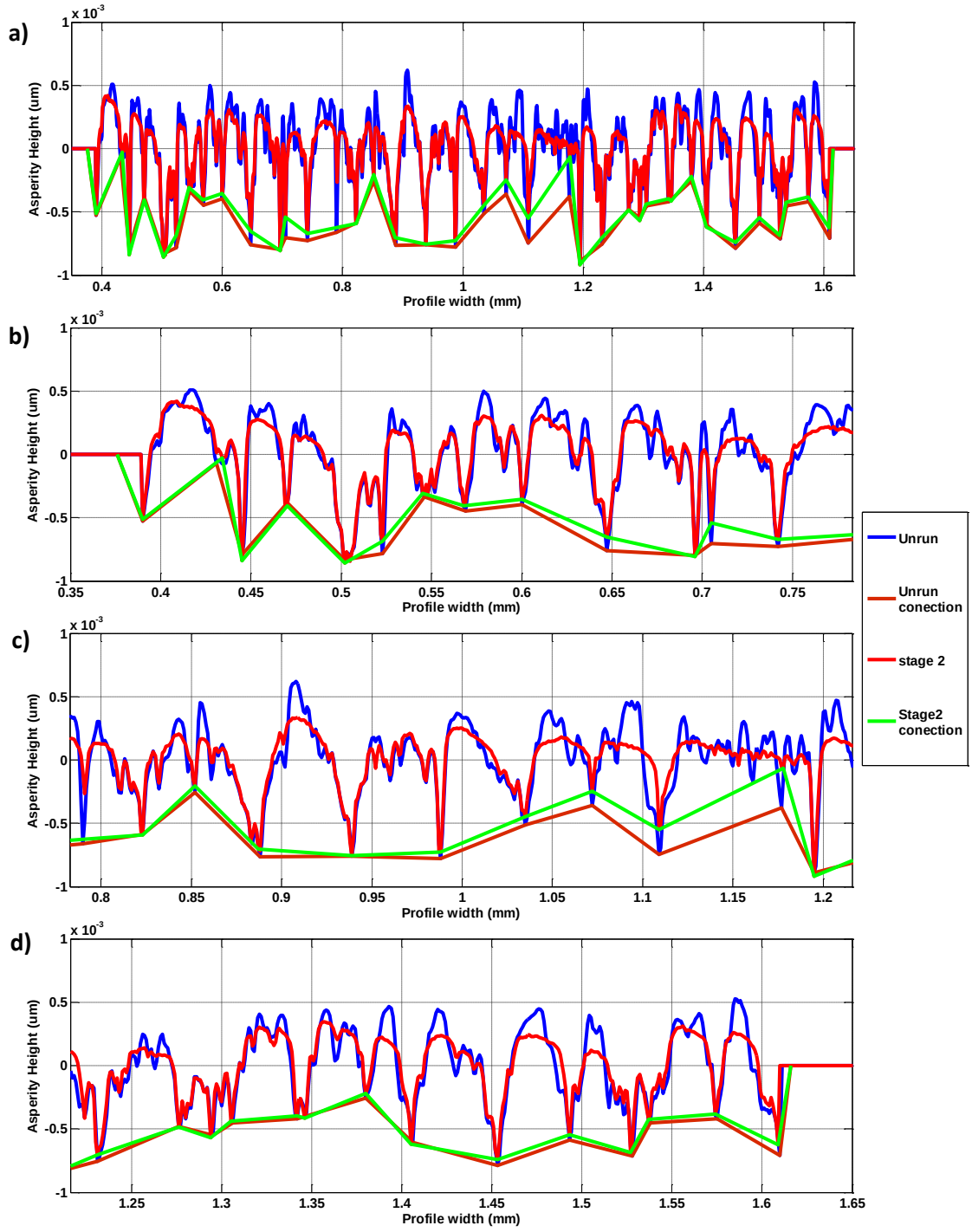

Figure 4.13 - Comparison of profiles with axial re-alignment and valley connection curves for pre and post running profiles; a) 1.2 mm profile, b) c) and d) 0.4mm detailed sub profiles.

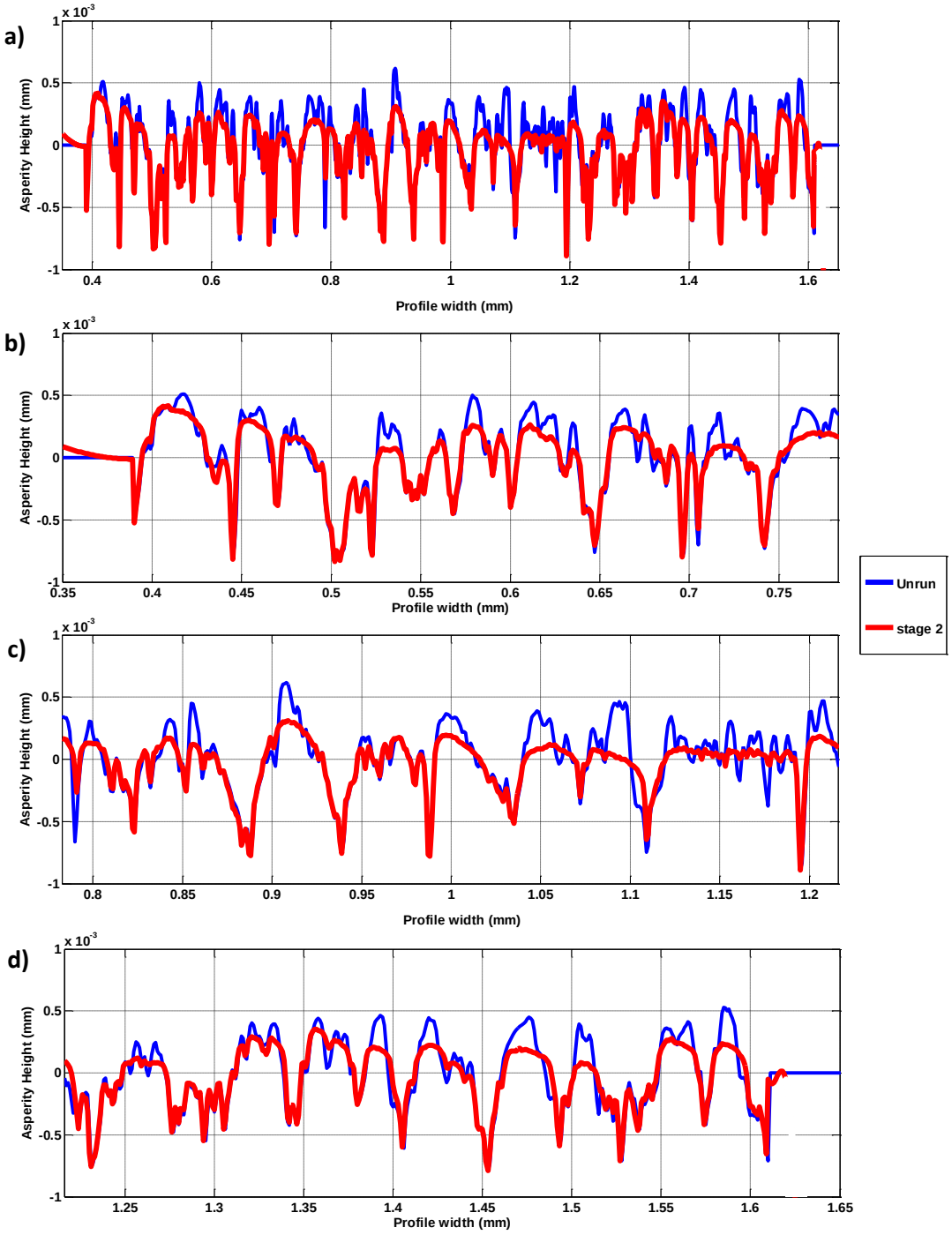

Figure 4.14- Comparison of profiles with axial and height re-alignment referred to the un-run profile deep valley positions; a) 1.2 mm profile for pre and post running ,b) c) and d) show shorter sub-lengths of the profile in sufficient detail to inspect individual asperity shape changes.

4.4.3 Comparison with FEA analysis profiles

To make comparisons with the residual FEA analyses the same local height alignment approach was used. Residual profiles were obtained from the Abaqus analysis for a

series of applied loads. For these profiles residual reference valley positions not affected by load i.e. where no significant plastic deformation occurred were selected as shown in figure 4.15. Valley connection curves were generated for each of the profiles and are shown in Figure 4.16. The loads used for the FEA analysis are referred to in terms of the distributed loads of 0.5 GPa, 1.0 GPa, 1.5 GPa, 2.0 GPa, 3.0 GPa and 4.0 GPa applied to the 6 mm length of the lower boundary the FEA model. Figure 4.15 shows a selection of these residual deflection profiles superimposed on the un-run and post running profiles with all profiles referred to the deep valley reference points of the un-run profile after implementing the above technique. The change in shape of the asperity features can now be seen to form a progression of curves corresponding to the increasing applied loads as shown in greater detail in Figures 4.15 (b) to (d). This is in marked contrast to the connections profiles before realignments shown in corresponding layout in Figure 4.16(a) to (d). The additional enlarged detail shows a short group of asperities in greater detail. The main observation in these figures is that the variation in profile height diminishes with increasing load. Comparison of the re-aligned profiles in Figure 4.15 show that for the subsections shown the residual deflection of the post-running profile shows a similar form to the results of the Abaqus analysis and is effectively bracketed by the residual profiles shown for the 1.0 GPa and 2.0 GPa load cases. It is therefore reasonable to estimate that the residual stress in the near surface material corresponding to this profile based on the residual stress fields of these two load cases, or of an intermediate load case that is a closer match to the experimental residual profile. Further analyses are discussed in chapter 5 section 5.3.2.

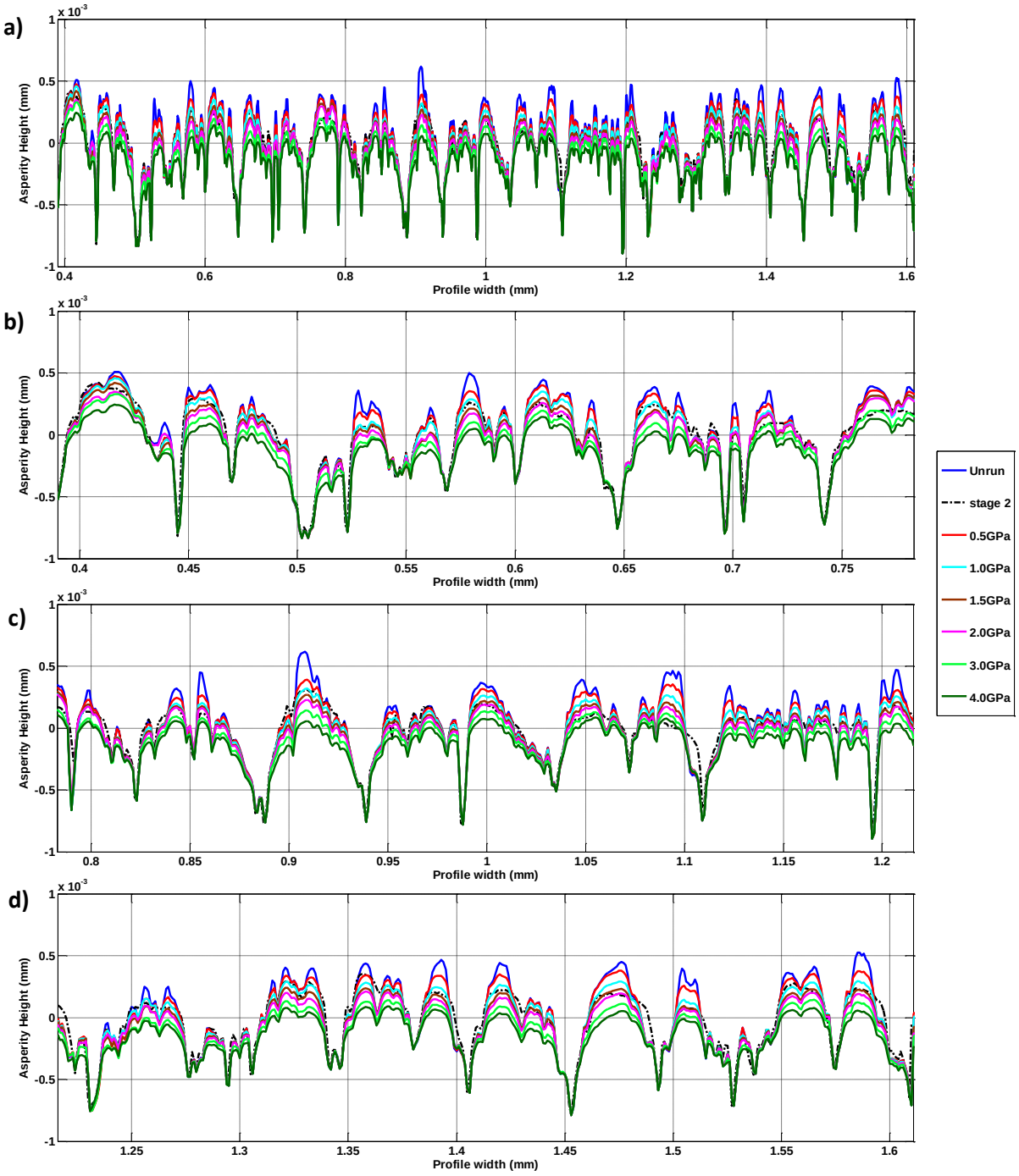

Figure 4.15 - Comparison between un-run, post-running and FEA residual profiles for a series of FEA load cases referred to the un-run profile valley reference positions, (a) shows the whole contacting roughness profile With (b) (c) and (d) showing subsections in greater detail.

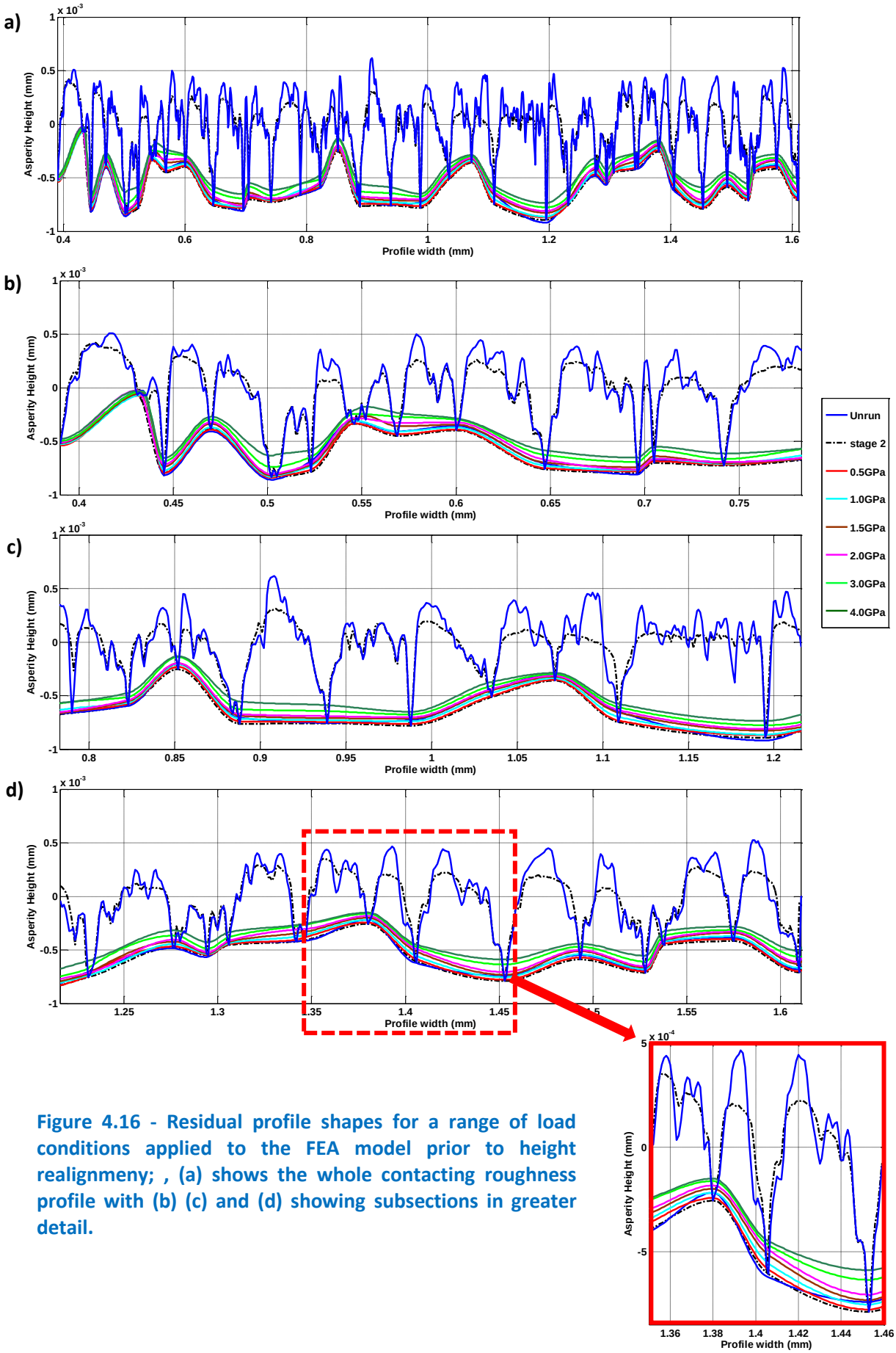

Figure 4.16 - Residual profile shapes for a range of load conditions applied to the FEA model prior to height realignmeny; , (a) shows the whole contacting roughness profile with (b) (c) and (d) showing subsections in greater detail.

4.5 Conclusion

This chapter presents the technique developed to find the optimal correspondence between two roughness curves based on the concept of smooth alignment curves that pass through deep valley reference positions that are little affected by the plastic deformation occurring at the asperity tips. It is a new research development that allows the level of plastic deformation actually occurring at significant surface asperity features to be observed and quantified. It also enables an associated FEA model to infer representative residual stress fields corresponding to the asperity shape changes evaluated by experimental measurements. Furthermore, this a new technique for aligning the pre and post running profiles, taking account of the distortion introduced by the profile filtering process and the profiles at the contact region.

Chapter 5

Details result of asperity residual stress

5.1 Introduction

Most surfaces we come across in our daily life have a certain amount of roughness. For instance, polished objects that appear perfectly smooth to the naked eye can reveal incredible complexity when investigated using a microscope. Once two such surfaces come in contact under pressure, a small fraction of what seems to be touching forms the real contact area. So, the contact area is one of the most significant parameters when studying contact between two surfaces. Peaks and valleys are the main two components of surface topography where peaks or higher hill type areas are called asperities. One single asperity contact is the most basic component of a profile of multiple asperity contacts. Understanding a single asperity is much simpler than understanding multiple asperity contacts. Therefore, this chapter includes detailed analysis of individual asperity contacts which consists of three sections. The first section includes a review of the mechanical contact behaviour revealed in studies on the effect of loads on a small contact area. This section endeavours to determine trends in residual stresses that may explain the findings in these studies. The second section describes the techniques employed on individual asperities within the entire contact region of the experimental disk contacts to match with same asperities in the simulated residual FEA analyses that have the same local height, and to be able to compare them in detail at the roughness level, so that the FEA residual stress for each asperity due to the applied load can be extracted allowing for further analysis to be

carried out based on these results. The third section of the chapter is an analysis of the asperities that will have their residual stress components used in the fatigue analysis. The residual stress components, such as the maximum principal stress, the vectors of the maximum principal stress and the von Mises stress are considered and investigated, looking for relationships between the asperity damage findings found in the literature and the residual stresses found at the asperities.

5.2 Asperity contact mechanical behaviour theory review

5.2.1 Contact mechanics (Hertizan contact) - Elastic regime

A distinguishing feature of EHL is that a high load is functional over a small contact area producing pressures that are high enough to result in considerable elastic deflection of both surfaces as well as to alter the properties of lubricating oil as it flows through the contact. The pressure distribution generated within an EHL contact is similar to that formed by the corresponding dry contact. Hertz (1881) presumed the line contact analysis of dry contact is based on two solid cylinders that are stationary and smooth being pressed together. This is considered to be the starting point for EHL studies and the first analysis of pressure and deformation of two elastic solid geometries defined by quadratic surfaces in contact. Hertz's work in this regard formed an important foundation for many contact theories. For a given geometry, load and elastic contact properties, the pressure distribution developed within that contact zone and the size of the elastic contact zone are established by Hertzian contact theory as shown in the Figure 5.1. For his study, Hertz made the following assumptions (Johnson, 1985):

1. The strains concerned lie within the range of elastic limit.

2. The contact region is much smaller when compared to the radii of curvature and dimensions of the bodies. The contact area plane has perpendicular applied pressures and the bodies are elastic half spaces.

3. The surfaces are non-conforming and continuous.

4. The surfaces do not have friction. (This condition is relaxed when dealing with friction).

A line contact problem where two similar cylinders are brought into contact with each other simulates the contact between a pair of spur gear involute teeth.

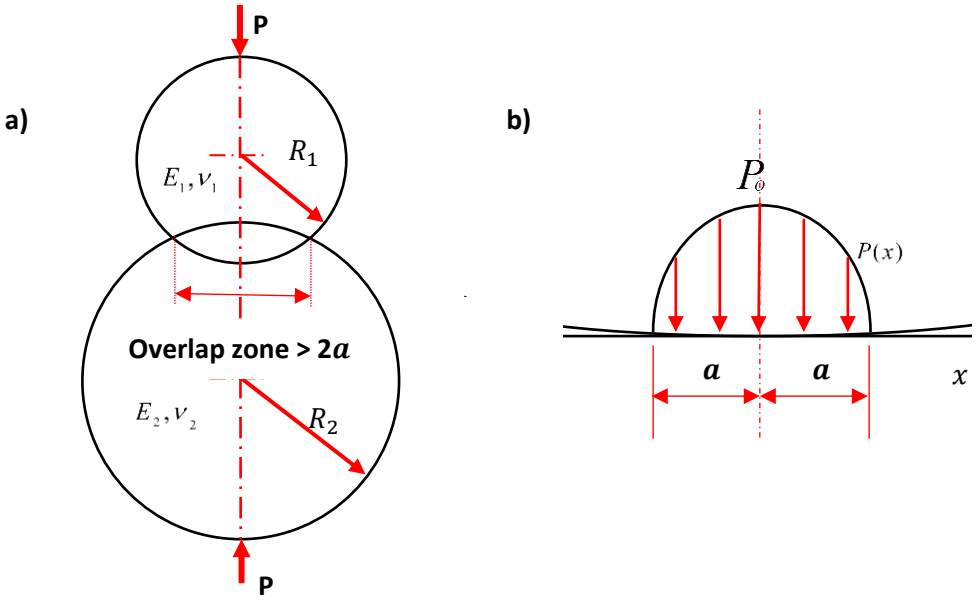

Figure 5.1 – Hertz line contact subject to a load applied; a) two overlapping cylinders in elastic contact at their loaded position, b) semi-elliptical pressure distribution develop over the contact zone.

If assuming that solid bodies have radii R_1 and R_2, respectively, Elastic moduli E_1 and E_2 with Poisson's ratios ν_1 and ν_2, R' is the radius of the cylinder for an equivalent cylinder/plane contact and E' the reduced Elastic (Young's) modulus can be expressed as follows(Johnson, 1985):

$$\frac{1}{R'} = \frac{1}{R_1} + \frac{1}{R_2} \tag{5. 1}$$

$$\frac{1}{E'} = \frac{1}{2}\left(\frac{1-v_1^2}{E_1} + \frac{1-v_2^2}{E_2}\right) \tag{5. 2}$$

If w' is the total load per unit length and $2a$ the width of contact, the Hertzian semi-contact width for a line contact is given by Williams (1994) :

$$a = \sqrt{\frac{8R'w'}{\pi E'}} \tag{5. 3}$$

The contact pressure distribution in a line contact is semi elliptical, that is in the form figure of half an ellipse as shown in the Figure 5.1 and the equation for the pressure is:

$$P(x) = P_o\sqrt{1-\left(\frac{x}{a}\right)^2} \tag{5. 4}$$

P_o is the maximum pressure that occurs at the centre of the contact. The load is actually the area under the pressure curve, and since the area of the full ellipse is $\pi P_o a$, it can be stated that:

$$w' = \frac{\pi}{2} P_o a \tag{5.5}$$

Therefore, the peak Hertz pressure equation at the centre is expressed as:

$$P_o = \frac{2w'}{\pi a} = \sqrt{\frac{E'w'}{2\pi R'}} \tag{5. 6}$$

5.2.2 Loading beyond the elastic limits-(Plastic Regime)

When two elastic-plastic bodies come in contact at small loads, the surface is deformed elastically with the maximum principal shear stress $\tau_{\max}$. This occurs below

the centre of the contact at a depth of 0.79 times the contact semi dimension for the line contact studied as shown in the figure 5.2 (a).

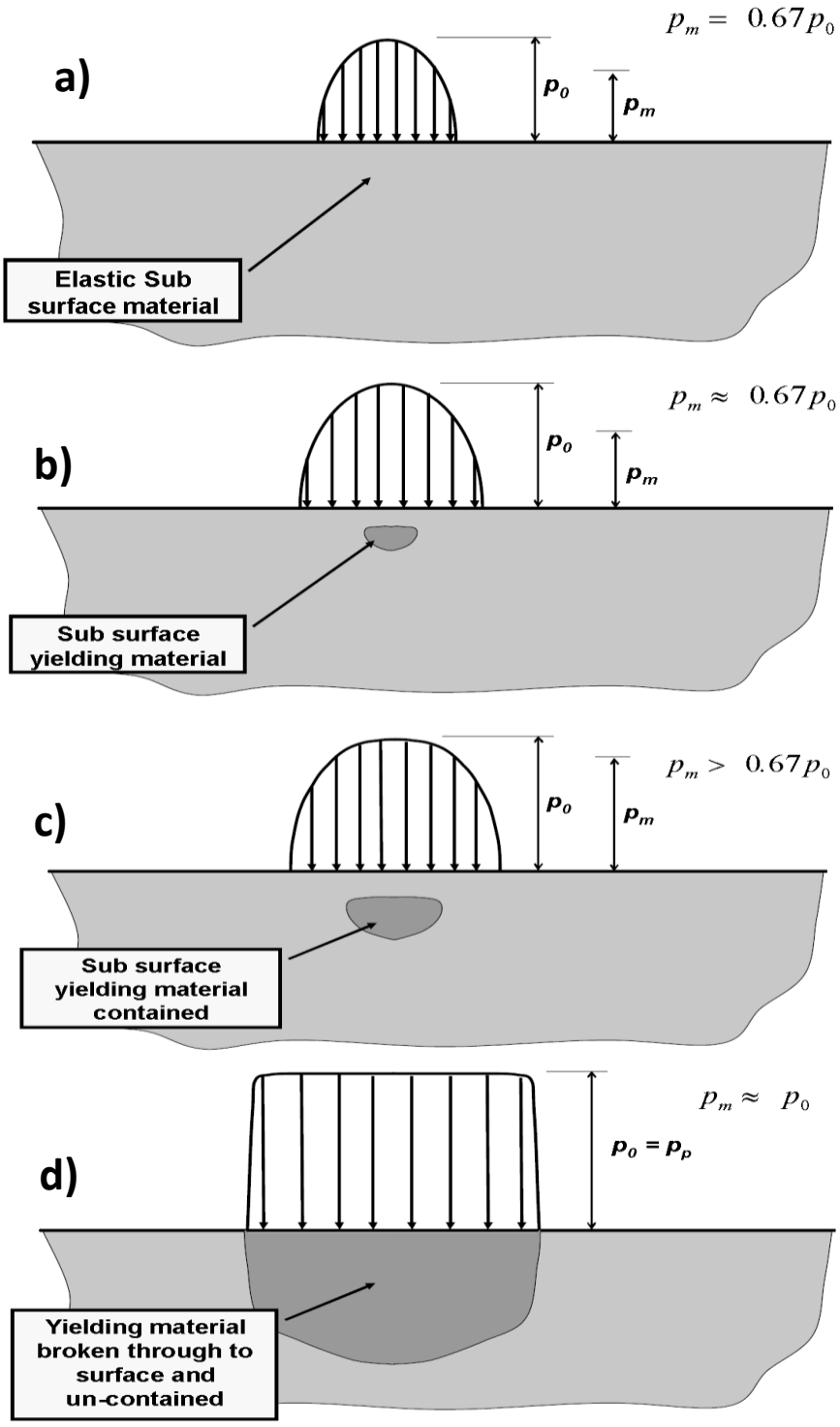

Figure 5.2 - Transition from Elastic to Plastic Conditions; a) Point Contact with Load less than Onset Load, b) Load just beyond the Onset Load, c) Load larger than the Onset Load, d) Load giving Fully Plastic Conditions.

At some critical load, τ_{max} is greater than the critical shear stress of the solid and a small amount of plastic flow occurs within the larger elastic surroundings as shown in figure 5.2 (b). With the increase in load, the plastic area grows and the contact pressure rises until finally, the plastic zone reaches the surface and covers the section around the source of applied load as shown in Figure 5.2 (d). Thus deformation transforms from purely elastic to elastic-plastic (contained) and then fully plastic (uncontained) conditions as the load is progressively increased as shown in Figure 5.2 (a-d). This is common for most engineering material combinations which behave in a ductile manner. In an elastic non-conformal contact the material experiences a complex stress distribution pattern. If the contact is frictionless, the pressure at the interface is distributed semi-elliptically and accompanied by radial direct stress at the surface. This radial stress is tensile outside the contact and reaches a maximum value at the boundary of the contact. It becomes compressive by nature inside the contact and the highest value compressive pressure occurs at the centre. The tensile radial stress at the contact boundary can create ring cracks in brittle materials such as glass (Evans, 2010). The variation of the stress components with depth below the centre of the contact is shown in Figure 5.3 for line and circular point contacts where it can be seen that the maximum shear stress occurs below the surface and this is the location of initial plastic deformation for ductile materials when the elastic limit is exceeded.

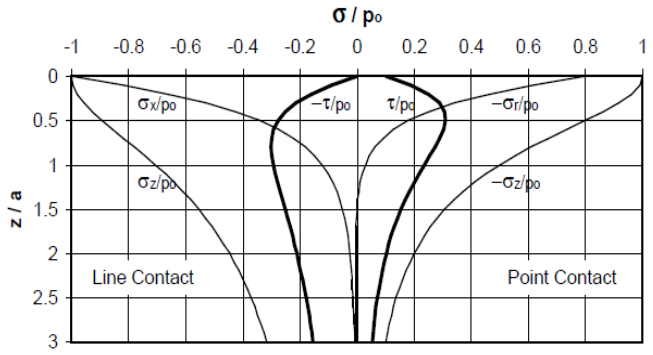

Figure 5.3 - Variation of stress components beneath surface on z/a axis. The left hand figure shows Line Contact results, the right hand figure shows the circular Point Contact case (Evans, 2010).

5.3 Single Asperity of contact surface modelling

5.3.1 Asperity layout

In modelling of asperity contacts they are usually assumed to be spherical (3-D) or cylindrical (2-D) as shown in Figure 5.4 (a) and (b) respectively. The latter figure shows a schematic elastic cylinder of radius R in contact with an elastic half-space. In the current research the samples used are crowned disks that have been ground in the axial direction (approximately). The asperity contacts are considered to be line contacts and the models developed are based on 2D plane strain contact analysis. The asperities used are real asperities extracted from the test disk profiles and have been numbered to aid identification as shown in Figure 5.5. As explained in Chapter 4, the FEA contact analysis used two profiles, which will be referred to as profiles A and B. Profile A is 1.2 mm long, profile B is 1.3 mm long.

The analysis and study of asperity contact through the Abaqus model consists of four steps which are the steps of the whole model simulation as explained in Chapter 4. These steps are the initial step required by the system and the second step which is an incremental displacement to create contact between the highest asperity and the rigid body. The third step is application of a specified normal load to find the elastic/plastic contact, and this is finally followed by an unloading step to obtain a certain distance between the highest asperity and the rigid body. Other conditions and circumstances involved in using Abaqus for this purpose were discussed in Chapter 4. All the asperity contact model results presented were based on a strain hardening material and used an adaptive mesh (ALE) to avoid the massive distortion that would otherwise occur when using Elastic-perfectly plastic and Elastic Plastic material behaviour.

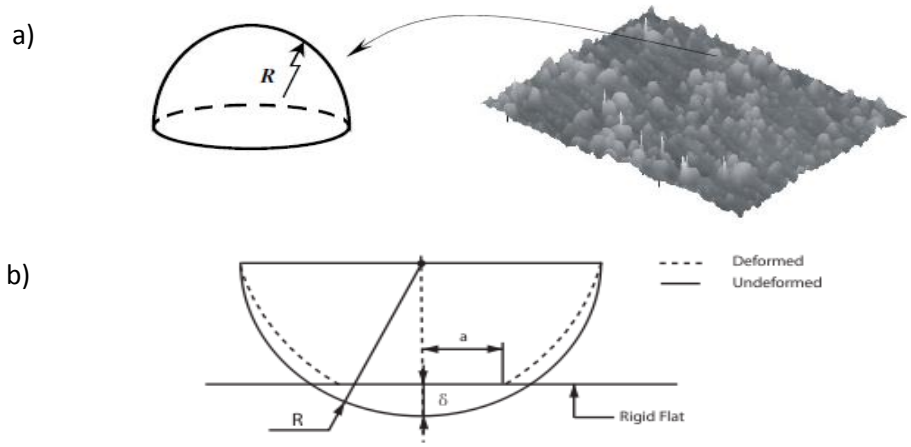

Figure 5.4 - A schematic of an asperity contact model; a) in three dimensional, b) in two dimensions with an elastic cylinder of radius R in contact with a rigid flat (Jamari and Schipper, 2006).

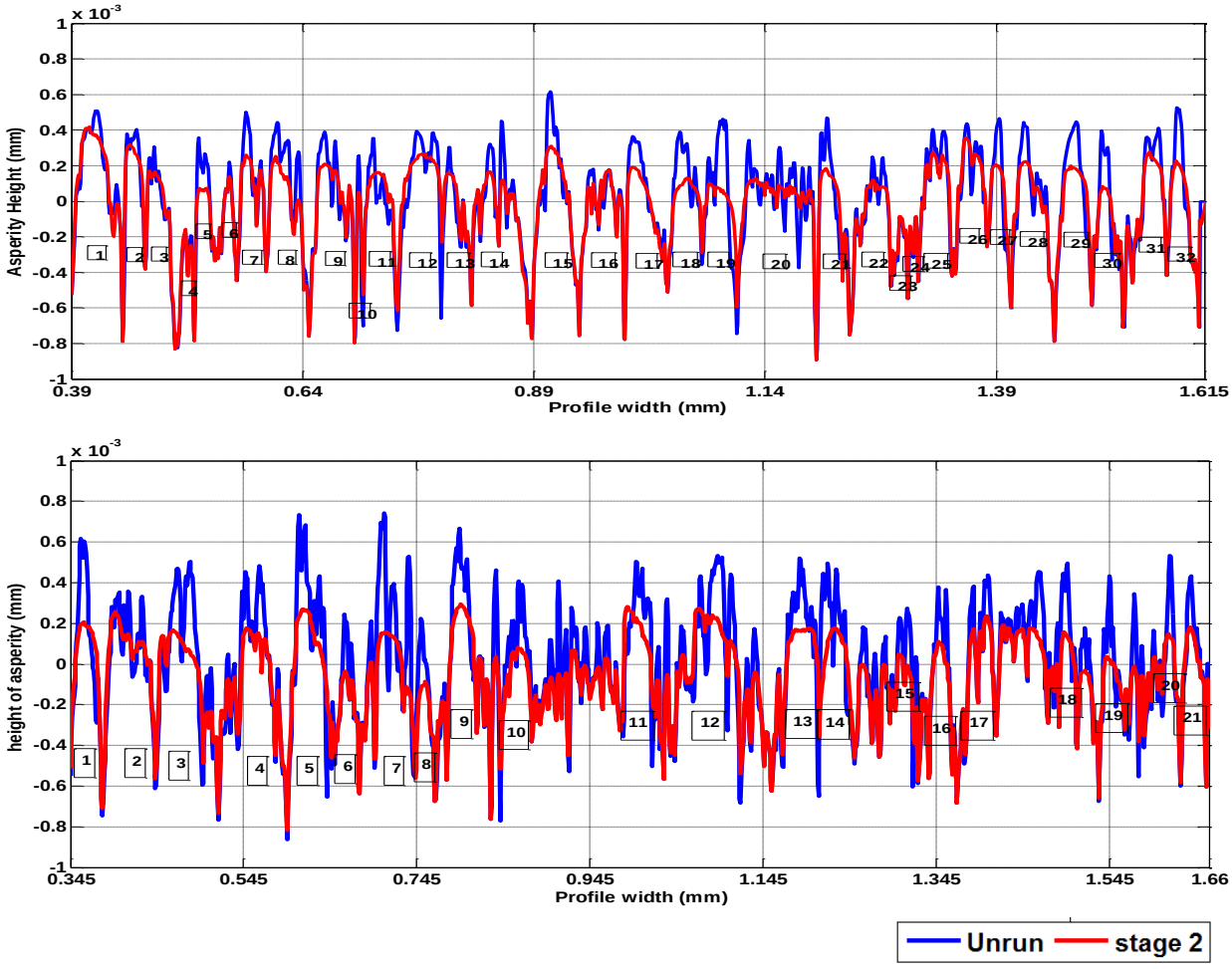

Figure 5.5 - The profiles' asperities are numbered for both profiles used in the contact analysis research; a) Profile A (1.2 mm long), b) Profile B (1.3 mm long).

5.3.2 The FEA residual stress determination for the asperities

In the fourth step of the simulation analysis run in Abaqus/Standard illustrated in Section 4.3.5 the load is removed which allows the profile surface contact to spring back and release the elastic strains, which creates the residual stresses developed in the material. Based on the contact conditions, an elastic-plastic material response can be initiated either in the bulk material or in the surface asperities. Asperities of different shapes and sizes will initially come to a limited amount of contact to support the normal load; however, if the normal load is increased the number of contacting asperities will increase and the area of contact will become larger as well as the contact deformation. Therefore, the response of the surface to an increase in the normal load depends on the height and size of the asperities. To make comparisons between the plastic deformations of asperity features observed in the experimental work with asperities in the simulated residual FEA analyses that have the same local height, and to be able to compare them in detail at the roughness level, it is necessary to apply a range of loads as shown in Figure 5.6.

Figure 5.6 (A) shows the residual shape of profile A for four different applied loads. The load experienced by individual asperity features in the EHL rolling/sliding conditions of the experiment depend on their interaction with asperities on the counterface. It is not possible to determine the actual maximum load values experienced by the asperities, but this can be deduced from their residual displacement which can be measured as discussed in chapter 4. The load applied to an asperity feature in dry contact is also not possible to specify as it depends on load sharing between the asperities involved in the contact. The approach adopted is thus to apply a sequence of loads to the contact and to infer the load applied to an asperity

feature from the resulting residual displacement and comparison with the experimental values observed. The analysis was carried out using the unrun profile to define the asperity shapes. This is included in the figure together with the profile measured after the second stage of the experiment. Sections (b) (c) and (d) of the figure show the same profiles at a higher resolution in the transverse direction. Section (b) of Figure 5.6 shows the profiles from $x = 0.40\,mm$ to $x = 0.80\,mm$, where the major asperity features are numbered from 1 to 12. Section (c) shows the profiles from $x = 0.80\,mm$ to $x = 1.20\,mm$, with major asperity feature numbered from 13 to 20, and section(d) which extends from $x = 1.20\,mm$ to $x = 1.60\,mm$, involves the asperities numbered from 21 to 32. As shown in the Figures (b-to-d), each figure has a group of asperities and each asperity has different levels of residual deflection in the FEA analyses corresponding to different applied loads. Therefore, by plotting the residual FEA profiles together with the post running profile an approximate fit can be found at a given load level. For example, for asperity number 7, the applied load of 1.0 GPa provides a good fit for the experimental profile. Similarly the asperities numbered 14,15,17,30 and 32 have residual FEA profiles that provide a good fit to the experimental profile for applied loads of 1.0, 1.0, 1.5, 1.5 and 1.5GPa respectively. This correspondence is illustrated in Figure 5.7 which shows these individual asperities in greater detail. In general, an appropriate FEA load can be determined to fit all of the major asperity features. Table 5.1 indicates the load level that gives the best approximate fit to the experiment for each major asperity feature. It can be seen from the table that most of the asperities achieved the measured residual deflection at FEA model loads of between 1.0 GPa and 2.0 GPa. Following that, the FEA residual stress for each asperity due to the applied load can be extracted

allowing for further analysis to be carried out based on these results. It is important to note that these loading values are for the whole contact and not for the individual model. The load carried by a particular asperity feature depends on its prominence and position along the modelled disk surface. The assumption made in the work is that the residual deflection observed at the asperity is associated with the residual stress developed in that asperity feature.

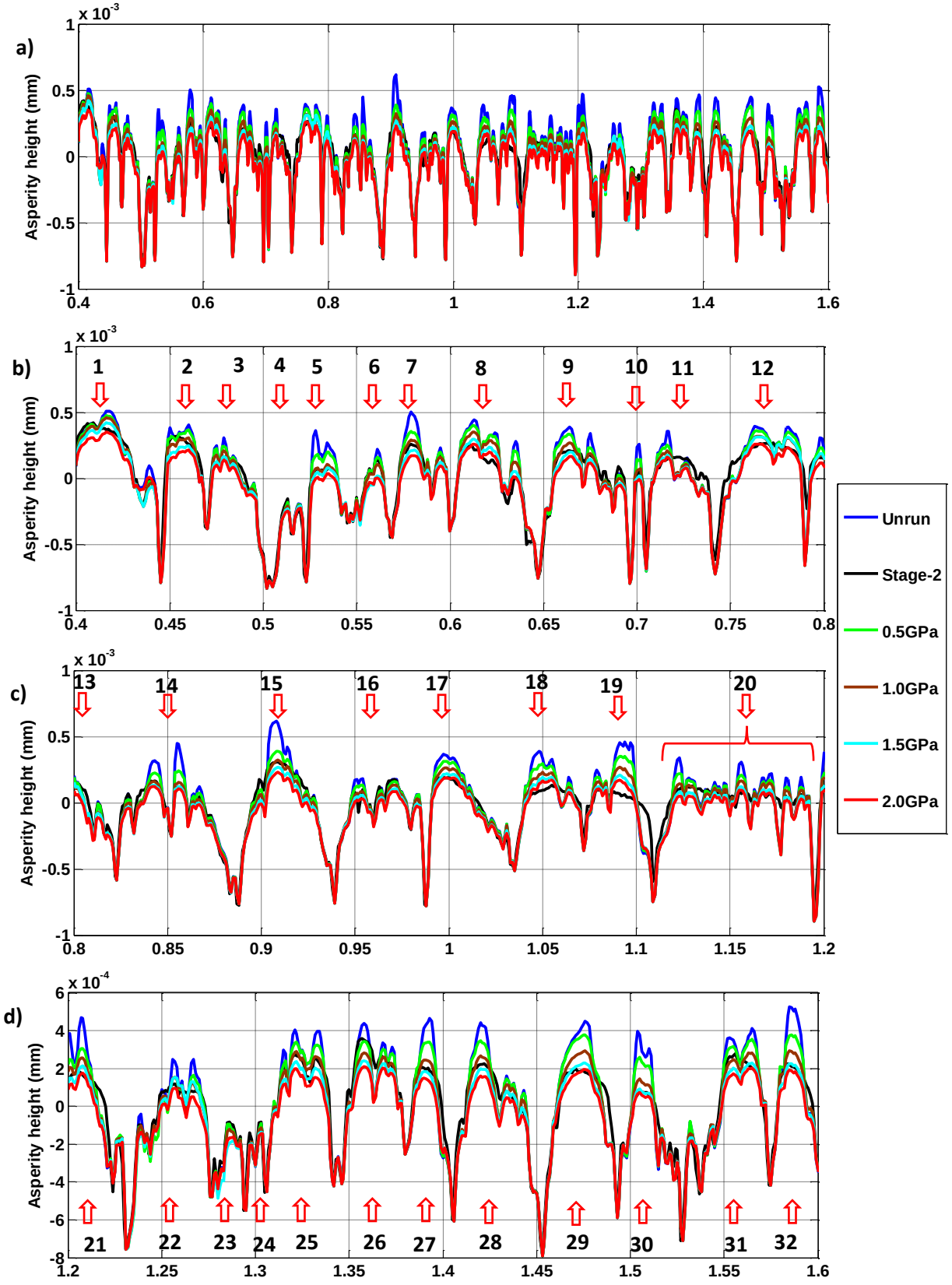

Figure 5.6 – Unrun and relocated profiles taken following the second experimental load stage together with residual profiles obtained by FEA contact analysis at a series of specified loads; (a) full profile length,(b), (c) and (d) detailed figures for parts of the profile.

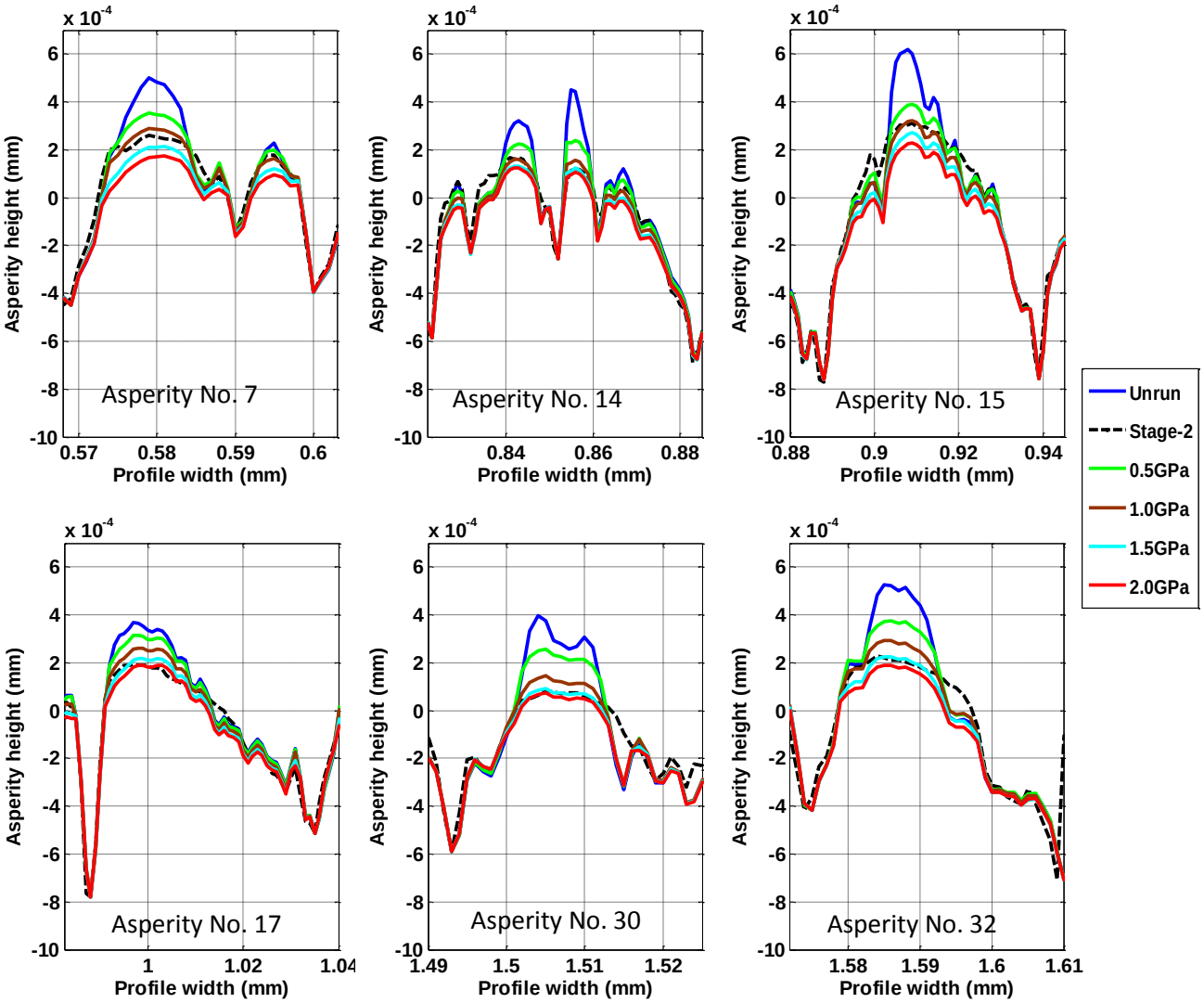

Figure 5.7 - Example of asperities in profile A that satisfy the conditions of comparison between the FEA residual profile and the experimental profile at the second stage.

Table 5.2-The FEA residual profile loads associated with asperity numbers for profile A.

Asperity Number	Optimum applied load value (MPa)	Applied load value (MPa)					
		500	1000	1500	2000	2500	3000
1.	**1500**			**X**			
2.	**1000**		**X**				
3.	**1500**			**X**			
4.	**500**	**X**					
5.	**1500**			**X**			
6.	**1000**		**X**				
7.	**1000**		**X**				
8.	**2000**				**X**		
9.	**1500**			**X**			
10.	**1000**		**X**				
11.	**1500**			**X**			
12.	**2000**				**X**		
13.	**2000**				**X**		
14.	**1000**		**X**				
15.	**1000**		**X**				
16.	**500**	**X**					
17.	**1500**			**x**			
18.	**2500**					**X**	
19.	**2500**					**X**	
20.	**1000**		**X**				
21.	**1500**			**X**			
22.	**2000**				**X**		
23.	**500**	**X**					
24.	**500**	**X**					
25.	**1500**			**X**			
26.	**500**	**X**					
27.	**1500**			**X**			
28.	**1500**			**X**			
29.	**2000**				**X**		
30.	**1500**			**X**			
31.	**1000**		**X**				
32.	**1500**			**X**			
TOTAL		**5**	**8**	**12**	**5**	**2**	

5.3.3 Modelling interpolation

In order to use the residual stress calculated in the FEA analysis for consideration in the fatigue calculation it is necessary for it to be transferred between the FEA mesh of nodes and the regularly spaced mesh points used for the fatigue analysis. This process involves two stages. The first stage is to obtain the stress components at each FEA node by tabulation within the Abaqus system. This also provides the coordinates of the mesh points in the residual unloaded position at the end of the analysis. The depth coordinate for each node is then adjusted so that it gives the depth below the surface, i.e. the form and residual roughness is removed. The second stage is to interpolate from the unstructured FEA mesh to the regular mesh to be used for further analysis. A Gaussian interpolation software programme was used to achieve this in the research. This routine finds the interpolated value at a mesh point in the regular mesh by drawing a circle centred at the point and considering the values of stress at each of the unstructured mesh points falling within the circle. These contribute to the interpolated value according to their distance from the regular mesh point. The radius of the circle used varies according to the fineness of the unstructured mesh. The radius is specified in terms of the finest resolution of the high density mesh and this is used for the interpolation along with a minimum number of points condition, which is four points. If there are fewer than these numbers of points in the circle, the programme doubles the radius and verifies the condition of the point. Figure 5.8 shows a contour plot of the von Mises stress as produced by the Abaqus system using the calculated values at each mesh points. The plot is for a 150 μm length of the surface which can be seen to undulate due to the roughness profile and the residual plastic deformations. The length shown is sufficiently short for the curvature of the surface not to be apparent.

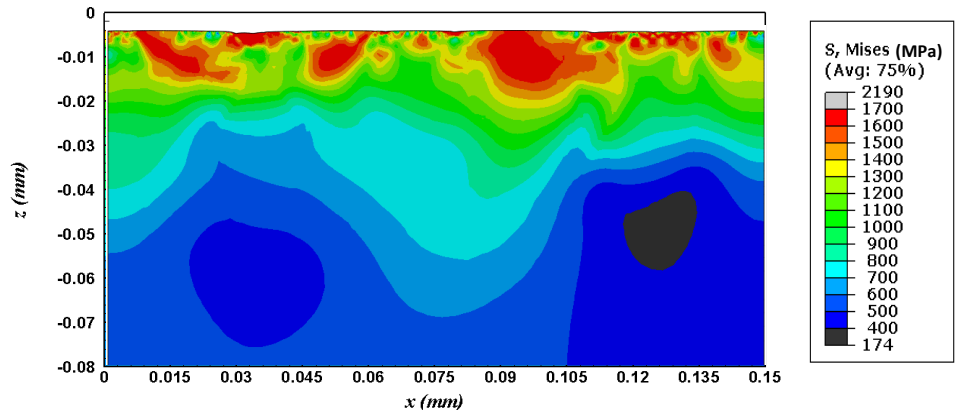

Figure 5.8 - Abaqus Von Mises stress contours for 0.15mm Elastic plastic body (σ_y =2293 MPa).

Figure 5.9 shows the result obtained by the interpolation procedure when the Von Mises data is transferred to the regularly spaced points of the fatigue analysis mesh. Figures 5.9 (a-d) shows the interpolation accuracy results at different interpolation circle radii of 1.0 µm, 2.0 µm and 4.0 µm. Figure 5.8 (a) used the 0.1 µm radius of interpolation which was able to provide a good reproduction of the intensity value of stress and smooth contours in the area which has a high density of mesh in between z=0.0 to z=-0.02mm when compared to the original data in Figure 5.8 . However, it gives poor contours in the area which has a low density in between z=-0.04 to z=-0.08mm. Figure 5.9 (b) used the 0.2 µm radius of interpolation that is neither able to pick up the values of a high stress component in the high density area nor able to give smooth contours in the area which has a low density. Figure 5.9 (c) used the 0.4µm radius of the interpolation circle that is not able to provide a good intensity value of stress and smooth contours in the area which has a high density of mesh. However, it gives good contours in the area which has low density. To avoid mapping and contouring problems in the interpolation process, the interpolation programme was modified to differentiate between the low and high density of points and then a convenient interpolation circle radius was assigned for each area (the high density

mesh and low density mesh). Thus, the research used the 0.1 µm radius for the FEA's densely meshed area and used the 0.4 µm radius for the low density area as shown in Figure 5.8 (d). This can effectively pick up the intensity value of stresses in the near surface area which can be seen in the red zone pocket between z = 0.0 to z = -0.02mm as well as the smooth contours for the area from z =- 0.04 to z =- 0.08mm as can be seen by comparison with the Abaqus result of figure 5.7.

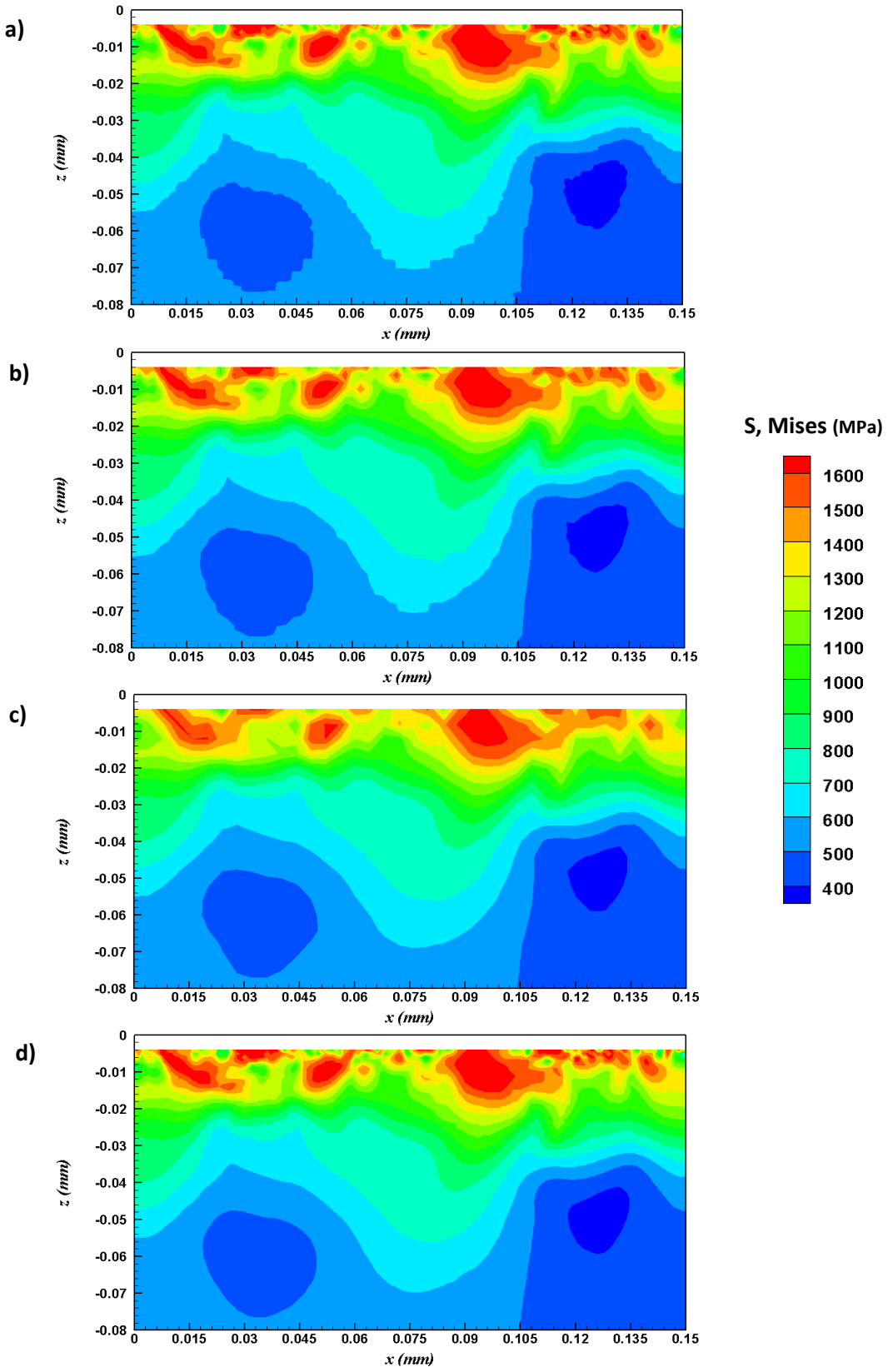

Figure 5.9 - Interpolation resolution contours for different interpolation circle radii as; a) 1.0 µm, b) 2.0 µm, C) 4.0 µm, d) 1.0 µm at the top and 4.0 µm at the bottom (σ_y =2293 MPa).

5.4 The effect of load on the asperity analysis

This section presents the study of four randomly selected asperity features that are involved in the profiles for which the residual stress is extracted from the FEA simulated model. It would be unreasonable to show and discuss the results for all the asperities for each applied load, so four asperities have been chosen for the investigation. These asperities have different shapes and were extracted from different positions in the profiles. Each of these four asperities includes the form of the 38.1 mm radius arc. They were loaded with different equivalent distributed loads that were applied in the complete contact Abaqus model step. Detailed residual stress and deflection results are shown for the four different asperities in Figures 5.10, 5.11, 5.12 and 5.15. Each asperity analysis includes the Von Mises stress at the complete contact load step, together with the maximum principal stress and the positive principal stress vectors at the removed load (residual) step. The aim of this investigation is to explain the findings noted in the literature review chapter that revealed experimental studies on the role of a single asperity in surface crack initiation, fatigue damage, propagation and micropitting failures. Figure 5.10 (a) shows the first analysis of the asperity feature (asperity 1, profile B) in a deformed profile shape before and after loading. It can be noticed that the maximum residual displacement that the asperity has experienced is approximately 0.323 µm due to application of the 1.0 GPa nominal load. Figures 5.10 (b) (c) and (d) are plots taken from the Abaqus software and are to the same scale in both directions. Figure 5.10 (b) shows the positive vectors of (tensile) maximum principal stress values at, and below, the surface. In areas where no principal stress value vectors are shown both principal stress components are compressive. The high values of principal stress at the surface and the direction of these stresses in relation

to the surface are considered as the main characteristics of the early stages of the growth of micropitting cracks (Olver, 2005). Figure 5.10(c) shows the surface stress in terms of the Von Mises stress at the full contact load step. It can be seen that the high magnitude of stresses that exceeds the yield stress (σ_y =2293 *MPa)* by the order of the yield strength, is shown concentrated beneath the asperity, where plastic flow is occurring. Figure 5.10 (d) shows the maximum principal residual stress in contours that surround the compressive principal stresses in the darker blue colours and encircle the plastic flow zone beneath the asperity. It can also be noticed that elevated magnitude values of maximum tensile principal stress occur at the surface of the asperity.

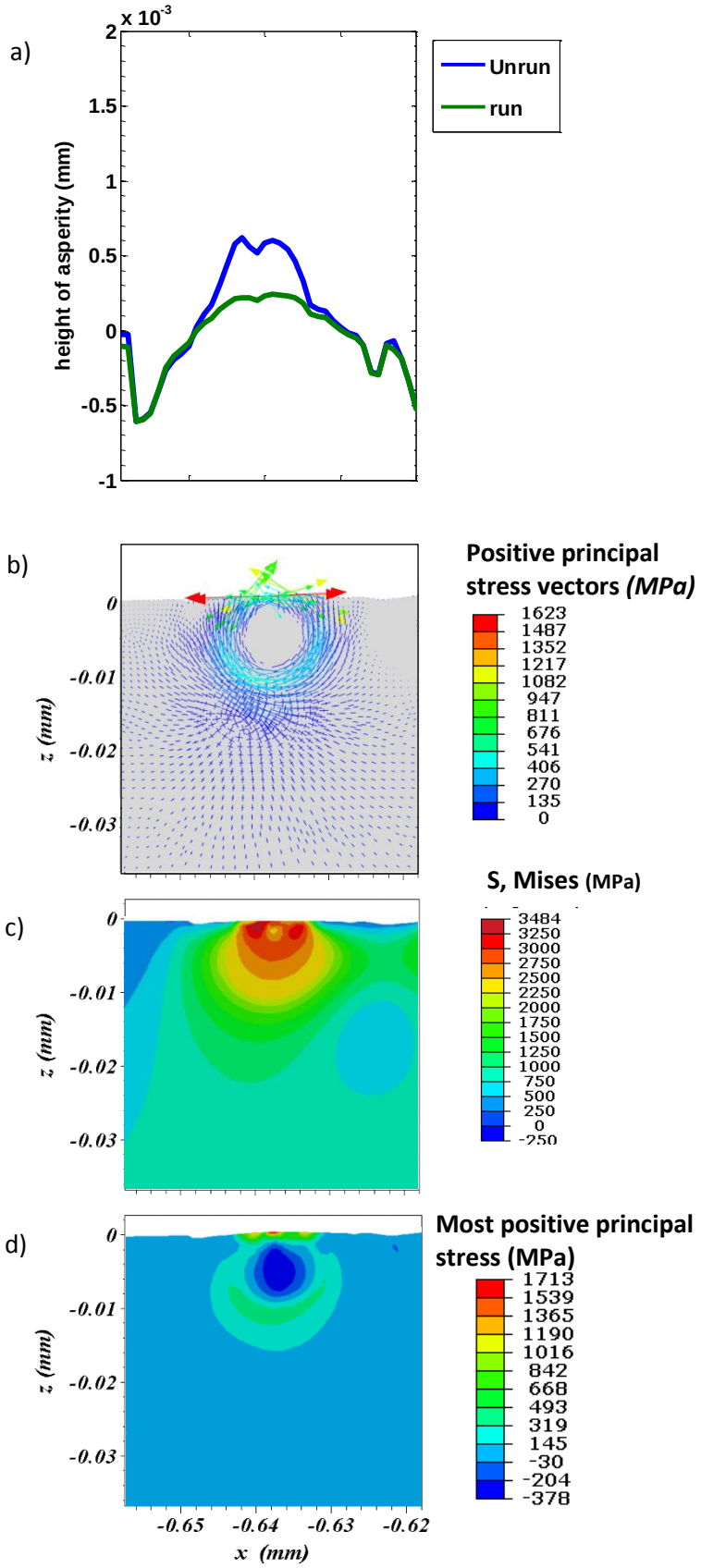

Figure 5.10- Analysis of asperity No. 1 profile B at load 1.0 GPa; a) pre/post loading profile for the asperity, b) tensile residual stress vectors, c) contours of Von Mises stress at complete load contact, d) contours of maximum principal residual stress (σy =2293 MPa).

Figure 5.11 details the second asperity in this section (asperity 9, profile B) following the pattern of the previous asperity shown in Figure 5.10. Figure 5.11 (a) shows the roughness of the asperity from x=-0.240 mm to x=-0.183 mm before and after loading and it can be seen to experience a maximum deflection of z=0.346 μm. The main part of the asperity experienced a high deformation and is labelled with a red arrow, while the adjacent sub-asperities are shielded from heavy interaction and the consequent plastic deformation. Figure 5.11 (b) shows positive tensile principal stress vectors while the compressive stresses are suppressed for the purpose of clarity as with Figure 5.10. The positive maximum principal stress vectors act at angles that are tangential to the surface or at shallow angles of as between 10° to 35° that are found at the outer edge of the middle section of the asperity. All of these findings can lead to vertical cracks growing into the subsurface material as has been elaborated in Chapter 1 and 2. A Von-Mises stress contour at the complete contact applied load step is shown in figure 5.11(c). The peak stress that is higher than σ_y =2293 *MPa* occurs towards the centre and edge of the heavily deformed regions. The maximum principal stress component contours are shown in Figure 5.11 (d) which shows that the subsurface material beneath the asperity feature experiences an incomplete and wide ring contour of positive residual stress surrounding the compressive residual stress zone. This can be seen in between x=-0.225 mm and x=- 0.205 mm , and at a depth of between z=-0.03 mm and z=0.0 mm . Also, it can be noticed that the regions that experienced residual stress correspond to an asperity with a high residual deflection.

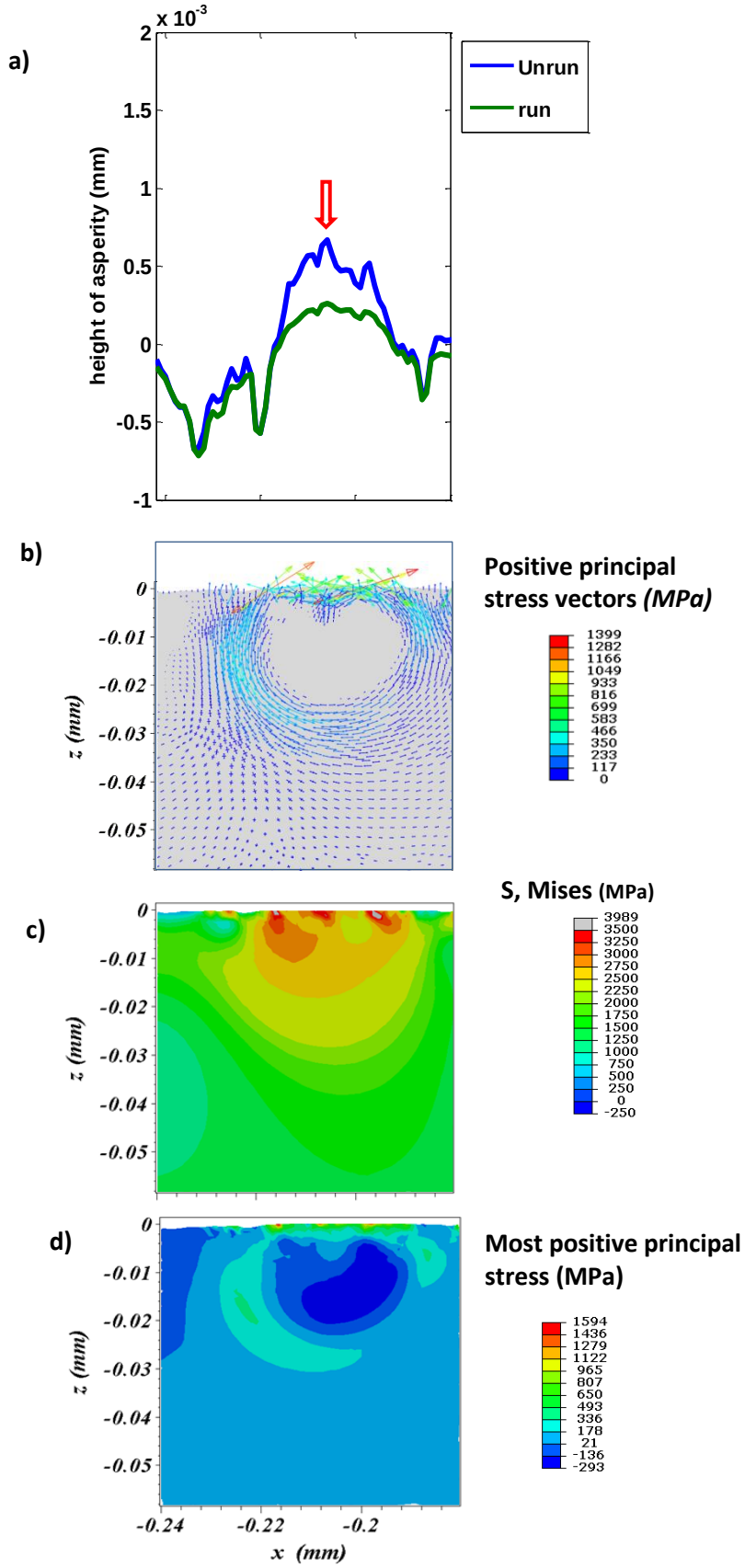

Figure 5.11 - Analysis of asperity No. 9 profile B at load 1.0 GPa; a) pre/post loading profile for the asperity, b) tensile residual stress vectors, c) contours of Von Mises stress at complete load contact, d) contours of maximum principal residual stress(σy =2293 MPa).

Figure 5.12 shows the third trial asperity (asperity 7, profile B) with a roughness profile located between x = - 0.325 mm and x=-0.275 mm . Figure 5.12 (a) shows the pre and post loading profile at a nominal load of 1.0GPa, and clearly shows three sub-asperities labelled with numbers 1, 2 and 3 that experience different residual deflections of $\delta = 0.500$ μm, $\delta = 0.208$ μm and $\delta = 0.083$ μm respectively. They also have different approximate asperity contact lengths of 8.46 μm, 4.62 μm and 2.31 μm respectively. The differences in the deflection and the length of contact occur due to the differences in asperity shape and height level. Sub-asperity 1 has carried most of the load, sub-asperity 2 has carried some of the load while the third asperity carries a much lower load. Figure 5.12 (b) shows the positive residual principal stress component vectors corresponding to the deflection of the sub-asperities. It can be seen that the highest tensile stress is related to sub-asperity number 1 which experiences the maximum deflection. Its residual stress interacts with that of sub-asperity 2, and it can be seen that, sub-asperity 3 does not have any significant tensile stress at or near its surface. Figure 5.12 (c) shows the contours of the Von Mises stress for all of the three sub-asperities at the completed load step, and this follows similar trends to those seen previously where the highest magnitude Von Mises stresses calculated correspond to the regions at the surface where high residual deflection and heavily loaded asperity contact has taken place. It can be seen that the sub-asperity 1 has a depth at which the Von Mises stress is greater than $\mathbf{1.1}\ \sigma_y\ (= 2.5\ \mathbf{GPa})$ of $z = -0.012\ mm$ whereas that for sub-asperity 2 is $z = -0.004\ mm$. This level of Von Mises stress is the source of the residual stresses that are part of initiating the micro cracking. However, there is not a region of high von Mises stress for sub-asperity 3, and therefore no plastic yielding zone, which is the source of residual stresses or micro cracking. Figure 5.12 (d) shows

that the maximum principal residual stress component value occurs at the surface and below the surface corresponding to the deflection of the sub-asperities. Magnitudes of principal residual stresses that are greater than $0.88\sigma_y = 2.0\ GPa$ occur corresponding to sub-asperity 1 and can be seen in two small red pockets at and just below the surface directly below where the asperity contacts take place (i.e. the high points of sub-asperity 1). Also, it can be seen that the regions of compressive stress in dark blue are mostly surrounded with residual positive stresses showing that the asperity is a local surface stress-raiser. This residual stress feature is highly relevant to the initiation of ring/cone cracks as shown in Figure 5.13 and Figure 5.14. These are initially perpendicular to the surface and then propagate into the material to create an asymptotic crack angle between 20° to 24° (Alfredsson et al., 2008).

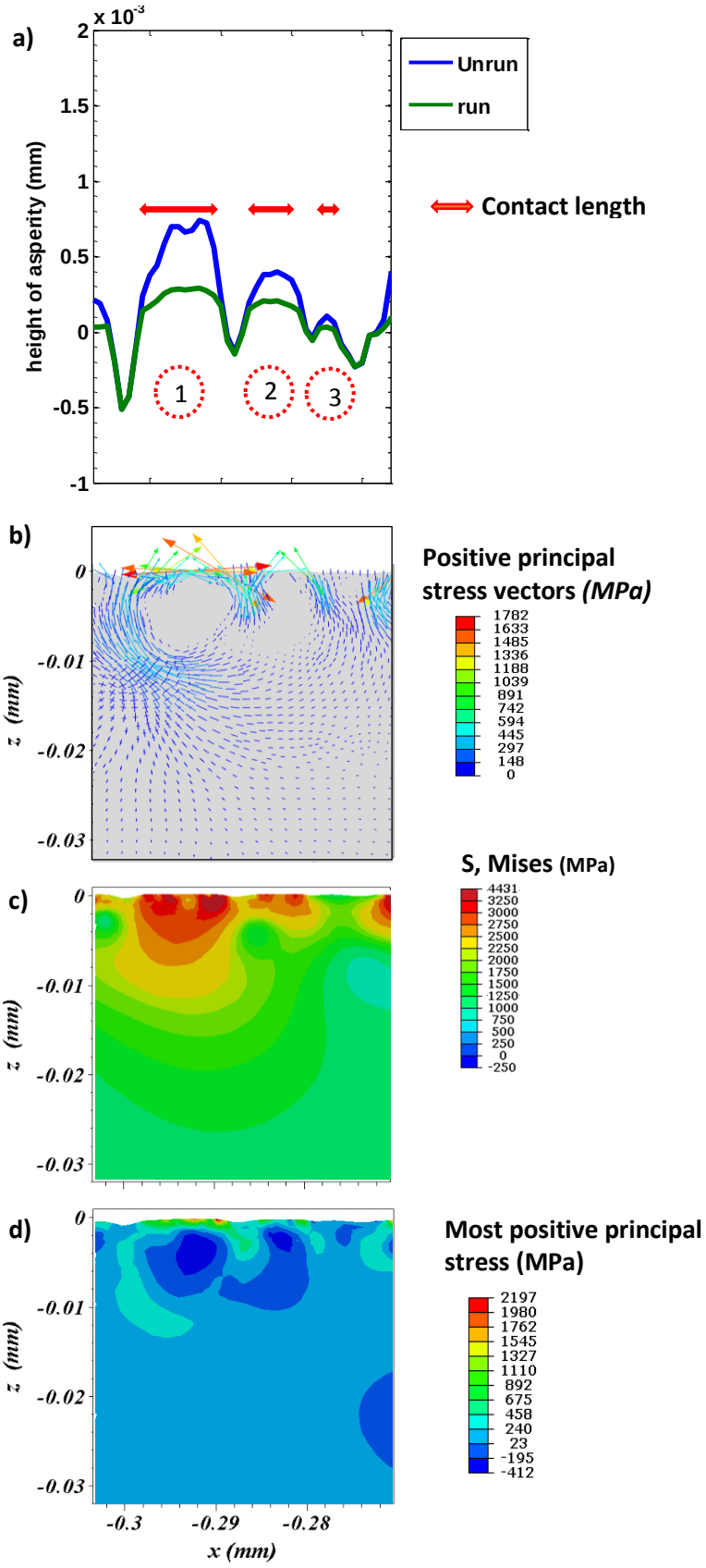

Figure 5.12 - Analysis of asperity No. 7 profile B at load 1.0 GPa; a) pre/post loading profile for the asperity, b) tensile residual stress vectors, c) contours of Von Mises stress at complete load contact, d) contours of maximum principal residual stress (σ_y =2293 MPa).

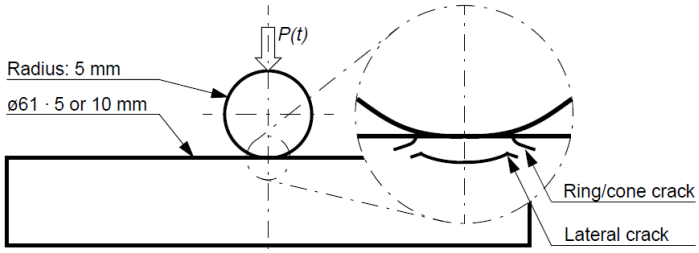

Figure 5.13-Schematics drawing of ring/con and lateral cracks (Alfredsson and Olsson, 2001).

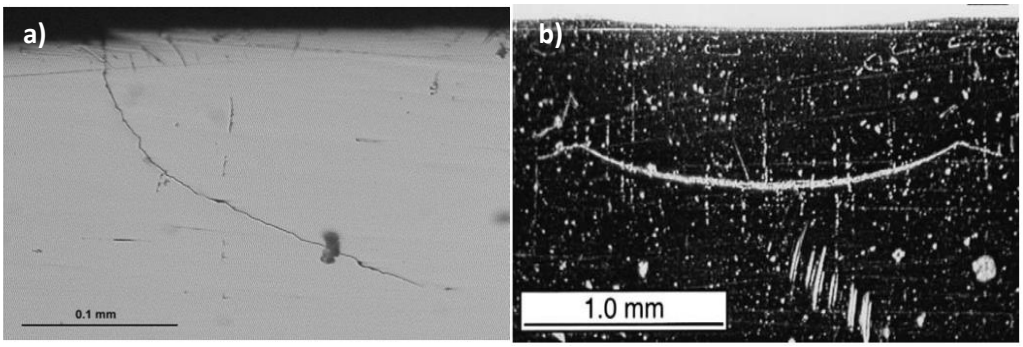

Figure 5.14 - Surface contact failure; a) section of a ring/cone crack at angle to the surface, b) section view of lateral crack (Alfredsson et al., 2008).

Figure 5.15, gives the results for the fourth trial asperity (asperity 31, profile A). It can be seen that the main asperity indicated by the red arrow consists of two approximately symmetrical heads with less space and only a shallow valley between them, which contrasts with the form of the previous asperities considered in detail. Figure 5.15 (b) shows the positive vector of the maximum principal residual stress component and follows a similar pattern to those seen in the last three figures of the asperities studied. The area of the positive high maximum principal stress vectors is found at the surface at locations where the surface of the asperity contact has been loaded and has experienced plastic deformation. Also it can be noticed that the maximum positive principal stress vectors act at angles that are tangential to the surface at shallow angles of between 10° to 35° which are found at the centre and the at the edges of the surface of the asperity. This could be a substantial factor in

originating micropitting failures and may potentially lead to vertical cracks growing into the subsurface material. Figure 5.15 (c) shows the Von Mises stress at the complete load contact and again shows that high magnitudes of the von Mises stress occur in close proximity to the surface in two pools corresponding to the double heads of the asperity. This asperity has a larger contact length of 0.017mm in comparison to the previous asperities. Figure 5.15(d) shows the contours of principal stresses where large values occur at and very near to the surface. At the same time the material at the middle area beneath the asperity is under a compressive state of stress which helps to create the common feature observed in the Micropitted gears (Oila A et al., 2005).

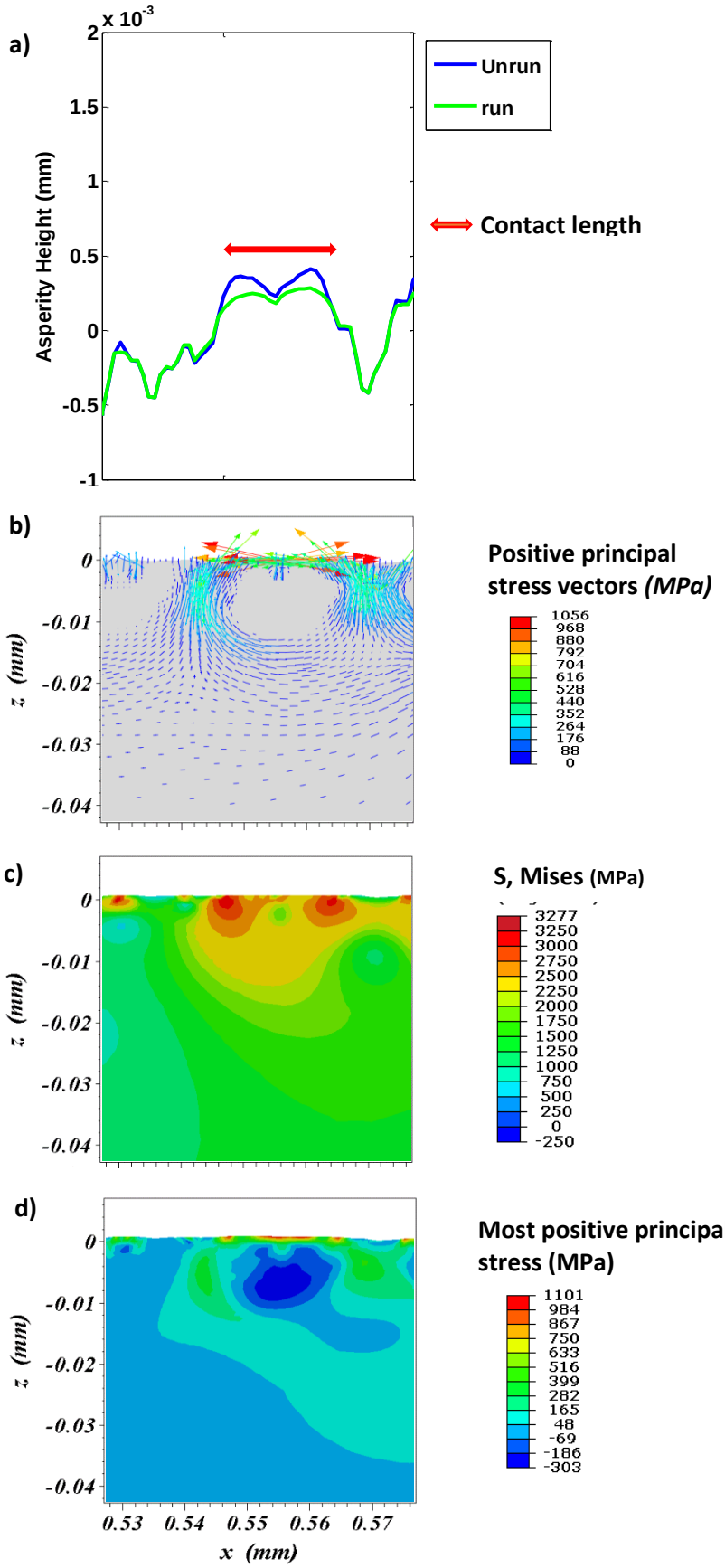

Figure 5.15 - Analysis of asperity No. 31 profile A at load 1.0 GPa; a) pre/post loading profile for the asperity, b) tensile residual stress vectors, c) contours of Von Mises stress at complete load contact, d) contours of maximum principal residual stress(σy =2293 MPa).

5.5 Analyses of load effects on a group of asperities

In order to verify the findings in Chapter 1 and 2 related to micropitting and to validate the finite element analysis, the effective comparison between the pre and post running profiles in terms of the asperity group at the applied load and stress components was investigated. It would be impractical to present all the results for the two profile asperities that have been used in the research. Therefore, three sections of roughness profiles which have prominent asperities have been selected for the study. Normally, these prominent asperity groups have contacts at each applied load.

Figures 5.16-18 show results for a 1GPa load for the selected sections of asperity groups of profile A that is shown in Figure 5.6. They will be referred to in the text as Surface 1, 2 and 3 for simplicity. They are located as follows. Surface 1 is located from x=-0.555 mm to x=-0.409 mm, and involves the asperities numbered from 2 to 7. Surface 2 is located from x=0.305 mm to x=0.452 mm where the asperity features are numbered from 25 to 28. Surface 3 extends from x=0.452 mm to x=0.608 mm with asperity features numbered from 29 to 32. Figures 5.16-18(a) show the real surface and the post FEA analysis profiles obtained with different loads (0.5 , 1.0, 1.5, 2.0 GPa) extracted from the surface of the Abaqus simulation model. They also include the profile measured after the second experimental loading stage for compression with the FEA profiles. It can be seen that all the profiles show a good agreement with the measured residual profile and good agreement with each other across the contacts. However, it can be noticed that in some locations of the surfaces there are differences between the experimental measured residual profile and each of the simulated post running profiles by different loads results particularly in the valley features which can be seen in Figure 5.15(a) surface 1 at x=-0.53 mm and x=-0.512 mm

Figure 5.16(a) surface 2, at x=0.362 mm,and x=0.43 mm and Figure 5.17(a) surface 3, at x=0.486 mm, x=0.514 mm,x=0.556 mm and x=0.594 mm. The lack of identical features between the valleys could be due to the plastic flow in the vicinity of the loaded contact where the material has been forced into a valley as a result, filtering process or because some debris has become located in these valleys. Also, a difference can be seen in the contact area which is increased by increased load both at existing contacts and as more asperities come into contact. The material combination of yield strength and linear strain hardening behaviour that have been selected for this study and previously discussed in Chapter 4 provide the effective analysis parameter choice and are related to the real experimental material.

The plastic deformation contours due to the applied loads of 1.0 GPa that exceed the yield point for all the selected surfaces are calculated by the Von Mises stress and can be seen in Figure 5.16-18(b). The von Mises stress values in the subsurface material are shown with high magnitude stress corresponding to the prominent asperities that can be seen in Figure 5.16(b) surface 1 at *x*=-0.54 mm *z*= -0.017 mm ,and at *x*=-0.468 mm *z*= -0.015mm; in Figure 5.17(b) surface 2 at *x*=0.32mm *z*=-0.022mm ,and *x*= 0.418mm *z* =-0.0125mm; and in Figure 5.18(b) surface 3 at *x*=0.47mm *z*= -0.0225mm, and *x* = 0.556 mm *z* = -0.0208 mm. This indicates that these asperities have carried the greater portion of the load applied and have experienced the greatest residual deflection. Hence, in the material experiencing the maximum deflection associated with the asperity contacts; highly stressed zones occur where the maximum stress exceeds 1.25σy, as shown for the main asperities, and is concentrated very close to the surface. The red double headed arrows included in Figure 5.16-18 (a) indicate the magnitude of residual deflection occurring in the individual asperities. Larger residual

deflection will produce more residual stress when the loads are removed as shown for all the surfaces and this can be seen in figures 5.16-18 (a). Also it can be seen that larger regions of the high magnitude of maximum principal residual stress occur for the asperities that experience the largest residual deflection and the Von Mises stress. The influence of surface roughness upon subsurface stress states decreases as the depth increases as shown in all the surface figures (c-d). Additionally, the regions of magnitude of residual Maximum principal stress by values above 0.2σy are concentrated near to the surfaces and can extend to a larger depth such as z = -0.028 mm between x=-0.476 mm and x=-0.468 mm, z = -0.026 mm between x=0.396 mm and x=0.416 mm, z=-0.032 mm between x=0.588 and x=0.598 mm in Figure 5.16(c) surface 1,Figure 5.17 (c) surface 2 and in Figure 5.18 (c), respectively . On the other hand, compressive stresses which are less than -0.1σy can be seen in the subsurface material beneath the prominent asperities in a dark blue colour. Figures 5.16-18(d) show positive principal residual stress vectors for the three surfaces while the compressive stresses are suppressed. It can be seen that the heavily loaded asperity features that are labelled with numbers in the profile figures provide the largest value of the positive principal residual stress vectors, and it could be advocated that the value of the positive principal residual stress vectors is related to the amount of residual deflection of the asperities. Table 5.3 shows the relation between the main asperities which are labelled in numbers in each surface corresponding to the maximum positive residual stress and the maximum principal residual stress vectors. It can be noticed in the table that some asperity features have the same residual deflection of $\delta = 0.00024 \ \ mm$, whilst they show different magnitudes of principal tensile residual stress, such as asperity number 7 in surface 1, asperity number 30 and 32 in surface 3

that achieved values of 1108 MPa, 1384 MPa and 1359MPa respectively. Thus, the residual principal tensile stress in an asperity does not depend completely on the residual deflection. However, in general terms the maximum residual stress corresponds to the maximum deflection as can be seen in Table 5.3. As an example, at surface 1, asperity 5 $\delta = 0.00028\ mm$ and the maximum principal residual stress is 1734 (MPa), whereas at asperity 26B of surface 2, $\delta = 0.00006896\ mm$ and the maximum principal residual stress is 879MPa.

Table 5.3 - Values of principal residual stress vectors and maximum deflections due to the removal load 1.0GPa for the prominent asperities.

surface number	Asperity number	Max. deflection for a load of 1.0 GPa	Maximum principal residual stress (MPa)
1	2	$\delta = 0.0001\ mm$	1025
1	3	$\delta = 0.00012\ mm$	927
1	5	$\delta = 0.00028\ mm$	1734
1	6	$\delta = 0.00018\ mm$	939
1	7	$\delta = 0.00024\ mm$	1108
2	25	$\delta = 0.00012\ mm$	1091
2	26(A)	$\delta = 0.000137\ mm$	1209
2	26(B)	$\delta = 0.00006896\ mm$	879
2	27	$\delta = 0.000206\ mm$	1246
2	28	$\delta = 0.0001724\ mm$	908
3	29	$\delta = 0.00016\ mm$	724
3	30	$\delta = 0.00024\ mm$	1384
3	31	$\delta = 0.00012\ mm$	1101
3	32	$\delta = 0.00024\ mm$	1359

Also, observations can be made across the three groups of asperities (three surfaces) such as a small residual deflection in the roughness profile at several locations in Figures 5.16-18 (a) is associated with very light asperity contact, von Mises stress and residual stress. Thus, it can be concluded that when high positive residual stresses are considered to be experienced by the material, there is a greater tendency for subsurface cracks to nucleate and for the material to experience a greater amount of damage.

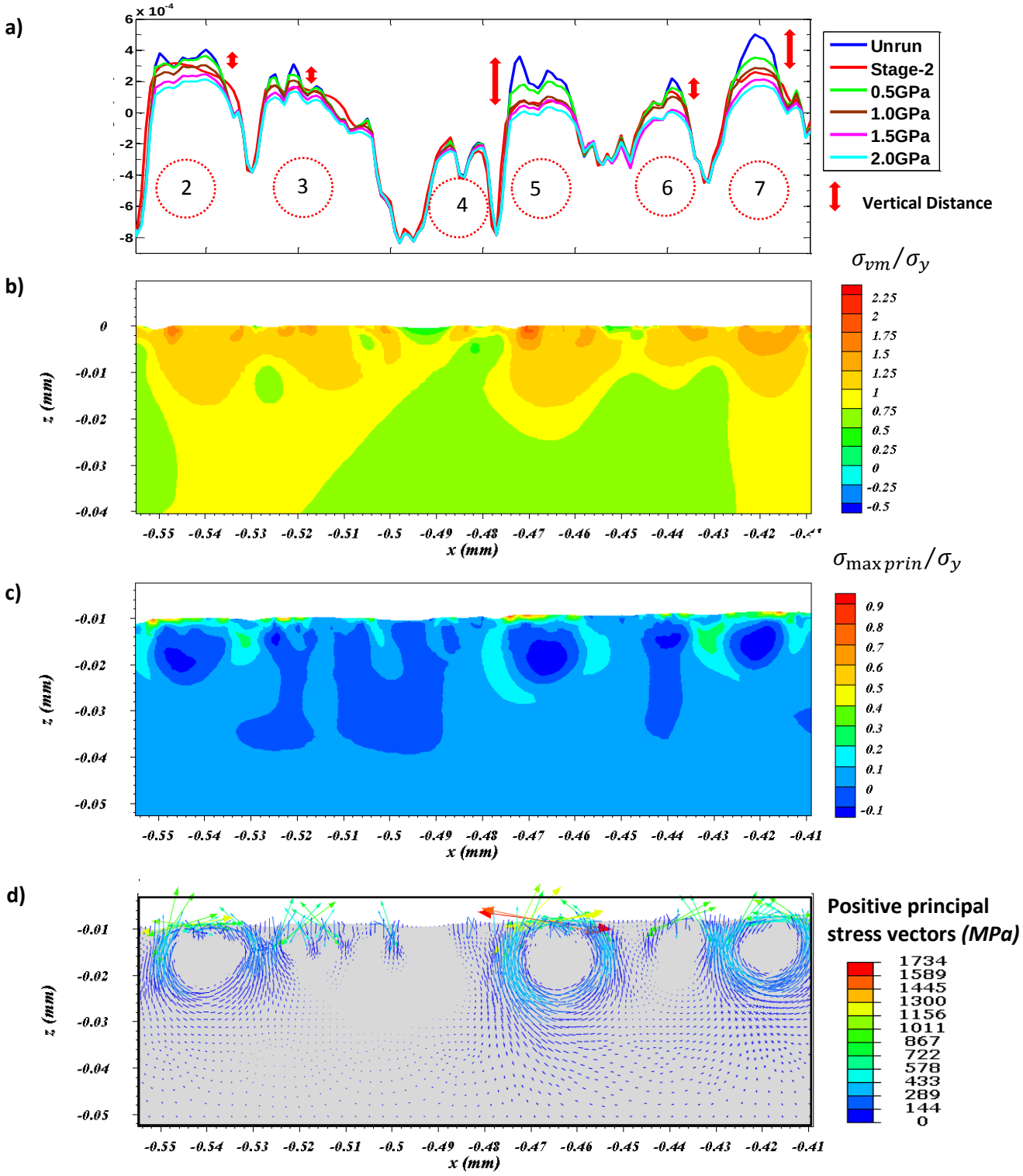

Figure 5.16 - Contours for surface 1 of roughness from x = -0.555 mm to x = -0.409 mm at load 1.0 GPa; a) Roughness profile at a range of loads, b) Normalised Von Mises stress at complete contact load, c) Normalised Maximum principal residual stress, d) Positive principal residual stress vectors(σ_y =2293 MPa).

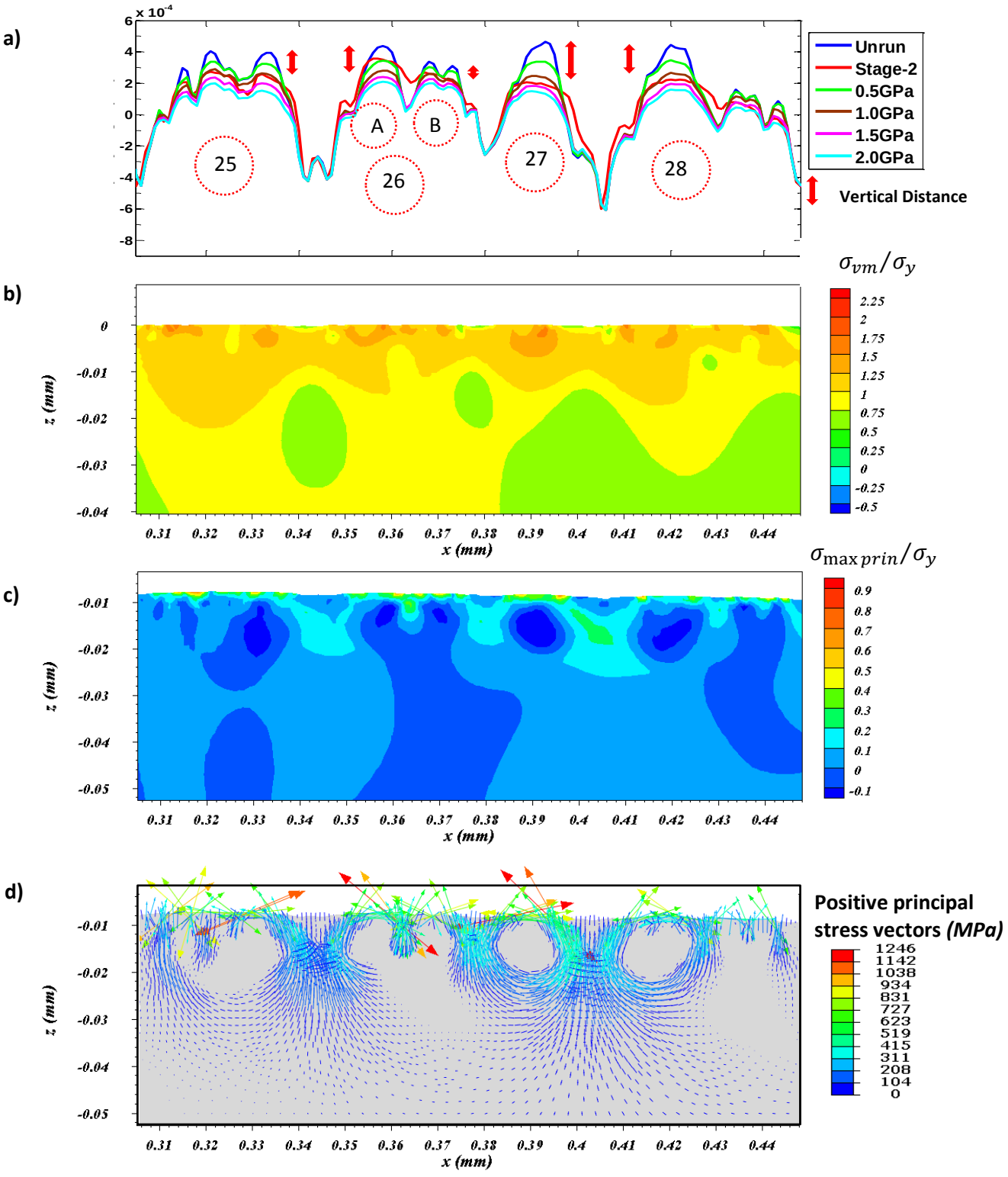

Figure 5.17 - Contours for *surface 2* of roughness from x = 0.305 mm to x = 0.452 mm at load 1.0 GPa; a) Roughness profile at range of loads, b) Normalised Von Mises stress at complete contact load, c) Normalised Maximum principal residual stress, d) Positive principal residual stress vectors (σy =2293 MPa).

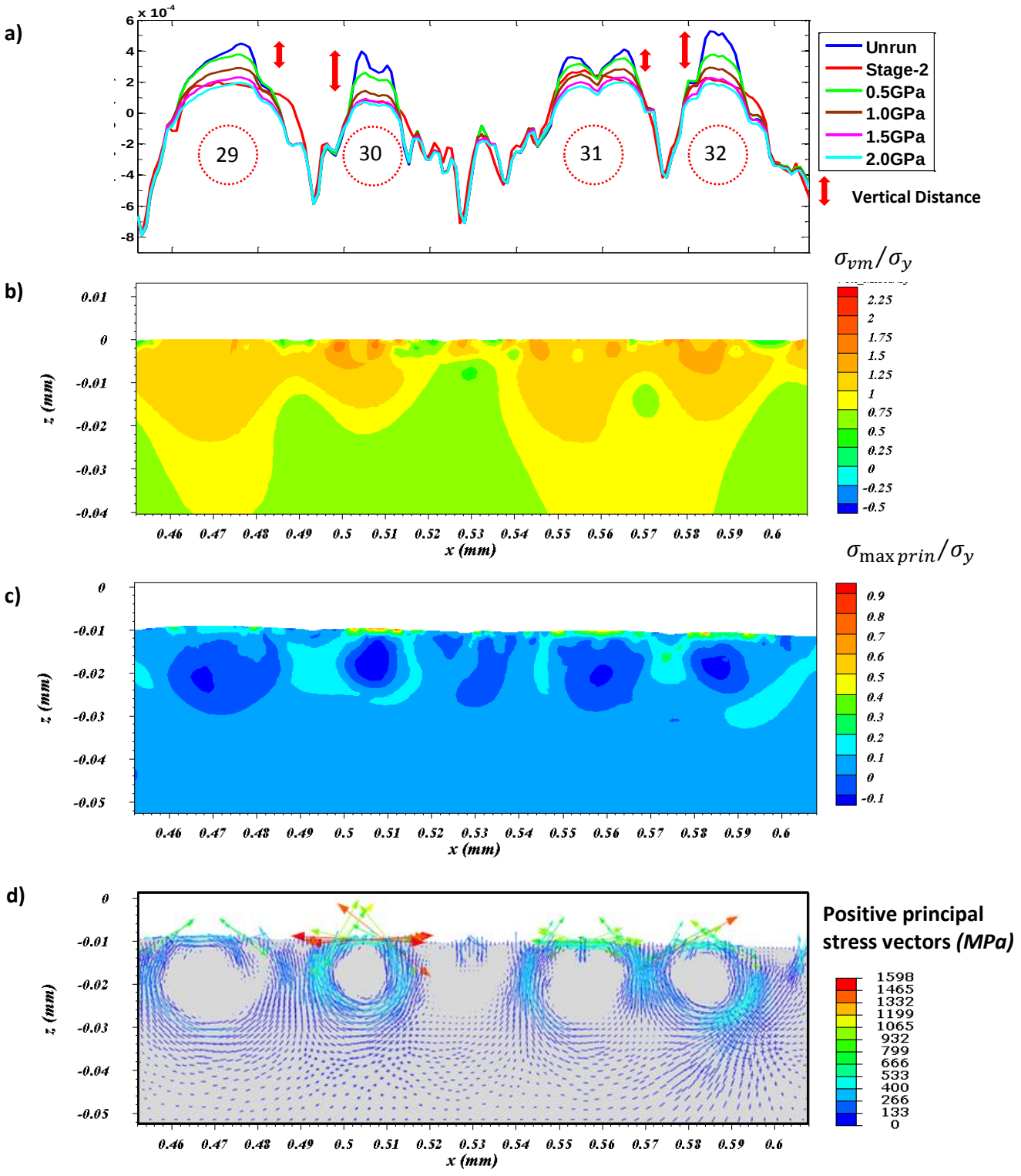

Figure 5.18 - Contours for *surface 3* of roughness from x = 0.452 mm to x = 0.608 mm at load 1.0 GPa; a) Roughness profile at range of loads, b) Normalised Von Mises stress at complete contact load, c) Normalised Maximum Principal residual stress, d) Positive principal residual stress vectors (σ_y =2293 MPa).

5.6 Further analysis of the residual stress at the asperity

This section discusses in detail the residual stress found at an individual asperity as a result of the contact modelling, which provides an illustrate example. In order to depict the influence of residual stresses on an asperity, the results are reported for the components of residual stress profiles in the form of sections parallel and normal to the surface as shown in Figure 5.19 and 5.20 respectively. In figure 5.19 the sections illustrated are normal to the surface as illustrated at x= -0.65, -0.64 and -0.63 mm denoted AA, BB and CC respectively. Figure 5.18(a) also shows how these sectional positions are related to the contours of the principal residual stresses. Figure 5.19 (b)(c) and (d) show the variation of the directional residual stress components σ_{xx}, $\sigma_{zz}$and τ_{xz} over sections AA,BB and CC. The components values and their position are tabulated in Tables 5.4 to 5.6. Variations of the components on sections parallel to the surface are shown in Figure 5.20. The sections used are denoted H01 to H08 and are illustrated in figure 5.20(a). Again the maximum values and positions along each section are tabulated in tables 5.7 to 5.12.

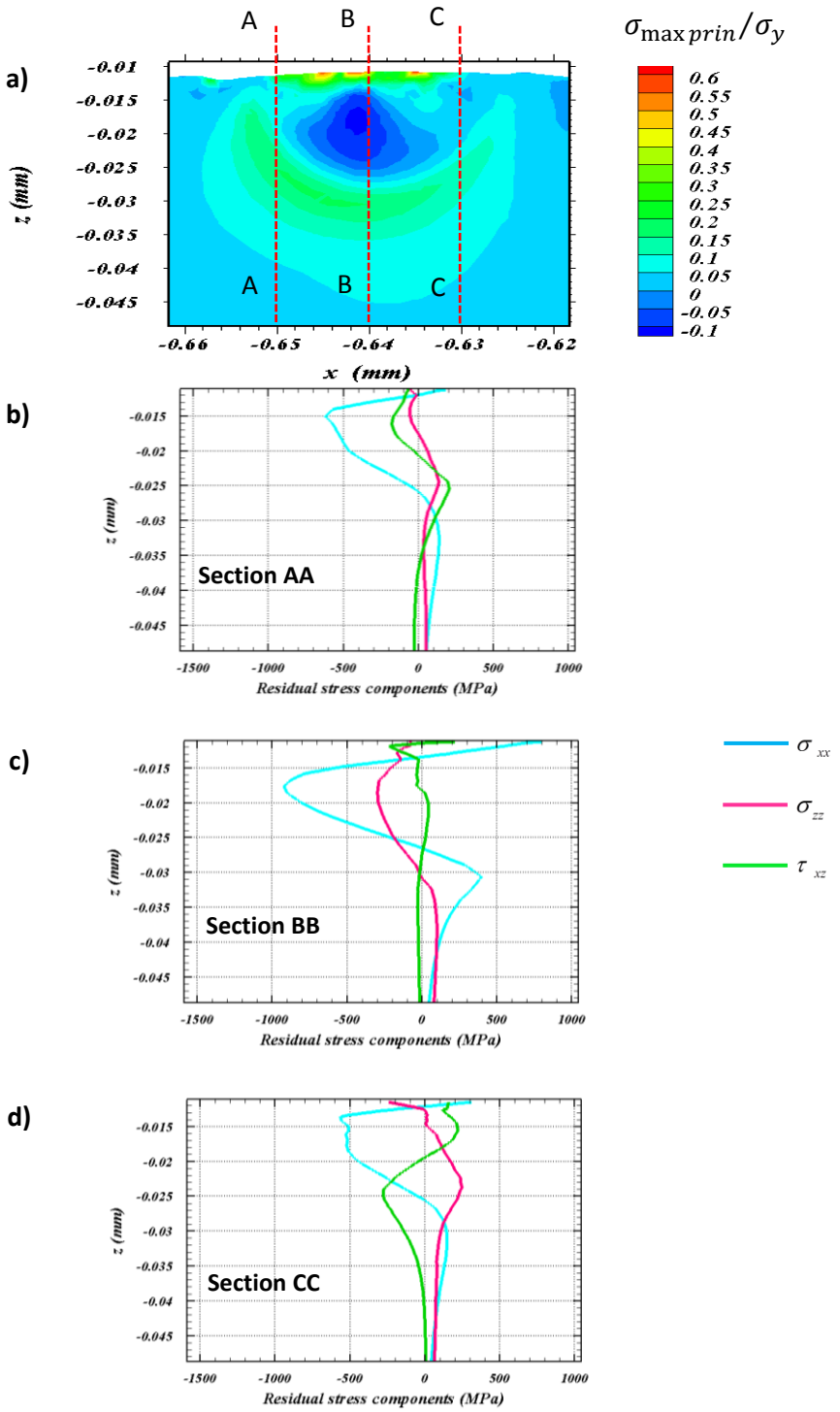

Figure 5.19 -Variation of the components of residual stress along part of the profile from x=-0.665 to x=0.622 mm at different sections normal to the surface (σ_y =2293 MPa).

Table 5.4 - Maximum residual stress components along the vertical section labelled 'AA'.

Material property components	Max. Tension residual stress/location	Max. compression residual stress/location
σ_{xx}	200 at z= -0.01	-650 at z= -0.015
σ_{zz}	120 at z= -0.025	-90 at z= -0.015
τ_{xz}	200 at z= -0.025	-200 at z= -0.017

Table 5.5 - Maximum residual stress components along the vertical section labelled 'BB'.

Material property components	Max. Tension residual stress/location	Max. compression residual stress/location
σ_{xx}	800 at z= -0.011	-900 at z= -0.017
σ_{zz}	98 at z= -0.0354	-300 at z= -0.018
τ_{xz}	210 at z= -0.011	-210 at z= -0.012

Table 5.6 - Maximum residual stress components along the vertical section labelled 'CC'.

Material property components	Max. Tension residual stress/location	Max. compression residual stress/location
σ_{xx}	300 at z= -0.012	-590 at z= -0.0135
σ_{zz}	250 at z= -0.0235	-230 at z= -0.012
τ_{xz}	220 at z= -0.016	-290 at z= -0.025

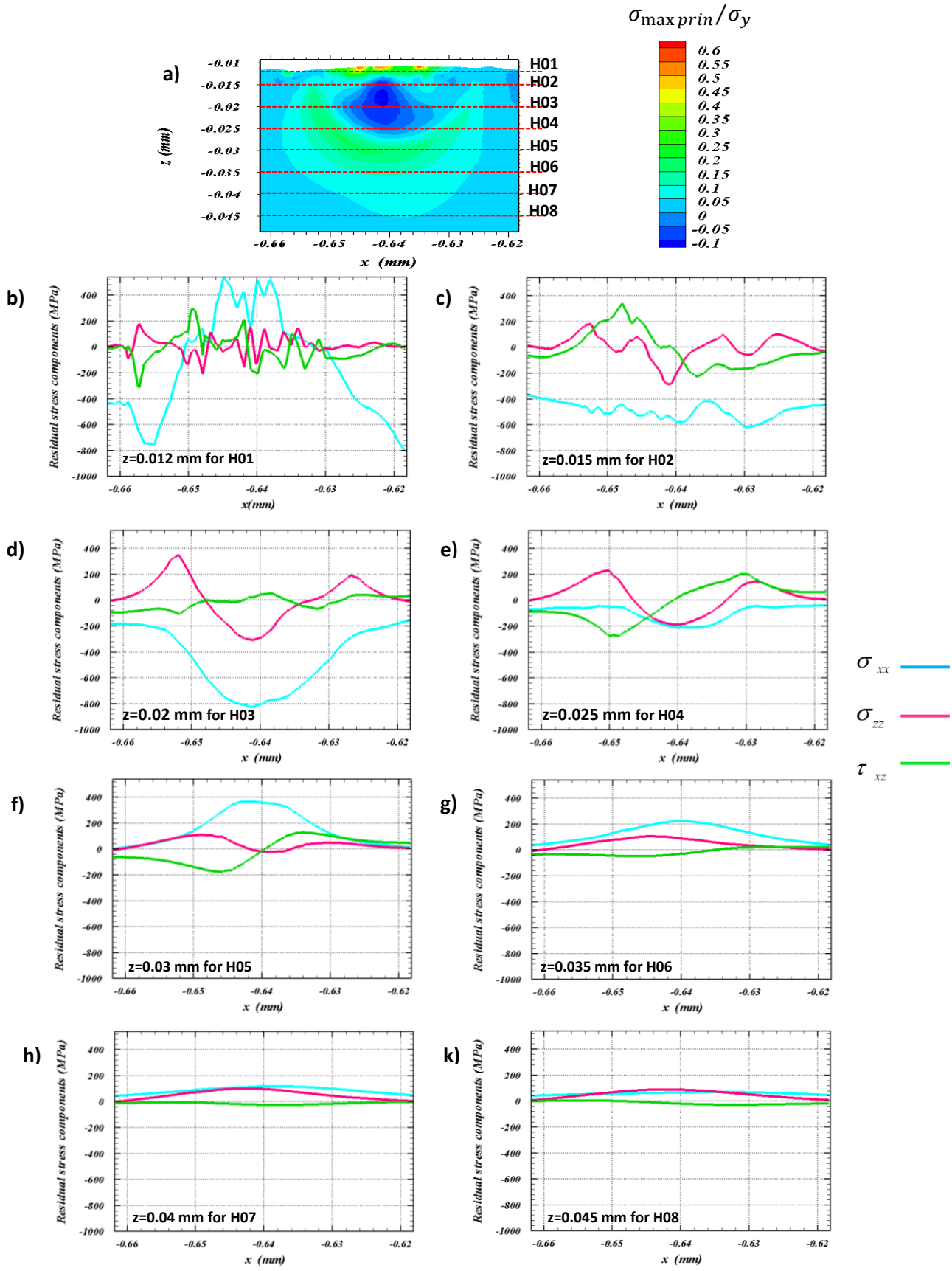

Figure 5.20 -Variation of the components of residual stress on sections parallel to the surface for the profile between x=-0.662 to x=-0.618 mm (σ_y =2293 MPa).

Table 5.7 - Maximum residual stress components along cross section number 01H.

Material property components	Max. Tension residual stress/location	Max. compression residual stress/location
σ_{xx}	530 at x=-0.645,-0.64 ,-0.638	-760 at x=-0.658
σ_{zz}	160 at -0.642,-0.657	-200 at x=-0.648
τ_{xz}	320 at -0.649	-320 at x= -0.657

Table 5.8 - Maximum residual stress components along cross section number 02H.

Material property components	Max. Tension residual stress/location	Max. compression residual stress/location
σ_{xx}	-400 at x=-0.635	-640 at x=-0.63
σ_{zz}	170 at x= -0.653	-280 at x=-0.641
τ_{xz}	330 at x= -0.648	-240 at x=-0.637

Table 5.9 - Maximum residual stress components along cross section number 03H.

Material property components	Max. Tension residual stress/location	Max. compression residual stress/location
σ_{xx}	-170 at x= -0.618,-0.66	-840 at x=-0.642
σ_{zz}	340 at x= -0.652	-290 at x=-0.642
τ_{xz}	80 at x= -0.638	-130 at x=-0.653

Table 5.10 - Maximum residual stress components along cross section number 04H.

Material property components	Max. Tension residual stress/location	Max. compression residual stress/location
σ_{xx}	-40 at x=-0.618	-230 at x=-0.639
σ_{zz}	240 at x=-0.651	-175 at x=-0.641
τ_{xz}	200 at x=-0.0631	-280 at x=-0.651

Table 5.11 - Maximum residual stress components along cross section number 05H.

Material property components	Max. Tension residual stress/location	Max. compression residual stress/location
σ_{xx}	360 at x=-0.642	0 at B.C
σ_{zz}	120 at x=-0.647	-40 at x=-0.638
τ_{xz}	120 at x=-0.0635	-180 at x=-0.645

Table 5.12 - Maximum residual stress components along cross section number 06H.

Material property components	Max. Tension residual stress/location	Max. compression residual stress/location
σ_{xx}	240 at x=-0.64	40 at B.C
σ_{zz}	120 at x=-0.644	0 at B.C
τ_{xz}	20 in between -0.618 to -0.0638	-30 at x=-0.0644

5.7 Conclusion

In attempting to understand and predict the mechanical behaviour of the contacting bodies and its effects on the fatigue calculation, an elastic-plastic asperity based contact model is presented in this chapter. The stress components of the asperity such as the maximum principal residual stress, the maximum principal residual stress vectors and the von Mises stress etc. are considered and were investigated, looking for relationships between the findings found in the literature and the residual stresses found at the asperities. Also, the process of determining the load that was subsequently used its FEA residual stress in the fatigue calculation is explained .This is based on the measured residual deflection of the asperity and the experimental deflection of the same asperity, and then the technique of interpolating the FEA residual stress components that was subsequently used in in the fatigue calculation reported in chapter 7 is presented.

Chapter 6

Fundamentals of fatigue

6.1 Introduction

Fatigue failures on most structural mechanical components are found to occur in those subjected to repeated, cyclic loading. This can be described as a local phenomenon, where cyclic evaluation of the stresses, deformations occurs within a certain critical volume of material. Modelling the mechanical behaviour of a material under multiaxial elastoplastic strain and cyclic deformation is fundamental in predicting damage and the safe operational life of many structural components. This chapter opens with an introduction to review the fundamentals fatigue theories that will be used in the study. Following that, fatigue occurs in mixed EHL in line contact is studied. The study is based on the numerical simulation of surface fatigue failure in the EHL environment. That leads to the study of the form of mild wear failure occurring at the gear contact surface at the scale of the surface roughness called micropitting. The innocuous mild wear of micropitting can, however, lead to rapid crack growth and even to complete tooth failure. This failure mechanism is associated with the rough surface EHL.

The research presented in this thesis has used a suite of a software programmes written in the FORTRAN language, which has been developed by the Cardiff tribology group to analyse rough surface EHL. This comprises a transient EHL analysis code that provides surface loading information concerning contact pressure and surface shear stress for subsequent stress analysis to determine material stress history, and fatigue analysis based on the evaluated stress history. This research has developed the capability of the fatigue analysis tool in two ways. Firstly, the stress cycles have been

analysed for points within the material experiencing high levels of calculated damage to be able to identify which surface features and which stress cycles of the surface loading are most significant in the damage calculation. Secondly, the modified software has been extended to include further fatigue models that will replicate the known observation that micropitting occur in the slowest moving surface.

In the analyses real experimentally measured surface roughness profiles are used for the contacting bodies with the surface profiles taken from components that have experienced initial loading and running in of the prominent surface asperities. These objectives are developed in the modified software by identifying points of interest which are surface asperities, approximately ten in number, in the fatigue analysis in order to see which area has the main effects it is important to isolate the pressure and shear stress experience for the areas centred on these asperities, isolate the stress cycles for the damage calculated for these points and rank the cycles in terms of their contribution to the calculated damage.

The fatigue analysis was carried out for the EHL line contact with rough surfaces without considering the residual stress associated with the plastic deformation occurring in the running in process. Corresponding fatigue analyses with residual stress added to the asperities or to the worst points of high damage will be repeated to assess the resulting changes in calculated damage are made in chapter 7.

6.2 Theories of Fatigue – A review

6.2.1 Fatigue of Materials

For more than 150 years, the term of “fatigue” has been an essential subject in the field of the engineering. In 1828, Albert W.A.J. tested mine hoist chains under cyclic loading which was the earliest study of fatigue (Dowling, 2013). Fatigue is a progressive failure that takes place in components of mechanics, vehicles and structures which are subjected to repeated, cyclic stresses or fluctuating loading. It can lead to the microscopic physical damage to the materials involved. Fatigue failure may occur at stress levels well below the ultimate strength of the components material. The process can be described as microscopic damage due to repeated cyclic loading or local plasticity which accumulates until microscopic cracks grow and develop. Then, the propagation of dominant cracks reaches a critical size, whereupon the mechanical resistance of the material will decrease and failure occurs. Nowadays, in terms of analysing and designing, fatigue failure can be classified by three major approaches. Firstly, the stress-based approach which is based on the nominal stresses in the damage zone of the component. The second approach is the strain based approach, which involves more detailed analysis of the localised yielding that may occur as stress increases during the cyclic loading. Thirdly, the fracture mechanics approach specifically treats growing cracks by the process of fracture methods (Dowling, 2013). Understanding the significant factors that influence the fatigue life is essential in order to prevent fatigue failure. However, fatigue behaviour is dependent upon a wide range of factors involved including both external and internal factors under service conditions, so predicting the fatigue life of a given mechanical component is very

complicated. External factors include the type of surface roughness that this research is studying, operating temperature and environment, applied loading (torsion or bending), loading pattern (variable amplitude or constant loading), manufacturing process, etc. However, the internal factors include mechanical properties, stress concentration, residual stress which is also the focus of by this study, composition, microstructure and macrostructure, material imperfections etc. (Boardman, 1990).

6.2.2 Fatigue Life.

Fatigue life can be considered as the total number of cycles of stress or strain of a specified character that a given component sustains before a crack initiates and then grows sufficiently to lead to catastrophic failure (Fatemi A. et al., 2000). Scientifically, *S-N* curves (Wöhler's curves) represent fatigue data which are usually obtained from a (rotating) bending test for a smooth specimen. *S-N* curves are plotted with applied stress (σ_a) as a y-coordinate against the total cycles to failure (*N*) as the x-coordinate. It can be divided into two parts, low cyclic fatigue life time (LCF), which is characterised by high cyclic stress levels, and high-cycle fatigue HCF which is characterised by low cyclic stress levels. The low cycle fatigue life time is based on a small numbers of cycles to cause damage or failure and the material is subjected to high stress levels that can produce significant macroscopic plastic strains. By using logarithmic scales LCF curves are represented by the total strain amplitude ε_a as the ordinate and number of cycles to failure N_f as the abscissa. High-cycle fatigue (HCF) needs a large number of cycles to cause failure and macroscopic plasticity although the material can be subjected to low stress levels. HCF curves are represented by stress amplitude (σ_a) as the ordinate and the number of cycles to failure (N_f) as the *x*_coordinate as shown in figure 6.1. The

stress-life relationship can be expressed as relating the stress amplitude in a fully reversed cycle, $\sigma_a = {}^{\Delta\sigma}/_{2}$, to the number of cycles leading to failure, $2N_f$ (Basquin relation) (Suresh S., 1998, Dowling, 2013).

$$\frac{\Delta\sigma}{2} = \sigma_a = \sigma'_f \left(2N_f\right)^b \qquad 6.1$$

Where σ'_f is the fatigue strength coefficient, b is known as the Basquin exponent or the fatigue strength exponent. As shown in Figure 6.1, the fatigue limit or endurance limit, σ_e, is a property of materials where the component may be cycled indefinitely below this stress amplitude level without failure. Another term used is the fatigue strength which specify stress amplitude at a particular life (number of cycles to failure) that is of interest, for example the fatigue strength at 10^4 cycles which represent the stress amplitude corresponding to $N_f = 10^4$.

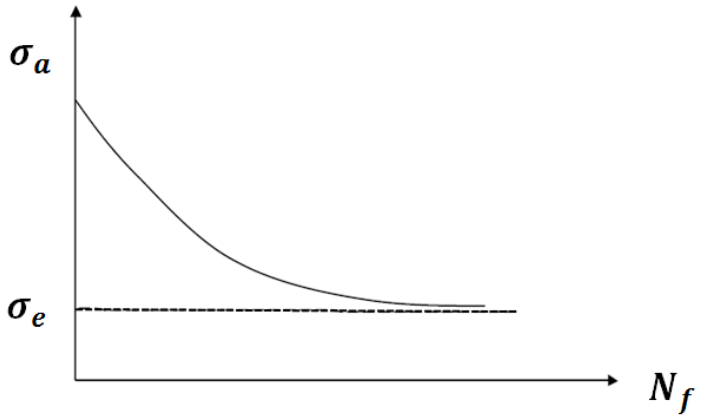

Figure 6.1 - Stress life relationship for HCF.

6.2.3 Cyclic Material Behaviour

In a fatigue test and in most practical applications the stress is cycled between the minimum and maximum values. This is called constant amplitude stressing, as illustrated schematically in Figure 6.2. Within the field of cyclic loading, several terms

are used such as the stress range, mean stress and alternating stress (which is called stress amplitude by some authors) and are expressed in the same order as follows:

$$\Delta\sigma = \sigma_{max} - \sigma_{min} \qquad 6.2$$

$$\sigma_m = \frac{\sigma_{max} + \sigma_{min}}{2} \qquad 6.3$$

$$\sigma_a = \frac{\Delta\sigma}{2} = \frac{\sigma_{max} - \sigma_{min}}{2} \qquad 6.4$$

Where tension is continuously considered to be positive $\sigma_{max} > \sigma_{min}$, the sign of σ_a and $\Delta\sigma$ are positive, however, in some cases the quantities of σ_{max} and σ_m can be negative or positive. It is also useful to note the following ratios:

$$\sigma_{max} = \sigma_m + \sigma_a \qquad 6.5$$

$$\sigma_{min} = \sigma_m - \sigma_a \qquad 6.6$$

$$R = \frac{\sigma_{\min}}{\sigma_{\max}} \qquad 6.7$$

$$A = \frac{\sigma_\sigma}{\sigma_m} \qquad 6.8$$

A refers to the amplitude ratio and R is the stress ratio. Based on the above ratios there are two common reference test conditions used for obtaining the fatigue properties $R = -1$ and $R = 0$. Condition R = - 1 is called fully reversed loading since σ_{min} is equal to $-\sigma_{max}$. Condition R = 0 is called pulsating tension or zero-to-tension loading, where $\sigma_{min} = 0$. There are also other conditions where R can take values ranging from - 1 to +1 namely(Dowling, 2013):

- Partially reversed loading, - 1 < R < 0.
- Loading between two tensile stresses, 0 < R < 1.
- Static loading, R = 1.

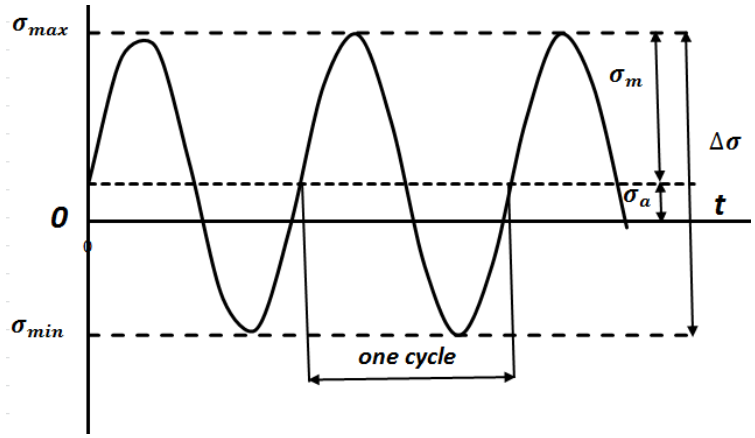

Figure 6.2 - Constant amplitude stressing.

6.2.4 The critical plane approach

Fatigue life determination for all mechanical components and structures is an essential subject in the operating and design stages. Real service loading often generates random and multiaxial stress/strain states. They must then be reduced to a uniaxial state which is called the 'equivalent' state, and can then be used in fatigue life calculations. Abundant multiaxial fatigue failure criteria have been developed in recent decades. Among these criteria, an approach called the critical plane has been used extensively in recent years because of its broad range of application and effectiveness. This approach assumes that the stresses and strains acting on a particular critical plane are used to assess the fatigue failure of the material. This is based upon the experimental observation that fatigue cracks initiate on planes of high shear stress (mode II) and grow on certain material planes of high tensile stress (mode I) as shown in Figure 6.3 (Dowling, 2013). A more detailed view is that fatigue cracks initiate in certain planes which experience maximum shear conditions and propagate along the grain boundary whose irregular surfaces would create a difficult environment for the crack to grow due to friction effects and mechanical interlocking. However, the normal stresses and strains acting upon that particular crack plane can help to open the crack,

allowing it to propagate. A group of models based on the critical plane approach is discussed and used in this study such as in section 6.3.

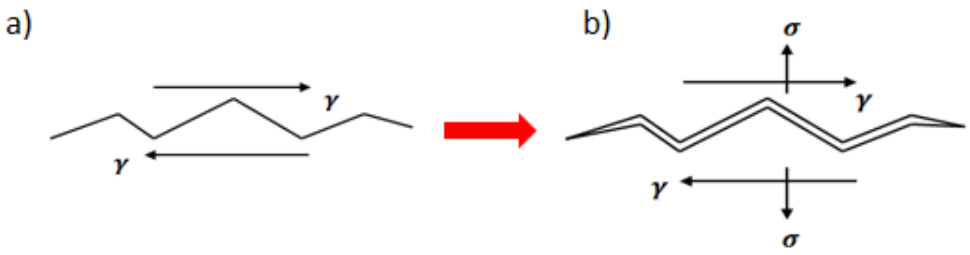

Figure 6.3 - Fatigue cracks: a) initiate on planes of high shear stress. b) grow on planes of high tensile stress.

6.2.5 Mean stress

The mean stress level has a significant impact on the fatigue behaviour of engineering materials as is shown in Figure 6.4 where the alternating stress is plotted against the number of fatigue life cycles for different mean stress values. The figure shows that the increase in the mean stress in the tensile direction results in a decrease in fatigue life, and that the life is increased when the mean stress is compressive (Fatemi A. et al., 2000).

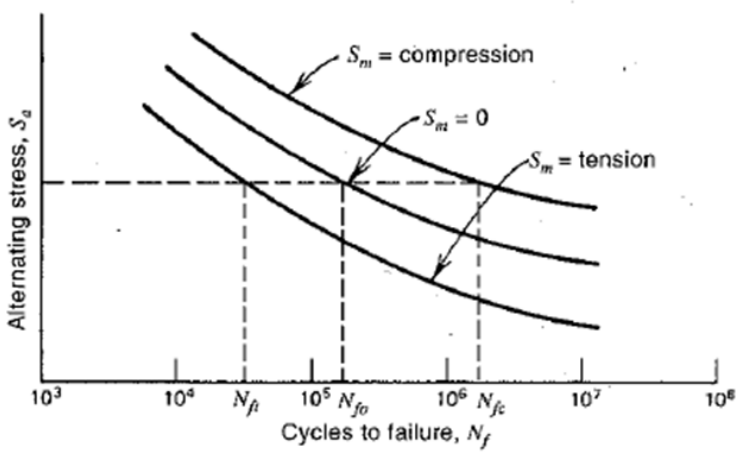

Figure 6.4 - The effect of mean stress on fatigue life (Fatemi A. et al., 2000).

6.3 Multiaxial Fatigue Theories

6.3.1 Introduction

Many engineering structures and components are subjected to multiaxial cyclic stresses due to complicated loadings and geometries. Multiaxial stress is common, and multiaxial strain is hard to avoid. Multiaxial fatigue models are usually dependent on uniaxial fatigue test data to estimate life in practice. Consequently, several multiaxial fatigue criteria have been developed to reduce the multiaxial stress state to an equivalent uniaxial stress condition. In the following sections, several multiaxial fatigue models are used to perform a fatigue analysis for the EHL line contact with rough surfaces based on the strain-based approach and the stress-based approach.

6.3.2 Stress and strain - based approach

The strain-based approach differs significantly from the stress_based approach. The strain-based approach considers the plastic deformation that may take place in the localised area where fatigue cracks might start. Therefore, the stresses and the strain in such on area are quantified and used for calculating the fatigue life. Also, the approach can give improved estimates for short life LCF and for HCF cases where there is little plastic deformation (Dowling, 2013).

6.3.2.1 Effective Strain Amplitude Approach

In the situation of applying uniaxial or torsional cyclic loading at the same frequency, the relation between the applied strain amplitude and fatigue life can be divided into two forms. Firstly, the effective strain under the uniaxial loading condition under complete stress reversal can be defined using the following equation:

$$\varepsilon_a = \frac{\Delta\varepsilon}{2} = \frac{\Delta\varepsilon_e}{2} + \frac{\Delta\varepsilon_p}{2} \qquad 6.9$$

Here $\frac{\Delta\varepsilon_p}{2}$ is the true plastic strain amplitude and $\frac{\Delta\varepsilon_e}{2}$ is the elastic strain amplitude that is related to the stress amplitude by $\varepsilon_a = \frac{\sigma_a}{E}$. When $\varepsilon_{ap} = \frac{\Delta\varepsilon_p}{2}$ and $\varepsilon_{ae} = \frac{\Delta\varepsilon_e}{2}$ are plotted separately versus the number of cycles to failure, the elastic strain(Basquin relationship) gives a straight line with a shallow slope on a log-log plot, and the plastic strain (Coffin-Manson relationship) is a straight line of a steeper slope as shown in Figure 6.5. This allows their relation to be fitted to the lines:

$$\varepsilon_{ae} = \frac{\Delta\varepsilon_e}{2} = \frac{\Delta\sigma}{2E} = \frac{\sigma'_f}{E}\left(2N_f\right)^b \qquad 6.10$$

$$\varepsilon_{ap} = \frac{\Delta\varepsilon_p}{2} = \varepsilon'_f\left(2N_f\right)^c \qquad 6.11$$

Where powers b and c are slopes on the log-log plot. Combining the above equations gives an equation relating the total strain amplitude and life (Dowling, 2013):

$$\varepsilon_a = \frac{\Delta\varepsilon}{2} = \frac{\Delta\varepsilon_e}{2} + \frac{\Delta\varepsilon_p}{2} = \frac{\sigma'_f}{E}\left(2N_f\right)^b + \varepsilon'_f\left(2N_f\right)^c \qquad 6.12$$

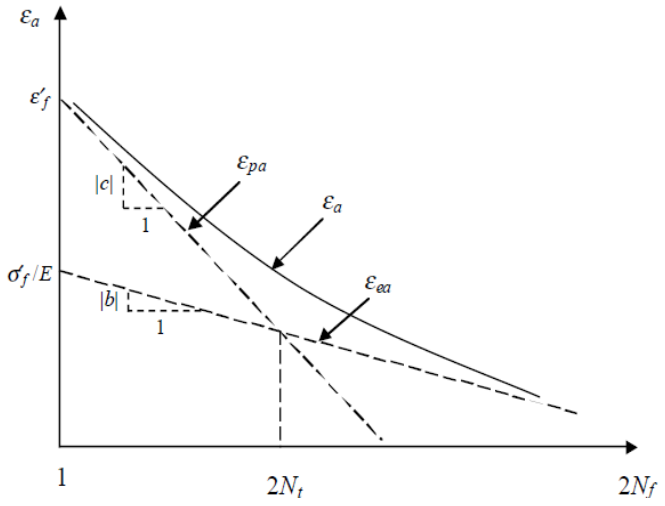

Figure 6.5 - Strain life relationship for LCF.

Secondly, the effective shear strain under the torsional loading can be expressed and separated into elastic and plastic parts:

$$\frac{\Delta\gamma}{2} = \frac{\Delta\gamma_e}{2} + \frac{\Delta\gamma_p}{2} \quad 6.13$$

$$\frac{\Delta\gamma_e}{2} = \frac{\tau'_f}{G}\left(2N_f\right)^{b_o} \quad 6.14$$

$$\frac{\Delta\gamma_p}{2} = \gamma'_f\left(2N_f\right)^{c_o} \quad 6.15$$

where τ'_f is the shear fatigue strength coefficient, b_o is the shear fatigue strength exponent, γ'_f is the shear fatigue ductility coefficient, and c_o is the shear fatigue ductility exponent. Combining the above two equation gives an equation relating the total strain, amplitude and life:

$$\frac{\Delta\gamma}{2} = \frac{\Delta\gamma_e}{2} + \frac{\Delta\gamma_p}{2} = \frac{\tau'_f}{G}\left(2N_f\right)^{b_o} + \gamma'_f\left(2N_f\right)^{c_o} \quad 6.16$$

6.3.2.2 Multiaxial Models based on critical plane

Although there is no universally completely accepted multiaxial fatigue criterion in order to carry out fatigue analysis, several models based on the critical plane approach have been developed for estimating fatigue life for components subjected to a complex loading. It has been commonly recognised that those models provide better approaches to predicting fatigue prediction. As stated previously, critical plane models are established on the physical interpretation of the fatigue progression where cracks can form and grow on the same critical planes (Fatemi A. et al., 2000).

The first trial model in this study by Fatemi and Socie (2000) is based on the critical plane concept. It is based on the strain-based approach method and is formulated on

the basis that shear stress dominates fatigue damage. The parameter calculated by Fatemi and Socie (2000) is

$$\frac{\Delta\gamma_{\max}}{2}\left(1+k\frac{\sigma_n^{\max}}{\sigma_\gamma}\right)=\frac{\tau'_f}{G}\left(2N_f\right)^{b_o}+\gamma'_f\left(2N_f\right)^{c_o} \qquad 6.17$$

Where $\frac{\Delta\gamma_{max}}{2}$ refers to the amplitude of shear strain on the critical plane, and σ_n^{max} refers to the maximum tensile stress which is normal to the critical plane. Parameter k is a material constant with the range, $0.6 < k < 1.0$.

The second trial model adopted is the Smith, Watson and Topper relationship based on the critical plane (SWT (cp)) which is a reasonable model for tensile stress dominated cracking (Dowling, 2013). This is based on the concept of a tensile crack where the crack is initiated in the direction of maximum normal stress amplitude and assumes that the fatigue life for any mean stress state depends on the product $\sigma_{max}\ \varepsilon_a$. Suppose $\sigma_m = 0$, $\sigma_{ar} = \sigma_{max}$ so, σ_{ar} and ε_{ar} are complete reversed stress and strain amplitudes, thus:

$$\sigma_{max}\ \varepsilon_a = \sigma_{ar}\ \varepsilon_{ar} \qquad 6.18$$

This model includes the mean stress effects and used to determine the fatigue life. It is expressed as follows (Dowling, 2013):

$$\sigma_{max}\varepsilon_a = \sigma'_f\left(2N_f\right)^b\left[\frac{\sigma'_f}{E}\left(2N_f\right)^b+\varepsilon'_f\left(2N_f\right)^c\right] \qquad 6.19$$

$$=\frac{\sigma'^2_f}{E}\left(2N_f\right)^{2b}+\sigma'_f\varepsilon'_f\left(2N_f\right)^{b+c}$$

Where $\sigma_{\max}$ the maximum normal is stress on the critical plane and ε_a is the amplitude of normal strain for the same plane as $\sigma_{\max}$.

The third trial model adopted is the Chu relationship which is a single multiaxial fatigue model combining both shear and normal components. This model was developed to consider different cracking behaviour. The model proposes that fatigue is predicted by the strain life relation of equation(Dowling, 2013, Chu C. C. et al., 1993):

$$2\tau_{max}\gamma_a + \sigma_{max}\varepsilon_a = f(N_f) \qquad 6.20$$

The first term in the fatigue parameter of the left hand side involves the shear strain amplitude, γ_a, and the maximum shear stress, τ_{max}. The second term in the fatigue parameter involves the maximum stress σ_{max} and the strain amplitude ε_a. This model can be thought of as generalization of the parameter of equation 6.19 (Dowling, 2013). The last trial model in this group is also based on the critical plane concept. LI J . et al. (2011) modified the SWT and CHEN X. et al. (1999)(CXH) model through considering the mean stress and include the different influence of the normal and shear components on fatigue life. It was generated to avoid the drawbacks of the SWT model and (CXH) model. This modification model can give satisfactory fatigue life prediction.

$$\sqrt{\left(\overline{\sigma_{max}}\,\frac{\overline{\Delta\varepsilon_{max}}}{2}\right)^2 + \left(\frac{\Delta\tau}{2}\frac{\Delta\gamma}{2}\right)^2} = \frac{\sigma_f'^{\,2}}{E}(2N_f)^{2b} + \sigma_f'^{\,2}\varepsilon_f'(2N_f)^{b+c} \qquad 6.21$$

The first term in the fatigue parameter of the left hand side involves $\overline{\sigma_{max}}$ and $\overline{\Delta\varepsilon_{max}}$ which are the maximum principal stress and the maximum principal strain range respectively. The second term, involves the shear stress range, $\Delta\tau$, and the shear strain range, $\Delta\gamma$, respectively.

6.3.2.3 Effective Stress Amplitude Approach

The stress-based approach is the second approach used in multiaxial cyclic stress calculations. It uses a nominal stress (average) instead of local stress and strain and

employs empirical modification and elastic stress concentration factors (Dowling, 2013). Consider mechanical components subjected to cyclic loads which are completely reversed. The effective stress amplitude can be computed in a similar way to the Von Mises yield criterion as follows (Dowling, 2013):

$$\bar{\sigma}_a = \frac{1}{\sqrt{2}}\sqrt{(\sigma_{1a}-\sigma_{2a})^2+(\sigma_{2a}-\sigma_{3a})^2+(\sigma_{3a}-\sigma_{1a})^2} \qquad 6.\ 22$$

Where σ_{ia} (i = 1, 2, 3) are the amplitudes of principal stresses. Also, the effective stress amplitude can be computed In terms of the amplitudes of the directional stress components,

$$\bar{\sigma}_a = \frac{1}{\sqrt{2}}\sqrt{(\sigma_{xa}-\sigma_{ya})^2+(\sigma_{ya}-\sigma_{za})^2+(\sigma_{za}-\sigma_{xa})^2+6(\tau_{xya}^2+\tau_{yza}^2+\tau_{zxa}^2)} \qquad 6.\ 23$$

If tensile or compressive loads are present those effects the effective stress amplitude such as the mean stress effect under uniaxial loading. One approach considers that the stable value of the hydrostatic stress is proportional to the control mean stress variable. Based on that, the effective mean stress can be calculated from three principal mean stresses or from the means of the stress components respectively as follows (Dowling, 2013):

$$\bar{\sigma}_m = \sigma_{1m}+\sigma_{2m}+\sigma_{3m} \qquad 6.\ 24$$

$$\bar{\sigma}_m = \sigma_{xm}+\sigma_{ym}+\sigma_{zm} \qquad 6.\ 25$$

An alternative form of the effective mean stress can be computed in a similar way to the Von Mises yield criterion as follows (Fatemi A. et al., 2000):

$$\bar{\sigma}_m = \frac{1}{\sqrt{2}}\sqrt{(\sigma_{1m}-\sigma_{2m})^2+(\sigma_{2m}-\sigma_{3m})^2+(\sigma_{3m}-\sigma_{1m})^2} \qquad 6.\ 26$$

The multiaxial stress situation can be transformed into an equivalent fully reversed uniaxial stress with a combined use of effective stresses and effective mean stress to provide another mean stress equation and can be written as (Dowling, 2013):

$$\sigma_{ar} = \frac{\sigma_a}{1 - \frac{\sigma_m}{\sigma_u}} \qquad 6.27$$

Generalization this equation 6.27 (Goodman eq.) to multiaxial fatigue then involves an equivalent fully reversed uniaxial cyclic stress lead to evaluate fatigue life under multiaxial cyclic stress involving nonzero mean stresses using Basquin equation. Also, the fatigue life can be calculated when the equivalent completely reversed uniaxial stress $\sigma_m = 0$, is used in the *S-N* curve by using the last equation 6.27 combined with the Basquin equation 6.1 as well to give the following equation(Suresh, 1998):

$$\sigma_{ar} = \sigma'_f \left(2N_f\right)^b \qquad 6.28$$

This approach is questionable if the normal and shear loading are not proportionate and this should be taken into consideration for any further work beyond the trial usage of the current thesis.

6.3.3 Variable Amplitude Fatigue

Taking into account the influence of mean stress and constant life diagrams, so, Different combinations of the mean stress and stress amplitude can be represented in terms of constant life diagrams such as in Figure 6.6.

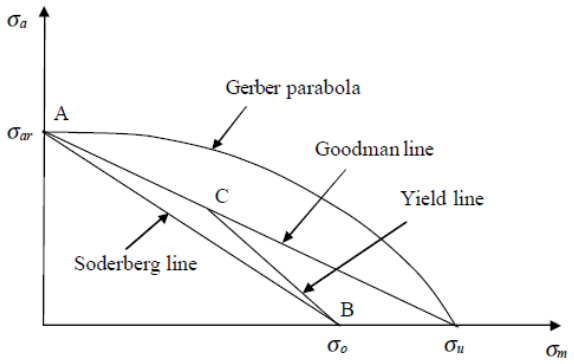

Figure 6.6 - Normalised amplitude mean diagram (Zahavi E. and Torbilo V., 1996).

Well-known models of this type are, the Gerber parabola relation, the Soderberg relation and the modified Goodman relation, respectively, with the following expressions (Dowling, 2013, Suresh S., 1998):

$$\frac{\sigma_a}{\sigma_{ar}} + \left(\frac{\sigma_m}{\sigma_u}\right)^2 = 1 \qquad 6.29$$

$$\frac{\sigma_a}{\sigma_{ar}} + \frac{\sigma_m}{\sigma_o} = 1 \qquad 6.30$$

$$\frac{\sigma_a}{\sigma_{ar}} + \frac{\sigma_m}{\sigma_u} = 1 \qquad 6.31$$

The main observations that can be made from the previously expressed equation models upon the effects of mean stress on fatigue life as follows:

- The Soderberg line is a completely conservative estimate of fatigue life.
- The Gerber curve is non-conservative and it incorrectly predicts the harmful effect of compressive mean stress, its use is therefore restricted to tensile stress cases.
- The Goodman curve can be intercepted by the yield line to give the two lines ACB and this is considered to be the most suitable relationship for design purposes (Zahavi E. and Torbilo V., 1996).

In an attempt to have a better fit to the central tendency of data and an approach to the conservative straight line that passes through the points $(\sigma_m, \sigma_a) = (\sigma_u, 0)$ and $(\sigma_m, \sigma_a) = (0, 1)$ when $\sigma_a = \sigma_{ar}$ Morrow proposed a modification of this straight line (Goodman line) by using either $\tilde{\sigma}_{f_b}$ or σ_f' rather than σ_u in equation 6.31 as follows (Dowling ,2013):

$$\frac{\sigma_a}{\sigma_{ar}} + \frac{\sigma_m}{\sigma_f'} = 1 \qquad 6.32$$

$$\frac{\sigma_a}{\sigma_{ar}} + \frac{\sigma_m}{\tilde{\sigma}_{f_b}} = 1 \qquad 6.33$$

Here the constant of σ_f' can be obtained from the un-notched axial *S-N* curve for fully reversed loading and the corrected true fracture strength $\tilde{\sigma}_{f_b}$ can be calculated from a tension test (Dowling, 2013). Another relation proposed by Smith, Watson and Topper (SWT) does not rely on the material constant as in the Morrow equation and it represents good fit data for aluminum alloys and the proper choice for normal use, the relation is:

$$\sigma_{ar} = \sqrt{\sigma_{\max}\sigma_a}, \ (\sigma_{\max} > 0) \qquad 6.34$$

$$\sigma_{ar} = \sigma_{\max}\sqrt{\frac{1-R}{2}}, \ (\sigma_{\max} > 0) \qquad 6.35$$

Where $\sigma_{max} = \sigma_a + \sigma_m$, $R = \frac{\sigma_{min}}{\sigma_{max}}$ this criteria predicts that no damage will take place when $\sigma_{max} < 0.0$. The final expression is proposed by Walker and uses a material constant γ and can be considered analogous to the SWT relation if the value of γ=0.5. The relation has two forms as follows:

$$\sigma_{ar} = \sigma_a^{\gamma}\ \sigma_{\max}^{1-\gamma}, \quad (\sigma_{\max} > 0) \qquad 6.36$$

$$\sigma_{ar} = \sigma_{\max}\left(\frac{1-R}{2}\right)^{\gamma}, \ (\sigma_{\max} > 0) \qquad 6.37$$

The data for steel is analysed and gives the following expression based on ultimate tensile strength where σ_u in MPa:

$$\gamma = -0.0002\sigma_u + 0.8818 \qquad 6.38$$

The prediction of fatigue life can be calculated for the previous models either on a fully reversed state where the mean stress effect is zero stress using the Basquin equation (6.1), or by using a common stress life equation that can be applied in non-fully reversed stress $\sigma_m \neq 0$ as follows:

$$\sigma_a = \left(\sigma'_f - \sigma_m\right)\left(2N_f\right)^b \qquad 6.39$$

6.4 Numerical procedure for damage calculation

The procedure given in this section is carried out numerically with the FORTRAN programming language. This allows the procedure to be applied quickly and gives the opportunity to apply several models and investigate the influence of all the model parameters on material deformation and fatigue life. Its basic format was created by the Cardiff tribology group and it has been modified significantly in this research to satisfy the new requirements of the investigation. These include: incorporating residual stress; introducing more fatigue models identified from the literature as being potentially useful in application to the compressive loading events that arise from asperity interactions in the EHL regime; and investigating ten significant points and isolating their effective loading cycles and corresponding contribution to the accumulated damage to rank cycles according to damage. This numerical procedure is appropriate for multiaxial fatigue life estimations of an engineering component subjected to variable amplitude loading and is implemented in the analysis software.

The investigations of the models based on the critical plane approach apply to rectangular trial blocks of material whose dimensions are taken to be $2a$ parallel to the surface and a perpendicular to the surface as shown in Figure 6.7. The evaluation of any particular fatigue model involves using the stress history for the block as it passes through the EHL contact zone so that the fatigue evaluated corresponds to one rolling contact cycle of the surface material, and one meshing cycle for the material in gear contacts.

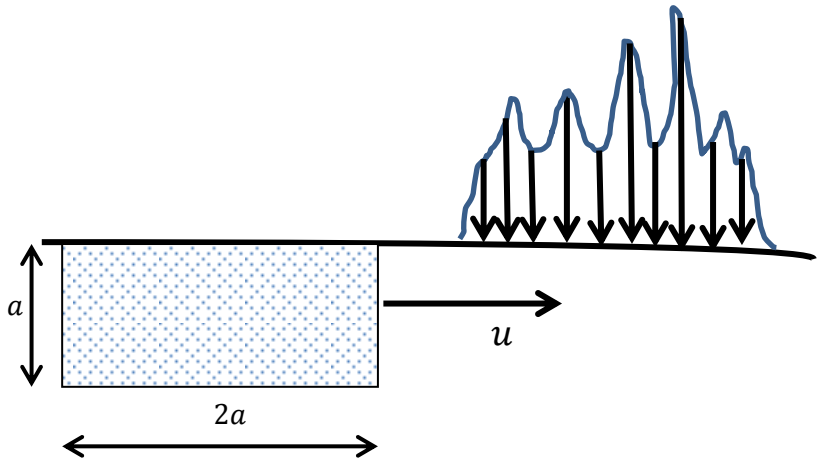

Figure 6.7 - Block of material left and solid surface considered.

The block of material is subdivided with a rectangular mesh of mesh of 201x24 points. The spacing is uniform parallel to the surface and non-uniform perpendicular to the surface. The spacing perpendicular to the surface has no bearing on the accuracy of the stress components calculated, which is determined by the EHL mesh spacing, but rather it specifies the points in a coordinate system (x', z') , fixed in the block, where the stress components are evaluated. A non-uniform grid is used normal to the surface to ensure a fine resolution near the surface where stress variations are rapid (i.e large stress changes with small positional changes) with a coarsening of the resolution with increasing depth as the stress variation becomes gentler. The procedures go through the following steps:

1. Carry out a stress analysis for all the evaluation points in the material block considered for all time steps in the mixed Elastohydrodynamic lubrication (EHL) analysis of the surface as the block progresses through the contact zone.

2. Sort the stress analysis results by position to give the time variation of stress at each evaluation point in turn. Stages (1) and (2) are time consuming and so the result of stage (2) is stored so that it can be used for subsequent stages with any fatigue model without recalculation.

3. For each evaluation point in turn use the stress component history to calculate the strain history by using Hook's law as follows :

$$\varepsilon_x = \frac{1}{E}\left\{\left(1-\nu^2\right)\sigma_x - \nu\left(1+\nu\right)\sigma_z\right\} \quad 6.40$$

$$\varepsilon_z = \frac{1}{E}\left\{\left(1-\nu^2\right)\sigma_z - \nu\left(1+\nu\right)\sigma_z\right\} \quad 6.41$$

$$\gamma_{xz} = \frac{\tau_{xz}}{G} = \frac{2\left(1+\nu\right)}{E}\tau_{xz} \quad 6.42$$

4. Consider a candidate plane (the critical plane is not known) which is defined by θ which is the angle between the normal of the plane and the x-axis. Calculate normal and shear stress, and in the same way calculate normal and shear strain respectively as follows:

$$\sigma = \sigma_x \cos^2\theta + \sigma_z \sin^2\theta + 2\tau_{xz}\sin\theta\cos\theta \quad 6.43$$

$$\tau = \tau_{xz}\left(\cos^2\theta - \sin^2\theta\right) + \left(\sigma_z - \sigma_x\right)\sin\theta\cos\theta \quad 6.44$$

$$\varepsilon = \varepsilon_x \cos^2\theta + \varepsilon_z \sin^2\theta + \gamma_{xz}\sin\theta\cos\theta \quad 6.45$$

$$\frac{\gamma}{2} = \frac{\gamma_{xz}}{2}\left(\cos^2\theta - \sin^2\theta\right) + \left(\varepsilon_z - \varepsilon_x\right)\sin\theta\cos\theta \quad 6.46$$

5. Refine the stress histories of the candidate plane and subdivide the stress history at each point in the material into a series of effective loading cycles using the rainflow method developed by Amzallag C. et al. (1994) to count

cycles and determine the effective loading cycles contained in the loading history. Find the corresponding stress level for each effective loading cycle.

6. At each cycle from step 5 on the candidate plane, determine the shear strain amplitude γ_a ,normal strain amplitude ε_a ,and the maximum normal stress σ_n as follows:

$$\gamma_a = \frac{\left|\gamma_{\max} - \gamma_{\min}\right|}{2} \quad 6.47$$

$$\varepsilon_a = \frac{\left|\varepsilon_{\max} - \varepsilon_{\min}\right|}{2} \quad 6.48$$

Where γ_{max}, ε_{max} , γ_{min} and ε_{min} are the extreme values for the cycle, and

$$\sigma_n^{\max} = \max_{\substack{\text{effective} \\ \text{loading} \\ \text{cycle}}} \sigma(t) \quad 6.49$$

7. At each cycle identified in step 5 by closed hysteresis loops in the stress-strain response, and after extracting the parameters in step 6, calculate the model's parameter such as Fatemi and Socie's shear damage parameters $F.B$ as follows:

$$F.B = \frac{\Delta\gamma_{\boldsymbol{max}}}{2}\left(1 + k\frac{\sigma_n^{\boldsymbol{max}}}{\sigma_y}\right) \quad 6.50$$

8. Solve for fatigue life N_f as per the shear model (Fatemi and Socie's example) for the current cycle of strain from Equation (6.17). The bisection method is used to solve the above equation, and then the fatigue damage associated with the current cycle will be determined on the kth candidate plane as per the shear damage models:

$$damag_{\,cycle} = \frac{1}{N_f} \quad 6.51$$

The Palmgren – Miner damage accumulation rule equation 6.51 is used to accumulate the damage for each effective loading cycle to give a measure of the damage experienced by material over the loading sequence:

$$D = \Sigma_{\substack{all\ effective\ loading\ cycles}} \frac{1}{N_f} = \Sigma_{i=1}^{n} \frac{1}{N_i} \qquad 6.52$$

This is the damage value for the current candidate plane where the value of *D* equal to unity then corresponds to fatigue failure. The process is repeated from step 4 for each candidate plane orientation in the range $0 < \theta < 180^0$, (1^0, one degree increments of θ are used in the current study). The damage value for the evaluation point is the maximum value of D obtained, and the critical plane is the plane which has this maximum value D.

9. To evaluate the fatigue damage of the component blocks the fatigue analysis steps (1-8) are repeated for each evaluation point in the material. So that the value of D and the orientation of the critical plane is established over the material block considered at all mesh points. The maximum damage $D_{\max}$ and the orientation of the critical plane can then be determined.

10. Finally determine the fatigue life of the component blocks as:

$$N_f = \frac{1}{D_{max}} \qquad 6.53$$

Note that according to (5) the effective cycles determined on each candidate plane depend only on the stress and strain history at that point for that plane. However, the critical plane is determined according to the fatigue model being applied as per (7&8).

The damage value varies over the material and its variation can be illustrated as a contour plot. The analyses reported in this chapter were carried out on a rough surface profile obtained from a previous study by the Cardiff tribology group. The rough surface profile was run against itself in a transient EHL analysis so that comparisons could be made between the same portions of roughness profile as shown in Figure 6.8.

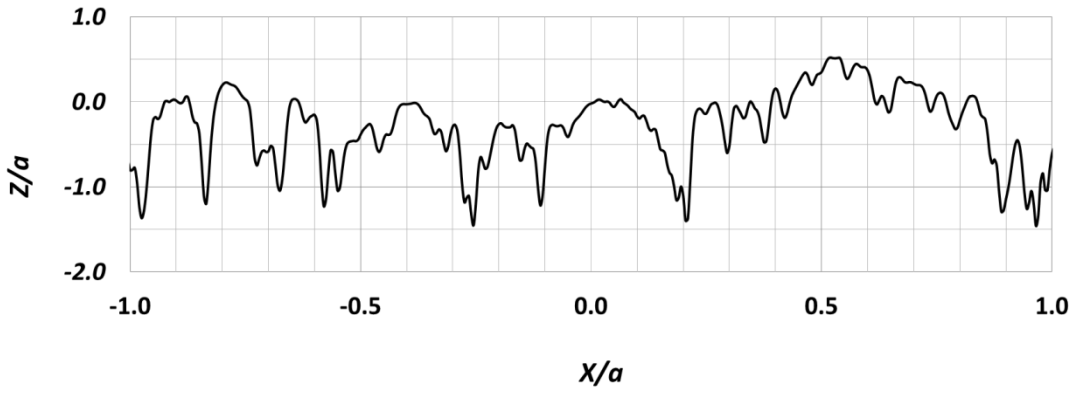

Figure 6.8 - Surface profiles for the material blocks used for the analyses.

6.5 Fatigue analysis_ applying the strain based approach

6.5.1 Introduction

The discussion up to this point has dealt with the basic theory of fatigue due to either uniaxial cyclic stress or multiaxial stress. However, research in this section deals with the analysis of fatigue damage and the factors that affect the fatigue behaviour occurring near the contact surface, in the mixed lubrication regime when the load support is a mixture of fluid film pressure and boundary lubrication. The Fatemi and Socie model was used as an illustrative example in section 6.4 to explain the calculation of accumulative damage for fatigue analysis. Its basis is now discussed and

results of its use for analysis presented. Following that, the results will be discussed for the other models.

6.5.2 Fatemi and Socie's fatigue model

Fatemi and Socie's fatigue model is based on the observation that cyclic shear drives the crack nucleation and small crack growth process. It is an example of the strain-life model that is used to establish the damage associated with each effective loading cycle. The criteria is based on the hypothesis that the fatigue will occur according to its parameters' influence that are shown in Equation (6.17), which are a combination of a normal direct stress and shear strain and based on the concept explained in section 6.2.4. The analysis for this model includes consideration of the influence of changing the value of a material constant in the Fatemi and Socie model, and other parameters such as and yield strength σ_y and hardness HP. Figure 6.8 compares the damage contours obtained for the slower moving surface using the Fatemi and Socie Fatigue Parameter with different values of the material constant, *k*, varying between zero and unity. In general, fatigue failure zones are coloured red when $D \geq 10^{-6}$ in the contours plots. *D* is the value of damage corresponding to a single passage of the trial material through the EHL contact zone. A value of $D = 10^{-6}$ thus corresponds to fatigue occurring in 10^6 repetitions of the loading experienced, i.e. 10^6 rotations of the test disk, or 10^6 meshing cycles of the gear if a gear roughness profile is being assessed. Figure 6.9(a) has k=0 so that the normal stress has no effect and in this case the model responds only to the shear strain amplitude. It is clear that the damage levels are highest in the case where k=0 and there is a progressive reduction as *k* is increased. Failure zones corresponding to particular damage levels, e.g. 10^{-6} becomes

bigger and increase as the value of k is decreased. Since increasing k increases the effect of the normal stress it is clear that the value of σ_n^{max} is negative (compressive) in the high damage zones so that the factor $1+k\frac{\sigma_n^{\max}}{\sigma_y}$ is reduced as *k* is increased. So the fatigue damage is affected by the changing value of k and the critical plane orientation also changes for different k values. On different planes, the effective loading cycles could be different with different values of k . However, the rainflow method gives the same cycles whatever the value of k and this feature may merit further investigation.

In figure 6.9 $\sigma_n^{\max}$ is normalised by the yield stress σ_y. It might be felt that normalising with respect to hardness approximated by $3\sigma_y$ would be more appropriate in contact problems. The effect of this change in normalisation is shown in figure 6.10 and as might be anticipated from the discussion of figure 6.9 this reduces the calculated damage for any given value of parameter k. In the fatigue model has an extreme effect and the damage appears to be more extensive where the asperity can be expected to have more loading cycles, and potentially experience higher damage value. This is confirmed by the data in the Tables (AA.1-AA.10) as shown in Appendix AA-2.

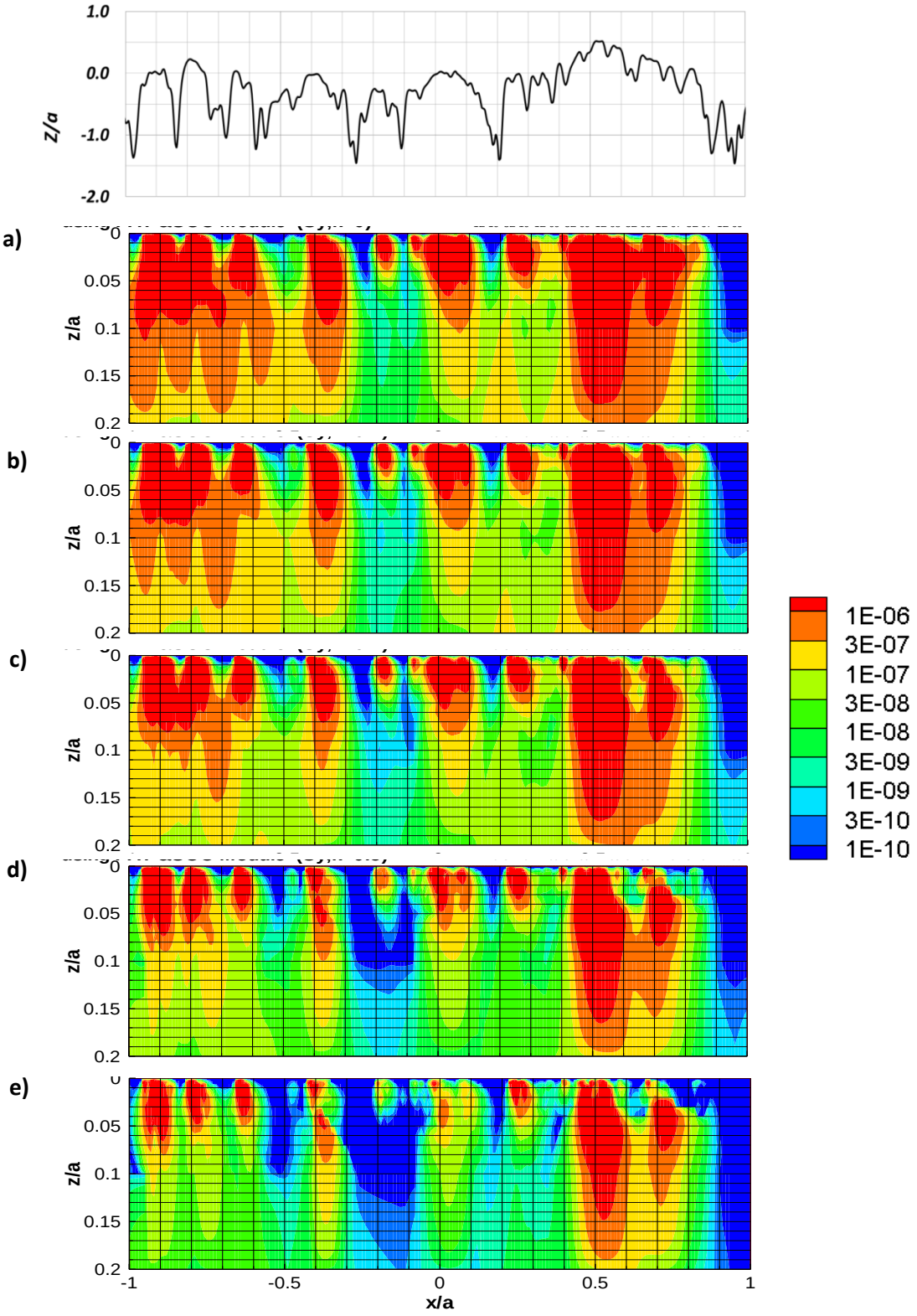

Figure 6.9 - Contours of Accumulated Damage based on the Fatemi and Socie fatigue model with σ_n^{max} normalised with σ_y; $(a)(k = 0.0)$, (b)$(k = 0.1)$, (c)$(k = 0.2)$, (d)$(k = 0.5)$, (e)$(k = 1.0)$.

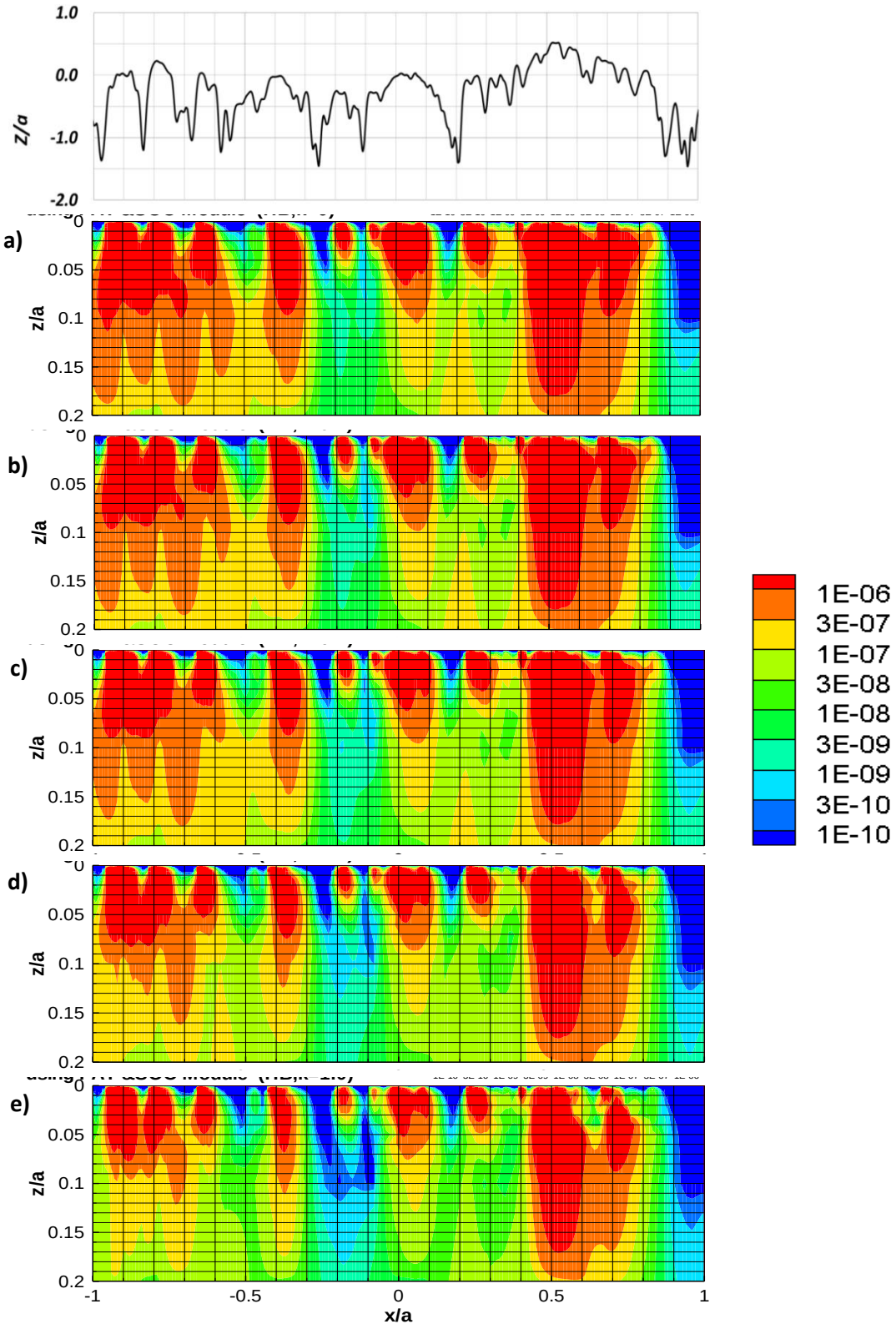

Figure 6.10 - Contours of Accumulated Damage based on the Fatemi and Socie fatigue model with σ_n^{max} normalised with HB; $(a)(k = 0.0)$, (b)$(k = 0.1)$, (c)$(k = 0.2)$, (d)$(k = 0.5)$, (e)$(k = 1.0)$.

As shown in appendix AA-2 the Tables AA.1-AA.5 were using σ_y in the normalisation calculation and Tables AA.6-AA.10 using the value of HB (Hardness) in the normalisation calculation. They illustrate numerically the effective loading cycles which have $D \geq 10^{-19}$. The cycles in the tables are sorted by the maximum damage values. The damage values show changes as the k values are changed. The critical plane orientations are shown in the tables and they also change with the different values of k. It is clear from the data that the fatigue damage is controlled by shear strain and is decreased by the value of negative normal stress (compressive) which increases the friction at the crack surfaces. Also it is noticed from all the tables that the majority of the damage was contributed by no more than two or three cycles.

6.5.3 Further multiaxial fatigue criteria based on critical plane

As explained in section 6.4, fatigue analysis is conducted on the contacting materials of dimension $2a \times a$ passing through the contact zone, where a is the Hertzian semi-contact width. In this section, three other multiaxial fatigue criteria based on critical plane are considered and corresponding fatigue analyses are carried out for them for the EHL line contact of rough surfaces. These are the Chu criterion, the Smith, Watson and Topper SWT(cp) criterion and Smith, Watson, Topper modified criterion (SWTM).The influence of roughness on calculated fatigue damage is investigated for the numerical results of all the models as illustrated consequently.

Figures 6.11 shows the contours of accumulated damage based on the Chu fatigue model whose strain life relationship is given in equation 6.20. It can be seen that high levels of damage are generated near the surface at positions corresponding to load bearing prominent asperity features. This is illustrated in the figure where the surface

roughness profile is seen in the upper part and the fatigue damage contours are in the lower part. The red double headed arrows added to the roughness profile figure correspond to the x boundaries of the closed highest contour pools. They can be seen to correspond in position to particular asperities in the rough surface profile. However, there are aggressively shaped asperities within the profile of roughness that have low damage values which indicate and evidence that loading is not wholly dependent on the shape of an individual asperity. This is probably survived to the loading stage at which the profile information was taken without being modified by plastic deformation because their prominent neighbours have protected them from heavy encounters with counter face asperities.

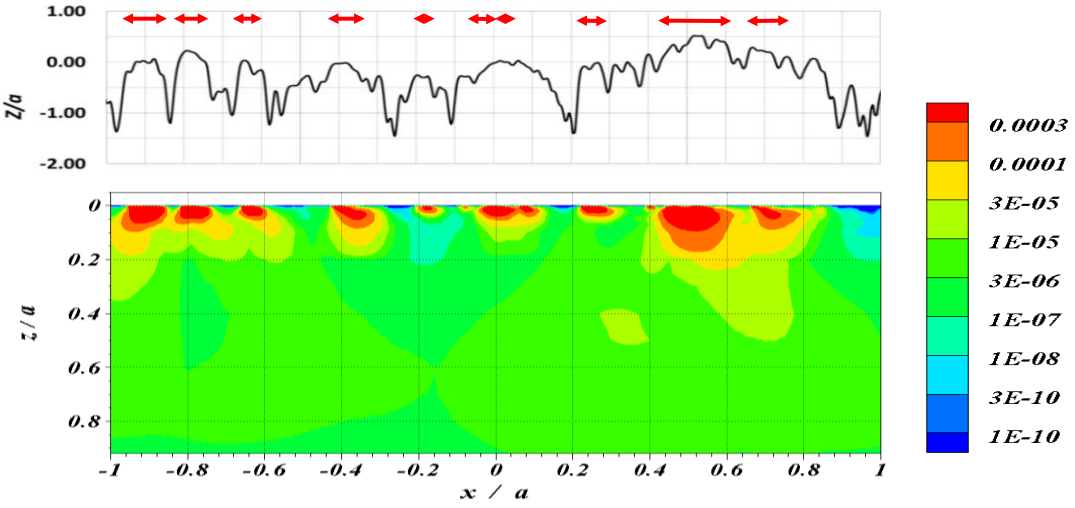

Figure 6.11 - Contours of Accumulated Damage based on the Chu fatigue model together with the surface roughness profile for the test block analysed.

The maximum values of calculated damage occurring in figure 6.11 exceed unity which indicates that fatigue is calculated to occur at those points during the first pass through the contact. This is clearly unrealistic and it is therefore likely that this model is not appropriate for the kind of loading experienced by the asperity material in an EHL contact. The value of damage calculated with the Chu model can be seen to be much higher than that for the Fatemi and Socie model shown in figure 6.12, as can be

seen by comparing the keys for figures 6.11 and 6.12 which have highest contour values of 3×10^{-4} and 10^{-6}, respectively. Figure 6.12 makes the same comparison between roughness profile and damage contour for the Fatemi and Socie model results where the damage contour plot for k = 0.5 taken from figure 6.9(d) is combined with the roughness profile. For the load experienced in an EHL contact the normal stress is protective in that the critical plane is found to have a compressive normal stress. This is shown in Figure 6.9 where the largest calculated damage occurs when k = 0, i.e. when the normal stress is not admitted to the calculation. This means that the direct stress normal to the identified critical plane is compressive so that it reduces the value of the LHS of equation 6.17, and hence the calculated damage. The value of k = 0.5 chosen for the analysis presented here is just below the range suggested by Fatemi and Socie as appropriate for general engineering applications. Again the red double headed arrows correspond to x boundaries of the highest value closed contours. They are identical in number to those in figure 6.11 indicating that high damage is associated with the same asperity features for both models but there are significantly differences in the highest contour values and depth.

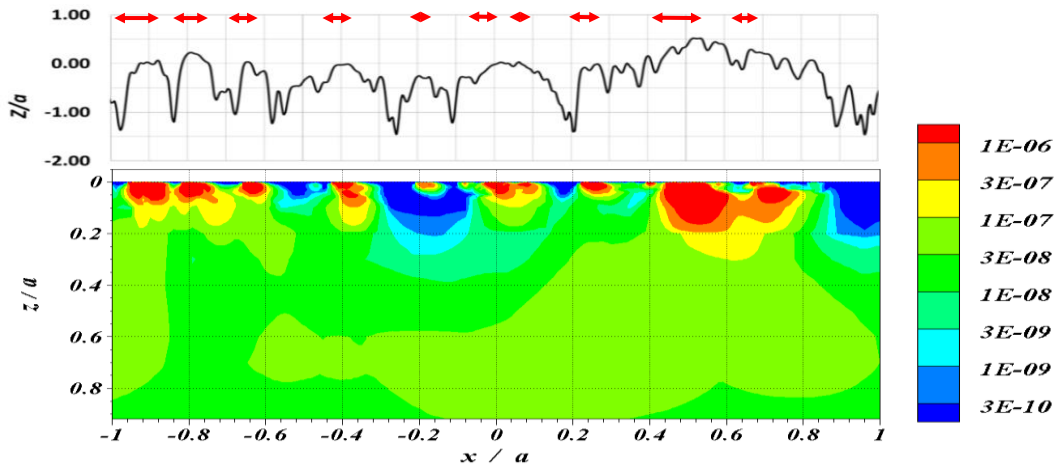

Figure 6.12 - Contours of Accumulated Damage based on the Fatemi and Socie fatigue model together with the surface roughness profile for the test block analysed.

Figure 6.13 shows the contours of accumulated damage based on the SWTM fatigue model whose strain life relationship is given in equation 6.21. The contour levels selected are the same as those for the Chu model in figure 6.11. It can be seen that the double headed arrows are considerably shorter than those for the Chu model and several have disappeared completely. The highest damage levels with this model occur very close to the surface. Comparing figures 6.11 and 6.13 it is clear that there is considerable difference between the highest fatigue damage zones that associated with the same asperity features but the red double headed arrows are associated with the most same asperity features for both previous models.

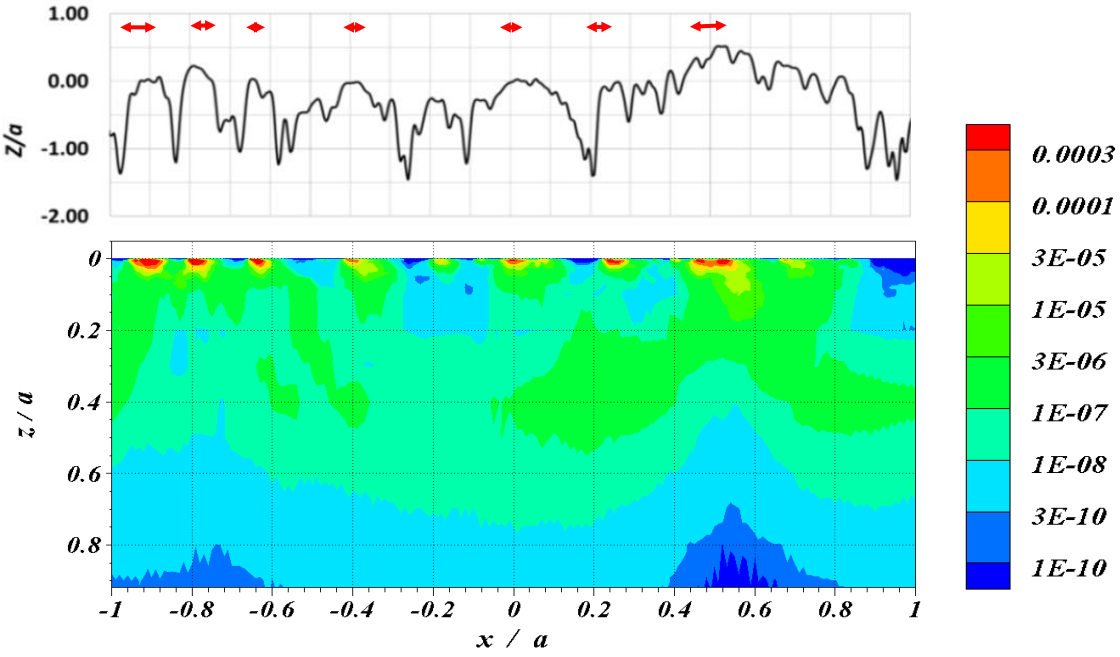

Figure 6.13 - Contours of Accumulated Damage based on the Smith, Watson, and Topper modified criteria (SWTM) model together with the surface roughness profile for the test block analysed.

The last criterion to be considered in this section based on the critical plane approach is that proposed by Smith, Watson and Topper SWT(cp) whose strain life relationship is given in Equation 6.19. The damage contours obtained for the SWT(cp) model are

shown in Figure 6.14 and can be seen to be very different to the other models presented in this section. The highest damage value obtained in this case is of the order 10^{-10}, and occurs at the actual surface of the material. The damage calculated by this criterion is very small unless a small proportion of the top surface experiences damage due to tensile stress. So this model which is expressed by equation 6.19 is exempt from the models which will be used to study the effect of residual stress in Chapter 7.

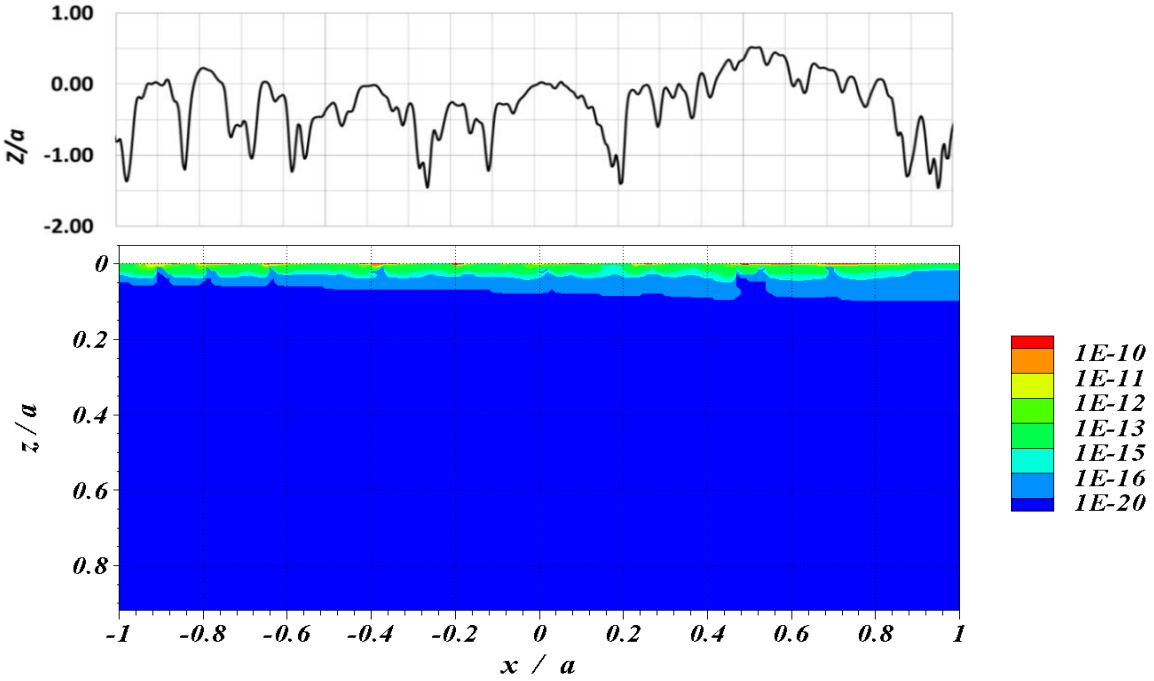

Figure 6.14 - Contours of Accumulated Damage based on the Smith, Watson and Topper (SWT) model together with the surface roughness profile for the test block analysed.

Comparison of the SWT(cp) and SWTM models makes it is clear that inclusion of the shear stress and shear strain in the fatigue criterion makes a very significant difference to the way in which the loading is assessed from a fatigue perspective. It seems that the SWT(cp) approach will not see any likelihood of fatigue in material subjected to the predominantly compressive asperity loading associated with mixed lubrication. Comparison of the Chu and SWTM models gives similar damage levels but with more

concentrated peak values for the SWTM case. The SWTM model has a hybrid nature in that the normal stress/strain enters into consideration in terms of the principal stress and strain, which does not vary with the plane considered so that the critical plane is determined by the shear stress and shear strain ranges. Chu's model in contrast has an attractive symmetry in the way that normal and shear stresses enter into the model.

6.6 Fatigue Analyses – Applying Variable Amplitude Multiaxial Fatigue theories

For the micro or mixed lubrication problem, the stress history shows that severe stress cycling with variable amplitude occurs in the material during the traverse of the contact area, especially close to the surface. For positions in the trial material block that experience high levels of damage, analysis of the actual cycles resulting from the rainflow counting method shows that there is usually one cycle that contributes the majority of the damage with no more than three other cycles as will be shown in section 6.7 that make a significant contribution to the damage suffered during transit of the EHL contact zone. This observation suggests that it may be worthwhile to study the effect of mean stress which is a substantial influence on fatigue behaviour. Compressive mean stress is beneficial and tensile mean stress is detrimental as far as fatigue is concerned. Decrease in fatigue life can be expected to occur when the detrimental tensile stress is part of the cyclic stress history.

This section presents variable amplitude multiaxial fatigue damage estimation models. These models deal with mean stress effects, but are not based on a critical plane approach. The models have been considered from a theoretical standpoint in section 6.3.3 and numerical simulations are now carried out and results are presented for line contact of rough surfaces. The models have been classified into three groups. The first group involves the Goodman and Morrow models which are expressed in Equations 6.31 and 6.32 respectively in section 6.3.3. Figures 6.15 and 6.16 show the contours of accumulated damage based on Goodman and Morrow respectively. They that have the same mean feature that matching the prominent asperities. However, the Goodman criterion is more conservative than that of Morrow in calculating damage. This can be seen when the comparison is made between the red zone located in Figure 6.15 at x/a =-0.85, x/a =-0.75 , at x/a =-0.45, x/a =-0.30 , at x/a =0.40, x/a = 0.60, and at x/a =0.6, x/a = 0.80 for the Goodman model and the same plastic zones for the Morrow model in Figure 6.16 .

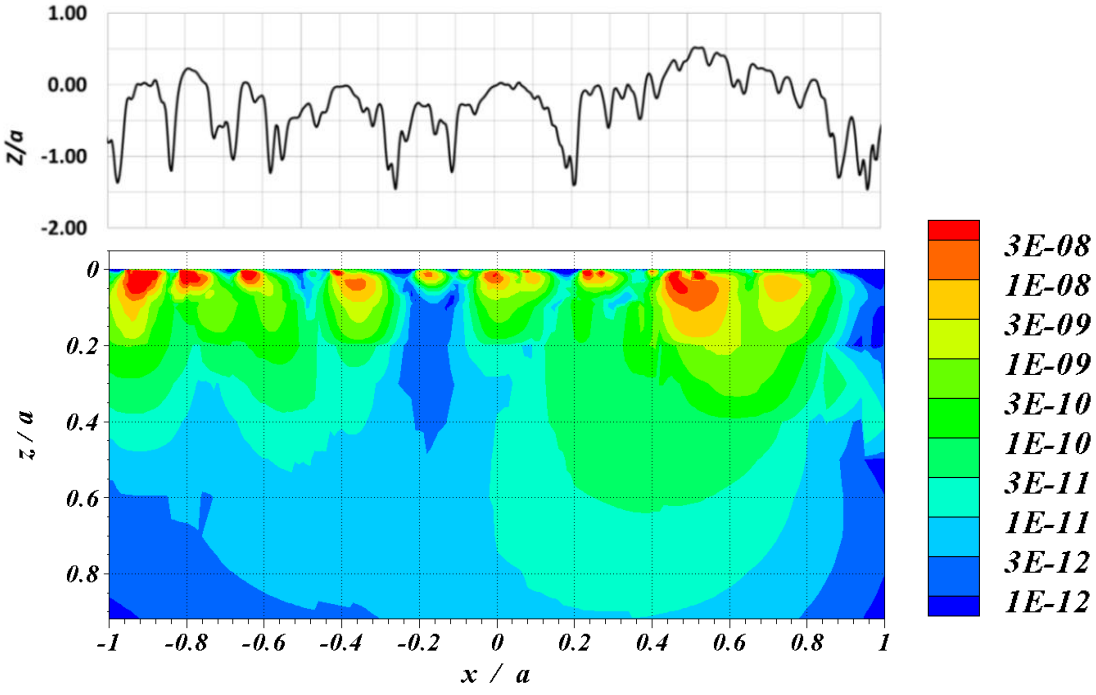

Figure 6.15 - Contours of Accumulated Damage based on Goodman model.

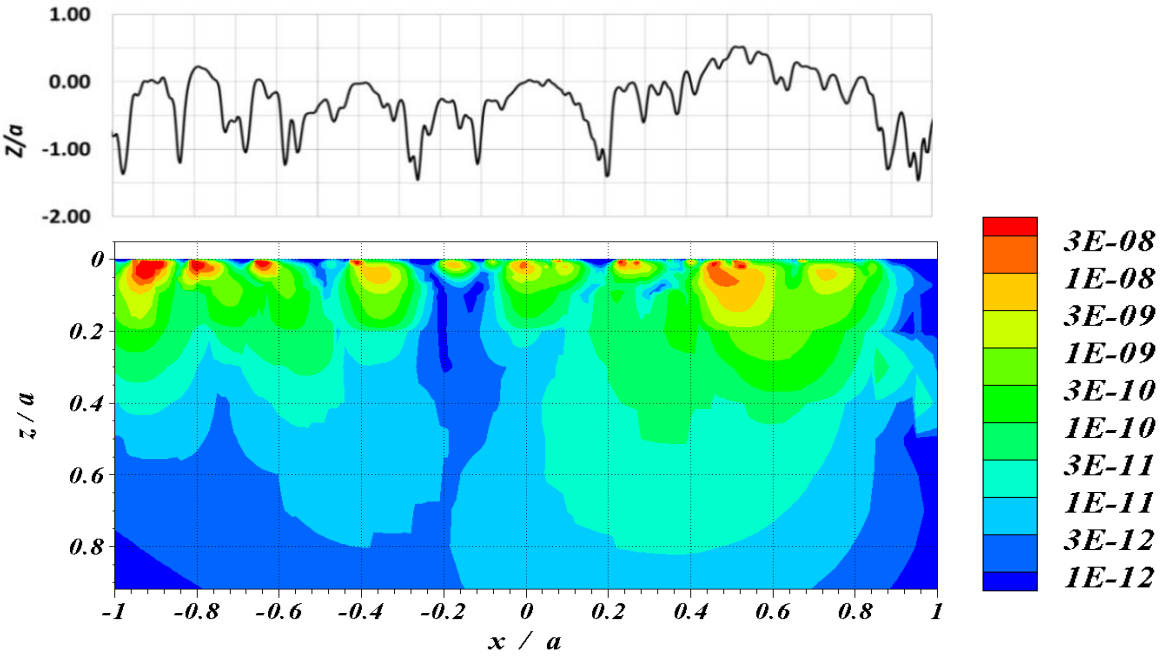

Figure 6.16 - Contours of Accumulated Damage based on Morrow Model.

The second group involves a further two models, the Walker model, and the Smith, Watson and Topper model (SWT) which are expressed theoretically in section 6.3.3. To avoid confusion, the SWT model presented in section 6.3.3 and Equation 6.34 is different to the SWT(cp) model discussed in section 6.3.2.2 and Equation 6.19 in that the section 6.3.3 model and Equation 6.34 is not based on the critical plane. Figure 6.17 and Figure 6.18 represent contours of accumulated damage based on these two models. In spite of the contours of damage being obtained for the same section of material of $2a \times a$ within the slower surface and under the same EHL operating conditions, the two models draw very different conclusions for the material based on the same stress history as can be seen from figures 6.17 and 6.18. These models do not associate high fatigue levels with surface roughness features on the scale of asperities and so it is clear that they are not an appropriate choice for a model of the micropitting which supposes that it is a fatigue process.

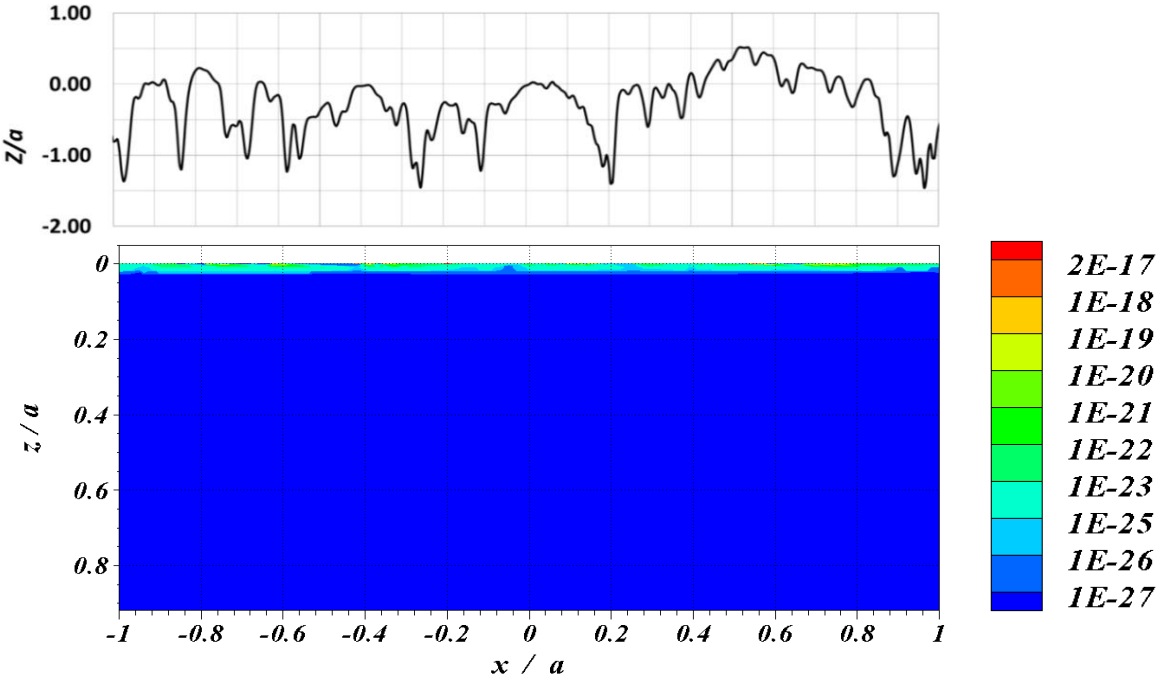

Figure 6.17 - Contours of Accumulated Damage based on Walker model.

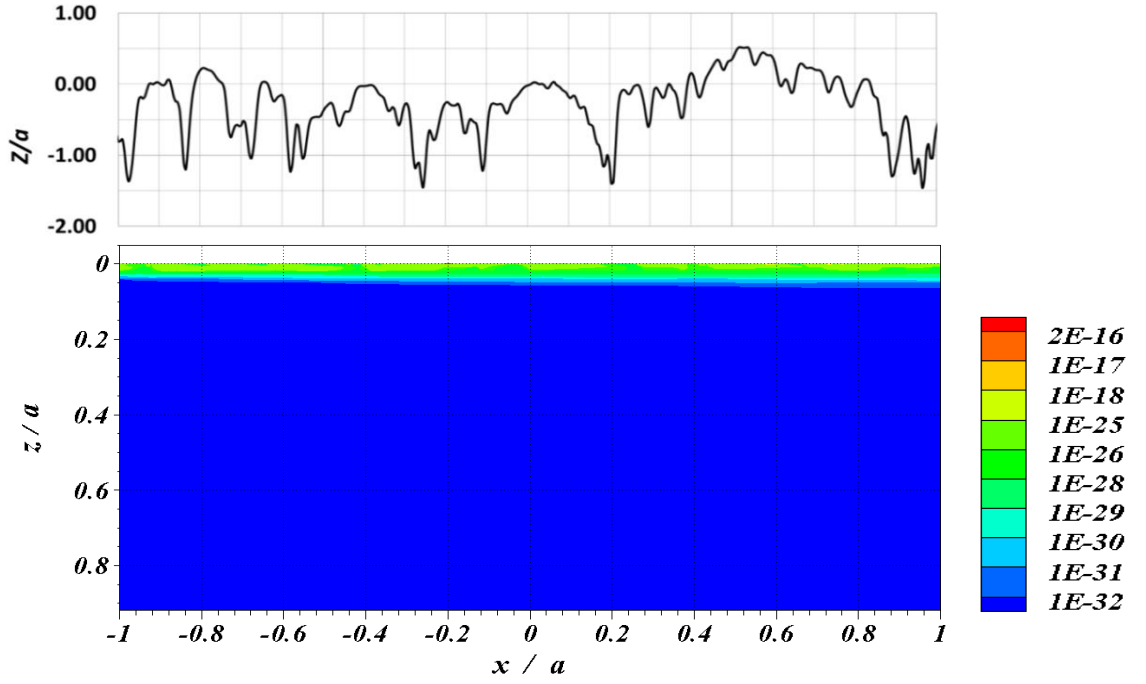

Figure 6.18 - Contours of Accumulated Damage based on the Smith, Watson and Topper (SWT) model.

Finally, the third group involves one criterion which is effective stress amplitude (Von Mises) expressed in equation 6.22. As for the previous groups, Figure 6.19 demonstrates the contours of fatigue damage obtained for the slower moving rough

surface at the same distance. It can be seen in Figure 6.19 that the islands of high damage (red zone) values calculated are separated by areas that are not subject to anything like the same level of damage and the accumulated damage calculated is localised near the surface of specific asperity features. Several prominent asperities are subject to greater damage levels such as those located in Figure 6.19 in between x/a=-0.95 and x/a=-0.85, x/a=-0.85 and x/a=-0.70, x/a=0.40 and x/a=0.60. This observation is in good agreement with the results obtained from the critical plane models and with Goodman equation 6.31 due to the reasons that were explained in section 6.3.2.3.

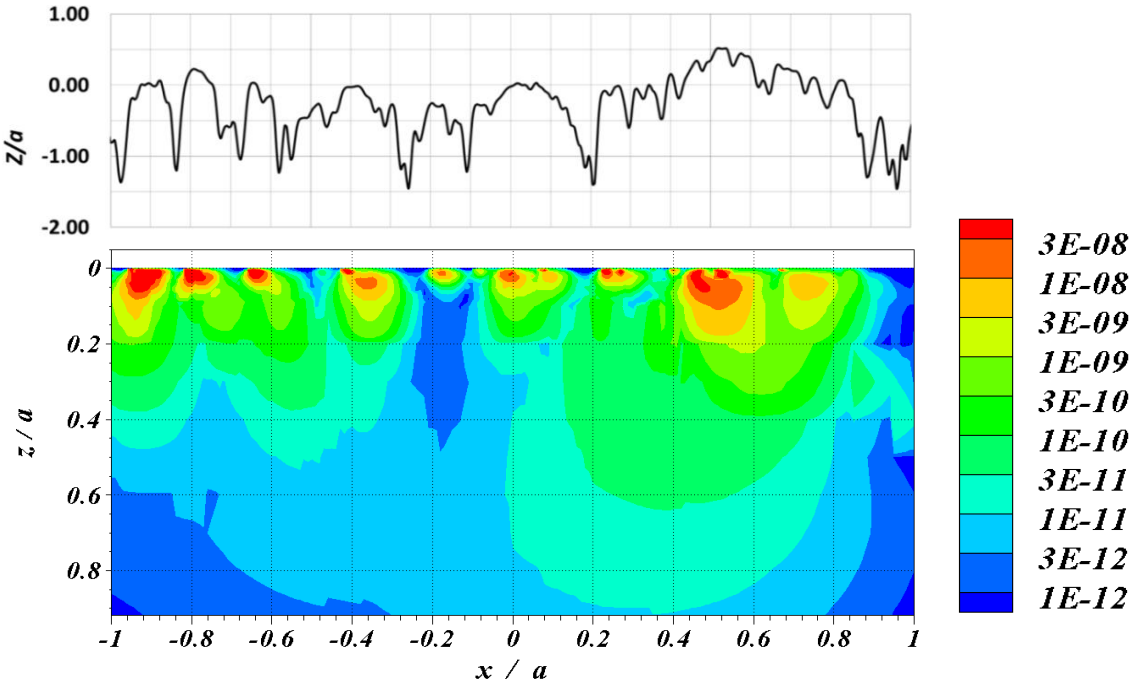

Figure 6.19 - Contours of Accumulated Damage based on effective stress amplitude (Von Mises) model.

6.7 Further numerical analysis for all models

A study was conducted to evaluate the loading cycles arising from the rainflow cycle counting method for the damage accumulation analyses carried out for the test material block in its passage through the EHL contact zone. Points in the test material

subject to the highest values of calculated damage were selected for this analysis. For each point analysed in this way, the cycles identified by the rainflow method were tabulated in terms of the start and end points in the stress history and the damage calculated. To illustrate the approach, the analysis for the Fatemi and Socie fatigue model is presented. Table 6.1 shows the results obtained for the point(-0.92*a*, -0.006*a*) in the test block which was found to have the greatest value of the calculated damage. There are 40 effective cycles identified by the rainflow method and the values tabulated are the cycle index, the start and end stress field of the cycle, the calculated damage and the model parameters, γ_a, $\sigma_n^{\max}/\sigma_y$, and *F.B*. The maximum value of damage obtained for a cycle is 1.29×10^{-4} for cycle 40. Only the 12 cycles with the highest damage values are tabulated. The number of cycles contributing to the overall damage is small.

Table 6.1 - Cycle Fatigue Parameter obtained by using the Fatemi and Socie critical plane model with *k* =1.0 at point (-0.92*a*, 0.006*a*).

Index	*Cycle start*	*Cycle End*	D_{cycle}	γ_a	$\sigma_n^{\max}/\sigma_y$	*F.B*
18	***123***	***125***	***1.86E-08***	***3.58E-03***	***-2.17E-01***	***2.80E-03***
20	***131***	***136***	***5.39E-07***	***7.12E-03***	***-4.54E-01***	***3.88E-03***
22	***149***	***152***	***3.05E-09***	***4.86E-03***	***-5.12E-01***	***2.37E-03***
23	***145***	***155***	***3.89E-07***	***5.38E-03***	***-3.02E-01***	***3.76E-03***
24	***130***	***139***	***4.24E-05***	***8.66E-03***	***-1.98E-01***	***6.94E-03***
28	***168***	***170***	***1.17E-18***	***3.59E-04***	***-8.26E-02***	***3.29E-04***
29	***181***	***183***	***1.19E-19***	***3.13E-04***	***-1.47E-01***	***2.67E-04***
31	***195***	***196***	***1.10E-16***	***5.89E-04***	***-1.55E-01***	***4.98E-04***
32	***188***	***192***	***1.60E-09***	***2.54E-03***	***-1.19E-01***	***2.23E-03***
38	***203***	***205***	***1.35E-19***	***2.84E-04***	***-4.71E-02***	***2.70E-04***
39	***186***	***199***	***5.54E-07***	***4.40E-03***	***-1.14E-01***	***3.90E-03***
40	***120***	***159***	***1.29E-04***	***9.18E-03***	***-4.24E-02***	***8.79E-03***

The Total damage at the point considered equals== 1.7312 $\times 10^{-4}$ and it is illustrative to rank the tabulated cycles in terms of the cycle damage value which is shown in Table 6.2. The accumulated damage obtained for such this point represents the maximum value of D obtained at nth plane (critical plane) by adding the damage values for these cycles. These methods have been explained in section 6.4 at fatigue analysis step 8. Also it was noticed there is one cycle that contributes the majority of the damage with only two or three other cycles making a discernible contribution.

Table 6.2- Cycle Fatigue Parameter values of Table (6.1) ranked by cycle damage.

Index	Cycle start	Cycle End	D_{cycle}	γ_a	σ_n^{max}/σ_y	F.B
40	120	159	1.29E-04	9.18E-03	-4.24E-02	8.79E-03
24	130	139	4.24E-05	8.66E-03	-1.98E-01	6.94E-03
39	186	199	5.54E-07	4.40E-03	-1.14E-01	3.90E-03
20	131	136	5.39E-07	7.12E-03	-4.54E-01	3.88E-03
23	145	155	3.89E-07	5.38E-03	-3.02E-01	3.76E-03
18	123	125	1.86E-08	3.58E-03	-2.17E-01	2.80E-03
22	149	152	3.05E-09	4.86E-03	-5.12E-01	2.37E-03
32	188	192	1.60E-09	2.54E-03	-1.19E-01	2.23E-03
31	195	196	1.10E-16	5.89E-04	-1.55E-01	4.98E-04
28	168	170	1.17E-18	3.59E-04	-8.26E-02	3.29E-04
38	203	205	1.35E-19	2.84E-04	-4.71E-02	2.70E-04
29	181	183	1.19E-19	3.13E-04	-1.47E-01	2.67E-04

Figure 6.20 illustrates the cycles identified by the rainflow method. The tabulated numbers are the stress history fields that form the limits of a cycle and the cycles are indicated by curly brackets. There are three levels of cycles. The first levels of cycles (on the left) have no cycles contained between their cycles limits. The second level of cycles have one or more first level cycles contained between their cycle limits, and the third level of cycles have one or more second level cycles contained between their cycle limits. In this example there are 8 first level cycles, three second level cycles and

one third level cycle. The highest ranked cycles are labelled with the cycle index and the rank order. It can be seen that the third order cycle is the 1st ranked cycle, two second level cycles are the 2nd and 3rd ranked cycles and a first level cycle is the 4th ranked cycle.

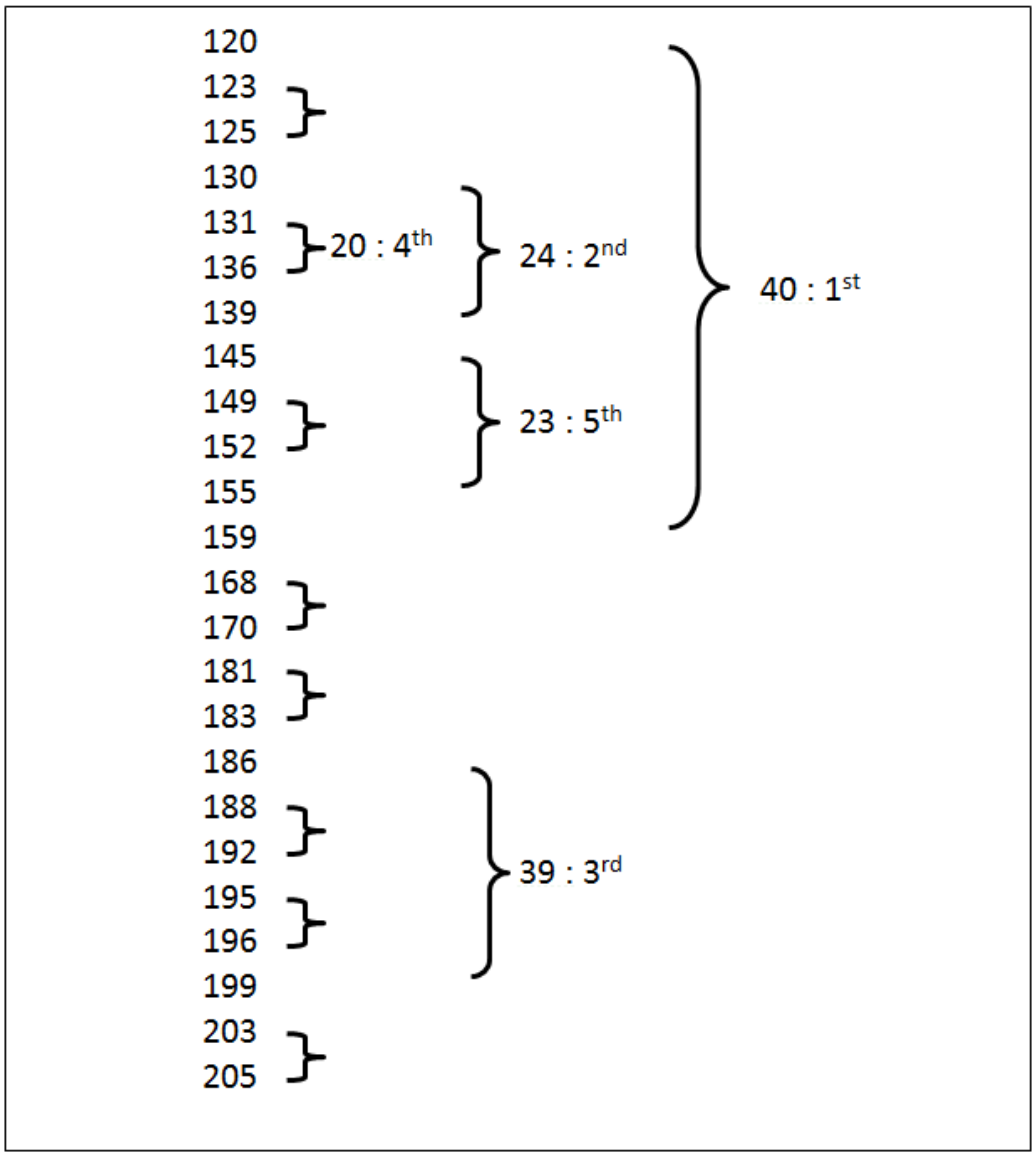

Figure 6.20 - Cycle Limits for Fatigue Parameter values of Table (6.2).

Table 6.3 shows the five points at which the greatest level of damage was calculated for each of the models applied in cumulative damage form. Each point occupies two

cells in the table. The upper of these gives the co-ordinates of the point in the form (x/a, z/a) with a letter labelling the point in the range A to W (note that I and O are not used as labels for clarity). The lower cell gives the value of damage calculated for the point. Points A to E are the maximum damage points for the Fatemi and Socie model. Points A to E are four of the five identified points for the Chu model, although the rank order is different, and three of the five points for the Smith Watson Topper modified model. The % difference between these points was calculated for each model in the form $100\times(D_{max}\text{-}D_{min})/D_{max}$ so that large values indicate that the point with the highest damage is an isolated extreme, whereas low percentage differences correspond to similar values of peak damage at different asperities. The five points for the Chu model have damage values that vary by 22%, and those for the SWTM model vary by 30%, whereas the points for the Fatemi and Socie model vary by 42%. Point C is the only common point between the five von Mises model points and the Fatemi and Socie points, and points G and H appears in the SWTM set of points, while points A, D and E are the common points between the five Fatemi and Socie, Chu and SWTM points. The Von Mises, Goodman and Morrow models identify the same five points, and do so with the same rank order. One of these points is C which is common with several of the previously discussed models. The five points for the Marrow model have damage values that vary by 49%, whereas the points for the Von Mises and Goodman model have the same range that vary by 52% due the same reasons which have been explained at section 6.3.2.3 . These six models all identify points that are close to the surface, but not at the surface as those that experience the greatest amount of damage. The remaining three models, SWT, SWT(CP) and Walker, all identify surface points as those subject to most damage and these points are not seen as heavily

damaged by any of other models. This group of models are similar and respond to normal stress and strain only with no influence of shear behaviour. They are not likely to have much relevance in the mixed lubrication situation and will not be considered further in this thesis.

Table 6.3 - A summary for the five material points assessed as having the greatest damage by the models considered.

Model	Rank 1	Rank 2	Rank 3	Rank 4	Rank 5
F&S	(-0.92,0.006) A	(-0.90,0.01) B	(-0.92,0.01) C	(-0.92,0.004) D	(-0.91,0.006) E
	0.1731×10^{-3}	0.1672×10^{-3}	0.1655×10^{-3}	0.1285×10^{-3}	0.1011×10^{-3}
Chu	(-0.92,0.01) C	(-0.91,0.01) F	(-0.92,0.006) A	(-0.91,0.006) E	(-0.92,0.004) D
	0.1159×10^{-1}	0.1146×10^{-1}	0.1123×10^{-1}	0.9631×10^{-2}	0.9115×10^{-2}
SWTM	(-0.92,0.004) D	(-0.91,0.006) E	(-0.92,0.002) G	(-0.64,0.004) H	(-0.92,0.006) A
	0.3936×10^{-2}	0.3194×10^{-2}	0.2832×10^{-2}	0.2795×10^{-2}	0.2768×10^{-2}
Von Mises	(-0.92,0.02) K	(-0.92,0.01) C	(-0.64,0.01) J	(-0.93,0.02) M	(-0.92,0.03) L
	1.04E-06	1.02E-06	6.92E-07	5.59E-07	4.98E-07
Goodman	(-0.92,0.02) K	(-0.92,0.01) C	(-0.64,0.01) J	(-0.93,0.02) M	(-0.92,0.03) L
	1.04E-06	1.02E-06	6.92E-07	5.59E-07	4.98E-07
Morrow	(-0.92,0.02) k	(-0.92,0.01) C	(-0.64,0.01) J	(-0.93,0.02) M	(-0.92,0.03) L
	4.39E-07	3.89E-07	2.84E-07	2.52E-07	2.26E-07
SWT (CP)	(0.55,0.0) N	(0.51,0.0) P	(0.53,0.0) Q	(0.54, 0.0) R	(-0.2, 0.0) T
	0.3313×10^{-7}	0.2982×10^{-7}	0.2752×10^{-7}	0.1760×10^{-7}	0.1549×10^{-7}
SWT	(-0.20,0.0) T	(-0.42,0.0) U	(0.55,0.0) N	(-0.38, 0.001) V	(-0.39, 0.0) S
	0.1172×10^{-14}	0.1373×10^{-16}	0.4433×10^{-17}	0.1054×10^{-17}	0.4739×10^{-18}
Walker	(-0.20,0.0) T	(0.55,0.0) N	(-0.42,0.0) U	(-0.38,0.001) V	(-0.35, 0.0) W
	0.7120×10^{-15}	0.3539×10^{-16}	0.5731×10^{-17}	0.2458×10^{-17}	0.1369×10^{-17}

6.8 Conclusion

This chapter presents a review of an introduction to the fundamentals fatigue theories that are used in fatigue analysis and their application to rolling contact fatigue in mixed EHL line contact is studied. The models are all applied in a varying amplitude multi-

axial fatigue context. The theory for this was discussed and applied numerically to the contact and the accumulated damage in a single pass through the contact area was evaluated. The EHL stress history can be used as the basis for calculation of the fatigue damage that occurs at the scale of the asperity features. The available fatigue programme was developed to identify high damage points on or near the surface, and sort the points by damage value. That enables the most highly damaged locations to be examined in detail. The models that responded to normal stress, strain and to the influence of shear behaviour, F&S, Chu, SWTM, Goodman, Marrow and VM as shown in the Table 6.4 will be used in chapter 7 to calculate fatigue damage and predicted fatigue lives after adding residual stress. However, the remaining three models (SWT, SWT (CP) and Walker as shown in the Table 6.4 are not likely to have much relevance in the mixed lubrication situation and will not be considered further in this thesis.

Table 6.4 - A summary for the Multiaxial fatigue models response for fatigue calculation based on EHL stress history and residual stresses.

	Fatigue models names	Response for fatigue calculation	Response for residual stress effects calculation
1	Chu	✓	✓
2	Fatemi and Socie	✓	✓
3	SWT (cp)	×	×
4	SWTM	✓	✓
5	Goodman	✓	Weak in responding
6	Marrow	✓	Weak in responding
7	Walker	×	×
8	SWT	×	×
9	Von Mises	✓	Weak in responding

Chapter 7

Fatigue comparison with and without Residual Stress

7.1 Introduction

Nowadays, an analysis of the influence of residual stresses on material fatigue and in fatigue design calculation is considered to be of the highest importance as explained in the literature review in Chapter 2. Residual stress distributions extracted from the FEA in the simulated contact body are considered in this chapter and used as the residual stress for the contacting components in evaluating the stress history under EHL condition. A simulated model based on the elastic plastic contact analysis explained in Chapter 4 was used to determine the residual stresses for a range of applied loads. The FEA values of residual stresses are calculated numerically by employing a plane strain deformation analysis model. Subsequently, a number of fatigue criteria as illustrated and discussed in Chapter 6 were used. This chapter starts with using these multiaxial fatigue criteria to carry out fatigue analyses both with and without the residual stresses. The fatigue calculation is carried out with residual stresses incorporated in three forms: firstly, by adding arbitrary constant residual stress to the EHL stress history profile; secondly, by adding a selected FEA asperity residual stress field based on research into asperities of similar in size to selected asperities in a rough surface used in an EHL analysis to determine the stress history; and finally, by calculating the fatigue damage with the residual stress evaluated by contact analysis of the actual profile used in the EHL analysis. Comparisons of the calculated residual stresses and the deformed profiles with corresponding measured experimental deformed profile

values allow the analysis model and thereby the effect of residual stress on the fatigue life calculations to be evaluated and investigated.

7.2 Fatigue analysis with artificial residual stresses

The residual stress used in this section is an artificial residual stress, which is added to the asperities at specific levels to see its effect on calculated fatigue damage and fatigue life. This was in the form of a positive value of σ_{zz} that varied with the depth from 0.3GPa to 1.0GPa as tabulated in Table 7.1 and shown in the Figure 7.1 (Evans, 2015). It can be seen that the high artificial tensile residual stress values are added near the running surface from $z/a = 0.0$ to $z/a = 0.001$ to represent the influence of the effects resulting from the pressure at the interface which is accompanied by radial direct stress at the surface which reaches a maximum value at the edge of the asperity contact. The added values of artificial residual stress are gradually decreased as they move down from the surface whereas the maximum shear stress in Hertzian contacts occurs below the surface of the contact bodies and occurs below the centre of the contact at a depth of between about half and three quarters of the smaller contact dimension.

Table 7.1 - Residual stress added to the asperities at specific levels$(\mathbf{a = 0.335\ mm})$ (Evans,2015).

Depth (z/a)	Stress σ_{zz} (MPa)
0	1000
0.001	800
0.002	300
0.01	400
0.02	800
0.03	400
$\frac{z}{a} > 0.03$	0.00

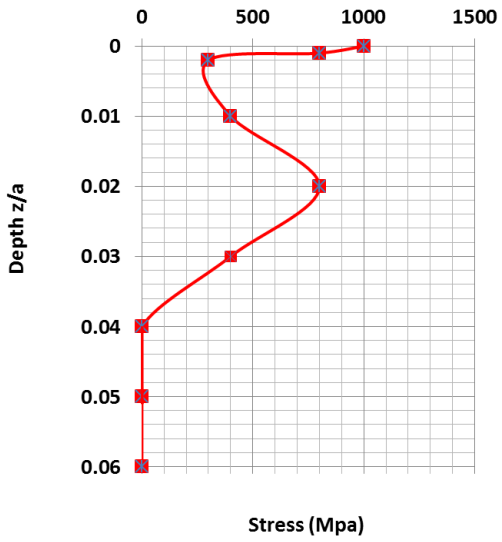

Figure 7.1- Residual stress of σ_{zz} MPa added to the asperities at specific Levels where a = 0.335 mm.

For the fatigue analysis, the Fatemi and Socie model was used in this application as an illustrative example of other models and for the reasons given in Chapter 6. This is an example of a strain-life model that is used to establish the damage associated with each effective loading cycle and whose strain life relationship is given in Equation 6.17. Figure 7.2(a) shows the EHL profile C which was used in the analysis while Figure 7.2(b) shows the damage contours obtained without including the artificial residual stress, and all the fatigue damage in the red zones can be seen to be associated with the prominent asperities. Figure 7.2(c) shows the corresponding result when the artificial residual stress is included. The damage in the red zones can be seen to become bigger in the area that is located across the whole profile to a depth of $z/a = 0.03$ due to adding the residual stress. This shows that a tensile residual stress as shown in figure 7.1 makes a significant difference to the material stress history under EHL contact conditions when the fatigue damage is calculated. The residual stress field associated with asperity plastic deformation is of course, more complex than this artificial one, but it is worth noting that the stress history at a material point depends on the residual

stress at that point only and the EHL surface pressure and shear stress does not depend on the residual stress field.

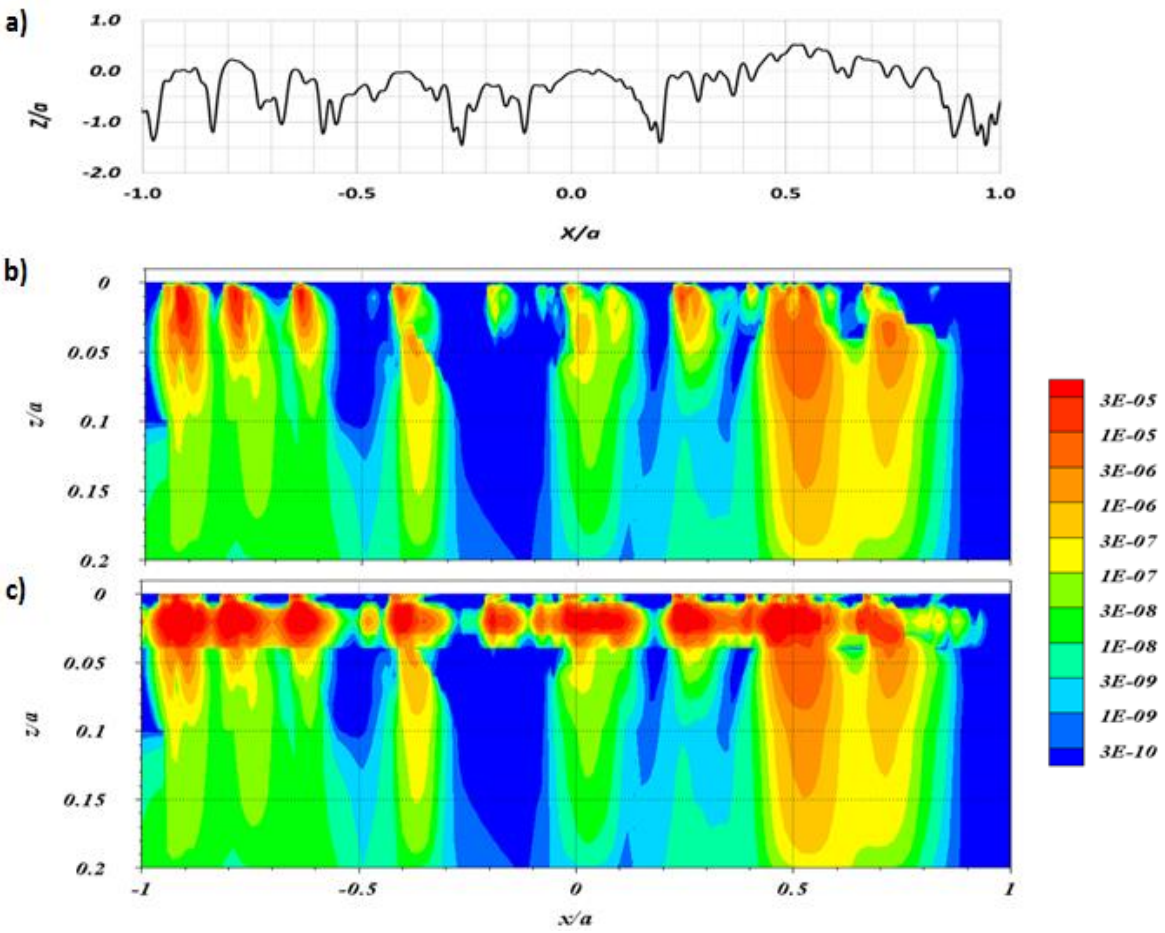

Figure 7.2 – Fatemi and Socie model contours of fatigue damage; a) EHL profile C , b) fatigue damage contours without residual stress , c) fatigue damage contours with artificial residual stress given in Figure 7.1 .

7.3 Fatigue analysis with certain asperity residual stresses applied to a similar asperity

Plans to conduct EHL analyses using the measured surface roughness profiles were frustrated for same time by unexpected factors beyond the author's control, and as a result an intermediate approach to provide a more realistic residual stress field had to be developed based on a measured roughness profile from a previous experimental program for which EHL analyses were available. The unrun profile was not available

however, and could not be measured. Consequently an approach based on the shape of the residual major asperity features was developed and used. The residual stress used in this section was the residual stress extracted from the FEA in a simulated elastic plastic contact of a body with a plane rigid body for several asperities as explained in Section 5.3.2 and then it was added to the EHL stress histories for approximately similar asperities for the different profile for which a detailed transient EHL analysis was available. The analysis of this application was achieved in three steps as follows:

7.3.1 The determination of asperity features

In order to compare between differently shaped asperities experiencing different residual deflections, the calculation of the asperity dimensions is based on four parameters of the residual shape of the asperity which is shown in Figure 7.3 and defined in Table7.2. The residual asperities tend to have a curved load bearing land in between steep valley feature sides. These lands were identified in terms of their width, w and heights, h, by identifying the points where the residual tip shape intersected the valley sides.

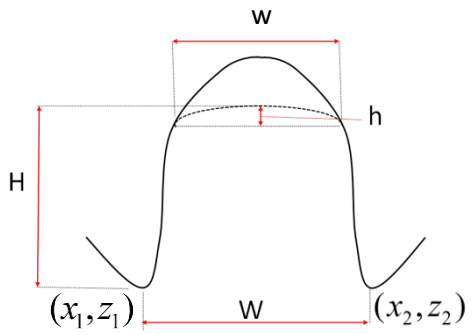

Figure 7.3 - Initial and residual asperity shape parameters.

Table 7.2 - The definition of the residual asperity main parameter.

Asperity Parameters label	Definition of parameters
H	Maximum residual height of the asperity.
h	Height of residual asperity land.
W	The Maximum land width for asperity taken from deep valley to deep valley.
w	Width of residual asperity land.

The parameters H, h, W and w of the asperity calculated feature was for all profiles asperities that indicated by red arrows in figure 7.4 these values are tabulated in Tables 7.4-6 for comparison purposes. Tables 7.4 and 7.5 show the asperity identification numbers and the four parameter dimensions of the selected asperities in the second stage post loading profiles A and B respectively. These asperities are considered to see which ones could be taken to have the same dimensions as candidate asperities of running profile C as given in Table 7.5. Tables 7.4 and 7.5 are structured so as to aid choosing the best asperity which can match one of the candidate EHL profile C asperities. The best match of parameters is used to select the asperity from the contact analyses that has a similar configuration to the profile C asperity so that the corresponding residual stress field may be assumed for the fatigue analysis. For simplicity, the application of the analysis of asperity determination and the three profiles that have been used in the analysis will be referred to in the text formula such as asperity number, profile name and the asperity number of EHL profile C in letter form. One example is 2AA, asperity two located in profile A is used with the asperity of EHL profile C denoted A. Another example is 21BC which means asperity twenty one located in the profile B is used with the asperity of EHL profile C denoted C, etc. The significant asperities of profiles A and B are numbered as shown in Figure 5.4.

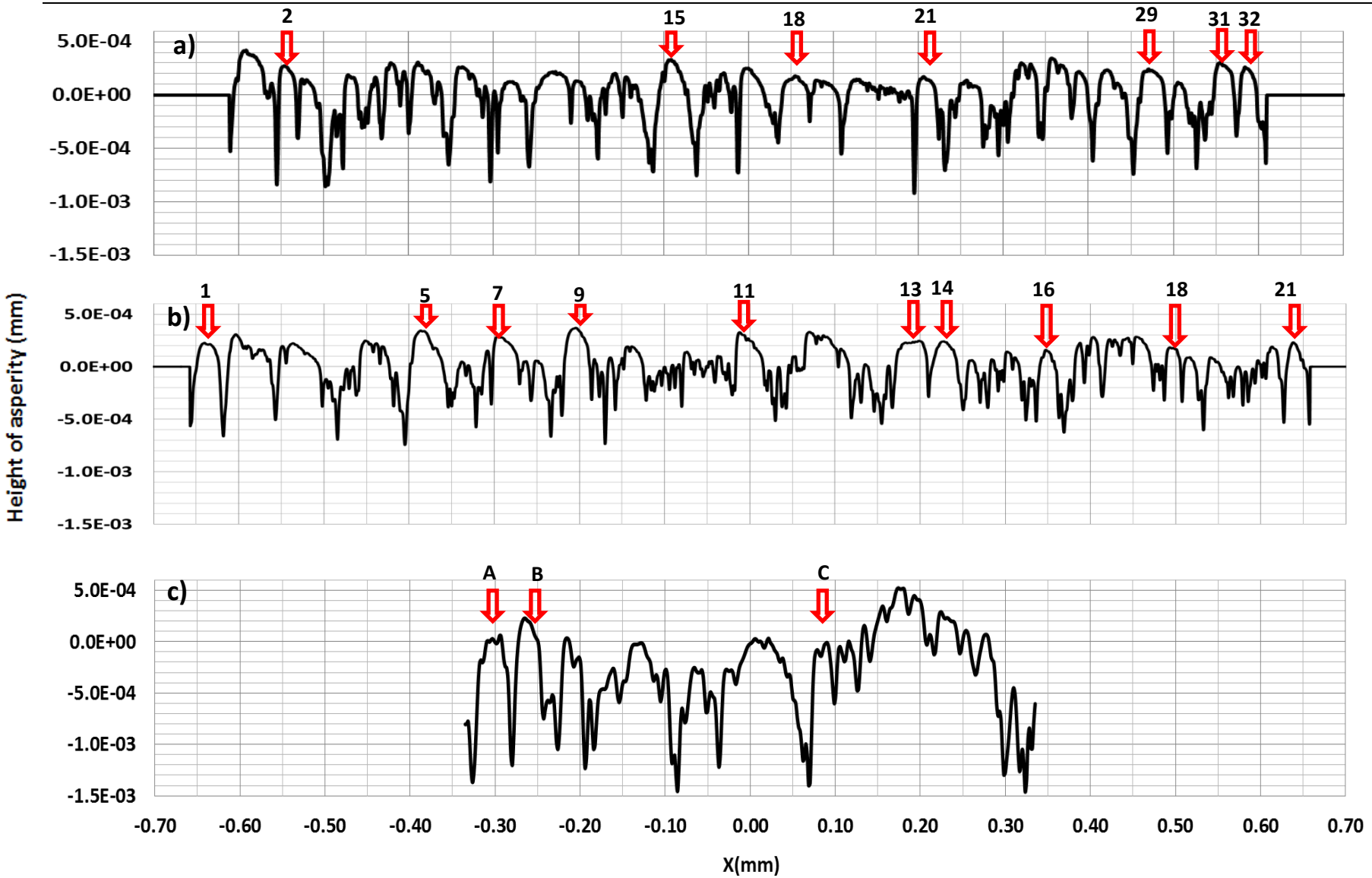

Figure 7.4 – Second stage for the profiles; a) profile A (1.2mm), b) Profile B (1.3mm long), c) EHL profile C.

Table 7.3 - The dimension parameters for the selected asperities of profile A.

Asperity name FOR Profile A	*Dimension in µm for the asperities*			
	H	*W*	w	h
2	0.914	19.4	12.9	0.086
15	1.100	40.9	10.8	0.057
18	0.629	30.0	21.5	0.086
21	1.000	30.1	17.2	0.085
29	0.942	30.0	17.2	0.071
31	0.743	30.0	17.2	0.129
32	0.657	29.2	12.9	*0.086*

Table 7.4 - The dimension parameters for the selected asperities of profile B.

Asperity name FOR Profile A	*Dimension in µm for the asperities*			
	H	*W*	w	h
1	0.829	34.3	22.9	0.086
5	1.030	45.7	34.3	0.229
7	0.686	42.9	22.9	0.057
9	0.486	34.3	20.0	0.086
11	0.686	34.3	28.6	0.229
13	0.743	40.0	28.6	0.057
14	0.743	45.7	25.7	0.186
16	0.743	31.4	20.0	0.143
18	0.514	20.0	20.0	0.086
21	0.800	28.6	17.1	0.186

Table 7.5 - The dimension parameters for the selected asperities of EHL profile C.

Asperity name	***The Dimension in µm for the candidate asperities***			
	H	***W***	**w**	**h**
A	**1.31**	**45.8**	**35.9**	**0.276**
B	**1.17**	**35.9**	**22.9**	**0.207**
C	**0.896**	**32.6**	**19.6**	**0.207**

Table 7.6 shows the asperities whose FEA residual stress can potentially be used for the asperities of interest in EHL profile C. They have been extracted from Tables 7.3 and 7.4 based on parameter similarities. Unfortunately, none of the selected asperities are completely identical to the candidate asperities so a choice is necessary. The residual stress fields for each of the asperities in Table7.6 were obtained from the FEA analyses and compared as candidates to present asperities A, B and C. The choice was made by considering the level of residual tensile stress and those candidates with highest value were selected to be used in the fatigue calculation comparisons. Table 7.7 list the five asperities whose FEA residual stress fields were used as explained in Section 5.4 for the fatigue analyses.

Table 7.6 - The asperities names whose FEA residual stress used.

Asperity name	*Dimension in μm for the asperities which their FEA residual stress can be used*			
	H	*W*	w	h
A	1.31	45.8	35.9	0.276
15AA	1.100	40.9	10.8	0.057
5BA	1.030	45.7	34.3	0.229
7BA	0.686	42.9	22.9	0.057
11BA	0.686	34.3	28.6	0.229
13BA	0.743	40.0	28.6	0.057
14BA	0.743	45.7	25.7	*0.186*
B	1.17	35.9	22.9	0.207
2AB	0.914	19.4	12.9	0.086
18AB	0.629	30.0	21.5	0.086
21AB	1.000	30.1	17.2	0.085
29AB	0.942	30.0	17.2	0.071
1BB	0.829	34.3	22.9	0.086
9BB	0.486	34.3	20.0	0.086
16BB	0.743	31.4	20.0	*0.143*
18BB	0.514	20.0	20.0	*0.086*
C	0.896	32.6	19.6	0.207
31AC	0.743	30.0	17.2	0.129
32AC	0.657	29.2	12.9	*0.086*
21BC	0.800	28.6	17.1	*0.186*

Table 7.7 - The asperities names whose FEA residual stress were used in the analysis.

Asperity name	*Dimension in μm for the asperities which their FEA residual stress were used*			
	H	*W*	w	h
1BB	0.829	34.3	22.9	0.086
2AB	0.914	19.4	12.9	0.086
7BA	0.686	42.9	22.9	0.057
31AC	0.743	30.0	17.2	0.129
32AC	0.657	29.2	12.9	*0.086*

7.3.2 Developing FEA residual stress for asperities in Abaqus

The FEA values of residual stresses are numerically calculated by employing the plain strain contact deformation analysis model described in chapter 4. The procedure to export the FEA residual stress from Abaqus for particular asperities to be ready for the fatigue analysis was achieved through Abaqus standard by creating a display group for the whole area around the nominated asperity as shown in Figure 7.5. An Abaqus display group is specified by defining two points, (x_1, z_1) and(x_2, z_2). The display group then contains all elements that have a node whose coordinates satisfy the condition $x_1 \le x \le x_2$ and $z_1 \le z \le z_2$ .This is achieved in two steps with x_1 and x_2 forming an initial display group which is subsequently reduced to the required display group by specifying z_1 and z_2 through entering z_1 and z_2 values or highlighting the required display area. Following this, the file output tool in the Abaqus main menu bar is then used to tabulate the coordinates of the deformed asperity and the residual stress components σ_{xx}, σ_{zz}, and τ_{xz} at the load removal step (residual step) in the analysis for all the finite element nodes in the display group as shown in Figure 7.5 stage 3. These data are in the form of separate tables that include the node number with each entry. A FORTRAN programme was written to read these files and to associate the different data items by node numbers prior to sorting by position, as required for further analysis. Then these data were interpolated to the rectangular mesh used for the EHL stress history, as discussed in section 5.3.3, so that the residual stress could be incorporated in the fatigue analysis.

Stage 1:

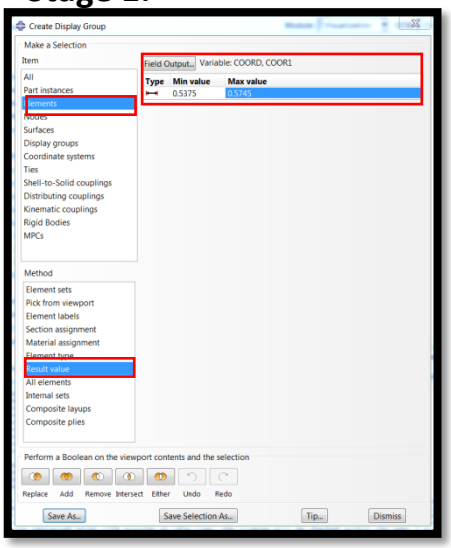

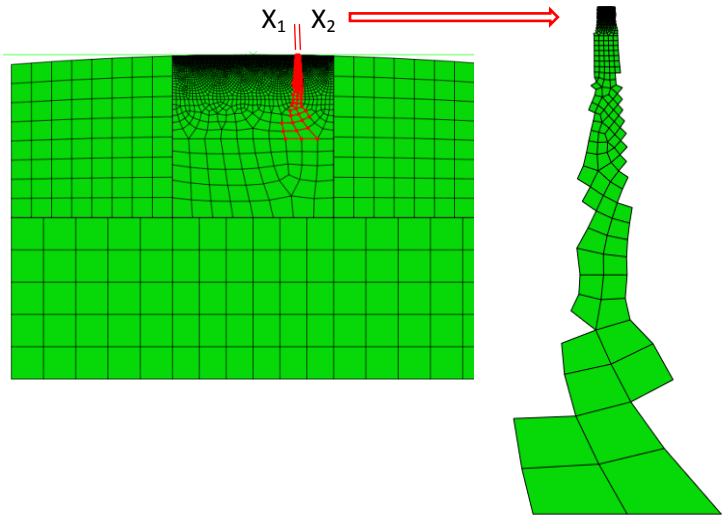

Stage 2:

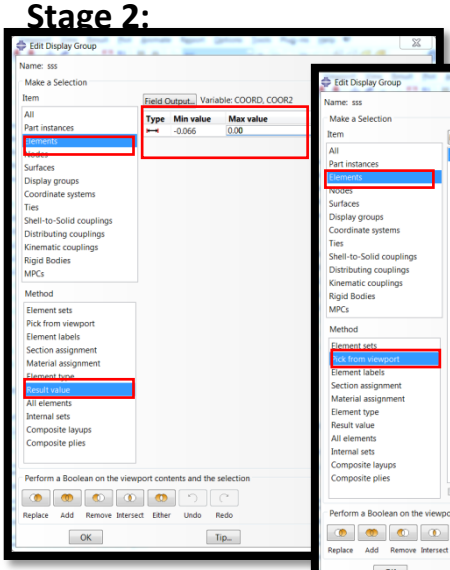

OR

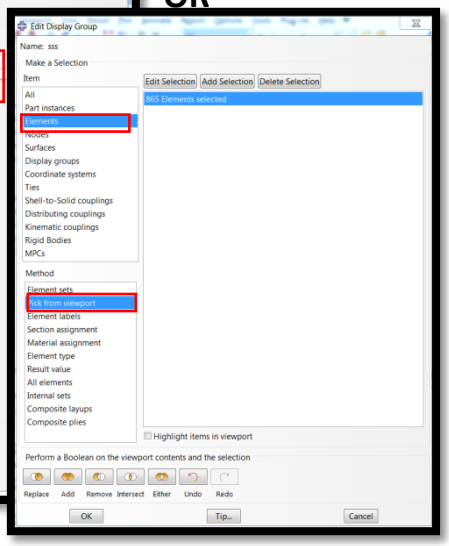

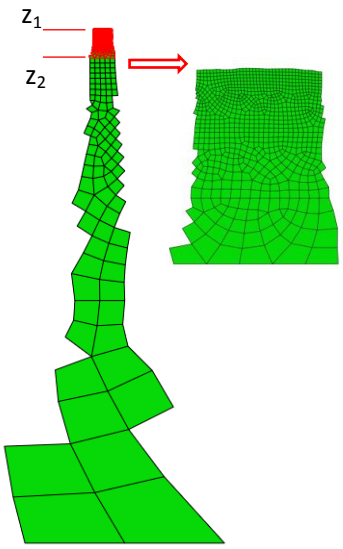

Stage 3:

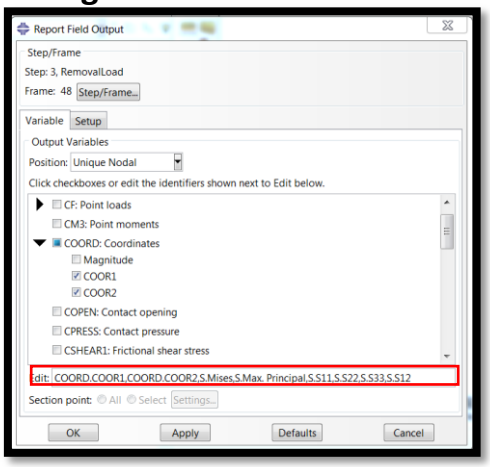

Figure 7.5- Abaqus snapshots for creating the display group tool using by defining it's coordinate limits x_1, x_2 and z_1, z_2.

7.3.3 Fatigue calculation based on a certain asperity size

The discussion up to this point has dealt with the preparation of the FEA residual stress data for specific asperities to be added to EHL stress history data for the previous profile. The research in this step deals with the analysis of fatigue damage that uses these data in the fatigue damage calculation with residual stress and compares that with the damage calculation obtained without residual stress in Chapter 6 for the corresponding models. In this section the results of the fatigue damage calculation for a chosen asperity were obtained without and with the addition of residual stress, and then assessed to find the material in which damage would occur using different models. In particular, it is aimed at disclosing the effect of tensile residual stress clearly.

Figure 7.6 presents a complete set of figures which can be used to compare damage contours for the asperity in question with residual stress included with damage contours for the same asperity without residual stresses. Figure 7.6(a) shows the EHL profile C which has the asperity named B (see figures 7.4) indicated with a red arrow. The calculation of fatigue damage for the contact between the two rough surfaces was carried out without residual stress as explained in Chapter 6 and is shown in Figure 7.6(b). Figure 7.6(c) shows the damage calculation with residual stress for asperity B included. Figure 7.6(d) shows the magnified sections of fatigue damage contours for damage with and without residual stress labelled (1) and (2), respectively, for the asperity number B on EHL profile C. The third figure, labelled (3), is the value of the difference (1)-(2) and only the positive differences are shown in the contours. The red contours thus indicate areas where the residual stress causes the greatest increase in calculated damage. These magnified sections of the figure used in the analysis in this

feature are referred to with text numbers 1, 2 and 3 at their bottom right hand corner. They show a magnified view of the damage, which illustrates the fatigue damage and plastic asperity deformation more clearly.

Figure 7.6(b) is the result of the Chu fatigue damage model calculation which is represented mathematically in Equation 6.20. The figure shows the high values of the accumulated fatigue damage calculated that is focussed near the surface of certain asperity features and is separated by areas between the asperities that are not subject to the same level of damage. Prominent asperities are subject to higher damage levels because the damage value is influenced by the asperity shape feature and its level in the contact. It can be noticed that those asperities of a similar shape but at different levels have different damage values. Figure 7.6(c) shows the accumulated damage for the same model and the same area of Figure 7.6(b) but includes the effect of the FEA residual stress for the indicated asperity in its fatigue calculation. So, the difference between the two figures represents the effects of the residual stress which is clear in the amount of red zone in that location. There is no change for the other asperities. The magnified sections in Figure 7.6(d) allow the effect of incorporating residual stress in the fatigue calculation to be assessed with the differences in the contour position for the highest damage level of $3x10^{-4}$ being apparent. Figure 7.6(d) (3) shows that there are differences of the order $3x10^{-4}$ between the damage values within area shown. There are significant differences that are not particularly apparent in comparing the damage contours because of the logarithmic scale used to illustrate the damage value. The largest increase in damage added to the material due to the incorporating residual stress exceeds 0.0003 in particular at the area in between

x/a=-0.81 and x/a=-0.76 and at depth z/a=0.01. Also, it can be noticed that most of the damage that is created by residual stress is built up near to the surface.

In terms of the numbers, Table 7.8 lists the damage difference percentage in decreasing order for ten most significant damage difference points using the Chu fatigue damage model calculation with residual stress and compares the damage values that those points experienced in the fatigue calculation without residual stress. The damage difference percentage $D\%$ is calculated by the following equation:

$$D\% = \frac{D(i)_{with\_Rs} - D(i)_{without\_Rs}}{D_{max\_without\_Rs}} \times 100$$

Where $D(i)_{with\_Rs}$ the damage at a particular point (i) with including residual stress, $D(i)_{without\_Rs}$ is the damage at the same particular point (i) without including residual stress and $D_{max\_without\_Rs}$ is the maximum damage for the entire material without including residual stress. It can be seen that damage values at these ten significant points respond to inclusion of residual stress. For example, the point (-0.8, 0.002) has a damage difference percentage by 19.7 %, hence the point will get decreases in cycle life. Also can be seen the points with the damage values in Table 7.8 to experience increase of range 19.7% and 13.0% when residual stress is concluded, however the other high damage points see less effect with residual stress causing small reduction in the calculated damage values.

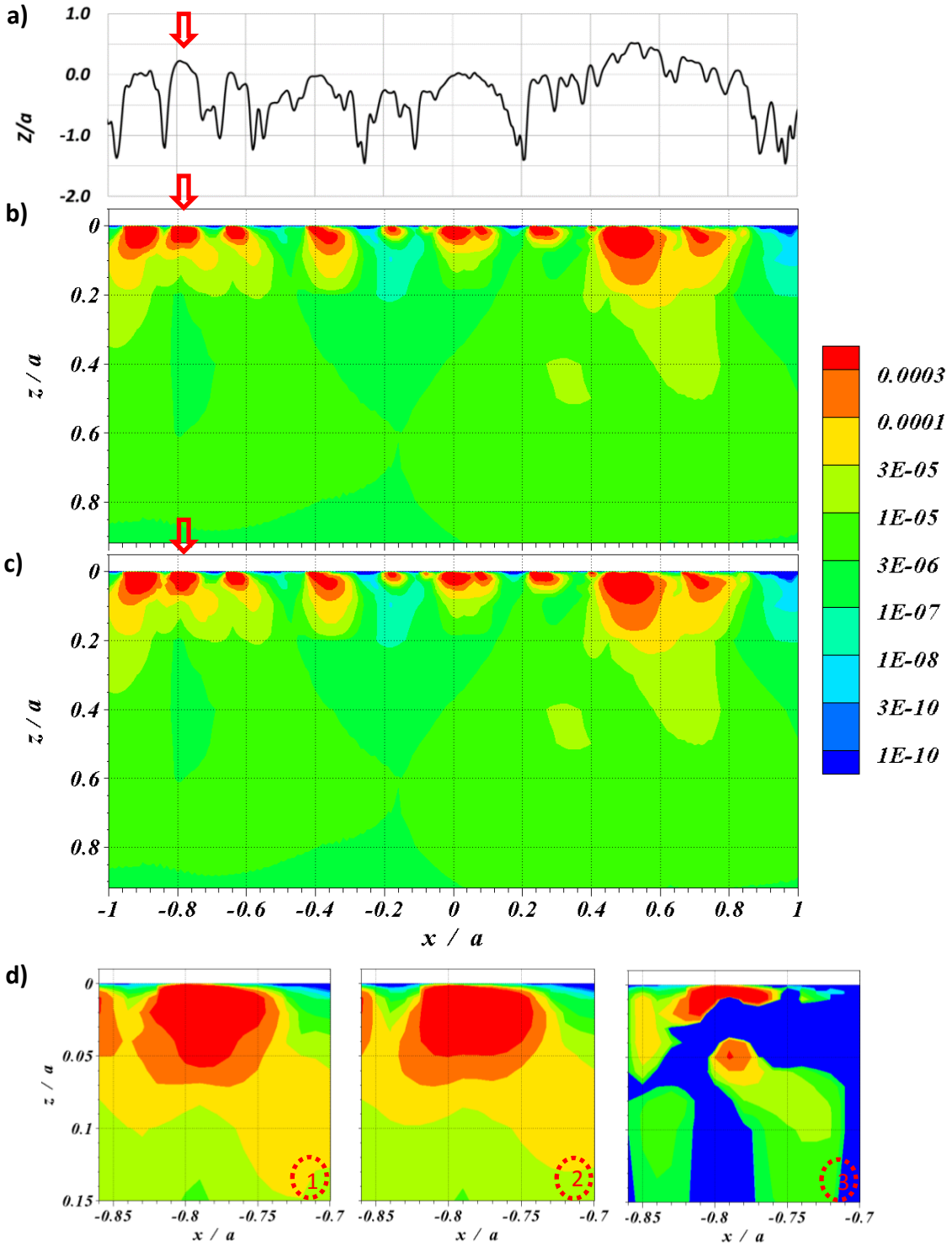

Figure 7.6 - Chu Model's contours of fatigue damage; a) EHL profile C, b) without residual stress, c) with residual stress, d) large scale plot for the asperity B at EHL profile C with and without residual stress and the positive difference caused by its inclusion as numbered 1,2 and 3 respectively.

Table 7.8 - The damage difference percentage comparison of the significant points of the Chu fatigue damage model calculation with and without adding residual stress.

X/a Position	*Z/a Position*	*Damage without residual stress*	*Damage with residual stress*	*Damage difference*	*% Percentage of damage difference*
-8.00E-01	*2.00E-03*	*1.57E-03*	*3.85E-03*	*2.29E-03*	*19.7*
-8.00E-01	*4.00E-03*	*3.78E-03*	*5.96E-03*	*2.19E-03*	*18.9*
-7.90E-01	*4.00E-03*	*3.74E-03*	*5.66E-03*	*1.91E-03*	*16.5*
-7.80E-01	*6.00E-03*	*3.18E-03*	*4.82E-03*	*1.64E-03*	*14.2*
-7.90E-01	*2.00E-03*	*8.08E-04*	*2.41E-03*	*1.61E-03*	*13.9*
-7.80E-01	*4.00E-03*	*1.54E-03*	*3.05E-03*	*1.51E-03*	*13.0*
-7.90E-01	*6.00E-03*	*5.70E-03*	*6.95E-03*	*1.25E-03*	*10.8*
-8.00E-01	*6.00E-03*	*4.80E-03*	*5.92E-03*	*1.12E-03*	*9.7*
-8.10E-01	*1.00E-02*	*1.06E-03*	*1.88E-03*	*8.22E-04*	*7.1*
-8.10E-01	*6.00E-03*	*9.79E-04*	*1.78E-03*	*7.97E-04*	*6.9*

Table 7.9 and Figure 7.7 show the damage difference percentage and fatigue damage contours obtained in this way for the four asperities using the corresponding residual stress fields indicated in Table 7.7 using the Chu model. All the asperities showed a response to the inclusion of residual stress. The findings of the calculation of the effect incorporating residual stress on the asperities using the Chu model can be concluded as the follows:

- The most significant damage is built up near to the surface where the asperity contact has occurred as shown in all asperities in Figure 7.7 (3).
- The most significant damage occurs directly beneath asperity contact as shown clearly in asperity 7.7 *(a-d)(3)*
- These areas of fatigue damage due to high tensile stress are separated by a band of protective area due to the effects of compressive stress.

- Also it can be seen the percentage of the increased damage for these asperities falls within range 19.7% to 9.5%.

Table 7.9 - The damage difference percentage comparison of the significant points of the Chu fatigue damage model calculation with and without adding residual stress for different asperities.

Asperity Name	*X/a Position*	*Z/a position*	*Damage without residual stress*	*Damage with residual stress*	*Damage difference*	*% Percentage of damage difference*
1BB	*-8.00E-01*	*2.00E-03*	*1.57E-03*	*3.85E-03*	*2.29E-03*	*19.7*
7BA	*-9.40E-01*	*1.00E-02*	*1.08E-03*	*2.19E-03*	*1.11E-03*	*9.5*
31AC	*2.30E-01*	*4.00E-03*	*1.30E-03*	*2.75E-03*	*1.45E-03*	*12.5*
32AC	*2.50E-01*	*6.00E-03*	*1.41E-03*	*2.57E-03*	*1.15E-03*	*9.9*

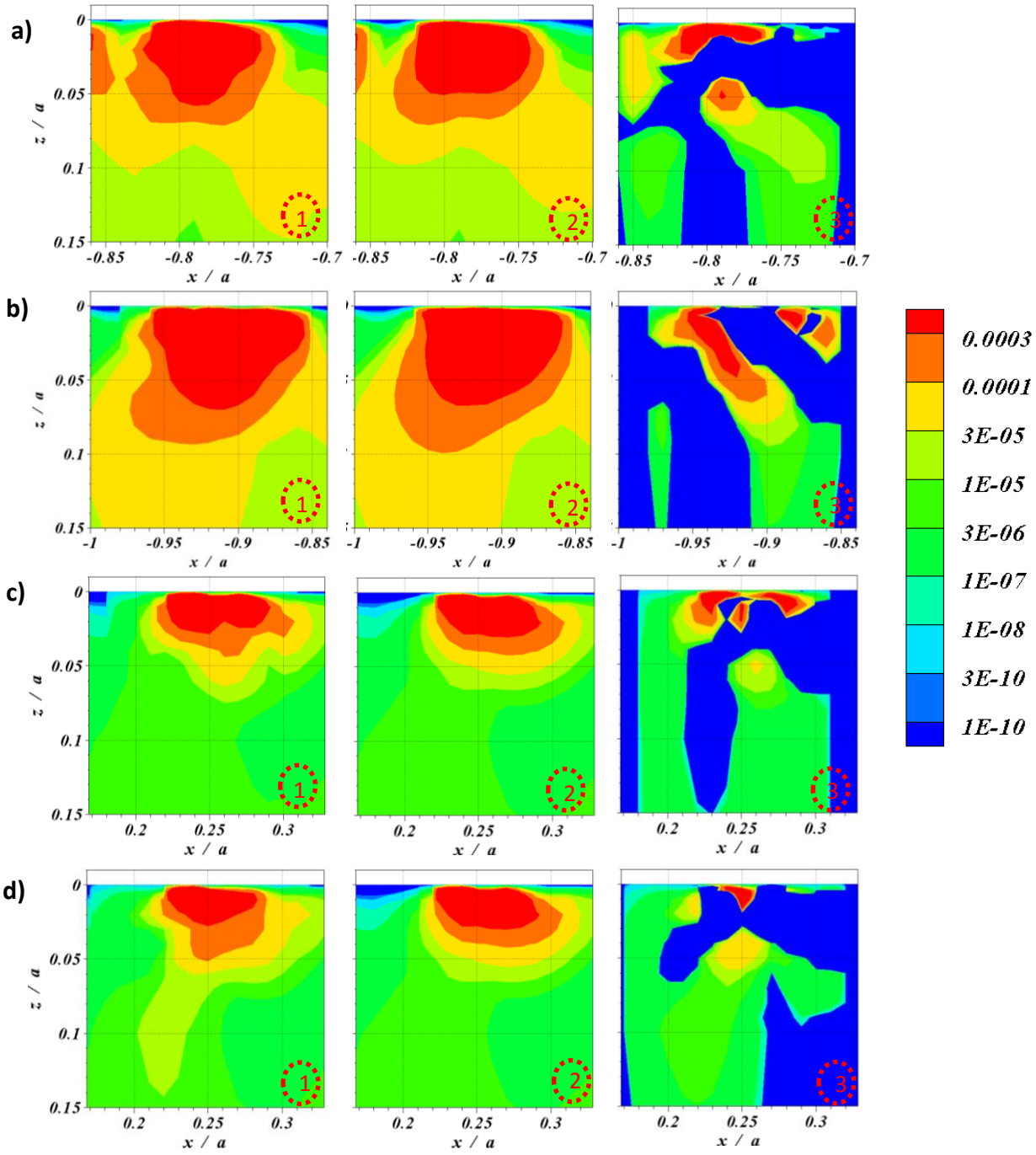

Figure 7.7-Chu model's contours of fatigue damage for different asperities/residual stress combinations; a) 1BB, b) 7BA, c) 31AC , d) 32AC. Figure(1) give damage with residual stress, Figure(2) give damage without residual stress, and Figure(3) give the positive difference.

Figure 7.8 represents the second result of the effect of residual stress on the fatigue damage calculated in this case using the Fatemi and Socie model (FS). The model has the mathematical form of Equation 6.17 which is based on the hypothesis that the fatigue will occur according to a mixture of normal direct stress and shear strain as explained in Section 6.5.2. Figure 7.8(b) represents the fatigue damage without residual stress as in the previous model while the effect of residual stress calculated with the FS model is shown in Figure 7.8(c) where the red arrow points to asperity B for which the residual stress is included. The red zone area of damage in figure 7.8(c) that incorporate residual stress is located between $x/a = -0.84$ and $x/a = -0.73$. This can be seen in more detail in Figure 7.8(d) numbers 1 and 3 which makes the comparison at a large scale. Also the fatigue damage was influenced by the compressive residual stress in the middle of the asperity which is considered a protective environment; however, the threat comes from the high tensile residual stresses that increase the damage near the boundary of the asperity as shown clearly in the magnified section in Figure 7.8(d) number 3. This show the significant effects of tensile residual stress where most of the effect occurs on the boundary of the asperity and near to the surface. This finding matches the location of the maximum residual principal tensile stress vectors shown in Figure 5.15-17 where they are concentrated beneath the surface, and around the boundary of the asperity and where plastic deformation has occurred.

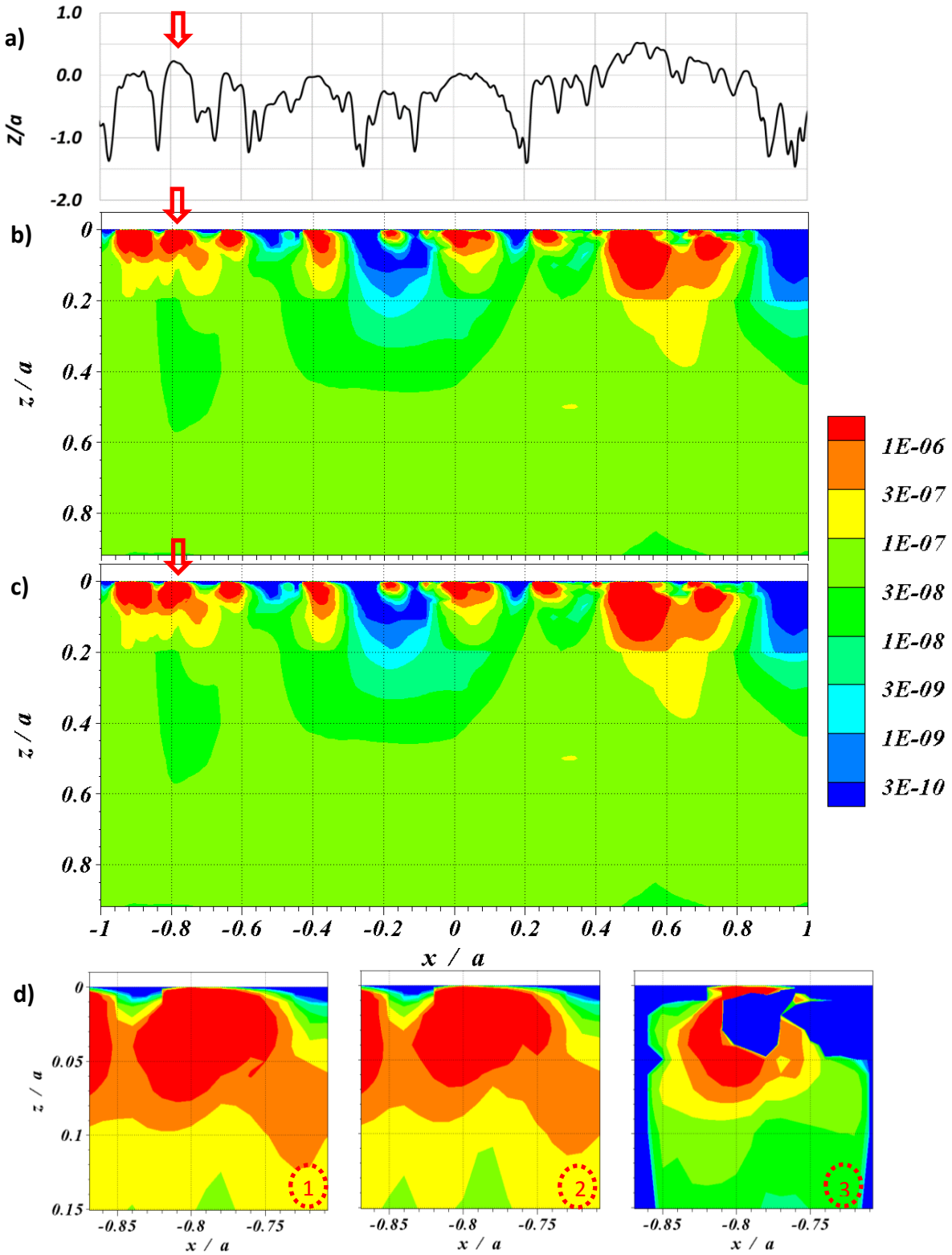

Figure 7.8 - Fatemi and Socie model's contours of fatigue damage; a) EHL profile C, b) without residual stress, c) with residual stress, d) large scale plot for the asperity B at EHL profile C with and without residual stress and the positive difference caused by its inclusion as numbered 1,2 and 3 respectively .

Table 7.10 lists the damage difference percentage in decreasing order for the ten points having the most significant damage difference using the Fatemi and Socie fatigue model calculation with residual stress and compares the damage value that the points experience in the fatigue calculation with and without residual stress. It can be seen that damage values at these ten significant points respond to inclusion of residual stress as well. The two points (-0.8, 0.004) (-0.8, 0.002) with the highest damage values in table 7.10 can be seen to experience a further increase of 25.9% and 20.3% when the residual stress is concluded, however the other damage points show less effect with residual stress causing small reductions in the calculated damage values.

Table 7.10 - The damage difference percentage comparison of the significant points of the Fatemi and Socie fatigue damage model calculation with and without adding residual stress.

X/a Position	*Z/a position*	*Damage without residual stress*	*Damage with residual stress*	*Damage difference*	*% Percentage of damage difference*
-8.00E-01	*4.00E-03*	*9.12E-05*	*1.36E-04*	*4.48E-05*	*25.9*
-8.00E-01	*2.00E-03*	*2.88E-05*	*6.39E-05*	*3.51E-05*	*20.3*
-8.00E-01	*6.00E-03*	*9.38E-05*	*1.09E-04*	*1.55E-05*	*9.0*
-8.00E-01	*5.00E-02*	*3.49E-06*	*1.15E-05*	*7.99E-06*	*4.6*
-7.90E-01	*4.00E-03*	*4.61E-05*	*5.28E-05*	*6.70E-06*	*3.9*
-7.90E-01	*2.00E-03*	*6.71E-06*	*1.28E-05*	*6.04E-06*	*3.5*
-8.10E-01	*5.00E-02*	*2.83E-06*	*8.08E-06*	*5.25E-06*	*3.0*
-8.20E-01	*3.00E-02*	*3.72E-06*	*8.87E-06*	*5.15E-06*	*3.0*
-7.80E-01	*2.00E-03*	*1.44E-06*	*6.24E-06*	*4.80E-06*	*2.8*
-8.00E-01	*1.00E-03*	*1.91E-06*	*6.41E-06*	*4.50E-06*	*2.6*

The results shown in Table 7.9 and Figure 7.7are presented in Table 7.11 and Figure 7.9 for analyses based on the Fatemi and Socie model. The findings of the calculation of the effect of the FEA residual stress on the selected asperities is that incorporating

residual stress in the fatigue calculation using the Fatemi and Socie model leads to the following observations:

- The two points (-0.8, 0.004) (-0.92, 0.002) corresponding to the asperities 1BB and 7BA respectively can be seen to experience an increase of the highest damage values by 25.9% and 14.0% as shown in Table 7.11 when the residual stress is included. However the other two selected asperities 31AC and 32AC show a smaller effect with residual stress causing small reduction in the calculated damage values.
- The fatigue life is decreased for these two asperities 1BB and 7BA more than the other asperities which can be calculated with a Palmgren equation.
- Figures 7.9(3) for all asperities show the effect that could be caused by compressive residual stress and shown in the figure by dark blue colour where concentrated in the middle of the asperities.

Table 7.11 - The damage difference percentage comparison of the significant points of the Fatemi and Socie fatigue damage model calculation with and without adding residual stress for different asperities.

Asperity Name	*X/a Position*	*Z/a position*	*Damage without residual stress*	*Damage with residual stress*	*Damage difference*	*% Percentage of damage difference*
1BB	*-8.00E-01*	*4.00E-03*	*9.12E-05*	*1.36E-04*	*4.48E-05*	*25.9*
7BA	*-9.20E-01*	*2.00E-03*	*4.93E-05*	*7.36E-05*	*2.43E-05*	*14.0*
31AC	*2.40E-01*	*2.00E-03*	*2.72E-05*	*4.19E-05*	*1.47E-05*	*8.5*
32AC	*2.40E-01*	*4.00E-03*	*5.37E-05*	*6.90E-05*	*1.54E-05*	*8.9*

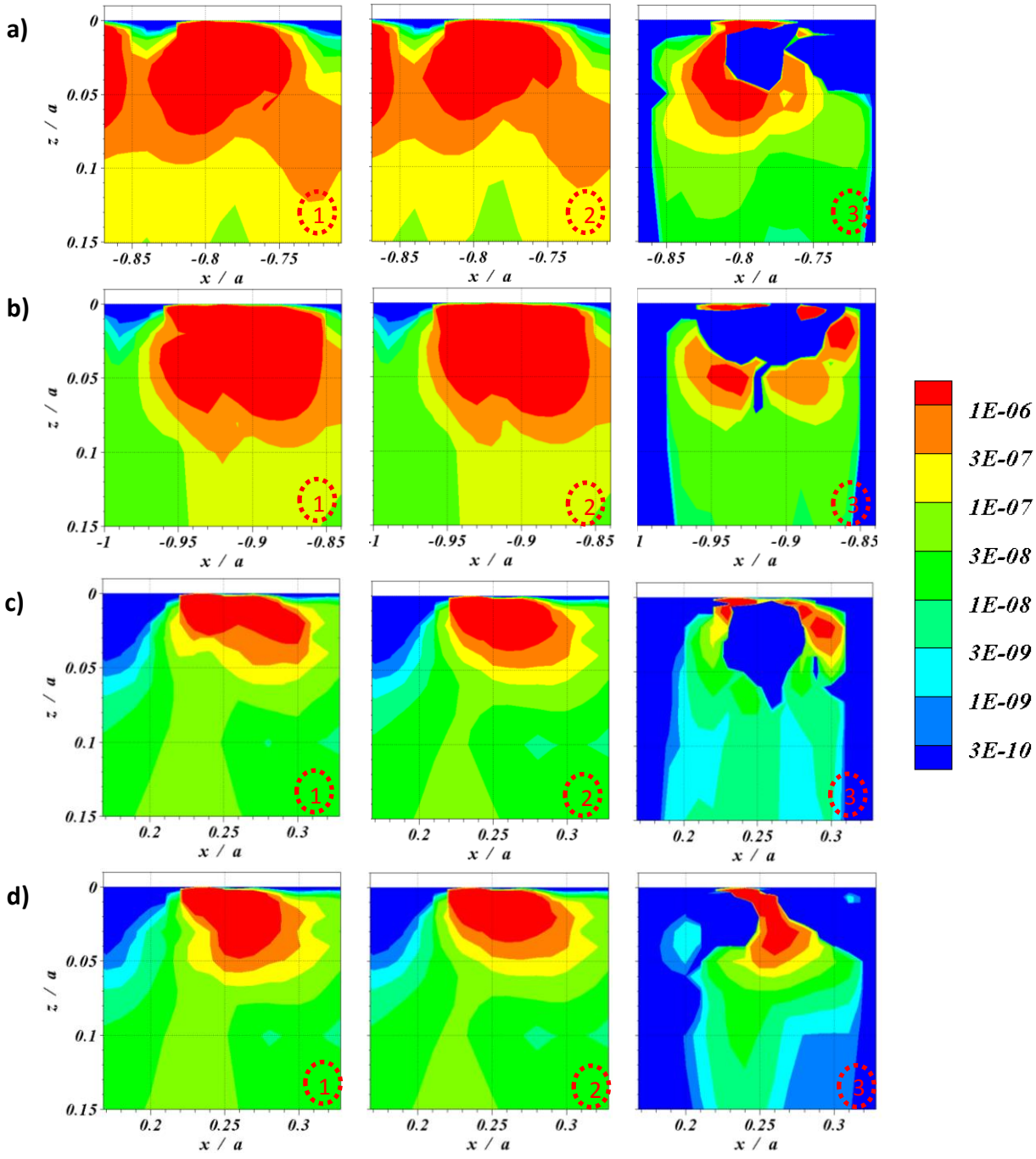

Figure 7.9 - Fatemi and Socie model's contours of fatigue damage for different asperities/residual stress combinations; a) 1BB, b) 7BA, c) 31AC ,d) 32AC. Figure(1) give damage with residual stress, Figure(2) give damage without residual stress, and Figure(3) give the positive difference.

The fatigue life calculations with residual stress and without residual stress in this section were also carried out using the rest of multiaxial fatigue criteria recommended in chapter 6, i.e. the modified Smith Watson Topper model SWTM, the Goodman model and the Marrow model. The fatigue analyses for these models followed the same technique as that for Chu and Fatemi and Socie models in terms of contour plots and table formats but without text explanation to avoid repetition. Each model analysis is presented in two groups. The first is a group of damage contours followed by a damage comparison table for the ten most significant points in the asperity have. Secondly, a group of four asperity evaluations in terms of damage contours and tables of the highest damage point in each asperity. In general, these three models showed response to incorporating residual stress to the fatigue calculations. The modified Watson and Topper SWT (M) in Figure 7.10-11 and Table 7.12-13 can be seen to experience higher damage when the residual stress is included, however the Goodman model in Figures 7.12-13 and Tables 7.14-15 and Marrow model in Figures 7.14-15 and Tables 7.16-17 indicate less effect with including residual stress which causes a small reduction in the calculated damage values.

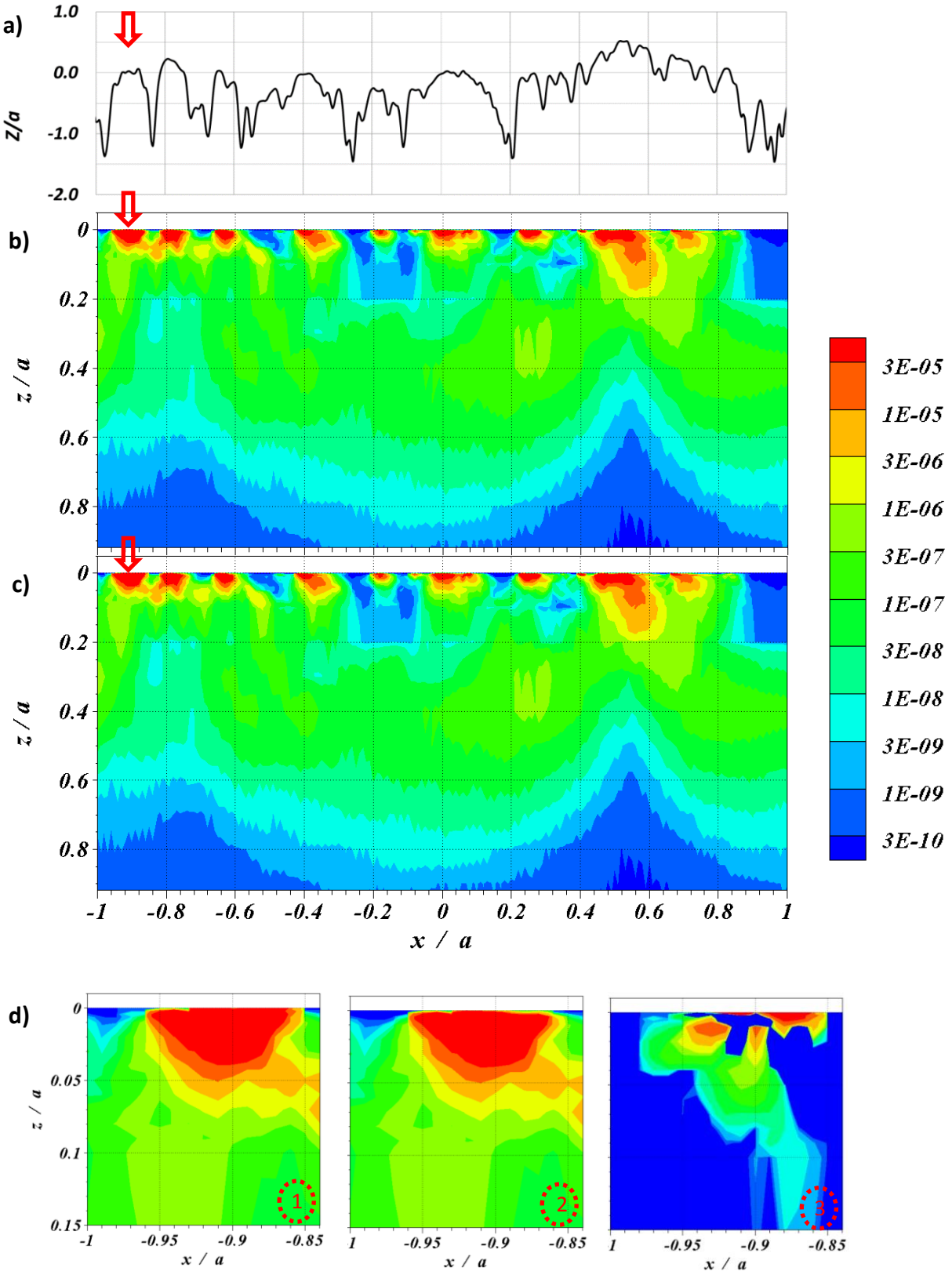

Figure 7.10 - SWTM model's contours of fatigue damage; a) EHL profile C, b) without residual stress, c) with residual stress, d) large scale plot for the asperity A at EHL profile C with and without residual stress and the positive difference caused by its inclusion as numbered 1,2 and 3 respectively .

Table 7.12 - The damage difference percentage comparison of the significant points of the SWTM fatigue damage model calculation with and without adding residual stress.

X/a_Position	Z/a_position	Damage without residual stress	Damage with residual stress	Damage difference	%Percentage of damage difference
-9.10E-01	0.00E+00	6.52E-06	4.67E-04	4.61E-04	11.7
-9.20E-01	0.00E+00	2.86E-05	3.20E-04	2.91E-04	7.4
-8.80E-01	1.00E-03	8.06E-07	2.07E-04	2.06E-04	5.2
-8.80E-01	0.00E+00	7.18E-08	2.05E-04	2.05E-04	5.2
-8.70E-01	0.00E+00	2.66E-07	1.77E-04	1.77E-04	4.5
-8.80E-01	2.00E-03	4.93E-06	1.37E-04	1.32E-04	3.3
-9.10E-01	1.00E-03	6.73E-05	1.76E-04	1.09E-04	2.8
-8.70E-01	1.00E-03	2.65E-06	9.51E-05	9.24E-05	2.3
-8.90E-01	0.00E+00	1.74E-07	6.34E-05	6.32E-05	1.6
-8.80E-01	4.00E-03	9.62E-05	1.47E-04	5.04E-05	1.3

Table 7.13 - The damage difference percentage comparison of the significant points of the SWTM fatigue damage model calculation with and without adding residual stress for different asperities.

Asperity Name	X/a Position	Z/a position	Damage without residual stress	Damage with residual stress	Damage difference	%Percentage of damage difference
1BB	-7.90E-01	1.00E-03	2.62E-05	1.60E-04	1.34E-04	3.4
7BA	-9.10E-01	0.00E+00	6.52E-06	4.67E-04	4.61E-04	11.7
31AC	2.70E-01	4.00E-03	1.93E-04	2.05E-04	1.14E-05	0.3
32AC	2.60E-01	6.00E-03	2.00E-04	2.18E-04	1.84E-05	0.5

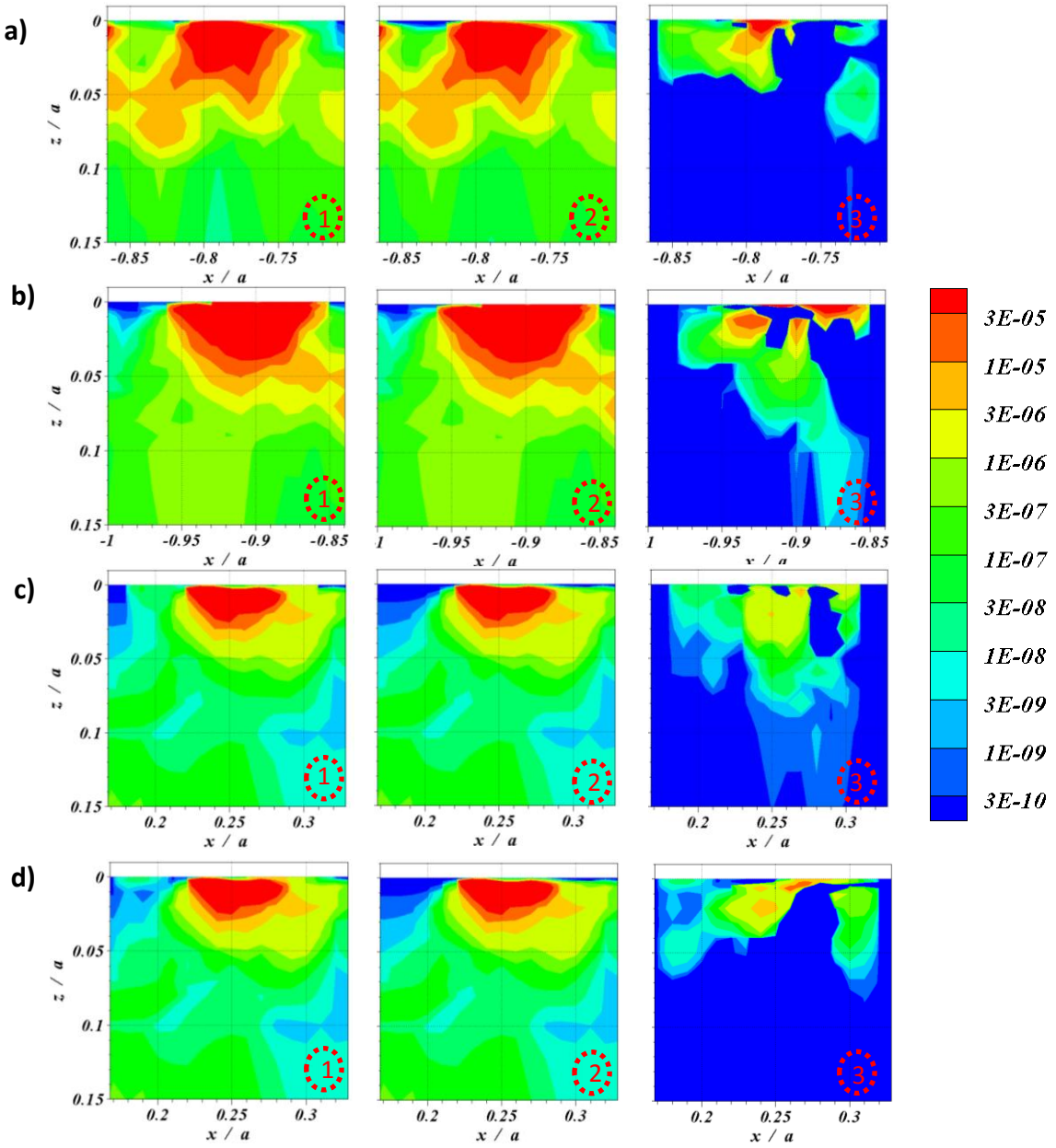

Figure 7.11 - SWTM model's contours of fatigue damage for different asperities/residual stress combinations; a) 1BB, b) 7BA, c) 31AC ,d) 32AC. Figure(1) give damage with residual stress, Figure(2) give damage without residual stress, Figure(3) give the positive difference.

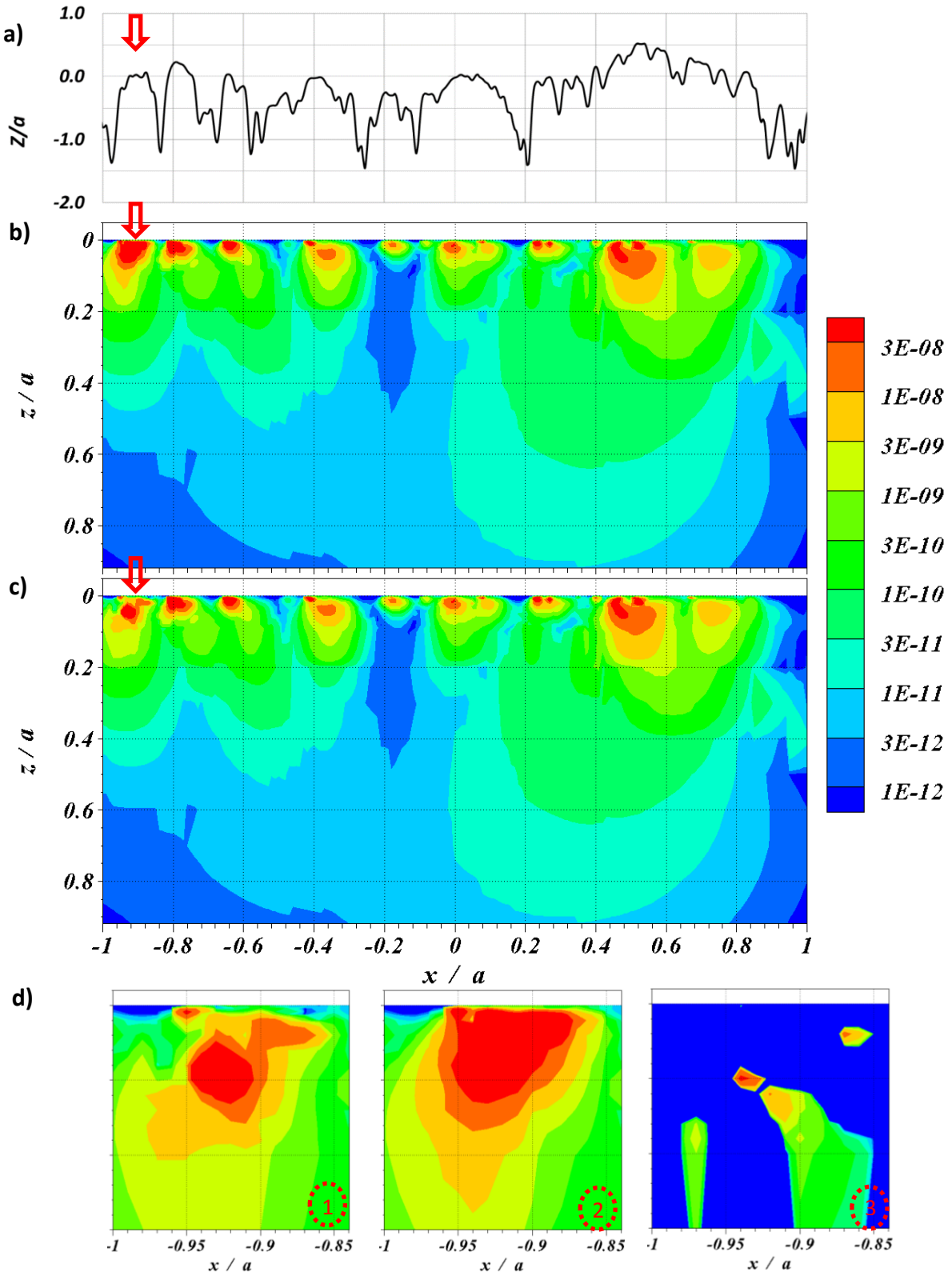

Figure 7.12 - Goodman model's contours of fatigue damage; a) EHL profile C, b) without residual stress, c) with residual stress, d) large scale plot for the asperity A at EHL profile C with and without residual stress and the positive difference caused by its inclusion as numbered 1,2 and 3 respectively .

Table 7.14 - The damage difference percentage comparison of the significant points of the Goodman fatigue damage model calculation with and without adding residual stress.

X/a_Position	Z/a_position	Damage without residual stress	Damage with residual stress	Damage difference	Percentage of damage difference
-9.40E-01	5.00E-02	5.43E-08	9.58E-08	4.15E-08	4.0
-9.30E-01	5.00E-02	9.03E-08	1.14E-07	2.33E-08	2.2
-8.70E-01	2.00E-02	4.69E-09	2.00E-08	1.53E-08	1.5
-9.20E-01	6.00E-02	3.42E-08	4.52E-08	1.10E-08	1.1
-9.10E-01	7.00E-02	1.20E-08	1.73E-08	5.33E-09	0.5
-8.60E-01	2.00E-02	2.30E-09	7.21E-09	4.91E-09	0.5
-9.20E-01	7.00E-02	1.59E-08	1.97E-08	3.76E-09	0.4
-9.10E-01	6.00E-02	2.54E-08	2.89E-08	3.56E-09	0.3
-9.10E-01	8.00E-02	6.30E-09	9.17E-09	2.87E-09	0.3
-9.70E-01	9.00E-02	2.67E-09	4.42E-09	1.75E-09	0.2

Table 7.15 - The damage difference percentage comparison of the significant points of the Goodman fatigue damage model calculation with and without adding residual stress for different asperities.

Asperity Name	X/a Position	Z/a position	Damage without residual stress	Damage with residual stress	Damage difference	%Percentage of damage difference
1BB	-7.90E-01	4.00E-03	2.00E-08	3.96E-08	1.96E-08	1.9
7BA	-9.40E-01	5.00E-02	5.43E-08	9.58E-08	4.15E-08	4.0
31AC	2.40E-01	2.00E-03	1.06E-08	1.44E-08	3.78E-09	0.4
32AC	2.50E-01	5.00E-02	7.49E-10	6.73E-09	5.98E-09	0.6

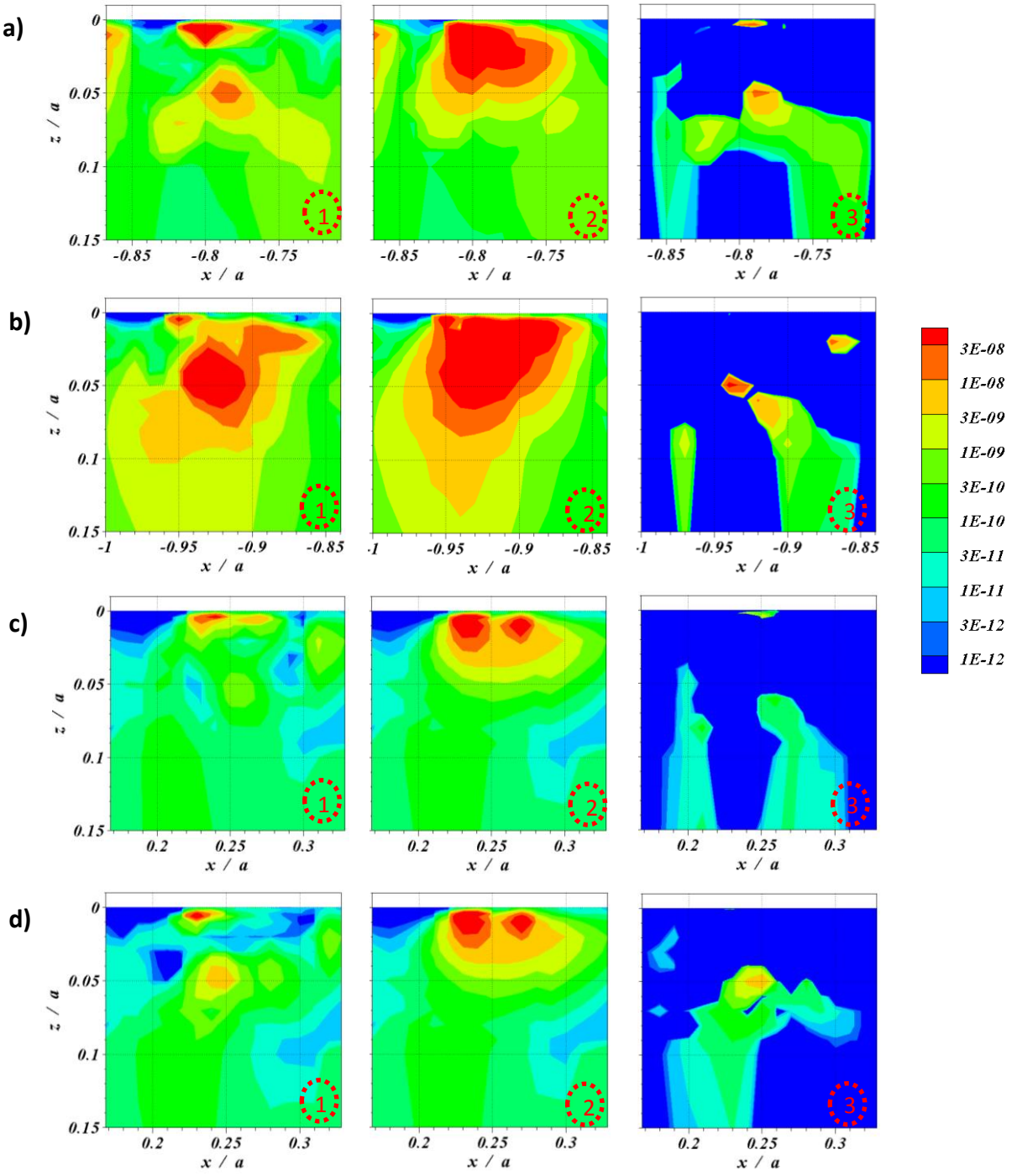

Figure 7.13 - Goodman model's contours of fatigue damage for different asperities/residual stress combinations; a) 1BB, b) 7BA, c) 31AC ,d) 32AC. Figure(1) give damage with residual stress, Figure(2) give damage without residual stress, and Figure(3) give the positive difference.

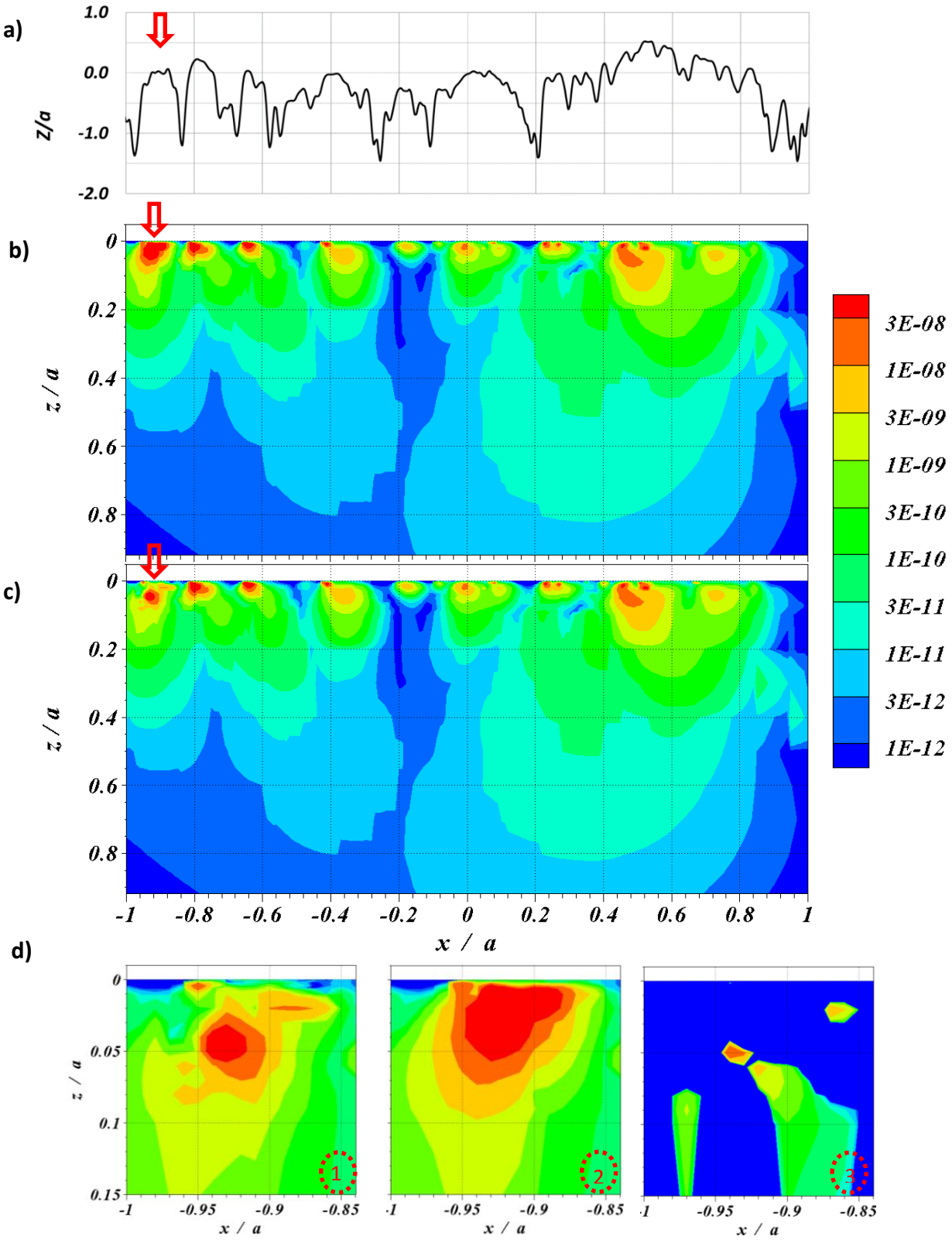

Figure 7.14 - Marrow model's contours of fatigue damage; a) EHL profile C, b) without residual stress, c) with residual stress, d) large scale plot for the asperity A at EHL profile C with and without residual stress and the positive difference caused by its inclusion as numbered 1,2 and 3 respectively.

Table 7.16 - The damage difference percentage comparison of the significant points of the Marrow fatigue damage model calculation with and without adding residual stress.

X/a_Position	Z/a_position	Damage without residual stress	Damage with residual stress	Damage difference	%Percentage of damage difference
-7.90E-01	4.00E-03	6.84E-09	1.36E-08	6.75E-09	1.5
-7.90E-01	5.00E-02	1.83E-09	8.28E-09	6.45E-09	1.5
-7.80E-01	5.00E-02	2.60E-09	7.68E-09	5.09E-09	1.2
-8.00E-01	4.00E-03	1.36E-08	1.74E-08	3.76E-09	0.9
-7.90E-01	6.00E-02	7.00E-10	3.48E-09	2.78E-09	0.6
-7.80E-01	6.00E-02	9.53E-10	3.46E-09	2.50E-09	0.6
-7.90E-01	2.00E-03	9.67E-10	2.78E-09	1.82E-09	0.4
-8.00E-01	2.00E-03	1.37E-09	2.74E-09	1.38E-09	0.3
-7.70E-01	6.00E-02	8.98E-10	1.98E-09	1.08E-09	0.2
-8.20E-01	7.00E-02	1.11E-09	2.14E-09	1.04E-09	0.2

Table 7.17 - The damage difference percentage comparison of the significant points of the Marrow fatigue damage model calculation with and without adding residual stress for different asperities.

Asperity Name	X/a Position	Z/a position	Damage without residual stress	Damage with residual stress	Damage difference	%Percentage of damage difference
1BB	-7.90E-01	4.00E-03	6.84E-09	1.36E-08	6.75E-09	1.5
7BA	-9.40E-01	5.00E-02	2.87E-08	5.39E-08	2.52E-08	5.7
31AC	2.40E-01	2.00E-03	3.76E-09	5.09E-09	1.33E-09	0.3
32AC	2.50E-01	5.00E-02	3.87E-10	3.83E-09	3.45E-09	0.8

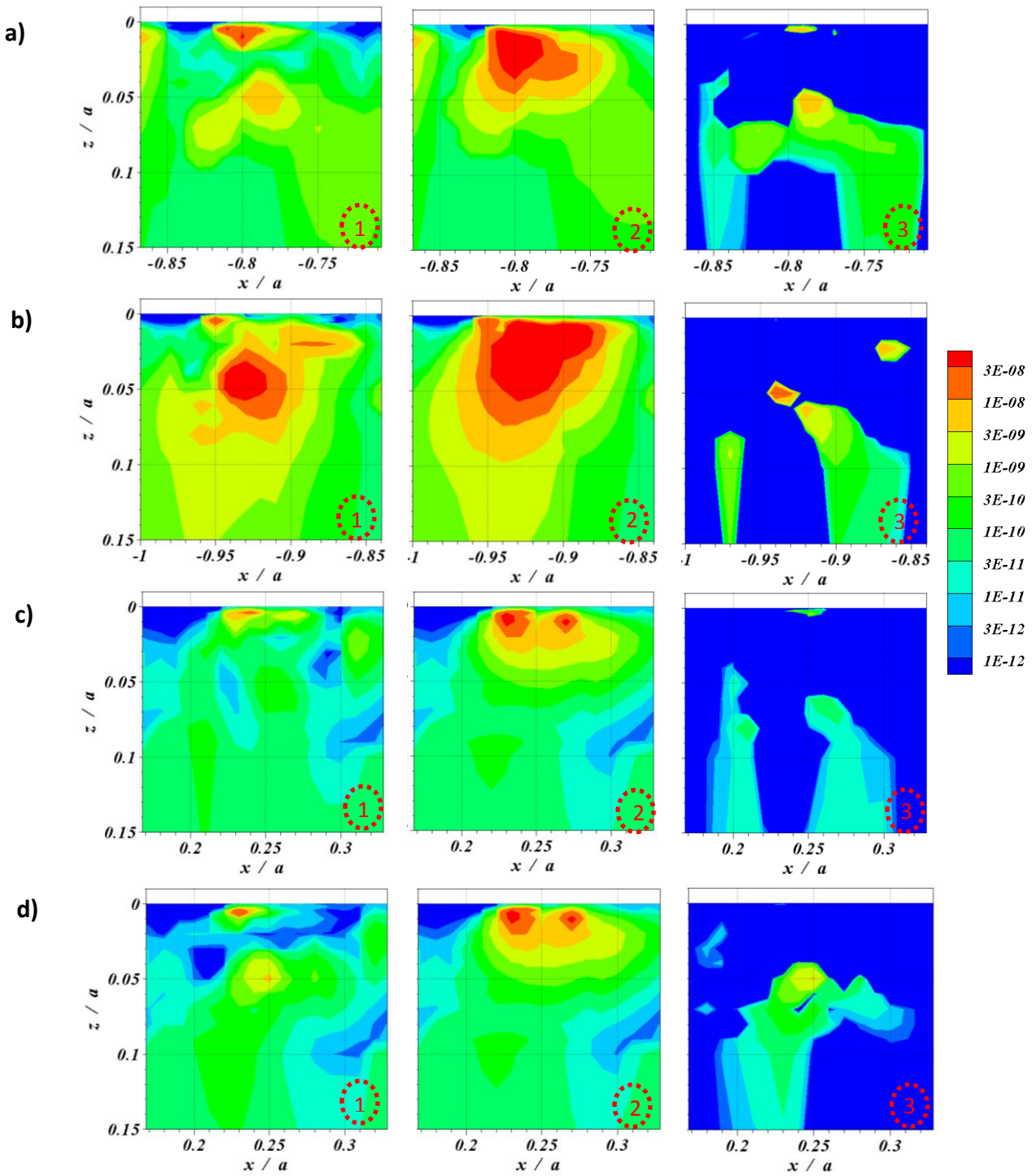

Figure 7.15 - Marrow model's contours of fatigue damage for different asperities/residual stress combinations; a) 1BB, b) 7BA, c) 31AC ,d) 32AC. Figure(1) give damage with residual stress, Figure(2) give damage without residual stress, and Figure(3) give the difference.

Figures (7.16-17) (a) to (e) compare the damage contours obtained for the slower moving surface using the same group of five models. The results are as presented previously but for these comparisons the contour levels are the same for each model which allows direct comparison of the calculated fatigue damage level. The comparison is applied to asperity evaluation 7BA in Figure 7.16 and asperity evaluation 1BB in Figure 7.17. The contours of the accumulated significant damage are coloured red, orange, dark yellow and light green when $D \geq 3\times10^{-4}$, $3\times10^{-4} \geq D \geq 1\times10^{-4}$, $1\times10^{-4} \geq D \geq 3\times10^{-5}$ and $3\times10^{-5} \geq D \geq 1\times10^{-5}$ respectively. In the contour plots, *D* is the value of damage corresponding to a single passage of the trial material through the EHL contact zone. For example, a value of $D = 10^{-4}$ thus corresponds to fatigue occurring in 10^4 repetitions of the loading experienced, i.e. 10^4 rotations of the test disk, or 10^4 meshing cycles of the gear if a gear roughness profile is being assessed. Failure zones corresponding to the damage calculation including the residual stress have the maximum damage is localized at and below the surface. This approved that the failures such micropitting are created at the surface through plastic deformation of the asperities. Tables 7.18-19 list the damage and damage difference values for each for the five models of the fatigue models applied to the asperities evaluated. For each model the point tabulated is the point that has the largest calculated damage difference. The table confirms that all these models' have points under the applied tensile residual stress and have gained more damage. It is clear that from the contours shown that the calculated damage is quite different when the different models are compared. There are differences of an order of magnitude or more between the different models. The way in which including residual stress affects the results is different with Chu, Modified SWTM and FS models showing the biggest increase.

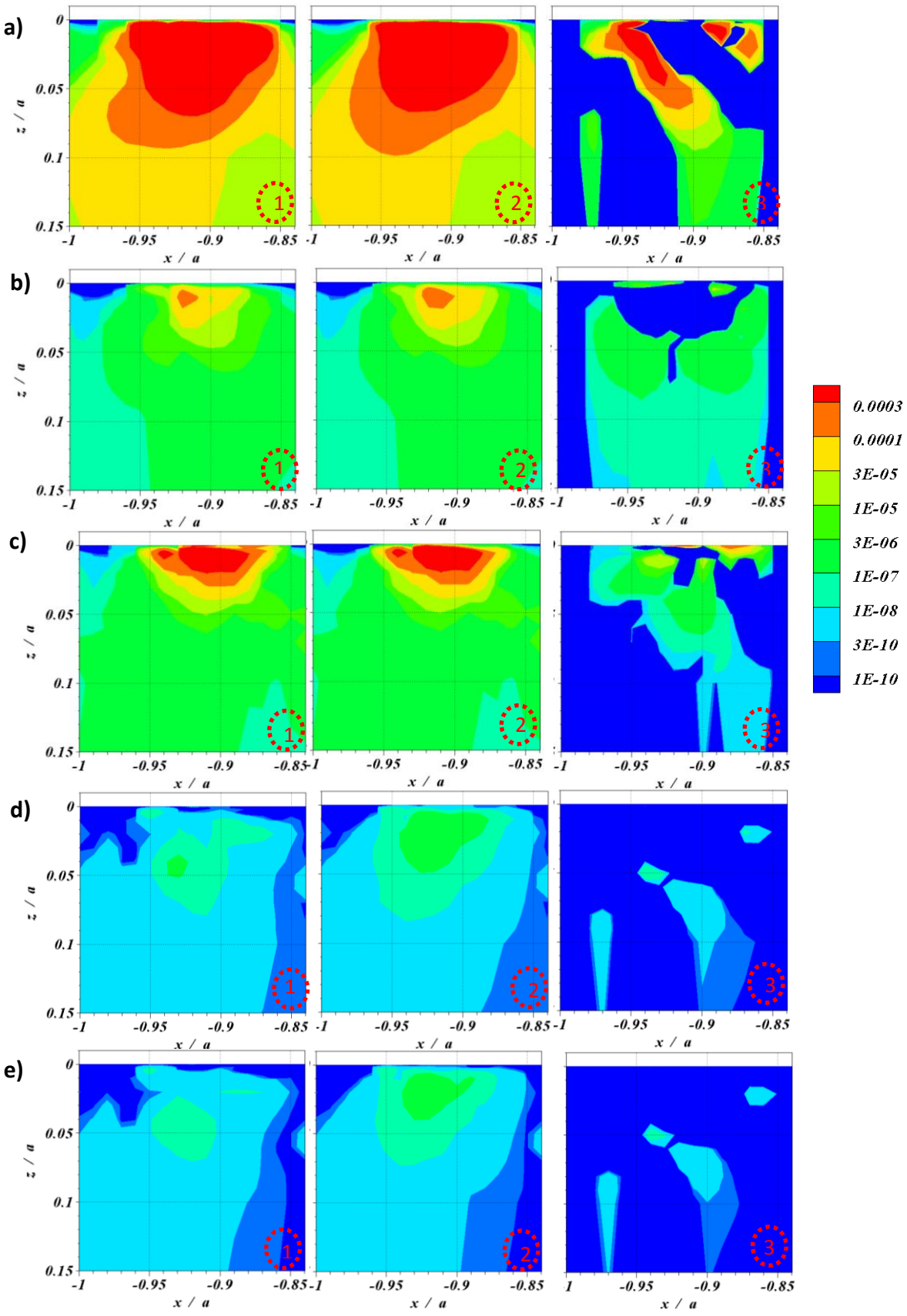

Figure 7.16 - Large scale fatigue damage contours for the asperity A at EHL profile C with and without and positive difference of residual stress as numbered 1,2 and 3 respectively for the models of a-e) Chu, Fatemi and Socie, SWTM, Goodman and Marrow respectively.

Table 7.18 - The damage differences percentage comparisons of fatigue damage significant points with and without residual stress for all five models at asperity 7BA.

Model Names	X/a Position	Z/a position	Damage without residual stress	Damage with residual stress	Damage difference	%Percentage of damage difference
Chu	-9.40E-01	1.00E-02	1.08E-03	2.19E-03	1.11E-03	9.5
Fatemi and Socie	-9.20E-01	2.00E-03	4.93E-05	7.36E-05	2.43E-05	14.0
SWTM	-9.10E-01	0.00E+00	6.52E-06	4.67E-04	4.61E-04	11.7
Goodman	-9.40E-01	5.00E-02	5.43E-08	9.58E-08	4.15E-08	4.0
Marrow	-9.40E-01	5.00E-02	2.87E-08	5.39E-08	2.52E-08	6.0

Table 7.19 - The damage difference percentage comparison of the significant points of fatigue damage with and without residual stress for all five models at asperity 1BB.

Model Names	X/a Position	Z/a position	Damage without residual stress	Damage with residual stress	Damage difference	%Percentage of damage difference
Chu	-8.00E-01	2.00E-03	1.57E-03	3.85E-03	2.29E-03	19.7
Fatemi and Socie	-8.00E-01	4.00E-03	9.12E-05	1.36E-04	4.48E-05	25.9
SWTM	-7.90E-01	1.00E-03	2.62E-05	1.60E-04	1.34E-04	3.4
Goodman	-7.90E-01	4.00E-03	2.00E-08	3.96E-08	1.96E-08	1.9
Marrow	-7.90E-01	4.00E-03	6.84E-09	1.36E-08	6.75E-09	1.5

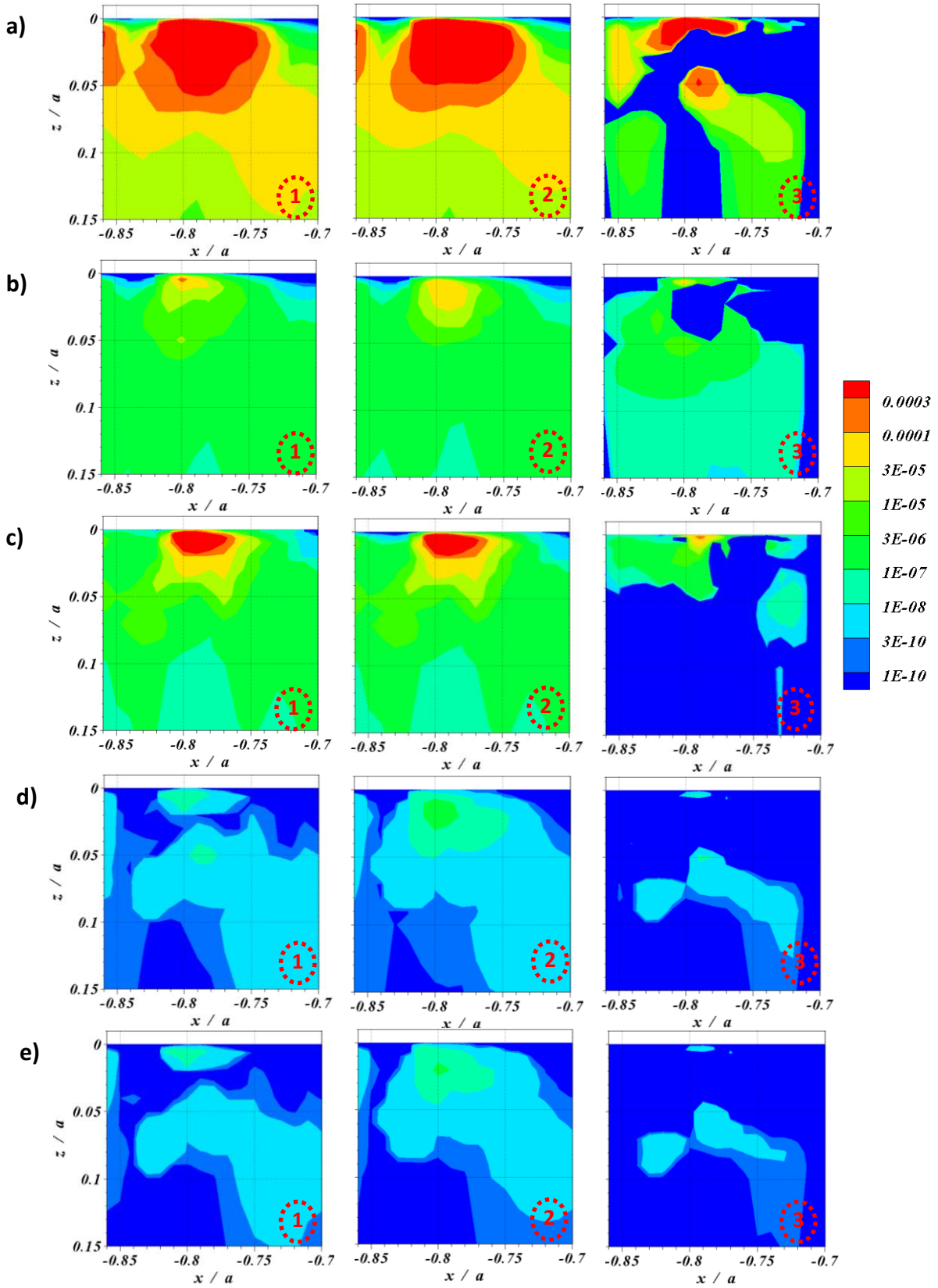

Figure 7.17 - Large scale fatigue damage contours for the asperity B at EHL profile C with and without and positive difference of residual stress as numbered 1,2 and 3 respectively for the models of; a - e) Chu, Fatemi and Socie, SWTM, Goodman and Marrow respectively.

In general the findings in this section has revealed similar area characteristics to those reported by Oila A et al. (2005) and can explain in terms of damage and stress analysis the relation between the microstructure aspects and micropitting. It can be concluded that:

1- Olia and Shaw state that a general feature seen in micropitted failure is the presence of small circular or semi-circular regions with diameter in the order of microns or tens of microns which are related to plastic deformation region which they denote PDR. They are located near the surface, and shows a very fine non-martensitic microstructure (no needles are observable) as shown in Figure 7.18 (a-c). These feature are similar to the area of compressive residual stress in the current research as shown in figure 7.19(a-b).

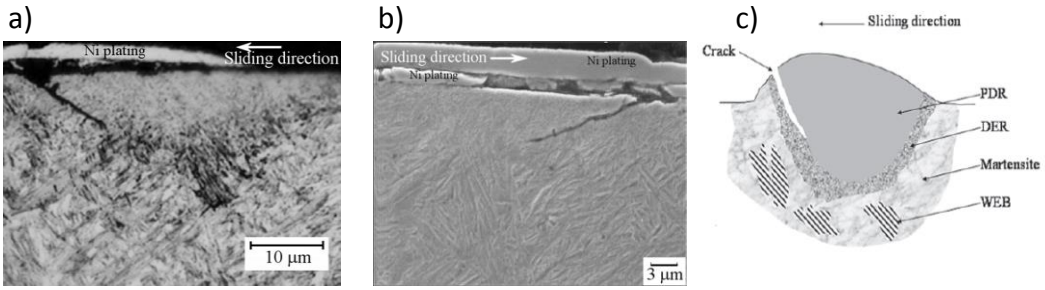

Figure 7.18 - Plastic deformation feature in terms of microstructure ; a) plastic deformation bordered by dark etching region DER , b)crack propagation at the border of PDR, c) Schematic figure for microstructure type (Oila A et al., 2005).

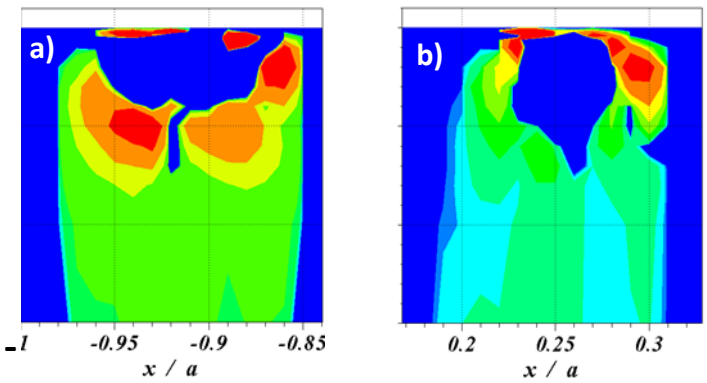

Figure 7.19 - Plastic deformation area related to compressive residual stress in terms of damage contour for different asperities using Fatemi and Socie; a) 1BA, b) 31AC .

2- Olia and Shaw also identify the Dark etching regions, denoted DER, that can be seen underneath the gear tooth surface either as a semi-circular zone as shown in figure 7.20(a) or as a continuous band, or most often as isolated zones as shown in figure 7.20(b). They state that the DER follow a semi-circular pattern and cracks are present at intersection points between the free surface and DER, however, the DER zone band does not reach the surface. It is also noted that the DER occur at provide the boundary of PDR. These boundaries are considered to be the critical zone where the crack initiation happens. All these features observed by material metallurgical analysis is can be seen to correspond to the circular band area of the residual stress and the corresponding damage as shown in the figure 7.21 (a-b). These observations may help to understanding of how these features take place, but it is important to note that the FEA is based on homogeneous material and does not include any metallurgical differences.

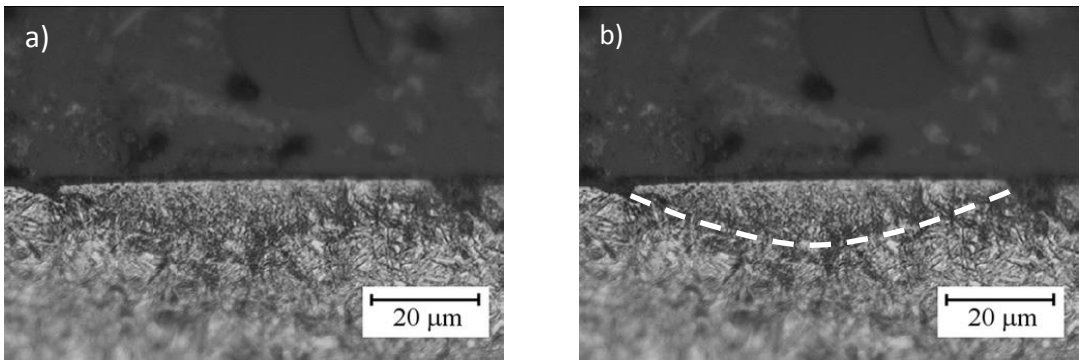

Figure 7.20 - Dark etching region DER in terms of microstructure; a) Figure from Oila et. Al. b) copy with semi-circular DER region indicated by broken curve, (Oila A et al., 2005).

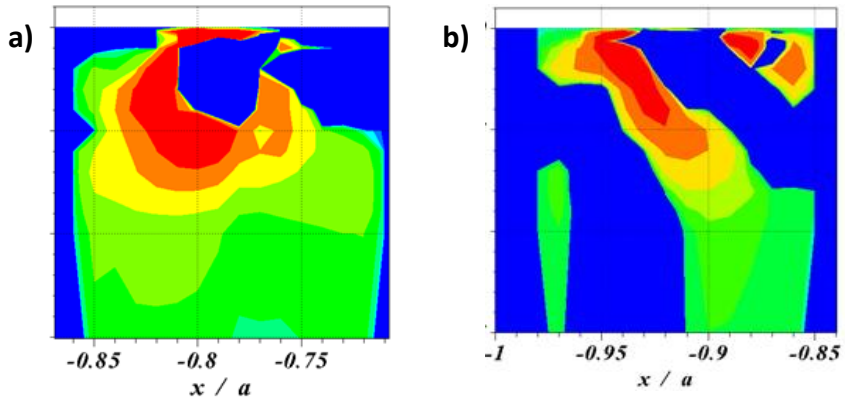

Figure 7.21 - Dark etching region DER area related to residual stress in terms of damage contour for different asperities using; a) 1BB using Fatemi and Socie, b) 7BA using Chu.

3- Olia and Shaw also showed the White etching region WER that reported in rolling element bearing, a certain directionality of microstructure has been seen in a group of specimens as shown in Figure 7.18(c) and 7.23. This feature can be seen to correspond to the feature of the damage in this study such that calculated by Chu and Fatemi Socie models as shown in figure 7.22(a-c).

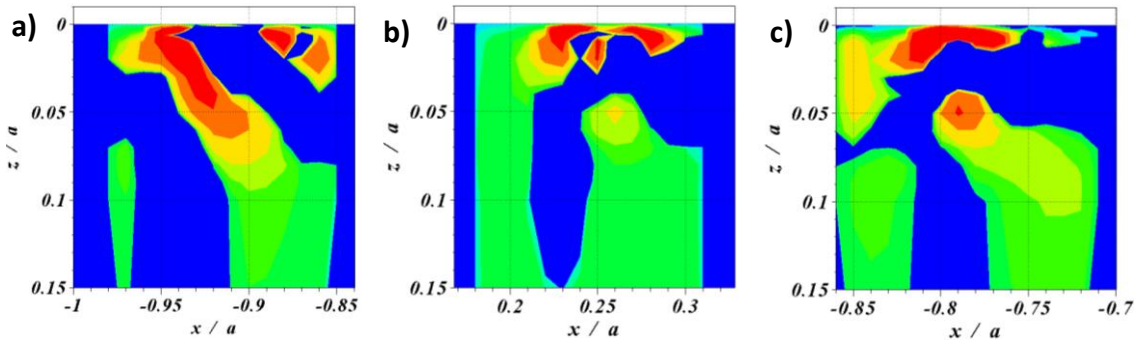

Figure 7.22- Dark etching region DER area and white etching region WER related to residual stress in terms of damage contours for different asperities using Chu ; a) 7BA, b) 31AC, c) 1BB.

4- Also it can be observed for both EDR , WER and PDR are located near to the surface $\sim 20\mu m$ similar to all the location of the damage take place due to the effect of residual stress that calculated by the above models.

5- Finally the positive maximum principal residual stress vectors that shown in Figures 5.10, 5.11 and 5.14 act at angles that are tangential to the surface or shallower angles such as between 10° to 35° that are found at the outer edge of the middle section of the asperity .This finding correspond to the inclination of WER reported by Olia, Shaw (2005) and as shown in the Figure 7.23.

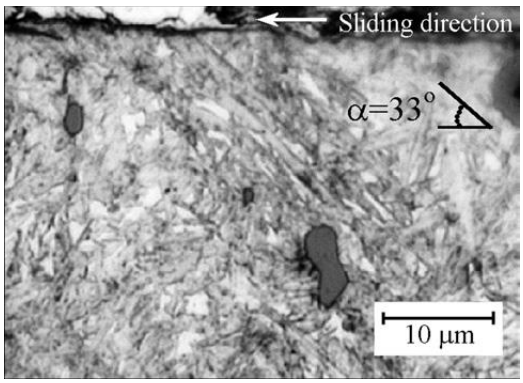

Figure 7.23 - White etching band WEB observed near to the surface where the angle of inclination to the surface is α=33^{o}.(Oila A et al., 2005)

7.4 Fatigue calculation based on a real profile

In this section, the fatigue damage calculations with and without residual stress were carried out on the real profiles of surface roughness of a test disk rig (Profile A and B) that were introduced in chapter 3 and 4. The multiaxial fatigue criteria that have been discussed in chapter 6 were used again and corresponding fatigue analyses were carried out for them for the EHL line contact of rough surfaces. The influence of the FEA residual stress for the same profiles and used for the fatigue damage calculations were investigated. The results are as presented previously and find that all the fatigue models can be seen to experience a further increase of damage when the residual stress is included. These comparisons are different for each model which shows they are quite different in the contours of the calculated damage and there are differences of an order of magnitude in the calculated accumulated damage.

Each Figure from 7.22 to7.27 and 7.29 to 7.30 shows a complete set of figures which can be used to compare damage contours for the real profile of surface roughness in question with residual stress included with damage contours for the same the real profile without residual stresses. At the first sight for all models fatigue damage contours related to the two profiles (A and B) appear very different. This is due to the amount of damage experienced with profile B which is greater than the damage experienced with profile A with all the fatigue damage calculations. That is because the number of asperities in profile B that are higher than 0.5μm is greater than the number of asperities involved in profile A for the same height. As a result profile B asperities experience more plastic deformation and then gain more residual stress. Figures 7.22(a) and7.23 (a) show the surface roughness profiles A and B extracted from the test disks and used in the fatigue calculation respectively. Figure 7.22(b) and 7.23(b) give the fatigue damage calculation results for the Chu model without residual stress. They show the high values of the accumulated fatigue damage calculated that is focussed near the surface of certain asperity features and is separated by areas between the asperities that are not subject to the same level of damage. Prominent asperities are subject to higher damage levels because the damage value is influenced by the asperity shape feature and its level in the contact as explained in chapter 6. Figures 7.22(c) and 7.23(c) give the corresponding results when the residual stress is included. It can be seen that significant differences are caused by including the FEA residual stress in the fatigue calculation. This is quantified in Figures 7.22(d) and 7.23(d) that present the damage difference calculated with and without residual stress. Also in both cases (Profile A and Profile B) the damage increases with increasing depth at the shallow region z/a< 0.1 as shown in Figures 7.22(b-d) and 7.23(b-d).

However, calculating fatigue damage corresponding to a much greater depth of z/a <0.1 give a trivial difference to the value of damage as shown from the figures, which confirms that the effect of the residual stress on the risk of predicted distress is limited to the a thin layer beneath the rough surface which is nearly to $\approx 30\mu m$. Higher shear stress levels that occur at z/a=0.79 in accordance with the Hertzian pressure distribution are not influenced by the plastic deformation of asperities. Figure 7.23 (d) shows the highest differences levels of predicted damage that exceed 0.0001 for profile B occur in the areas such as in between x/a=-0.8 and x/a=-0.744, x/a=-0.6 and x/a=-0.544, x/a=-0.256 and x/a=-0.2, x/a=0.084 and x/a=0.14, and between x/a=0.8 and x/a=1.0. However, profile A has a level of difference of order more than $3x10^{-5}$ which occurs in the areas between x/a=0.6 and x/a=0.656, x/a=0.856 and x/a=0.94 and between x/a=1.0 and x/a=1.07. Finally, it can be noticed for both profile A and B that most of the damage that is created by including the residual stress is built up at or very near to the surface.

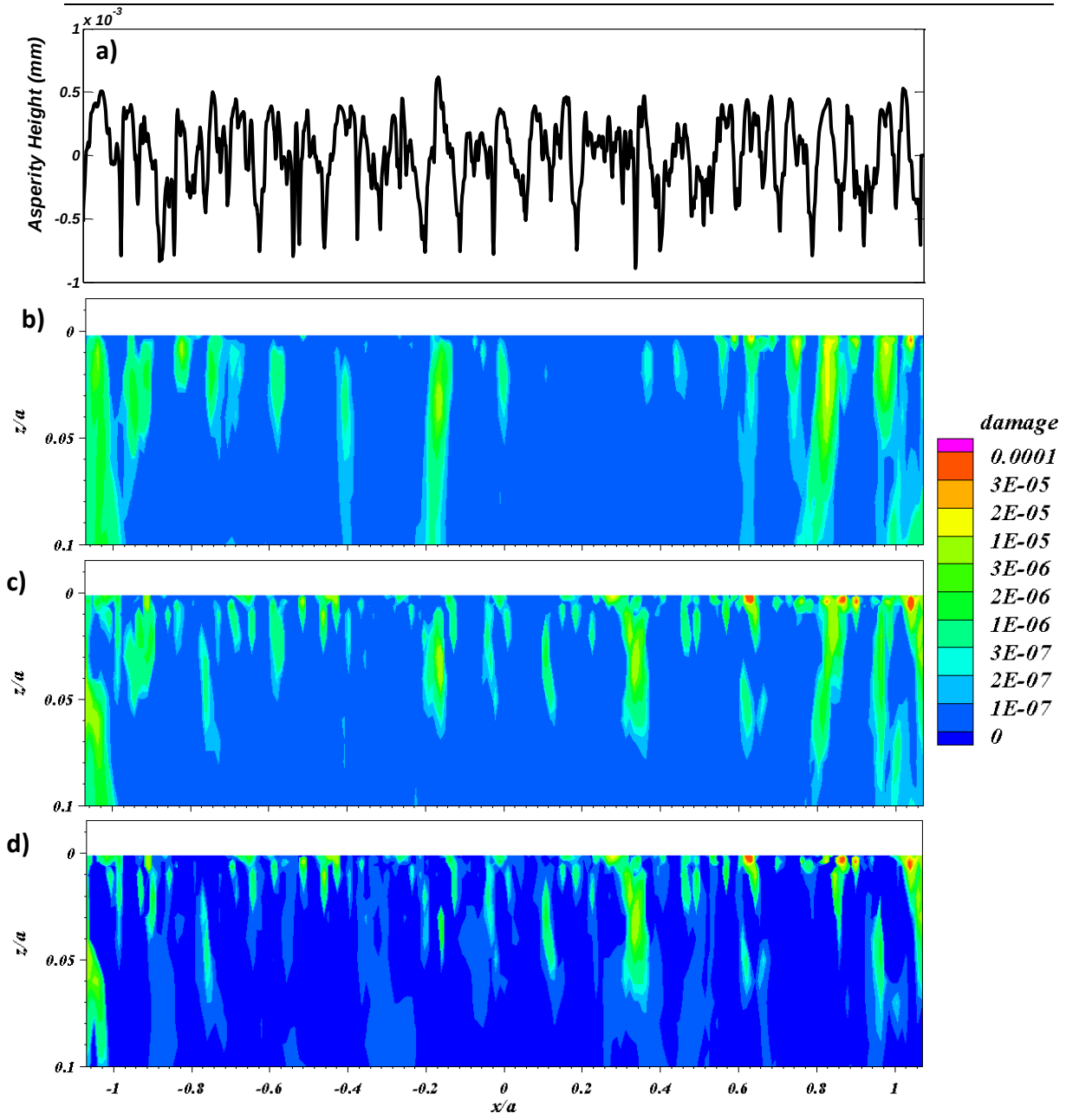

Figure 7.22 - Chu Model's contours of fatigue damage; a) EHL profile A, b) without residual stress, c) with residual stress, d) the positive difference.

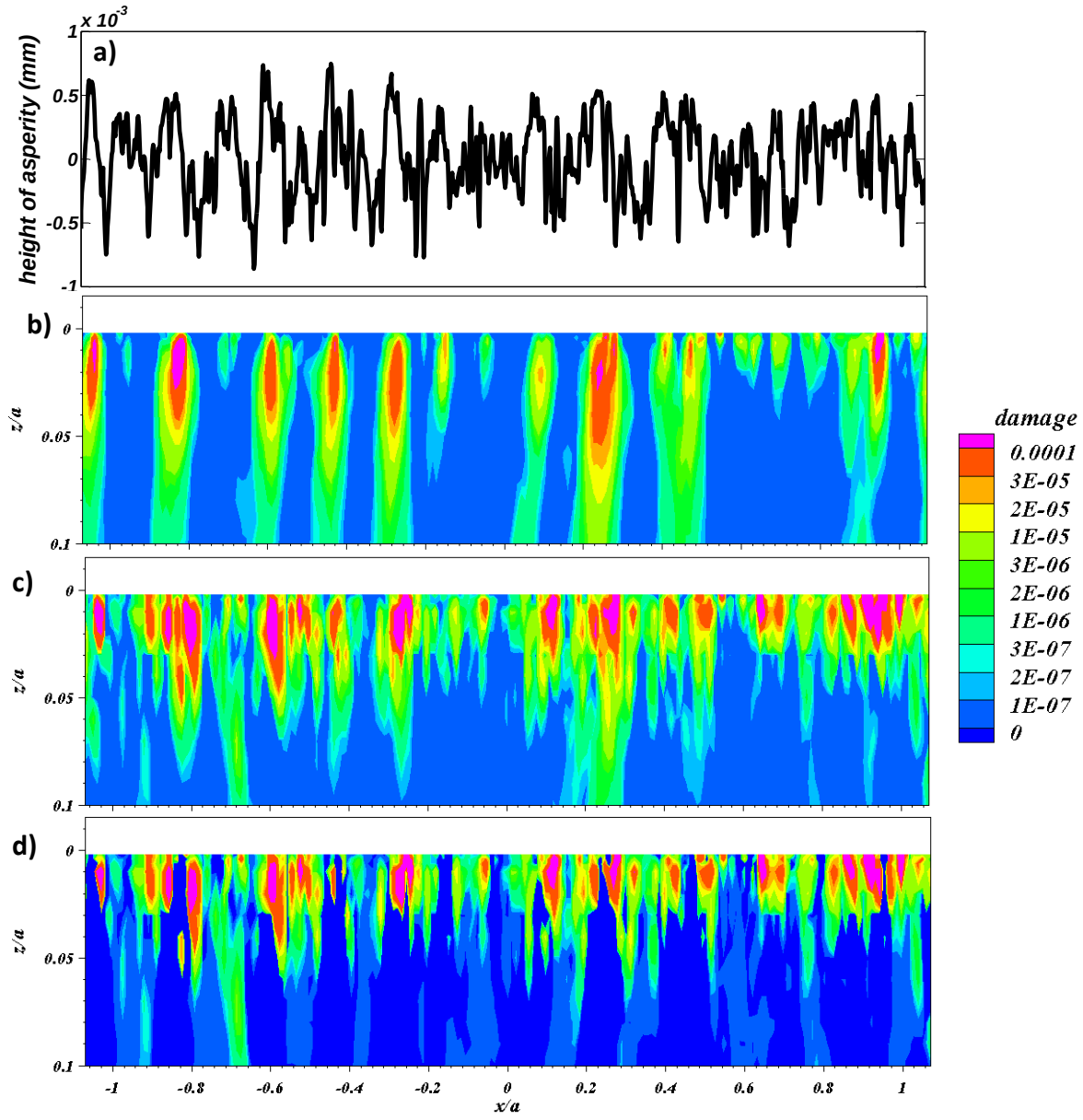

Figure 7.23- Chu Model's contours of fatigue damage; a) EHL profile B, b) without residual stress, c) with residual stress, d) the positive difference.

Tables 7.20 and 7.21 list the damage difference in decreasing order for the ten most significant damage difference points in Figures 7.22 and 7.23 and confirm that most of the damage caused by the residual stress occurs near the surface. Also it shows the residual stress influences that corresponding to the relatively high damage located in the surface layer which is most exposed to fatigue, and which includes the depth in which micropitting is seen to take place in practice. The calculated damage values

without residual stress for the ten points for profile A are in the range 2.48 to 3.85 and for profile B are in the range 4.04 to 5.96. These are of the similar magnitudes and cannot be picked out in the contour plot as the highest contour covers a large range of values.

Table 7.20 - The damage difference comparison of the significant points in profile A of the Chu fatigue damage model calculation with and without adding residual stress.

Index	*x/a*	*z/a*	*Damage without Residual stress*	*Damage with Residual stress*	*Damage difference between with and without Residual stress*
1	*-4.18E-01*	*0.00E+00*	*3.10E+00*	*3.57E+00*	*4.73E-01*
2	*6.21E-01*	*0.00E+00*	*3.85E+00*	*3.91E+00*	*6.12E-02*
3	*-4.39E-01*	*0.00E+00*	*3.01E+00*	*3.05E+00*	*4.58E-02*
4	*-9.96E-01*	*0.00E+00*	*2.48E+00*	*2.53E+00*	*4.56E-02*
5	*-6.64E-01*	*0.00E+00*	*3.66E+00*	*3.70E+00*	*4.45E-02*
6	*2.79E-01*	*0.00E+00*	*3.22E+00*	*3.26E+00*	*4.01E-02*
7	*-1.03E+00*	*0.00E+00*	*2.76E+00*	*2.80E+00*	*3.89E-02*
8	*-6.75E-01*	*0.00E+00*	*3.69E+00*	*3.73E+00*	*3.67E-02*
9	*2.89E-01*	*0.00E+00*	*3.17E+00*	*3.21E+00*	*3.27E-02*
10	*4.82E-01*	*0.00E+00*	*3.33E+00*	*3.36E+00*	*2.93E-02*

Table 7.21 - The damage difference comparison of the significant points in profile B of the Chu fatigue damage model calculation with and without adding residual stress.

Index	*x/a*	*z/a*	*Damage without Residual stress*	*Damage with Residual stress*	*Damage difference between with and without Residual stress*
1	*-3.32E-01*	*0.00E+00*	*4.60E+00*	*4.85E+00*	*2.51E-01*
2	*-3.21E-01*	*0.00E+00*	*4.81E+00*	*4.99E+00*	*1.81E-01*
3	*-5.03E-01*	*0.00E+00*	*5.39E+00*	*5.55E+00*	*1.60E-01*
4	*-3.64E-01*	*0.00E+00*	*4.38E+00*	*4.51E+00*	*1.24E-01*
5	*6.64E-01*	*0.00E+00*	*5.62E+00*	*5.74E+00*	*1.20E-01*
6	*6.75E-01*	*0.00E+00*	*5.28E+00*	*5.39E+00*	*1.15E-01*
7	*9.64E-01*	*0.00E+00*	*5.96E+00*	*6.07E+00*	*1.13E-01*
8	*-2.25E-01*	*0.00E+00*	*4.04E+00*	*4.14E+00*	*1.04E-01*
9	*2.68E-01*	*0.00E+00*	*5.62E+00*	*5.70E+00*	*8.56E-02*
10	*-3.43E-01*	*0.00E+00*	*4.33E+00*	*4.41E+00*	*8.38E-02*

Figure 7.24 and 7.25 represent the second result of the effect of residual stress on the fatigue damage calculated in this case using the Fatemi and Socie model (FS). Figures 7.24 and 7.25 have the same format as figures 7.22 and 7.23. The profiles are shown in parts (a), the calculated fatigue damage without residual stress in parts (b), the damage with residual stress in parts (c), and the positive damage differences in parts (d). Tables 7.22 and 7.23 then list the damage difference in decreasing order for the ten points having the most significant damage difference in the figures.

The same general effects of including residual stress can be seen in these figures and tables as was the case for the Chu model with the significant effects of including residual stress again occurring at or near the surface. However, using FS model in fatigue calculation shows less effect with residual stress causing smaller changes in the calculated damage values compare to Chu model. Figure 7.24 (d) and 7.25 (d) show the detrimental effects of the residual stress which is clear in the amount of coloured zones (excluding dark blue) that occur near to the surface area. These effects are much more apparent for profile B than profile A as shown in Figure 7.25(d) Tables 7.22 and 7.23 show the calculated damage values without residual stress for the ten points for profile A are in the range 0.0334 to 0.148 and for profile B are in the range 0.0731 to 0.371 respectively. These ranges confirm that using FS model in fatigue calculation would be less effect with residual stress that causing small reductions in the calculated damage values compare to Chu model.

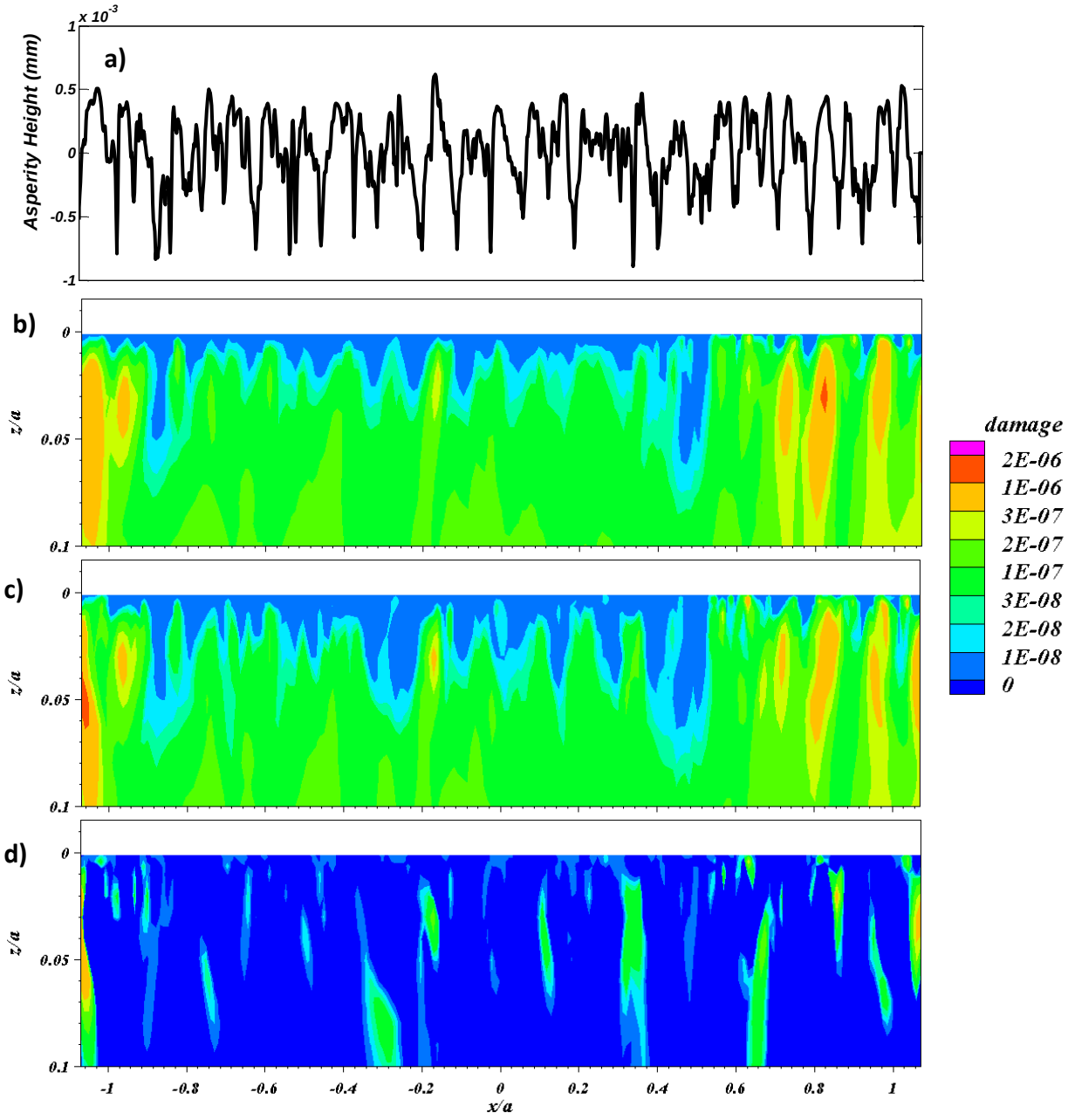

Figure 7.24 - Fatemi and Socie Model's contours of fatigue damage; a) EHL profile A, b) without residual stress, c) with residual stress, d) the positive difference.

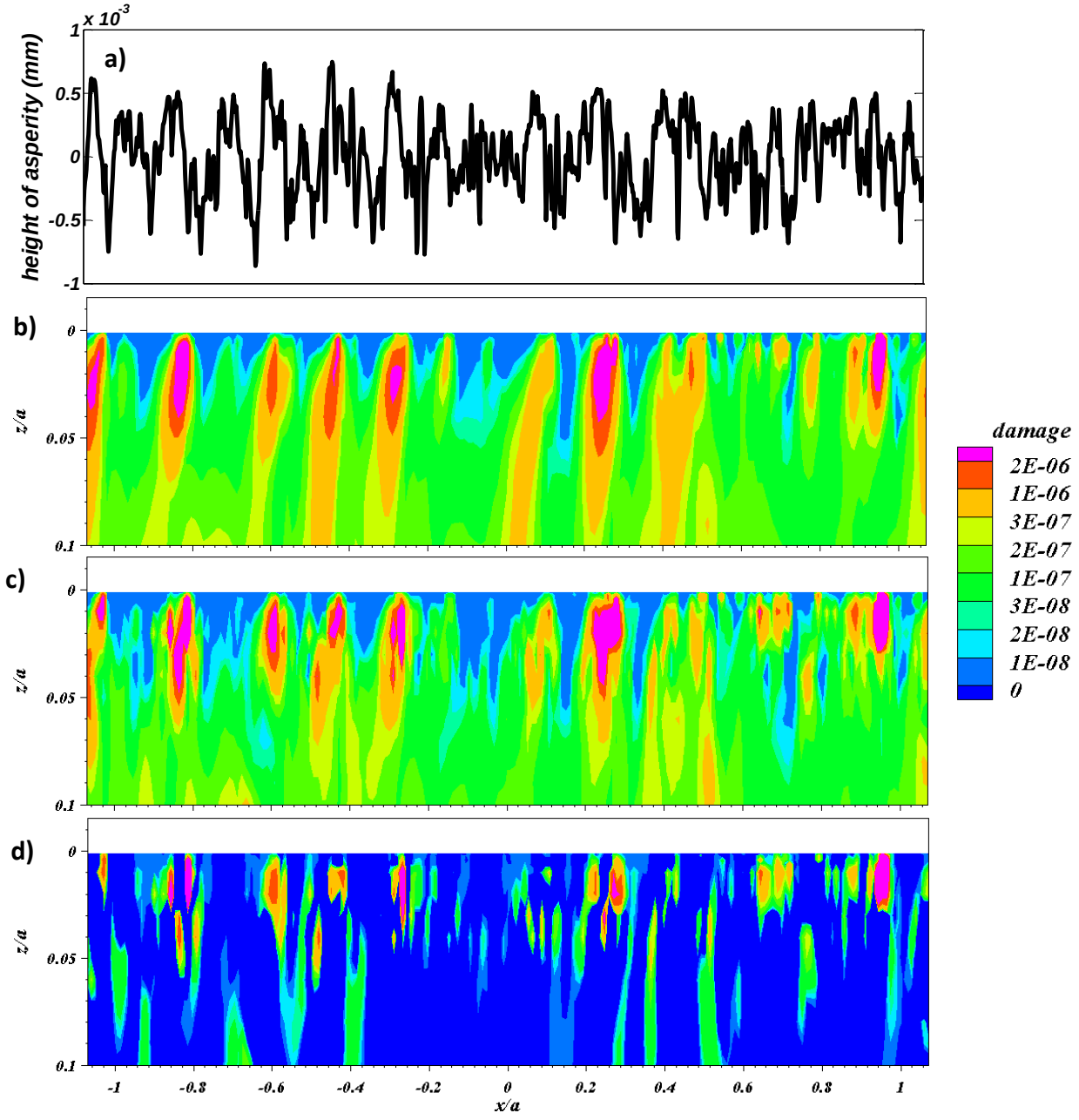

Figure 7.25 - Fatemi and Socie Model's contours of fatigue damage; a) EHL profile B, b) without residual stress, c) with residual stress, d) the positive difference.

Table 7.22 - The damage difference comparison of the significant points in profile A of the FS fatigue damage model calculation with and without adding residual stress.

Index	x/a	z/a	Damage without Residual stress	Damage with Residual stress	Damage difference between with and without Residual stress
1	1.02E+00	0.00E+00	1.04E-01	1.06E-01	2.27E-03
2	2.79E-01	0.00E+00	5.96E-02	6.13E-02	1.66E-03
3	2.89E-01	0.00E+00	6.03E-02	6.19E-02	1.63E-03
4	-1.04E+00	0.00E+00	1.48E-01	1.49E-01	1.36E-03
5	6.21E-01	0.00E+00	7.65E-02	7.78E-02	1.29E-03
6	6.32E-01	0.00E+00	7.70E-02	7.81E-02	1.08E-03
7	2.68E-01	0.00E+00	5.92E-02	6.02E-02	9.95E-04
8	3.86E-01	0.00E+00	6.43E-02	6.52E-02	9.56E-04
9	6.11E-01	0.00E+00	7.60E-02	7.70E-02	9.33E-04
10	-4.50E-01	0.00E+00	3.34E-02	3.43E-02	9.13E-04

Table 7.23 - The damage difference comparison of the significant points in profile B of the Fatemi and Socie fatigue damage model calculation with and without adding residual stress.

Index	x/a	z/a	Damage without Residual stress	Damage with Residual stress	Damage difference between with and without Residual stress
1	6.64E-01	0.00E+00	3.00E-01	3.10E-01	1.04E-02
2	9.64E-01	0.00E+00	3.71E-01	3.81E-01	9.61E-03
3	6.75E-01	0.00E+00	3.04E-01	3.12E-01	8.78E-03
4	2.68E-01	0.00E+00	2.35E-01	2.43E-01	7.93E-03
5	7.07E-01	0.00E+00	3.20E-01	3.27E-01	7.45E-03
6	2.89E-01	0.00E+00	2.26E-01	2.33E-01	6.74E-03
7	-9.00E-01	0.00E+00	7.31E-02	7.89E-02	5.80E-03
8	7.18E-01	0.00E+00	3.16E-01	3.22E-01	5.53E-03
9	-9.10E-01	0.00E+00	7.37E-02	7.91E-02	5.49E-03
10	-2.25E-01	0.00E+00	1.47E-01	1.52E-01	5.47E-03

Figure 7.26 and 7.27 show the effect of residual stress on the fatigue damage calculated for profiles A and B using the modified Smith Watson Topper model SWTM. The model has the mathematical form of Equation 6.21 which proposes that the fatigue damage under complex multiaxial loading can be calculated and the model is

more suitable for Mode I failure. Also the model considers the additional cyclic hardening that is created by rotating the principal stress and strain axis that leads to increase the stress terms (Li and Liu, 2011). This increasing of terms increases the fatigue damage as shown in Figures 7.26 and 7.27 and Tables 7.24 and 7.25 and then decreases the fatigue life as a result. The fatigue analyses presented for this model follow the same pattern as that for the Chu and the Fatemi and Socie models in terms of contour plots and table formats. This model shows very high response to incorporating residual stress in the fatigue calculations as shown Figures 7.26 and 7.27 and Tables 7.24 and 7.25. These show the regions of relatively high damage exceeding $3X10^{-6}$ are concentrated close to the surface within the approximate range $0.0 < z/a < 0.07$. It can be noticed from profile B in Figure 7.27 (b) that the particularly high damage areas are consequently quite localised having dimensions matching with the scale of surface roughness features. Therefore, the regions of high damage corresponding to the profile B are aligned with prominent asperity features however, this is not apparent in figure 7.26 (b) for profile A due to the low scale of surface roughness features.

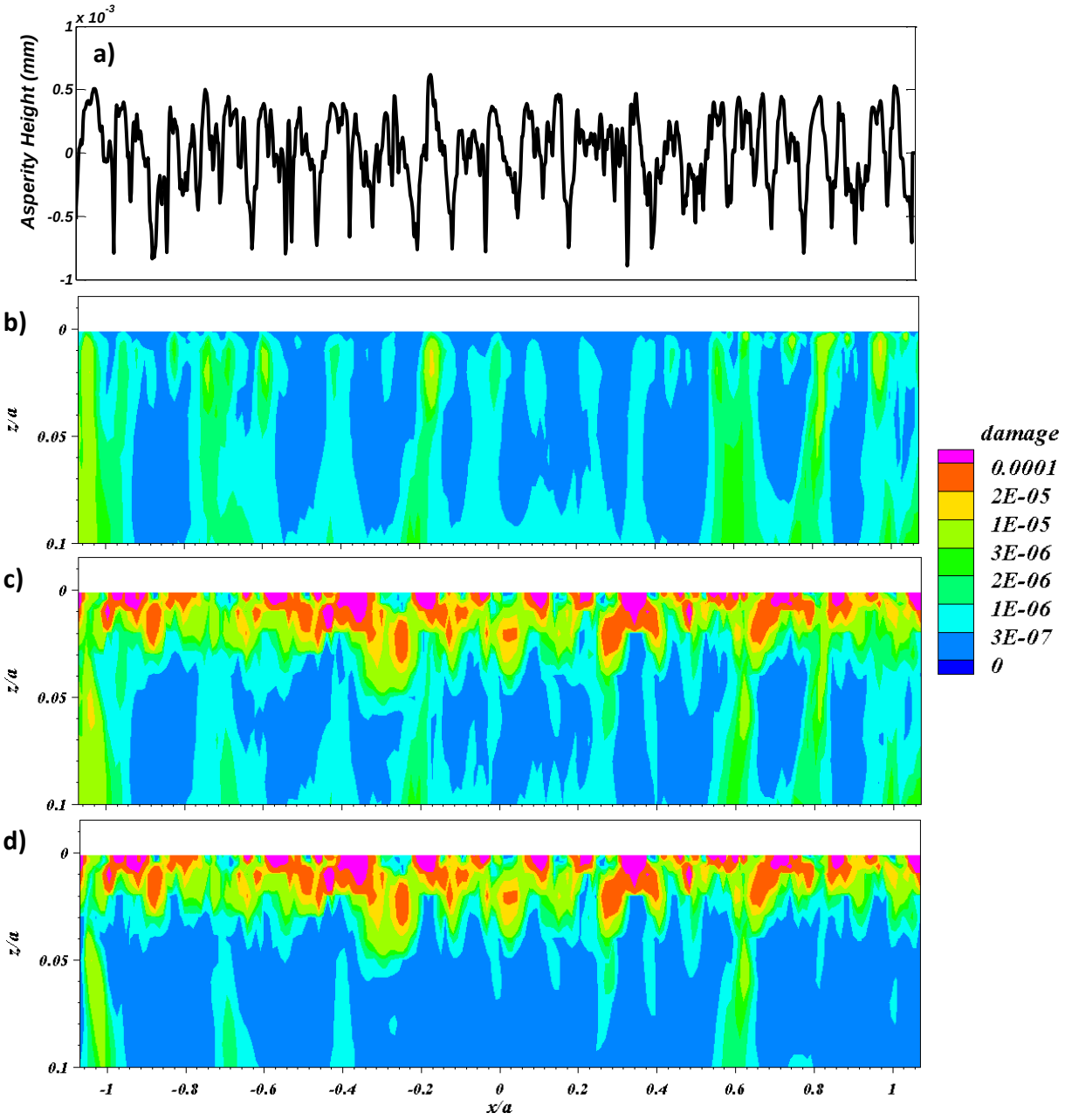

Figure 7.26- SWT (M) Model's contours of fatigue damage; a) EHL profile A, b) without residual stress, c) with residual stress, d) the positive difference.

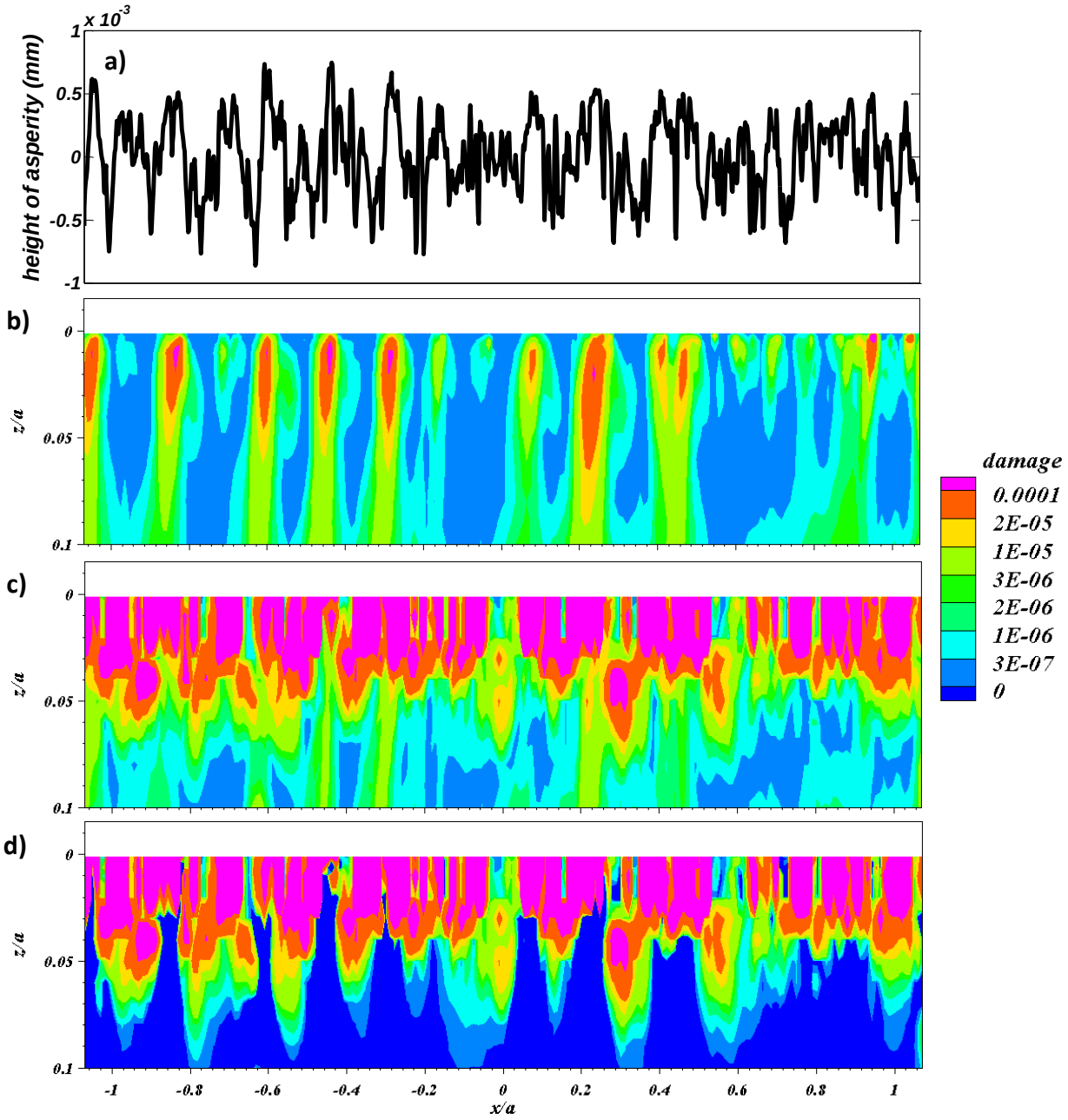

Figure 7.27 - SWT (M) Model's contours of fatigue damage; a) EHL profile B, b) without residual stress, c) with residual stress, d) the positive difference.

Bryant (2013) demonstrated that asperity residual stresses have the potential to initiate cracks perpendicular to the principal stress vector and to grow from the edge of the asperity towards the centre as can be seen in Figure 7.28 (a-b). Also Johnson (1989) confirmed that the failures initiate at the surface through plastic deformation of surface irregularities (asperities) whose height exceeds the thickness of the lubricant film and then propagate into the material solid at a critical angle (15^{o}-30^{o}) to the

surface which appears as a V-shaped in plan, pointing in the direction of motion of the surface as shown in the Figure 7.28(a-b) as well. All these features observed by researchers analysis can be seen to correspond to the finding of the residual stress effects and the corresponding damage as shown in the figure 7.28 (c) (d) as a circular band area beneath the surface. These observations may help to understanding of how these features occurred, but it is important again to note that the FEA is based on homogeneous material and does not include a metallurgical differences.

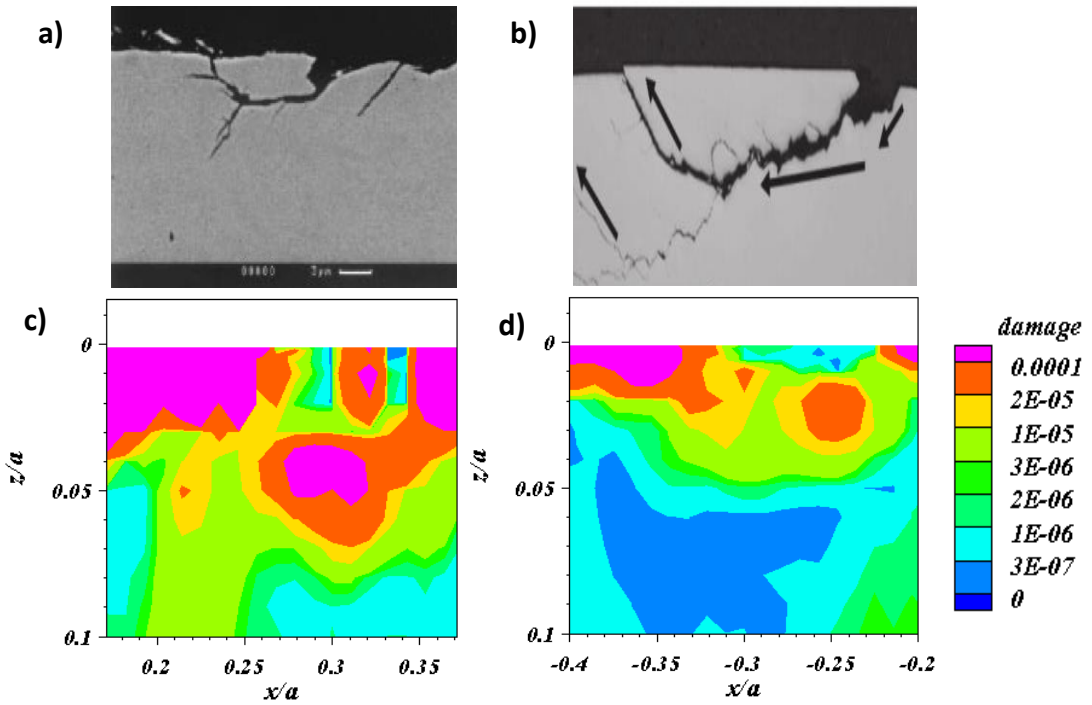

Figure 7.28 – Formation of micropits; a) a section of the crack path taken during the micropitting process. (Bull et al. 1999), b) V-shaped in plan for macro pits from the growth of micro-cracks (Moorthy and Shaw, 2013) , c) damage contours related to profile B, d) damage contours related to profile A.

Tables 7.24 and 7.25 have the same format as Tables 7.20 and 7.21 that list the damage difference in decreasing order for the ten points having the most significant damage difference in the Figures 7.26 and 7.27. They show the calculated damage

where most of the residual stress effects occur are on the boundary of the asperity and near to the surface. This finding matches the location of the maximum residual principal tensile stress vectors shown in Figure 5.15-17 where they are concentrated beneath the surface, and around the boundary of the asperity and where plastic deformation has occurred. It can be seen Table 7.24 and 7.25 show the calculated damage values without residual stress for the ten points for profile A are in the range $1.15x10^2$ to $1.42x10^2$ and for profile B are in the range $1.32x10^2$ to $1.71x10^2$. These ranges confirm that that profile B has more damage than profile A due to the effect of maximum residual stress that corresponds to the maximum deflection of profile's asperities B experienced. Also the two tables show that using the SWTM model in fatigue calculation shows high effects of asperity residual stress that cause significant increases in the calculated damage values compare to Chu and FS models.

Table 7.24 - The damage difference comparison of the significant points in profile A of the SWTM fatigue damage model calculation with and without adding residual stress.

Index	*x/a*	*z/a*	*Damage without Residual stress*	*Damage with Residual stress*	*Damage difference between with and without Residual stress*
1	*6.00E-01*	*0.00E+00*	*1.33E+02*	*1.37E+02*	*3.90E+00*
2	*5.68E-01*	*0.00E+00*	*1.32E+02*	*1.35E+02*	*2.69E+00*
3	*3.43E-01*	*0.00E+00*	*1.35E+02*	*1.37E+02*	*1.93E+00*
4	*3.54E-01*	*0.00E+00*	*1.27E+02*	*1.28E+02*	*1.70E+00*
5	*3.64E-01*	*0.00E+00*	*1.21E+02*	*1.23E+02*	*1.63E+00*
6	*2.46E-01*	*0.00E+00*	*1.31E+02*	*1.32E+02*	*1.40E+00*
7	*5.57E-01*	*0.00E+00*	*1.29E+02*	*1.31E+02*	*1.40E+00*
8	*-1.07E-02*	*0.00E+00*	*1.42E+02*	*1.43E+02*	*1.39E+00*
9	*3.75E-01*	*0.00E+00*	*1.15E+02*	*1.17E+02*	*1.39E+00*
10	*9.64E-01*	*0.00E+00*	*1.37E+02*	*1.38E+02*	*1.35E+00*

Table 7.25 - The damage difference comparison of the significant points in profile B of the SWTM fatigue damage model calculation with and without adding residual stress.

Index	*x/a*	*z/a*	*Damage without Residual stress*	*Damage with Residual stress*	*Damage difference between with and without Residual stress*
1	*6.86E-01*	*0.00E+00*	*1.69E+02*	*1.73E+02*	*4.19E+00*
2	*-4.50E-01*	*0.00E+00*	*1.40E+02*	*1.43E+02*	*3.14E+00*
3	*3.86E-01*	*0.00E+00*	*1.52E+02*	*1.56E+02*	*3.10E+00*
4	*4.71E-01*	*0.00E+00*	*1.71E+02*	*1.74E+02*	*3.10E+00*
5	*4.61E-01*	*0.00E+00*	*1.65E+02*	*1.68E+02*	*2.82E+00*
6	*-7.71E-01*	*0.00E+00*	*1.32E+02*	*1.35E+02*	*2.72E+00*
7	*-6.96E-01*	*0.00E+00*	*1.38E+02*	*1.41E+02*	*2.58E+00*
8	*2.57E-01*	*0.00E+00*	*1.56E+02*	*1.59E+02*	*2.40E+00*
9	*-3.21E-01*	*0.00E+00*	*1.45E+02*	*1.47E+02*	*2.27E+00*
10	*-5.03E-01*	*0.00E+00*	*1.46E+02*	*1.48E+02*	*2.18E+00*

Finally, the last trial criterion in this section involves is effective stress amplitude (Von Mises) expressed in equation 6.22. As for the previous trials, Figure 7.29 and 7.30 demonstrate the contours of fatigue damage obtained for the two profiles. It can be seen in Figures 7.29(b) and 7.30 (b) that the islands of damage values calculated are separated by areas that are not subject to anything like the same level of damage and the accumulated damage calculated is localised near the surface of specific asperity features. Several prominent asperities are subject to more damage levels such as those located in Figure 7.30 at x/a =-1.02, x/a =-0.7 , at x/a =-0.6, x/a = -0.2 and at x/a =0.9, x/a = 1.0 etc. This observation is in good agreement with the results obtained from the previous critical plane models. However, this criterion shows a smaller effect with residual stress causing small reductions in the calculated damage values and does not respond in a significant way to inclusion of the FEA residual stress induced in the material. That is could be because, this approach dose not be accurately captured the differing effects of axial tension and compression mean stresses in multiaxial stress

loading. In addition, the orientation of fatigue cracks with respect to loading axes is not quantitatively determined from this criterion. Also Tables 7.26 and 7.27 shows that the ten high damage points experience a reduction in damage when the residual stress is included. Both of the Tables show that most of the damage that is created by residual stress is built up below the surface not at the surface as took place with the previous models.

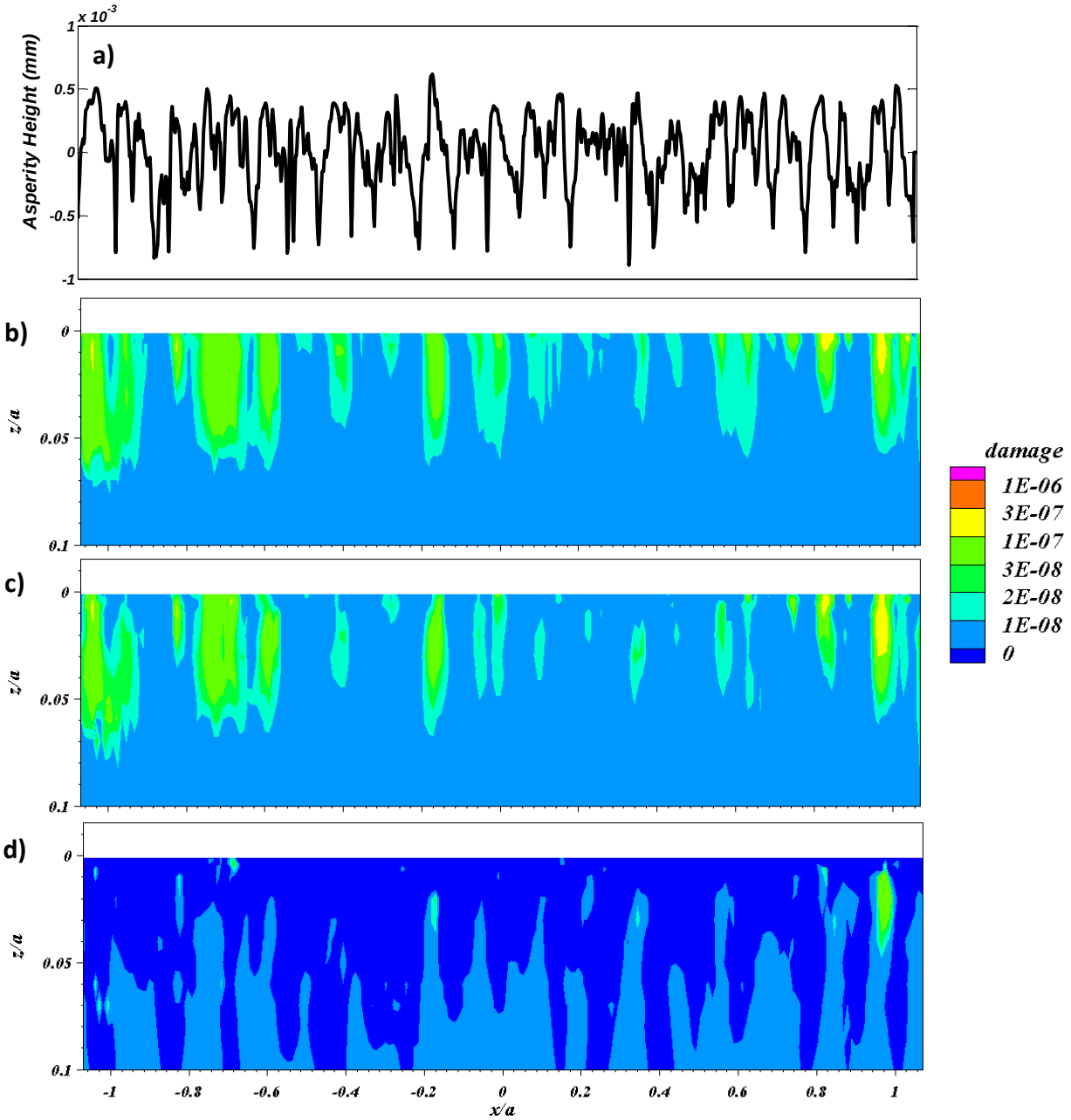

Figure 7.29 - Von Mises Model's contours of fatigue damage; a) EHL profile A, b) without residual stress, c) with residual stress, d) the positive difference.

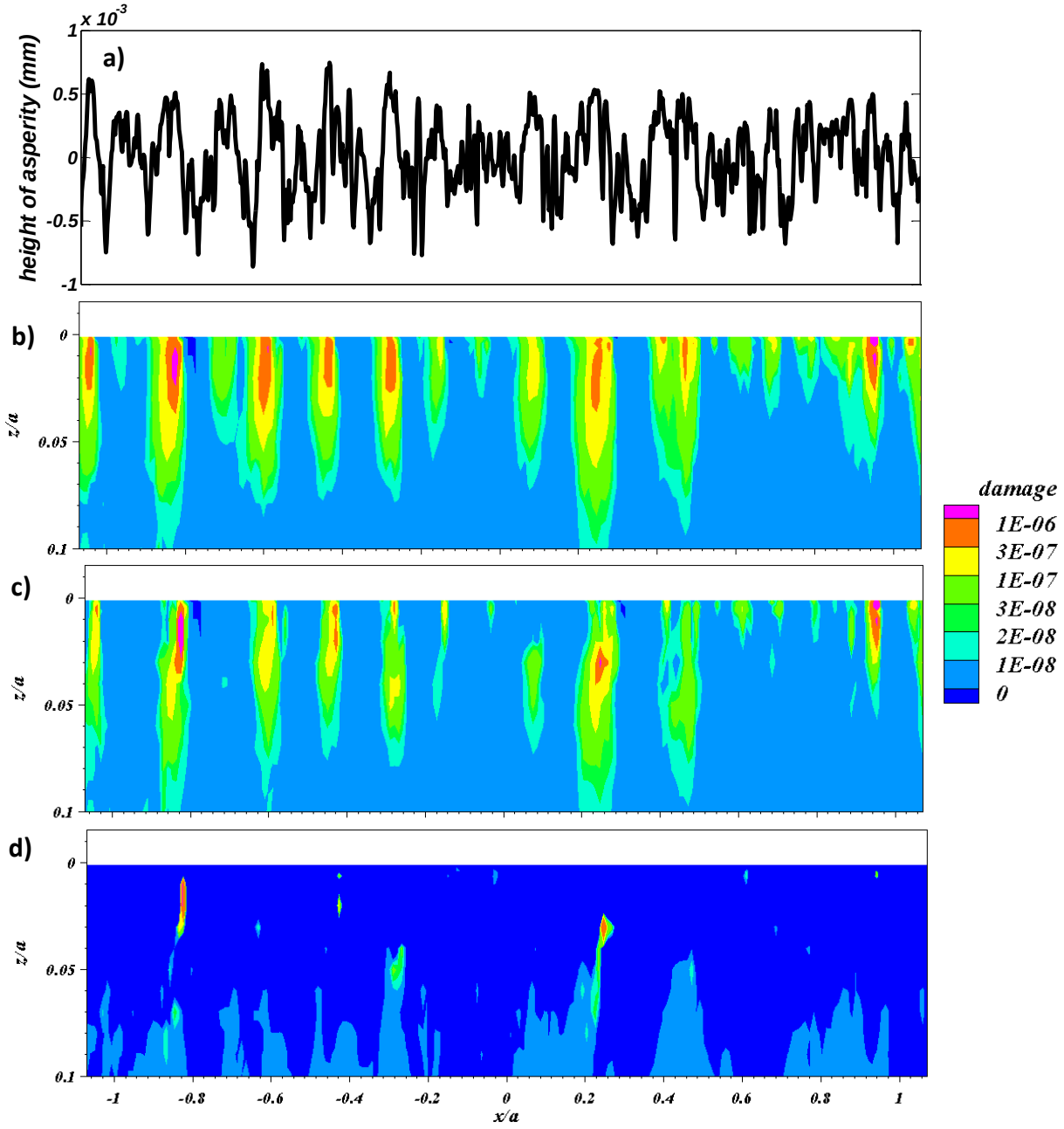

Figure 7.30 - Von Mises Model's contours of fatigue damage; a) EHL profile B, b) without residual stress, c) with residual stress, d) the positive difference.

Table 7.26 - The damage difference comparison of the significant points in profile A of the Von Mises fatigue damage model calculation with and without adding residual stress.

Index	*x/a*	*z/a*	*Damage without Residual stress*	*Damage with Residual stress*	*Damage difference between with and without Residual stress*
1	*9.64E-01*	*2.00E-02*	*9.16E-08*	*1.85E-07*	*9.31E-08*
2	*9.85E-01*	*2.00E-02*	*8.02E-08*	*1.59E-07*	*7.90E-08*
3	*9.75E-01*	*2.00E-02*	*1.03E-07*	*1.66E-07*	*6.23E-08*
4	*9.64E-01*	*1.00E-02*	*1.24E-07*	*1.79E-07*	*5.46E-08*
5	*9.75E-01*	*1.00E-02*	*1.45E-07*	*1.99E-07*	*5.43E-08*
6	*9.75E-01*	*3.00E-02*	*5.37E-08*	*9.56E-08*	*4.18E-08*
7	*9.64E-01*	*3.00E-02*	*6.71E-08*	*1.01E-07*	*3.43E-08*
8	*-6.86E-01*	*4.00E-03*	*7.86E-08*	*1.09E-07*	*3.08E-08*
9	*9.85E-01*	*3.00E-02*	*5.94E-08*	*8.71E-08*	*2.77E-08*
10	*9.64E-01*	*4.00E-02*	*2.43E-08*	*5.08E-08*	*2.65E-08*

Table 7.27 - The damage difference comparison of the significant points in profile B of the Von Mises fatigue damage model calculation with and without adding residual stress.

Index	*x/a*	*z/a*	*Damage without Residual stress*	*Damage with Residual stress*	*Damage difference between with and without Residual stress*
1	*-8.25E-01*	*2.00E-02*	*1.32E-06*	*2.54E-06*	*1.22E-06*
2	*-8.25E-01*	*1.00E-02*	*1.66E-06*	*2.85E-06*	*1.19E-06*
3	*2.46E-01*	*3.00E-02*	*4.20E-07*	*1.30E-06*	*8.83E-07*
4	*-8.36E-01*	*3.00E-02*	*3.61E-07*	*5.48E-07*	*1.87E-07*
5	*-4.28E-01*	*2.00E-02*	*3.87E-07*	*5.67E-07*	*1.80E-07*
6	*9.43E-01*	*6.00E-03*	*8.71E-07*	*9.95E-07*	*1.24E-07*
7	*-4.28E-01*	*6.00E-03*	*6.10E-07*	*6.98E-07*	*8.77E-08*
8	*-8.25E-01*	*3.00E-02*	*5.69E-07*	*6.54E-07*	*8.56E-08*
9	*2.57E-01*	*3.00E-02*	*2.77E-07*	*3.55E-07*	*7.76E-08*
10	*9.43E-01*	*4.00E-03*	*8.32E-07*	*8.97E-07*	*6.43E-08*

7.5 Conclusion

Fatigue life calculations with residual stress and without residual stress were carried out on a real profile of surface roughness of a test disk rig. The fatigue analysis confirms the effect of the tensile and compressive residual stresses in a negative and

positive direction respectively on the fatigue damage and fatigue life. All the fatigue models that have been used in this chapter have been applied with and without residual stresses, to obtain the theoretical life of the material that experienced the EHL stress history and the induced residual stress. All models showed response to incorporating residual stress in the fatigue calculations where the models fatigue life analysis reveals the shortest fatigue life for the models involving the tensile residual stress compared to the fatigue life obtained using the same model without induced residual stresses. The calculated damage contours are quite different when the different models are compared. The findings in this chapter have explained in terms of damage and stress analysis the relation between the residual stress effects and surface failure such as micropitting. Also it shows that using the SWTM model in fatigue calculation shows high effects of asperity residual stress that cause significant increases in the calculated damage values compare to Chu, FS and Von Mises models. So, there are differences of an order of magnitude or more between the different models. Finally, the way in which including residual stress affects the results is different such as with Chu and Modified SWTM models.

Chapter 8

Conclusion and future work

3.1 Summary

This study has been concerned with using EHL analysis to study the contact mechanics that are related to calculating surface contact fatigue such as micropitting and evaluating the residual stress effect. It gives an explanation as to why sub-surface initiated contact fatigue happens and why the effects of residual stress are of particular importance to understand the failure mechanism associated with rough surface EHL. Prior to achieving the main objective of this thesis, there are various aspects of the analyses carried out and results which lead to the conclusions presented in section 8.2. In addition the research has identified a number of areas for future work, given in section 8.3, that would develop the initial ideas brought together in this thesis as the basis for one or more future research projects.

3.2 Conclusions

- The profile alignment procedure presents an effective technique for finding the optimal correspondence between two roughness profiles that have different mean lines following filtering to remove form and waviness. It is based on the concept of smooth alignment curves passing through deep valley reference positions that are not affected by the plastic deformation occurring at the asperity tips.

  It can be concluded that this technique makes it possible to quantify the change in surface roughness at asperity features due to plastic deformation by careful

comparison of profiles before and after running-in. These changes take place rapidly

and lead to a stable surface that then evolves slowly due to subsequent wear processes.

- A FEA plane strain contact analysis the experimental rollers set up to replicate semi-infinite body contact allows the process of plastic deformation of surface asperities to be explored. It is not possible to determine the worst loadcase for the actual asperities in contact, but loading the surface against a rigid counterface determines the residual shape of the asperity when the load is removed and the corresponding residual stress field.

  It can be concluded that the changes of shape observed in the FEA contact analysis over a series of loads form a family of shape changes that are similar to those observed from the experimental comparisons. The change of shape can thus be used to tie the FEA analysis result at a specific asperity load to the experimentally observed change of shape and thus infer the most adverse contact load experienced by the asperity in the experiment, indirectly. This also identifies the form of the associated residual stress field to which the asperity will be subjected by the running-in process that it has experienced.

  It can be concluded that very high residual tensile stresses are developed in a zone that surrounds the compressed core of plastically deformed asperities. The greatest residual tensile stresses occur at or near the surface where the tensile zone is very thin. This may well be instrumental in the formation of surface cracks that can propagate to form micropitting fatigue damage. This possibility is underlined by the observation that the largest residual tensile stresses are often

seen to occur just beyond the limits of the load bearing land formed at the modified asperity where crack propagation by fluid pressurisation during over-rolling has been hypothesised by other researchers without any consideration of residual stress.

- The effects of including asperity residual stress in fatigue calculations was tested by carrying out a range of fatigue analyses with and without inclusion of the residual stress field determined by the methods established in the research.

  It can be concluded that the residual stress due to running-in of asperities does cause changes in the damage prediction and calculated fatigue life of the surfaces. These changes can be significant at some positions in the material but are not necessarily detrimental. For the cases investigated and fatigue models used in this research the changes due to residual stress do not indicate that significant changes to the calculated fatigue lives are caused by the residual stress fields imposed.

3.3 Suggestions for Future Work

The present study is based on FEA analysis with homogeneous material for reasons of simplicity in this first study, although this could have a significant effect. Therefore, considering metallurgical differences in the FEA analysis for future work could be incorporated and will allow the approach to more closely model the real condition of the material.

Another possibility for future work would to investigate whether the loading condition of normal contact with no friction is able to capture the residual asperity shape and

residual stress field correctly. Since the asperity loading in the real contact occurs due to the sliding motion of the surfaces, introducing frictional loading to the contact in the FEA analysis would be worthwhile to test the sensitivity of the residual shape to this. A further development would be to load the asperities on two rough surfaces by modelling their sliding motion in the FEA analysis.

The present study considered a plane strain line contact elastic-plastic model whose roughness is extruded perpendicular to the plane to pretend the contact between a rigid body and an arc. This is a good initial model of transverse ground surfaces and spur gear flanks, for example, but in helical gears the asperity features often cross each other at low angles typically in the range of 0 to 5 °. Modelling this situation in a 3D FEA contact analysis would be challenging from a consideration of the demands of mesh resolution. However it would be valuable to understand the difference between the residual stress fields caused by elastic-plastic contact of crossing asperities and the less demanding plane strain case modelled in this thesis. This question could be approached with analytic shapes to specify the asperities as a first approach.

The influence of compressive residual stress has been investigated by other researchers as referred to in the literature review. However, these studies did not take tensile residual stress into account or contain any detailed discussion of fatigue damage with and without residual stress. Thus there is an opportunity to develop the investigation of the influence of a generic roughness profile built with geometrical parameters as shown in the figure 2.13 by incorporating this study's simulation model to evaluate the influence of tensile/compressive residual stresses due to running-in operation on fatigue lifetime. The prediction of pitting and micropitting for the rough

surface contact is an area where more understanding is required and should be considered for future investigation.

Appendix AA-1

Table A.1 - The composition of RR6010 steel for the disk were manufactured from case-carburising Nickel-Chromium alloy steel (Rolls-Royce specification RR6010).

Element	C	Si	Mn	P	S	Ni	Cr	Mo
Max.	0.18	0.35	0.55	0.015	0.012	4.30	1.40	0.30
Min.	0.14	0.10	0.25	0.0	0.0	3.80	1.00	0.20

Table A.2 - The typical heat treatment for aerospace gear's specification were used for disk.

Normalise @ 930°C ± 10°C for 3 hours ± 15 minutes
Harden @ 850°C ± 10°C for 3 hours ± 15 minutes
Temper @ 530°C ± 10°C for 3 hours ± 15 minutes
Carburise @ 927°C ± 10°C to yield a carburised case depth (Rc 50) of 0.036" to 0.042", with a surface carbon (second 0.002" cut) of 0.65% to 0.95% carbon
Cool to room temperature after carburising
Stress relieve @ 566°C to 621°C for 4 hours ± 15 minutes, then air cool
Harden @ 788°C to 829°C for 30 minutes, then oil quench (24°C to 60°C)
Subzero treat, within 60 minutes of quenching, for 3 hours minimum at -79°C or lower
Temper @ 160°C ±5°C for 3 hours ± 15 minutes
Final carburised surface hardness to be HRC 60 to 63
Case depth (HRC 50) to be 0.036" to 0.042"
HRC 60 depth to be 45% of 0.036" (0.016" of case)
Core hardness to be HRC 36 to 41
Normalise @ 930°C ± 10°C for 3 hours ± 15 minutes

Appendix AA-2

Table AA.1 - Fatigue Parameter obtained by using the critical plane model (the Fatemi and Socie model) with σ_n^{max} normalised with σ_y, $(K = 0.0)$.

The numbers of effective loading cycles in the plane orientation equals== 36

The total damage equals== 3.3631953E-04

The angle in radian == 0.4886922, The angle in degree == 28 °

index	Cycles start	Cycles End	Cycles damage	γ_a	$\frac{\sigma_n^{max}}{\sigma_y}$	F.B
36	142	160	0.16593E-03	0.93421E-02	-0.10381E+01	0.93421E-02
35	125	130	0.12785E-03	0.87633E-02	-0.89973E+00	0.87633E-02
16	132	136	0.31051E-04	0.65628E-02	-0.13463E+01	0.65628E-02
19	148	155	0.10944E-04	0.55633E-02	-0.10381E+01	0.55633E-02
18	150	152	0.32197E-06	0.36861E-02	-0.13467E+01	0.36861E-02
34	121	123	0.22342E-06	0.35541E-02	-0.54029E+00	0.35541E-02
33	194	199	0.52419E-08	0.24917E-02	-0.48082E+00	0.24917E-02
23	187	188	0.26596E-11	0.12467E-02	-0.58695E+00	0.12467E-02
32	201	206	0.39408E-13	0.84965E-03	-0.74032E-01	0.84965E-03
26	195	197	0.78000E-15	0.59460E-03	-0.51360E+00	0.59460E-03
21	169	172	0.24363E-15	0.53486E-03	-0.36260E+00	0.53486E-03
25	190	191	0.15847E-15	0.51433E-03	-0.53622E+00	0.51433E-03
20	163	165	0.98384E-18	0.32389E-03	-0.48342E+00	0.32389E-03
22	182	184	0.15434E-18	0.27365E-03	-0.59881E+00	0.27365E-03

Table AA.2 -Fatigue Parameter obtained by using the critical plane model (the Fatemi and Socie model) with σ_n^{max} normalised with σ_y, $(K = 0.1)$

The number of effective loading cycles in the plane orientation equals== 37

The total damage equals== 2.4041531E-04

The angle in radian == 0.9424778, The angle in degree == 54 °

index	Cycles start	Cycles End	Cycles damage	γ_a	$\frac{\sigma_n^{max}}{\sigma_y}$	F.B
37	138	159	0.12465E-03	0.92664E-02	-0.59799E+00	0.87123E-02
36	120	129	0.10877E-03	0.85540E-02	-0.13506E+00	0.84385E-02
19	146	154	0.45215E-05	0.54477E-02	-0.93225E+00	0.49398E-02
17	132	136	0.15847E-05	0.50394E-02	-0.13438E+01	0.43622E-02
35	186	199	0.59923E-06	0.40640E-02	-0.33608E+00	0.39274E-02
18	149	152	0.28612E-06	0.41988E-02	-0.13247E+01	0.36425E-02
28	188	192	0.72259E-09	0.21497E-02	-0.33608E+00	0.20774E-02
16	123	125	0.97257E-10	0.18430E-02	-0.61269E+00	0.17301E-02
27	195	196	0.15959E-15	0.53682E-03	-0.41314E+00	0.51464E-03
24	168	170	0.29403E-17	0.36715E-03	-0.25423E+00	0.35782E-03
25	181	183	0.49973E-18	0.31830E-03	-0.43227E+00	0.30454E-03
34	202	204	0.44558E-19	0.24845E-03	-0.16414E+00	0.24437E-03

Table AA.3 -Fatigue Parameter obtained by using the critical plane model (the Fatemi and Socie model) with σ_n^{max} normalised with σ_y, $(K = 0.2)$

The number of effective loading cycles in the plane orientation equals== 36

The total damage equals== 2.0205716E-04

The angle in radian == 0.9773844, The angle in degree == 56^{o}

index	Cycles start	Cycles End	Cycles damage	γ_a	$\frac{\sigma_n^{max}}{\sigma_y}$	F.B
36	120	159	0.14097E-03	0.91905E-02	-0.11848E+00	0.89727E-02
20	129	138	0.58525E-04	0.85783E-02	-0.69278E+00	0.73897E-02
19	145	154	0.17934E-05	0.54481E-02	-0.94071E+00	0.44231E-02
35	186	199	0.44172E-06	0.40794E-02	-0.33480E+00	0.38062E-02
17	131	136	0.28814E-06	0.50007E-02	-0.13555E+01	0.36450E-02
18	149	152	0.43214E-07	0.41573E-02	-0.13521E+01	0.30331E-02
28	188	192	0.49861E-09	0.21526E-02	-0.33480E+00	0.20085E-02
16	123	124	0.70335E-11	0.16284E-02	-0.81776E+00	0.13621E-02
27	195	196	0.11847E-15	0.54549E-03	-0.40888E+00	0.50088E-03
25	168	170	0.20432E-17	0.36439E-03	-0.25022E+00	0.34616E-03
26	181	183	0.73550E-18	0.34479E-03	-0.42574E+00	0.31543E-03
29	202	204	0.21638E-19	0.23676E-03	-0.16710E+00	0.22885E-03

Table AA.4 -Fatigue Parameter obtained by using the critical plane model (the Fatemi and Socie model) with σ_n^{max} normalised with σ_y, $(K = 0.5)$.

The number of effective loading cycles in the plane orientation equals== 37

The total damage equals== 1.4798369E-04

The angle in radian == 1.256637, The angle in degree == 72 °

index	Cycles start	Cycles End	Cycles damage	γ_a	$\frac{\sigma_n^{max}}{\sigma_y}$	F.B
37	118	127	0.13279E-03	0.89860E-02	-0.31757E-01	0.88433E-02
36	137	158	0.14920E-04	0.83213E-02	-0.60020E+00	0.58241E-02
35	167	199	0.27124E-06	0.40808E-02	-0.22426E+00	0.36232E-02
28	188	191	0.26283E-10	0.19220E-02	-0.40207E+00	0.15356E-02
18	131	135	0.22754E-11	0.57527E-02	-0.15727E+01	0.12290E-02
20	145	153	0.36889E-13	0.54933E-02	-0.16925E+01	0.84453E-03
17	122	124	0.46503E-15	0.11981E-02	-0.10531E+01	0.56725E-03
19	149	151	0.29164E-15	0.35362E-02	-0.16925E+01	0.54365E-03
27	194	196	0.55543E-16	0.58597E-03	-0.40416E+00	0.46755E-03
24	169	174	0.58001E-18	0.35209E-03	-0.24649E+00	0.30870E-03
25	183	185	0.15874E-18	0.34695E-03	-0.41843E+00	0.27436E-03

Table AA.5 -Fatigue Parameter obtained by using the critical plane model (the Fatemi and Socie model) with σ_n^{max} normalised with σ_y, $(K = 1.0)$

The number of effective loading cycles in the plane orientation equals== 37

The total damage equals== 1.2413740E-04

The angle in radian == 1.256637, The angle in degree == 72 °

index	Cycles start	Cycles End	Cycles damage	γ_a	$\frac{\sigma_n^{max}}{\sigma_y}$	F.B
37	118	127	0.12396E-03	0.89860E-02	-0.31757E-01	0.87006E-02
36	137	158	0.11380E-06	0.83213E-02	-0.60020E+00	0.33269E-02
35	167	199	0.67850E-07	0.40808E-02	-0.22426E+00	0.31657E-02
28	188	191	0.10880E-11	0.19220E-02	-0.40207E+00	0.11492E-02
27	194	196	0.22449E-17	0.58597E-03	-0.40416E+00	0.34914E-03
24	169	174	0.10984E-18	0.35209E-03	-0.24649E+00	0.26530E-03

Table AA.6 -Fatigue Parameter obtained by using the critical plane model (the Fatemi and Socie model) with σ_n^{max} normalised with HB , (K = 0.0)

The number of effective loading cycles in the plane orientation equals== 36

The total damage equals== 3.3631953E-04

The angle in radian == 0.4886922, The angle in degree == 28^o

index	Cycles start	Cycles End	Cycles damage	γ_a	$\frac{\sigma_n^{max}}{\sigma_y}$	F.B
36	142	160	0.16593E-03	0.93421E-02	-0.34603E+00	0.93421E-02
35	125	130	0.12785E-03	0.87633E-02	-0.29991E+00	0.87633E-02
16	132	136	0.31051E-04	0.65628E-02	-0.44877E+00	0.65628E-02
19	148	155	0.10944E-04	0.55633E-02	-0.34603E+00	0.55633E-02
18	150	152	0.32197E-06	0.36861E-02	-0.44889E+00	0.36861E-02
34	121	123	0.22342E-06	0.35541E-02	-0.18010E+00	0.35541E-02
33	194	199	0.52419E-08	0.24917E-02	-0.16027E+00	0.24917E-02
23	187	188	0.26596E-11	0.12467E-02	-0.19565E+00	0.12467E-02
32	201	206	0.39408E-13	0.84965E-03	-0.24677E-01	0.84965E-03
26	195	197	0.78000E-15	0.59460E-03	-0.17120E+00	0.59460E-03
21	169	172	0.24363E-15	0.53486E-03	-0.12087E+00	0.53486E-03
25	190	191	0.15847E-15	0.51433E-03	-0.17874E+00	0.51433E-03
20	163	165	0.98384E-18	0.32389E-03	-0.16114E+00	0.32389E-03
22	182	184	0.15434E-18	0.27365E-03	-0.19960E+00	0.27365E-03

Table AA.7 - Fatigue Parameter obtained by using the critical plane model (the Fatemi and Socie model) with σ_n^{max} normalised with HB , $(K = 0.1)$

The number of effective loading cycles in the plane orientation equals== 36

The total damage equals== 2.8885476E-04

The angle in radian == 0.4886922 , The angle in degree == 28 °

index	Cycles start	Cycles End	Cycles damage	γ_a	$\frac{\sigma_n^{max}}{\sigma_y}$	F.B
36	142	160	0.14397E-03	0.93421E-02	-0.34603E+00	0.90188E-02
35	125	130	0.11226E-03	0.87633E-02	-0.29991E+00	0.85004E-02
16	132	136	0.23707E-04	0.65628E-02	-0.44877E+00	0.62683E-02
19	148	155	0.85221E-05	0.55633E-02	-0.34603E+00	0.53708E-02
18	150	152	0.20306E-06	0.36861E-02	-0.44889E+00	0.35206E-02
34	121	123	0.18611E-06	0.35541E-02	-0.18010E+00	0.34901E-02
33	194	199	0.43912E-08	0.24917E-02	-0.16027E+00	0.24518E-02
23	187	188	0.21420E-11	0.12467E-02	-0.19565E+00	0.12223E-02
32	201	206	0.38370E-13	0.84965E-03	-0.24677E-01	0.84755E-03
26	195	197	0.64520E-15	0.59460E-03	-0.17120E+00	0.58442E-03
21	169	172	0.21348E-15	0.53486E-03	-0.12087E+00	0.52840E-03
25	190	191	0.13017E-15	0.51433E-03	-0.17874E+00	0.50514E-03
20	163	165	0.82302E-18	0.32389E-03	-0.16114E+00	0.31867E-03
22	182	184	0.12361E-18	0.27365E-03	-0.19960E+00	0.26819E-03

Table AA.8 - Fatigue Parameter obtained by using the critical plane model (the Fatemi and Socie model) with σ_n^{max} normalised with HB , (K = 0.2)

The number of effective loading cycles in the plane orientation equals== 37

The Total damage equals== 2.5743846E-04

The angle in radian == 0.8203048, The angle in degree == 47 °

index	Cycles start	Cycles End	Cycles damage	γ_a	$\frac{\sigma_n^{max}}{\sigma_y}$	F.B
37	139	159	0.13149E-03	0.92259E-02	-0.21852E+00	0.88227E-02
36	120	130	0.10786E-03	0.85410E-02	-0.69059E-01	0.84230E-02
17	132	136	0.91425E-05	0.59520E-02	-0.44403E+00	0.54234E-02
19	147	155	0.80676E-05	0.56282E-02	-0.26487E+00	0.53301E-02
18	149	152	0.47056E-06	0.41824E-02	-0.42016E+00	0.38310E-02
35	186	199	0.39753E-06	0.38556E-02	-0.11728E+00	0.37652E-02
16	123	125	0.11995E-07	0.28021E-02	-0.19981E+00	0.26902E-02
28	188	192	0.49861E-09	0.20575E-02	-0.11925E+00	0.20084E-02
27	195	196	0.61631E-16	0.48627E-03	-0.14679E+00	0.47199E-03
34	202	205	0.93741E-17	0.40085E-03	-0.40662E-01	0.39759E-03
24	168	170	0.27874E-17	0.36271E-03	-0.91331E-01	0.35608E-03
25	182	183	0.16511E-18	0.28413E-03	-0.15450E+00	0.27535E-03

Table AA.9 -Fatigue Parameter obtained by using the critical plane model (the Fatemi and Socie model) with σ_n^{max} normalised with HB , $(K = 0.5)$.

The number of effective loading cycles in the plane orientation equals== 36

The total damage equal== 2.1364642E-04

The angle in radian == 0.9773844, The angle in degree == 56^{o}

index	Cycles start	Cycles End	Cycles damage	γ_a	$\frac{\sigma_n^{max}}{\sigma_y}$	F.B
36	120	159	0.14336E-03	0.91905E-02	-0.39493E-01	0.90090E-02
20	129	138	0.66696E-04	0.85783E-02	-0.23093E+00	0.75878E-02
19	145	154	0.24882E-05	0.54481E-02	-0.31357E+00	0.45939E-02
17	131	136	0.52066E-06	0.50007E-02	-0.45184E+00	0.38709E-02
35	186	199	0.49637E-06	0.40794E-02	-0.11160E+00	0.38517E-02
18	149	152	0.81222E-07	0.41573E-02	-0.45070E+00	0.32204E-02
28	188	192	0.56823E-09	0.21526E-02	-0.11160E+00	0.20325E-02
16	123	124	0.10023E-10	0.16284E-02	-0.27259E+00	0.14065E-02
27	195	196	0.13925E-15	0.54549E-03	-0.13629E+00	0.50831E-03
25	168	170	0.22481E-17	0.36439E-03	-0.83406E-01	0.34920E-03
26	181	183	0.87184E-18	0.34479E-03	-0.14191E+00	0.32032E-03
29	202	204	0.23050E-19	0.23676E-03	-0.55700E-01	0.23017E-03

Table AA.10 -Fatigue Parameter obtained by using the critical plane model (the Fatemi and Socie model) with σ_n^{max} normalised with HB ,$(K = 1.0)$

The number of effective loading cycles in the plane orientation equals== 37

The total damage equals== 1.6978345E-04

The angle in radian == 1.256637 , The angle in degree == 72^{o}

index	Cycles start	Cycles End	Cycles damage	γ_a	$\frac{\sigma_n^{max}}{\sigma_y}$	F.B
37	118	127	0.13572E-03	0.89860E-02	-0.10586E-01	0.88909E-02
36	137	158	0.33640E-04	0.83213E-02	-0.20007E+00	0.66565E-02
35	167	199	0.40829E-06	0.40808E-02	-0.74752E-01	0.37758E-02
18	131	135	0.14419E-07	0.57527E-02	-0.52424E+00	0.27369E-02
20	145	153	0.33906E-08	0.54933E-02	-0.56417E+00	0.23941E-02
28	188	191	0.63620E-10	0.19220E-02	-0.13402E+00	0.16644E-02
19	149	151	0.27338E-10	0.35362E-02	-0.56417E+00	0.15412E-02
17	122	124	0.14880E-13	0.11981E-02	-0.35102E+00	0.77752E-03
27	194	196	0.13539E-15	0.58597E-03	-0.13472E+00	0.50703E-03
24	169	174	0.95926E-18	0.35209E-03	-0.82165E-01	0.32316E-03
25	183	185	0.40248E-18	0.34695E-03	-0.13948E+00	0.29856E-03

References

ABUDAIA, F. B., EVANS, J. T. and SHAW, B. A. 2005. Spherical indentation fatigue cracking. *Materials Science and Engineering, A* 391**,**pp. 181-187.

AHLROOS, T., RONKAINEN, H., HELLE, A., PARIKKA, R., VIRTA, J. and VARJUS, S. 2009. Twin disc micropitting tests. *Tribology International,* 42**,** pp.1460-1466.

ALANOU, M. 2006. *Study of parameters influencing surface distress of gears.* PhD Thesis. Cardiff University.

ALFREDSSON, B., DAHLBERG, J. and OLSSON, M. 2008. The role of a single surface asperity in rolling contact fatigue. *Wear,* 264**,** pp. 757-762.

ALFREDSSON, B. and OLSSON, M. 2001. Applying multiaxial fatigue criteria to standing contact fatigue. *International journal of fatigue,* 23**,** pp. 533-548.

AMZALLAG C., GEREY J. P., and ROBERT, J. L. 1994. Standardization of the rainflow counting method for fatigue analysis. *Int. J. Fatigue,* 16**,** pp. 287-293.

BERNARD, J., HAMROCK, S. R. S., BO, O. and JACOBSON. 2004. *Fundamentals of Fluid Film Lubrication*, CRC Press Inc.

BJÖRLING, M., LARSSON, R., MARKLUND, P. & KASSFELDT, E. 2011. Elastohydrodynamic lubrication friction mapping–the influence of lubricant, roughness, speed, and slide-to-roll ratio. Proceedings of the Institution of Mechanical Engineers, Part J: Journal of Engineering Tribology, 225, 671-681.

BHUSHAN, B. 2002. *Introduction to Tribology*, John Wiley & Sons.

BOARDMAN, B. 1990. Fatigue resistance of steels. In: Metals Handbook,Tenth Edition. *Properties and Selection: Irons, Steels, and High-Performance Alloys.* Prepared under the direction of the ASM International Handbook Committee the direction of the ASM International Handbook Committee, 1, pp. 673-688.

BRYANT, M. J. 2013. *Running-in and residual stress: finite element contact analysis of as measured rough surfaces and comparison with experiment.* PhD Thesis , Cardiff University.

CHEN X. , XU S. and HUANG D. 1999. A critical plane-strain energy density criterion for multiaxial low-cycle fatigue life under non-proportional loading. *Fatigue Fract Engng Mater Struct,* 22**,** pp. 679-686.

CHALLEN, J. M. and OXLEY, P. L. B. 1979. An explanation of the different regimes of friction and wear using asperity deformation models. *Wear,* 53**,** pp. 229-243.

CHOI, Y. and LIU, C. R. 2006. Rolling contact fatigue life of finish hard machined surfaces: Part 1. Model development. *Wear,* 261**,** pp. 485-491.

CHATTERJEE, B. and SAHOO, P. 2012. Effect of Strain Hardening on Elastic-Plastic Contact of a Deformable Sphere against a rigidflat under full stick contact condition. *Advances in Tribology,* 2012**,** pp. 1-8.

CHU C. C., CONLE, F. A and BONNEN, J. F. 1993. Multiaxial stress-strain modeling and fatigue life prediction of SAE axle shafts. *In: Advances in Multiaxial Fatigue, ASTM STP 1191 (Edited by D. L. McDowell and R. Ellis), American Society for Testing and Materials, Philadelphia, PA,* pp. 37-54.

D'ERRICO, F. 2011. Micropitting Damage Mechanism on Hardened and Tempered, Nitrided, and Carburizing Steels. *Materials and Manufacturing Processes,* 26**,** pp. 7-13.

DOWLING, N. E. 2013. *Mechanical behavior of materials: engineering methods for deformation, fracture, and fatigue.Fouth edition,Pearson education,Inc.*

DOWSON, D. and DOWSON, D. 1979. *History of tribology, Longman London.*

EDWARDS, C. and HALLING, J. 1968. An analysis of the plastic interaction of surface asperities and its relevance to the value of the coefficient of friction. *Journal of Mechanical Engineering Science,* 10**,** pp. 101-110.

EVANS. H. P. 2015. Private Comunications.

EVANS, H. P. 2010. *Contact Mechanics Note,* Cardiff University.

EVANS, H. P. & SNIDLE, R. W. 2009. Some aspects of gear tribology. *Proceedings of the Institution of Mechanical Engineers, Part C: Journal of Mechanical Engineering Science,* 223**,** pp. 103-141.

EVANS, H. P., SNIDLE, R. W. and SHARIF, K. Analysis of micro-elastohydrodynamic lubrication and surface fatigue in gear micropitting tests. ASME 2011 International

Design Engineering Technical Conferences and Computers and Information in Engineering Conference, 2011. American Society of Mechanical Engineers, pp. 585-591.

EVANS, H. P., SNIDLE, R. W., SHARIF, K. J., SHAW, B. A. and ZHANG, J. 2012. Analysis of Micro-Elastohydrodynamic Lubrication and Prediction of Surface Fatigue Damage in Micropitting Tests on Helical Gears. *Journal of Tribology,* 135**,** pp. 11501-11510.

EVANS, H. P. & SNIDLE, R. W. 1996. A Model for Elastohydrodynamic Film Failure in Contacts Between Rough Surfaces Having Transverse Finish. Journal of Tribology, 118, 847-857.

FABRE, A., BARRALLIER, L., DESVIGNES, M., EVANS, H. P. and ALANOU, M. P. 2011. Microgeometrical influences on micropitting fatigue damage: multi-scale analysis. *Proceedings of the Institution of Mechanical Engineers, Part J: Journal of Engineering Tribology,* 225**,** pp. 419-427.

FABRE, A., EVANS, H. P., BARRALLIER, L., SHARIF, K. J. and DESVIGNES, M. 2013. Prediction of microgeometrical influences on micropitting fatigue damage on 32CrMoV13 steel. *Tribology International,* 59**,** pp. 129-140.

FATEMI A., STEPHENS R.I, STEPHENS R.R. and FUCHS H.O. 2000. *Metal Fatigue in Engineering*, Wiley Interscience.

FAULKNER A. , A. R. D. 2000. The development of a finite element model to simulate the sliding interaction between two, three-dimensional, elastoplastic, hemispherical asperities. *Wear,* 242**,** pp. 114-122.

FERNANDEZ RICO, J. E., HERNANDEZ BATTEZ, A. and GARCIA CUERVO, D. 2003. Rolling contact fatigue in lubricated contacts. *Tribology International,* 36**,** pp. 35-40.

FLODIN, A. and ANDERSSON, S. 2000. Simulation of mild wear in helical gears. *Wear,* 241**,** pp. 123-128.

GREEN, A. P. 1955. Friction between Unlubricated Metals: A Theoretical Analysis of the Junction Model. *Proceedings of the Royal Society of London A: Mathematical, Physical and Engineering Sciences,* 228**,** pp. 191-204.

GUPTA, B. 1991. *Handbook of tribology: materials, coatings, and surface treatments*, New York : McGraw-Hill.

HALME, J. and ANDERSSON, P. 2010. Rolling contact fatigue and wear fundamentals for rolling bearing diagnostics-state of the art. *Proceedings of the Institution of Mechanical Engineers, Part J: Journal of Engineering Tribology,* 224**,** pp. 377-393.

HANNES, D. and ALFREDSSON, B. 2011. Rolling contact fatigue crack path prediction by the asperity point load mechanism. *Engineering Fracture Mechanics,* 78**,** pp. 2848-2869.

HEGADEKATTE, V., HUBER, N. & KRAFT, O. 2005. Finite element based simulation of dry sliding wear. *Modelling and Simulation in Materials Science and Engineering,* 13**,** pp. 57-75.

HE, T., WANG, J., WANG, Z. & ZHU, D. 2015. Simulation of Plasto-Elastohydrodynamic Lubrication in Line Contacts of Infinite and Finite Length. Journal of Tribology, 137, 041505.

ISMAIL, R., TAUVIQIRRAHMAN, M., JAMARI and SCHIPPER, D. J. 2010. Two-Dimensional Finite Element Analysis on Running-in of Elastic-Plastic Rolling Contact. *AIP Conference Proceedings,* 1325**,** pp. 190-193.

ISMAIL, R., TAUVIQIRRAHMAN, M., JAMARI and SCHIPPER, D. J. 2011. The Observation of the Steady State Phase on Rolling Contact Using Finite Element Analysis. *AIP Conference Proceedings,* 1415**,** pp. 136-139.

ISMAIL, R., TAUVIQIRRAHMAN, M., SAPUTRA, E., JAMARI, J. and SCHIPPER, D. J. 2013. Modeling of Repeated Rolling Contact of Rigid Ball on Rough Surface: Residual Stress and Plastic Strain Analysis. *Procedia Engineering,* 68**,** pp. 593- 599.

JACKSON, R., CHUSOIPIN, I. and GREEN, I. 2005. A Finite Element Study of the Residual Stress and Deformation in Hemispherical Contacts. *Journal of Tribology,* 127**,** pp. 484-493.

JACKSON, R. L. and GREEN, I. 2005. A Finite Element Study of Elasto-Plastic Hemispherical Contact Against a Rigid Flat. *Journal of Tribology,* 127**,** pp. 343-354.

JAMARI, J., DE ROOIJ, M. B. and SCHIPPER, D. J. 2007. Plastic Deterministic Contact of Rough Surfaces. *Journal of Tribology,* 129**,** pp. 957-962.

JAMARI, J. and SCHIPPER, D. J. 2006a. An elastic–plastic contact model of ellipsoid bodies. *Tribology Letters,* 21**,** pp. 262-271.

JAMARI, J. and SCHIPPER, D. J. 2006b. Experimental Investigation of Fully Plastic Contact of a Sphere Against a Hard Flat. *Journal of Tribology,* 128**,** pp. 230-235.

JAMARI, J. and SCHIPPER, D. J. 2007a. Deformation due to contact between a rough surface and a smooth ball. *Wear,* 262**,** pp. 138-145.

JAMARI, J. and SCHIPPER, D. J. 2007b. Plastic deformation and contact area of an elastic–plastic contact of ellipsoid bodies after unloading. *Tribology International,* 40**,** pp. 1311-1318.

JAMARI, J. and SCHIPPER, D. J. 2008. Deterministic repeated contact of rough surfaces. *Wear,* 264**,** pp. 349-358.

JOHNSON, K. 1989. The strength of surfaces in rolling contact. *Proceedings of the Institution of Mechanical Engineers, Part C: Journal of Mechanical Engineering Science,* 203**,** pp. 151-163.

JOHNSON, K. L. 1985. *Contact Mechanics*.

KAPOOR, A. and WILLIAMS, J. 1994. Shakedown limits in sliding contacts on a surface-hardened half-space. *Wear,* 172**,** pp. 197-206.

KAPOOR, P. A., FLETCHER, D. D. I. and FRANKLIN, D. F. J. 2006. *Management and understanding of rolling contact fatigue.* Rail Safety and Standards Board.

KOGUT, L. and ETSION, I. 2002. Elastic-Plastic Contact Analysis of a Sphere and a Rigid Flat. *Journal of Applied Mechanics,* 69**,** pp. 657-662.

KORRES, S. 2013. *On-Line Topographic Measurements of Lubricated Metallic Sliding Surfaces*, KIT Scientific Publishing.

KRANTZ, T. L. and KAHRAMAN, A. 2004. An Experimental Investigation of the Influence of the Lubricant Viscosity and Additives on Gear Wear. *Tribology Transactions,* 47**,** pp. 138-148.

KUDISH, I. I. and BURRIS, K. W. 2000. Modern State of Experimentation and Modeling in Contact Fatigue Phenomenon: Part II—Analysis of the Existing Statistical Mathematical Models of Bearing and Gear Fatigue Life. New Statistical Model of Contact Fatigue. *Tribology transactions,* 43**,** pp. 293-301.

LI J ., LIU J. , SUN Q. , ZHANG Z. P . and QIAO Y. J. 2011. A modification of Smith–Watson–Topper damage parameter for fatigue life prediction under non-proportional loading. *Blackwell Publishing Ltd. Fatigue Fract Engng Mater Struct,* 35, pp. 301-316.

MCKELVEY, S. A. and FATEMI, A. 2012. Surface finish effect on fatigue behavior of forged steel. *International Journal of Fatigue,* 36**,** pp. 130-145.

MOORTHY, V. and SHAW, B. A. 2013. An observation on the initiation of micro-pitting damage in as-ground and coated gears during contact fatigue. *Wear,* 297**,** pp. 878-884.

MULVIHILL, D. M., KARTAL, M. E., NOWELL, D. and HILLS, D. A. 2011. An elastic–plastic asperity interaction model for sliding friction. *Tribology International,* 44**,** pp. 1679-1694.

NELIAS, D., DUMONT, M. L., CHAMPIOT, F., VINCENT, A., GIRODIN, D., FOUGERES, R. and FLAMAND., L. 1999. Role of Inclusions, Surface Roughness and Operating condition on rolling contact fatigue. *Transactions of the ASME,* 121.

NOVEXA.COM. 2015. *Gear - Defects treated* [Online] [Accessed 09 October 2015]. http://novexa.com/en/engrenage-defauts.php.

OILA, A. and BULL, S. J. 2005. Assessment of the factors influencing micropitting in rolling/sliding contacts. *Wear,* 258**,** pp. 1510-1524.

OLVER, A. 2002. Gear lubrication—a review. *Proceedings of the Institution of Mechanical Engineers, Part J: Journal of Engineering Tribology,* 216**,** pp. 255-267.

OLVER, A. V. 2005. The Mechanism of Rolling Contact Fatigue: An Update. *Proceedings of the Institution of Mechanical Engineers, Part J: Journal of Engineering Tribology,* 219**,** pp. 313-330.

OILA A, SHAWB A, AYLOTT C J and J, B. S. 2005. Martensite decay in micropitted gears. *Proc. IMechE Part J: J. Engineering Tribology,* 219, pp. 77-83.

ÖSTVIK, R. and CHRISTENSEN, H. Changes in surface topography with running-in. Proceedings of the Institution of Mechanical Engineers, Conference Proceedings, 1968. *SAGE Publications*, pp. 57-65.

PALIWAL, M. 1987. *Running-in and scuffing failure of marine gears.* PhD thesis, Cardiff University.

PAZDANOWSKI, M. 2014. Residual stresses as a factor of railroad real fatigue. Cracow University of Technology. Faculty of Civil Engineering. *TECHNICAL TRANSACTIONS* 4-B (12),pp. 39-46.

PETTERSSON, A. 2007. High-performance base fluids for environmentally adapted lubricants. *Tribology international,* 40**,** 638-645.

RABINOWICZ, E. R., E. 1966. *Friction and Wear of Materials (Science & Technology of Materials)*, John Wiley & Sons Inc.

RINGSBERG, J. W. 2001. Life prediction of rolling contact fatigue crack initiation. *International Journal of Fatigue,* 23**,** pp. 575-586.

SAHOO, P., CHATTERJEE, B. and ADHIKARY, D. 2010. Finite Element based Elastic-Plastic Contact of Strain Hardening. *International Journal of Engineering and Technology,* 2(1)**,** pp. 1-6.

SHANKAR, S. and MAYURAM, M. M. 2008. A Finite Element Based Study on the Elastic-Plastic Transition Behavior in a Hemisphere in Contact With a Rigid Flat. *Journal of Tribology,* 130**,** pp. 1-6.

SHARIF, K., EVANS, H. and SNIDLE, R. 2012. Modelling of elastohydrodynamic lubrication and fatigue of rough surfaces: The effect of lambda ratio. *Proceedings of the Institution of Mechanical Engineers, Part J: Journal of Engineering Tribology,* 226**,** pp. 1039-1050.

SNIDLE, R. W., EVANS, H. P., Alanou, M. P. and Holmes, M. J. A. 2004. Understanding scuffing and micropitting of gears. Presented at: Paper presented at NATO Research and Technology Organisation Specialists' Meeting on The Control and Reduction of Wear in Military Platforms, Virginia, USA, , vol. RTO-MP. NATO Publication.

SNIDLE, R. W., EVANS, H. P. and QIAO, H. 2008. Comparison of fatigue model results for rough surface elastohydrodynamic lubrication. *Proceedings of the Institution of Mechanical Engineers, Part J: Journal of Engineering Tribology,* 222**,** pp. 381-393.

SNIDLE, R. W., DHULIPALLA, A. K., EVANS, H. P. and COOPER, C. V. 2008. Scuffing Performance of a Hard Coating Under EHL Conditions at Sliding Speeds up to 16 m⁄s and Contact Pressures up to 2.0 GPa. *Journal of Tribology,* 130**,** pp. 1-10.

SWAHN, H., BECKER, P. and VINGSBO, O. 1976. Martensite decay during rolling contact fatigue in ball bearings. *Metallurgical transactions A* 7**,** 1099-1110.

SURESH S. 1998. *Fatigue of Materials*, Cambridge University Press.

TALLIAN, T. E. 1992. The Failure Atlas for Hertz Contact Machine Elements.New York, N.Y., ASME Press.

TANGENA AG. and PJM., W. 1985. Finite element calculations on the influence of surface roughness on friction.pdf. *Wear,* 103(4)**,** pp. 345-354.

TORBACKE, M. and KASSFELDT, E. 2014. *Lubricants: Introduction to Properties and Performance*, John Wiley & Sons.

TORRANCE, A. A., GALLIGAN, J. and LIRAUT, G. 1997. A model of the friction of a smooth hard surface sliding over a softer one. *Wear,* 212**,** pp. 213-220.

TURNER, M., CLOUGH R. W., MARTIN H. C. and TOPP L. J. 1956. Stiffness and Deflection Analysis of Complex Structures. 23(9)**,** pp. 805-823.

WEEKS, I. 2015. *An Experimental Investigation into the Mixed Lubrication of Steel Surfaces.* PhD, Cardiff University.

WIDMARK , M. and MELANDER , A. 1999. Effect of material, heat treatment, grinding and shot peening on contact fatigue life of carburised steels. *International Journal of Fatigue,* 21**,** pp. 309-327.

WILLIAMS, J. 1994. *Engineering tribology*, Cambridge University Press.

WYMAN Z. ZHUANG A, G. R. H. 2001. Investigation of residual stress relaxation under cyclic load. *International Journal of Fatigue,* 23**,** pp. 31-37.

ZAHAVI E. and TORBILO V. 1996. *Fatigue Design, Life Expectancy of Machine Parts,* CRC Press.